ABSTRACT

Title of Dissertation: A NEW HOPE:
CAN WE PREDICT
GEODYNAMO DYNAMICS?

Artur Perevalov
Doctor of Philosophy, 2023

Dissertation Directed by: Professor Daniel P. Lathrop
Department of Physics
Department of Geology

The Earth's magnetic field is hugely important, as it protects the surface of the planet from cosmic radiation and charged particles coming from the Sun and enables navigation for many living species. However, how it is generated and why it changes its value and configuration in time is poorly understood. The leading theory for the generation of the Earth's magnetic field is the geodynamo: an electrically conductive fluid in the Earth's core creates and maintains a magnetic field over an astronomical time scale. To probe this theory experimentally, the Three Meter Experiment—a 3 meter diameter spherical-Couette apparatus—was built to model the Earth's core. The experiment consists of two rotating concentric spheres with liquid sodium between them. The rotating spheres generate fluid motion and reproduce the dynamics similar to those that occur in the planet's core. The previous generation of the experiment was not able to generate a self-sustaining magnetic field. However, numerical studies suggest that increasing the roughness of the liquid to

the solid boundary should allow enable entering the dynamo regime. To test this, we first built a scaled-down model of the Three Meter sodium experiment. This was a 40-cm water experiment to examine the increase in helicity of the flow from installing baffles on the inner sphere. We then drained 12 tons of liquid sodium from the Three Meter experiment, cleaned, fixed, and upgraded it with baffles to increase surface roughness. We then re-filled the Three Meter experiment with sodium and performed several experiments. Here, we present the results of studying the torque scaling in the experiment. We show that the experiment's highest Reynolds number is limited by the maximum torque and power in the driving motors. We further investigate the magnetic data from various experiments and show that we are likely on the edge of the dynamo action. We present observation of traveling magneto-Coriolis modes and analyze their dynamics in different conditions. These structures are important for understanding some changes in celestial objects' magnetic fields and their mechanical properties. We also present a software tool developed to mimic the observed behavior of this magnetohydrodynamic experiment. This gives us a proper tool to predict the near future of dynamos, and allows us take a deeper look into its internal structure.

A NEW HOPE:
CAN WE PREDICT GEODYNAMO DYNAMICS?

by

Artur Perevalov

Dissertation submitted to the Faculty of the Graduate School of the
University of Maryland, College Park in partial fulfillment
of the requirements for the degree of
Doctor of Philosophy
2023

Advisory Committee:
Professor Daniel P. Lathrop, Chair/Advisor
Professor Yanne Chembo
Professor Sarah Eno
Professor Brian R. Hunt
Professor Vedran Lekić

Посвящяется моему главному преподавателю физики Кумачевой Н.К.

Acknowledgments

The one person who is responsible for all this happening is my advisor Prof. Daniel P. Lathrop. I want to thank him for inviting me to the laboratory and guiding me through this forest of incredibly hard problems full of all the possible traps and puzzles. Dan, you showed me more professional respect than anyone, you treated me not like a student but like a colleague. I learned from you not only the way to do research in this field that I was new in when I started, not just the ethics and the way systems function but also what the hell is going on around here. The first year I was totally lost and confused, finding myself in a tough spot and you were always supportive, even when I got stuck in Russia twice. That was a good long ride that I would advise anyone to take. Also, while you are not a big fan of Star Wars, I consider myself your padawan, and you let me name the project "A New Hope"! So May the force be with you!

Another significant role during this journey definitely goes to Rubén G. Rojas. We've spent six years shoulder to shoulder, fighting with all these new things. Crawling through the trenches covered in debris, cleaning unrealistic amount of hazmat waste, fighting for the colors on the plots, hating the imperial system, the "ninety-one elevenths" wrench haunts me in my dreams ($91/11 - 11/16$). All of these would be unbearable without you. Eres la razon principal por la que puedo hablar una idioma nueva. Y por supuesto verte todos los diaz ma ayudaba mucho. Espero que podamos vernos en el futuro! Muchas gracias por todo.

Special thanks to Brian Hunt and Sarah Eno, your help with research and teaching, regular conversations, and even jokes let me not just understand better the way science and education work, but also the way people in this field interact with each other.

I have to mention National Science Foundation for sponsoring the research.

Working with heavy machinery is hard, that's why I have to mention Nolan Ballew and Don Martin. Nolan seems to be a genie, you just need to explain what kind of part you want, or what kind of problem you have, and poof! it's solved. All of that with a pleasant conversation that just makes your day much better. And Don, even if I count all the words in English that I know, that wouldn't be even half of the tricks you showed me. I keep using your advice in the lab and in my regular life, you are definitely full of technical wisdom, thank you for showing me a part of it. Other people who were there and helped are Don Schmadel and Bryan Quinn: soldering, lifting, moving things, thank you.

I am also very thankful to people in IREAP and Physics department: Jessica Crosby, Josiland Chambers, Donna Hammer, Judi Gorsky, Dorothea Brosius, Roxanne Defendinni, Taylor Prendergast, Meredith Pettit, and, of course, my number one helper with documents Nancy Boone: you made it possible for me to go through all the bureaucracy (I even can spell this word now) and not go crazy. Surely I need to mention people who were here before me and put an incredible amount of work to make this experiment happen: Santiago and Axl.

And there is no way I would be able to handle these six years without my friends, thank you: Monica (for TH), Mary (for freak on a leash), Vlad (for Ba'aba), Dina (for breakfasts), Giulia (for despashivers), Landry (for microwaves), Tasha (for wine tasting), Natalia (for lunches), Harry (for US 101), Liz (for GradComm), Katya (for Venice), Annie

(for GSG), Juan (for три idiomas), Stan (for пупк), Tornike (for stronk), Fenya (for engine). All those days we were able to leave the work behind us and just enjoy sports, a drink, nature, or just a regular human conversation. Some of you were a huge support in my professional growth. Showing your perspectives, sharing your experience, or just giving advice on how to setup a LAN, debug my code, or write a letter, all these things helped a lot. The climbing hispanohablantes: Isra, Moni, Kris, Denis, Sergio, Maddie, y Quique, estoy agradecido por encontrarlos y pasar tanto tiempo con ustedes escalando en los gimnasios y afuera, tomar chelas y comer pizzas, y de todos modos hablar y reir. Another side thanks goes to my DC area comrades: Сергей, Мария, Соня, Паша, мне было приятно встретить людей с которыми было много общего, с которыми было смешно и весело и заодно можно было разговаривать на первом языке, шарить мемасики, орать и, в отдельных случаях, рыдать вместе из за происходящего вокруг ужаса. До того как вы появились рядом, я очень сильно недооценивал насколько мне было необходимо общаться по-русски.

Kudos to my colleagues and collaborators: Itamar, Jaideep, Sarah, Heidi M., Heidi K., Santiago, Henri-Claude, Ankit, Liam, Peter, you were there when I needed you! And special kudos to Elaine and Shelley: please take care of her.

Additional huge thanks to that dude who sold me an old E46 BMW without telling me it has a rebuilt title. I didn't even know the meaning of this, but I added another 50k on that beast and it is still running nicely (but not smoothly). I've spent numerous hours repairing that car. I am not even sure this car hasn't turned into The Ship of Theseus - not that many parts are original. I've spent two summers driving that 230 hp small car in over 90 F and only on the third year I realized that I know how to design and fabricate a

pressurized/vacuum system and just fixed that AC in one day.

And of course thanks to my family: my mom and my dad. You let me leave you knowing we will be separated for quite a while, you wanted a better education, exposure to ideas, and life experience for me even though I would be so far away and the world around us would not let us meet for many years. I don't know how one can do that and I respect you and love you.

Table of Contents

List of Tables

List of Figures

List of Abbreviations

E	Ekman Number
Re	Reynolds Number
Rm	Magnetic Reynolds Number
Ro	Rossby Number
Pm	Magnetic Prandlt Number
Le	Lehnert Number
Ek	Ekman Number
Em	Magnetic Ekman Number
$\vec{U}$	Fluid Velocity
$\vec{B}$	Magnetic Field
ν	Kinematic Viscosoty
η	Magnetic diffusivity
σ	Conductivity
ρ	Mass Volume Density
P	Pressure
S	Power spectral density
ω	Velocity/Magnetic field angular frequency
Ω	Containers angular frequency
ℓ	Degree of the Spherical Harmonics
m	Order of the Spherical Harmonics, azimuthal number
T	Temperature
α	Thermal diffusivity
τ_D	Dipole diffusion time scale
τ	Dimensional torque.
G	Dimensionless torque
G_∞	Dimensionless torque at $Ro = \infty$
$\vec{t}_l^m$	Toroidal vector spherical harmonics
$\vec{s}_l^m$	Poloidal vector spherical harmonics
Y_ℓ^m	Scalar spherical harmonics
$\mathcal{E}$	Electromotive force
MHD	Magnetohydrodynamics
IM	Inertial Modes
CFD	Computational Fluid Dynamics / Colorful Fluid Dynamics
RMS	Root Mean Square

PSD	Power Spectral Density
RC	Reservoir Computer
AR	Auto-Regressive
LSTM	Long short-term memory
Na	sodium, Not available
LAN	Local Area Network
OSTE	One Time Step Error
DC	Direct current, District of Columbia
PTFE	Polytetrafluoroethylene
SOP	Standard Operation Procedure
PIV	Particle Image Velocimetry
FPS	Frames Per Second
SSM	Seconds Since Midnight
3M	The Three Meter Experiment
40-cm	The Forty centimeter experiment
IREAP	Institute for Research in Electronics and Applied Physics
NSF	National Science Foundation
UMD	University of Maryland College Park
ESSR	Environmental Safety, Sustainability and Risk
TraMon	Transfer Monitor application
BigMo	Big Momma application

Chapter 1: Introduction

1.1 Motivation

1.1.1 Where do we see magnetic fields?

Planet Earth is the home of our civilization, life appeared on this planet and evolved for approximately four billion years, and during all these years the surface of the planet has likely been shielded by the magnetic field from the harmful effects of charged particles [10, 11] allowing the organisms to live long and prosper.

William Gilbert in 1600 [12] realized that compass arrows point to the north and south because the planet itself is a giant magnet, and even though travelers across the oceans and seas have been logging the direction of the magnetic field, we haven't been able to model the field until 1835 when Carl Friedrich Gauss fit the Earths magnetic field [13] to spherical harmonics with high precision. Along the way he also invented the least-square fitting and came up with the idea of Gauss coefficients. Since then we have been tracking the configuration and dynamics of the field. We can see that the magnetic field has decayed approximately 10% over the last 170 years [14], and also the shape of the field has been changing. Current models say that the northern magnetic pole in the last seven thousand years moved chaotically around the geographic pole without a specific preference

in location. More recently it has been quasi-stably wiggling in northern Canada between the sixteen and twentieth centuries. Even closer to our times, during the twentieth century, it was moving north with the characteristic speed on the order of ten kilometers per year, but in the last thirty years, it started accelerating and is currently running towards Siberia at 50-60 km/yr [3]. Fig. 1.1 demonstrates the observational position of the north magnetic pole. It is known that the magnetic field is changing, but there is no understanding of the mechanisms that generate it, nor is there a reasonable tool to predict its behavior.

When paleomagnetic methods were developed and rocks magnetism, paleointensity, magnetic mineralogy, etc was analyzed, it was discovered that the direction of the field was not always the same. Even more than that, the magnetic poles have been switching many times in the planet's history. For example, in the last ten million years there were four to five polarity switches every million years on average [15, 16, 17]. Moreover, several hundred reversals in the last 160 million years have been estimated, and the most recent one happened 380 thousand years ago; the reversals expect to take several thousand years to complete, that is incredibly slow for a human being but unbelievably fast on the timescale of the planet [18]. Plus, there is evidence of a brief reversal 41-42 thousand years ago that some researchers even connect with Laschamps Excursion [19].

Outside the Earth, other astronomical objects also have (or at least had) magnetic fields: Mercury has a weak magnetic field, Venus does not, Mars has signs of having had a magnetic field in the past, Jupiter has the strongest planetary magnetic field, incredibly symmetric Saturn's field stays a huge mystery, fields on Uranus and Neptune are quite different in shape from others and on the top of dipole field have strong quadrupoles and the angles between rotation axles and the magnetic fields are unusually large. The moon

had a field a long time ago, and helioseismology with other tools give a lot of information about the Sun's interior and its magnetic field [20, 21, 22, 23, 24, 25, 26, 27, 28, 29, 30]. The mechanisms of generation of these fields are also important for humanity.

However, we will focus here on the Earth's magnetic field. The tools to understand the processes that happen inside the Earth's core come from seismology - the science that investigates phenomena that normally comes with a negative connotation, earthquakes. Qualitative measurements of waves propagating through the planet give information about interior structure of the Earth and show that under a thin layer of crust there is a thick mantle that is almost solid. Under that, there is a core that consists of a liquid outer part and a solid inner part, with the radii ratio $\Gamma = r_i/r_o = 0.35$ [31, 32, 33, 34]. This number will follow us for quite a while in this thesis. The author would like to specifically mention work by Inge Lehman, who hypothesized the liquid composition of the part of the core [35].

1.1.2 What does theory say?

It started with the Cowling anti-dynamo theorem [36], which tells us that two dimensions is not enough to understand the formation of the Earth's magnetic field. Later quantitative works by Elsasser [37, 38, 39] and Bullard [40, 41, 42] created the tools that we are using today when we talk about processes creating self-sustainable magnetic fields (dynamos). However, the first experimental examples of these dynamo systems appeared later with works of Backus [43] and Herzenberg [44]. After that researchers like Parker [45], Steenbeck [46], and Roberts [47] came up with the idea that poloidal and toroidal fields can generate each other (α and ω effects) and with some stretching (hence amplification)

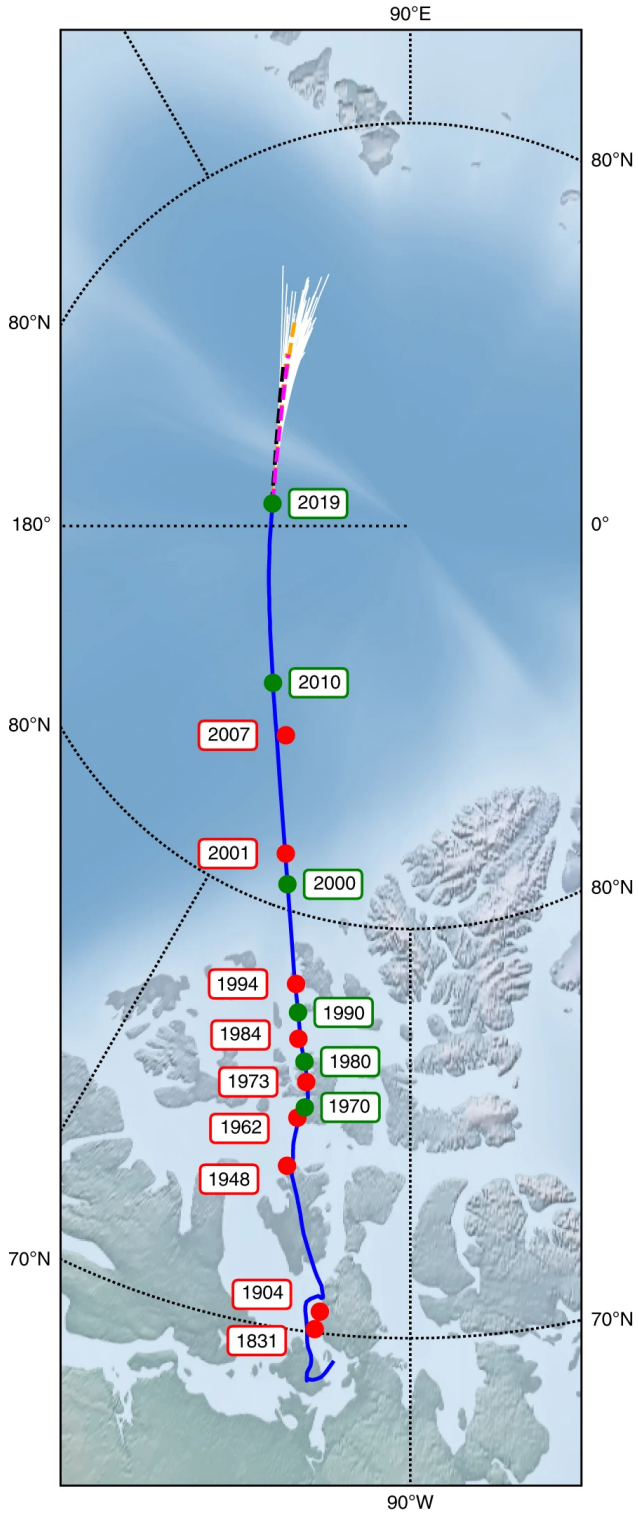

Figure 1.1: North Magnetic Pole movements during the last two centuries, picture credits to Livermore, Nature Geoscience 2020 [3].

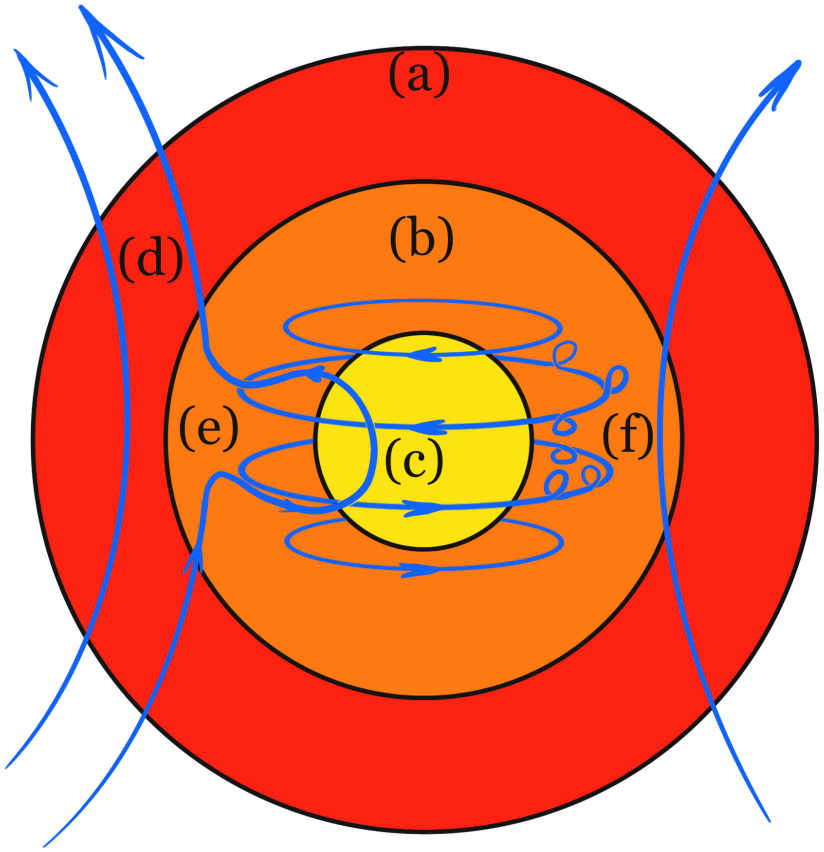

Figure 1.2: Schematics of $\alpha\omega$ dynamo: (a) Mantle, (b) liquid outer core , (c) solid inner core, (d) dipole magnetic field lines, (e) Ω-effect where B_z gets twisted and amplified to produce azimuthal field, (f) α-effect where azimuthal field is converting into dipole field to reinforce original B_z.

create dynamos.

An example of a kinetic spherical dynamo [48] is demonstrated schematically in Fig. 1.2. The outer core is an ocean of liquid iron and nickel. It is located between the solid inner core (1220 km) and solid mantle (3470 km). In the presence of a moving conductive fluid, the magnetic field gets stretched, twisted, and folded [30, 49, 50], in such way that on the left the original dipole field transforms into a toroidal field which later transforms into a dipole field. These effects are shown to be connected with the vorticity ($\vec{\omega} = \nabla \times \vec{U}$) and helicity ($H = \int_V \vec{U} \cdot \vec{\omega}\, dV$) of the flow [51, 52, 53, 54, 55, 56, 57, 58].

1.1.3 Laboratory experiments

Even now when we have so much computational power available, running to a computer and asking it to solve your dynamo problem might not be the most fruitful approach. These simulations are computationally expensive and stay several orders of magnitude away from the Earth in their Ekman, Reynolds, and Prandtl numbers (defined in Section 2.1) [47, 59, 59, 60, 61, 62, 62, 63, 64, 65, 66, 67, 68]. On the other hand there are people working on and building laboratory experiments that in many situations demonstrate incredibly complex dynamics and provide rich and interesting data. For instance there are experiments like the twisted pipe flow by Benton [69], or cylinder flows in Riga, Latvia [70, 71, 72, 73], Cadarache, France [74, 75, 76], Karlsruhe, Germany [77], Dresden, Germany [78]. However, these experiments, while in some cases able to show magnetic field generation, do not match the geometrical properties of interest for astronomical objects - they are not spheres. However, the lack of physical restrictions in a sphere creates more difficulties on the experimental side.

Spherical experiments are important in the topics of rotation turbulence, dynamo, magneto-rotational instabilities, and planetary dynamics [4, 79, 80, 81]. An example is spherical-Couette flow experiments, where the fluid is constrained between two concentric spheres. This configuration mimics the inner core by the inner sphere and the outer-core boundary by the outer sphere shell. Here, flows are driven by shear forces due to the interaction via shear rotation and with Coriolis forces. These experiments evolved from similar cylindrical setups known as Taylor-Couette flows [2, 80, 82, 83, 84, 85]. On the other hand, the reader might think that shear rotation and Coriolis would not be enough

to reproduce the dynamics of the planet, where we don't have such difference between rotation rates, but we have Rayleigh-Bernard convection due to buoyancy and gravity. Thankfully, there is a well investigated analogy between these drivers that says that if you reach a high Reynolds number (spin it with a strong shear) the statistical difference becomes negligible [34, 86, 87, 88, 89, 90, 91].

There are several recent spherical MHD experiments. DTS in Grenoble, France has a permanent magnet magnetic field in the inner sphere and liquid sodium, and it has shown magnetic field generation [92, 93]. MPDX - The Madison Plasma Dynamo eXperiment at the University of Wisconsin, USA [94] is build to reach the values that liquid metal experiments are not capable of achieving. And, we have the Geodynamo laboratory at The University Of Maryland, College Park, USA with quite a history of experimental devices with the same aspect ratio as the Earth's core. The group of Prof. Daniel P. Lathrop in IREAP has been building spherical shell experiments for quite a while: multiple dissertations were developed on these apparatuses: Sisan [4], Kelley [95], Zimmerman [96], Triana [7], Adams [97], Mautino [98], Burnett [99], and the sibling thesis to this one by Rubén Rojas [100].

We have built the Dynamo II (30-cm) experiment that was able to reach a magnetic Reynold number $Rm \approx 25$. We reported the observation of a Magnetorotational Instability, but did not yield a dynamo [4, 101, 102, 103, 104]. Later, Dynamo III and Dynamo 3.5 (60-cm experiment) were built, where inertial modes were observed and analyzed, but did not succeed in creating the necessary velocity fields to generate a self-sustainable magnetic field [5, 105, 106, 107, 108, 109]. The photos of these two apparatuses are shown on Fig. 1.3. And finally, the big one - The Three Meter, demonstrated in Fig. 1.4; this one

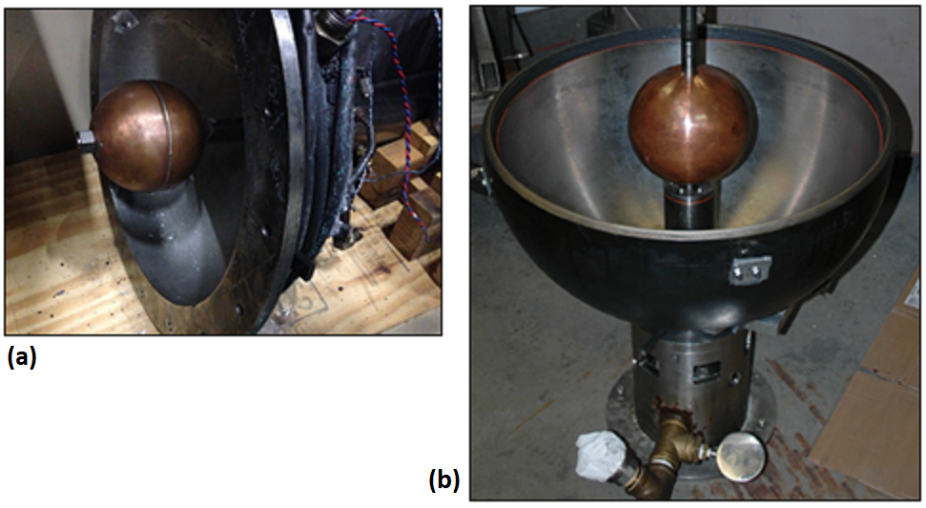

Figure 1.3: Photos of 30-cm dynamo experiment (a) and 60-cm dynamo experiment (b) at UMD. Photo credits to Sissan [4] and Kelley [5]

approximately matched the Earth's Magnetic Reynolds number $Rm \approx 1000$, reported such phenomena as inertial modes, precessional states, and bi-stability of the hydrodynamic flow [8, 58, 110, 111].

Even though the observed magnetic field turns and stretches, and the amplification in the azimuthal direction reached 8 times the externally applied field, plus the radial magnetic field gain reaches 20%, this biggest rotating liquid sodium device in the world has not created a self-sustainable magnetic field. On top of that, after less than four years of experiments, the experiment broke. At this point, we knew that we need to use this opportunity not just to repair the damage, but also to upgrade it.

According to numerical simulations [112, 113, 114] made specifically to analyze the effects of roughening the surface of the sphere, higher friction changes the boundary layer from viscosity-coupled to fully pressure-dominated, and this leads to a significantly more efficient angular momentum transfer from the sphere to the liquid. The simulation done by Finke and Tilgner, which was done directly in the configuration of spherical-Couette

Figure 1.4: Photo of Three-Meter Dynamo experiment, the outer sphere is visible through the cube door in the center of the picture, the rolling door (on the left) was one of the main designing constrains, because one cannot fit a sphere wider than the opening.

flows, concluded that increasing roughness of the inner sphere leads to a better coupling between the inner sphere and liquid sodium and it should lower the threshold for reaching the dynamo state in a parameter space with a factor of five allowing getting the dynamo with a lower magnetic Reynolds number [114].

Meanwhile, we didn't have a straightforward idea of how exactly we should "roughen" the inner sphere, so we created a model of the 3M experiment - a 40-cm water spherical-Couette experiment - and tested various options to proceed with the repair/upgrade.

Our big hopes were to upgrade the sphere, run new experiments, achieve the dynamo, analyze it using the available modern nonlinear dynamic techniques, and create a tool that would be able to mimic and predict the dynamics of the dynamo.

1.2 How to read this thesis

"At first I was planning to keep the sodium jokes away from this thesis, but then I was like, - Na, it's fine, people will get it" - Artur Perevalov

This thesis represents multiple research projects the author has been involved in between 2016 and 2022. The big goal here was to modify the experiment, observe the dynamo, and develop a qualitative and quantitative instrument with forecasting abilities.

So far we have introduced the reader to the problem of the existence and the evolution of the planet's magnetic field, and we showed the existing experimental setups. In the second chapter, we will develop vocabulary and present the basic theory of the phenomena that we are interested in.

Chapter 3 will be dedicated to the long project of rebuilding, fixing, and upgrading

the Three Meter Sodium Experiment. Here we will show the way we approached solving the engineering problems and safety protocols. In addition, there we will talk about the software and hardware that was developed. This part can also be used as storage of the techniques we applied to do all the things we had to do to fix and upgrade the experiment. Some of those things were known before us but got lost and forgotten in time so we had to reinvent them. So this chapter should be quite useful for people working with the experiment in the future.

In Chapter 4 we will switch to the software world and try to show the way we have been digging from the other side of the tunnel. Here we present the results of developing a software tool that would be capable of reproducing the dynamics of this MHD experiment and thus the magnetic fields of the Earth.

In Chapter 5, we will come back to the experimental data. Here we will look at many experimental runs in specific regimes where we can observe different interesting oscillating structures in this huge conductive fluid ball. We will show that we have found something interesting that we don't really understand.

Chapter 6 (*Return of the Sphere*) will be about our "New Hope" experiments that we have done after upgrading the apparatus, our findings and problems, our almost tragic experience of breaking the experiments after we repaired it, and the huge relief after we fixed it yet again.

In Chapter 7 we will talk about torque in rotating systems and its scalings. How much power do we need to spin the spheres with depending on the sizes or shapes or roughness of said spheres? Stay tuned.

And finally, in the last Chapter 8, we will conclude the results of these projects, and

make suggestions for future research.

Regarding other sources of information, the reader should also consider the dissertation of Rubén Rojas [100], which contains many details about the experiment and the research we were doing that are not explained in this thesis. And even more, technical details about the process of designing and developing the Three Meter Experiment can be found at Santiago Triana's thesis [7] and Daniel Zimmerman's thesis [96].

During all these years of working in the Geodynamo lab, we have been constantly using Akin's Laws of Spacecraft Design [115]. This set of simple rules was incredibly useful in many situations, sometimes to do sanity checks, sometimes to slow down and think about your next steps, or even to make a decision to go back. Therefore, in this thesis, I will add the Akin's Laws in the text to represent the ideas that we were following on different occasions.

Chapter 2: Basic theory

In this chapter, first, we will be developing the vocabulary by defining the dimensionless parameters, second, we will be building up the theory that is necessary for fluid dynamics, rotating fluids, magneto-hydrodynamics, dynamo effect, inertial waves and modes, and their magnetic siblings. After that, we will provide some origins of the predictive models we will be using in Chapter 4.

2.1 Dimensionless Parameters

In this section, we will define the necessary terminology related to the dimensionless parameters used in this field.

2.1.1 Reynolds number

To describe the level of nonlinearity in fluid we use the Reynolds number. It is usually defined as the ratio between inertial and viscous forces: $Re \equiv uL/\nu$, where u is the estimated magnitude of the characteristic velocity, L is a characteristic length scale, and ν is the kinematic viscosity. With large Re the fluid becomes turbulent, with small Re it is laminar. In the case of two concentric spheres we will rewrite the length as the gap

between the spheres and the velocity as the gap times difference of the rotational rates:

$$Re = \frac{|\Omega_i - \Omega_o|(r_i - r_o)^2}{\nu}, \tag{2.1}$$

here Ω_i and Ω_o are the angular frequencies of the inner and outer spheres, r_i and r_o are their radii respectively, and ν is liquid sodium kinematic viscosity at given temperature. For The Three Meter Experiment with this definition, Reynolds number can go as high as 7×10^8.

2.1.2 Magnetic Reynolds number

The magnetic analogue of the Reynolds number is represented by Rm - the ratio between the advection and induction of a magnetic field in a conductive fluid system:

$$Rm = \frac{|\Omega_i - \Omega_o|(r_i - r_o)^2}{\eta}, \tag{2.2}$$

here the kinematic viscosity (ν) is replaced with the magnetic diffusivity (η) of sodium. This number represents how much faster the fluid can drag the magnetic field compared with magnetic field diffusion. The 3M highest Rm was on the scale of 1000, which matches the Earth's estimated value [116].

2.1.3 Rossby number

To characterize the differential rotation of the spinning fluid we use the Rossby number. It is defined by the ratio between the rotational shear inertial force and the

Coriolis force:

$$Ro = \frac{\Omega_i - \Omega_o}{\Omega_o} \ . \tag{2.3}$$

Small Rossby numbers represent systems highly affected by Coriolis forces and large Rossby is mostly driven by inertial forces. In the case of Spherical-Couette experiments, we are able to vary the direction of the relative rotation so we can have positive and negative Ro. Also, because of the nature of division by outer sphere rotation rate, we can achieve a reasonably large Rossby number, but we have some difficulties with small Ro because of the way the motors work. We later will focus on the experiments with $-20 < Ro < -0.5$ and $1 < Ro < 20$.

2.1.4 Ekman number

The ratio of viscous forces to Coriolis forces is described by Ekman number:

$$E = \frac{\nu}{\Omega_o (r_i - r_o)^2}. \tag{2.4}$$

The Earth's Ekman number is on the scale of 10^{-15} [117], and for Three Meter it can go as low as 10^{-9}, which is many orders of magnitude away from the planet but is one of the lowest for an experimental apparatus.

2.1.5 Magnetic Ekman number

Our regular Ekman number but we will have magnetic diffusivity instead of kinematic viscosity:

$$E_m = \frac{\eta}{\Omega_o (r_i - r_o)^2}. \tag{2.5}$$

For a given material, this can be rewritten in terms of E and Prm.

2.1.6 Lehnert number

To describe the effects of the external magnetic field we will use the Lehnert number that is defined as the ratio between Alfvén speed ($V_a = B/\sqrt{\mu_o \rho}$) [118] and rotational velocity:

$$Le = \lambda = \frac{B}{\Omega_o r_o \sqrt{\mu_0 \rho}}, \tag{2.6}$$

where ρ is the liquid sodium mass volume density, and B is the approximate value of the external magnetic field in the center of the spheres. Like with the Rossby number here we have a division by Ω_o, so we could achieve a large number if desired, but to keep other numbers in a reasonable range will mostly talk about experiments with $Le < 0.1$.

2.1.7 Magnetic Prandtl number

The ratio between viscosity and magnetic diffusivity is constant for a given uniform material and does not depend on the properties of the flow:

$$Prm = \frac{\nu}{\eta}. \tag{2.7}$$

For liquid sodium, $Pr_m \approx 10^{-5}$.

2.1.8 Lundquist number

The ratio between the time is takes Alfvén wave to propagate across the system and the timescale of the resistive diffusion [119]:

$$S = \frac{B(r_o - r_i)}{\eta\sqrt{\mu_0 \rho}}. \tag{2.8}$$

The maximum value for 3M is $S = 10$.

2.1.9 Control parameters

During the experimental runs, the operators can control each of the rotation rates of the spheres. Their difference defines the Reynolds numbers, their ratio defines the Rossby number, and the operators can control the current in the external magnetic coils which defines the Lundquist number, and with the outer rotation rate they define Lehnert number. When we talk about experimental runs we will be mostly talking about Re, Ro, Le. All other numbers are either defined by the material or can be calculated via the known three ones.

2.2 Hydrodynamics

"Help me, Navier-Stokes Equation. You're my only hope." - R2R'ito

At some point, I was talking to my friend who was finishing her Ph.D. in mathematics in Finland working on parabolic equations solvers, and she told me that her advisors and

mentors from the field were all telling her that whatever she plans to do with her life, she should never even think about doing anything related to the Navier-Stokes equation. I took that advice seriously and in a couple of years I found myself seeing this formula everywhere, and six years later I am putting this masterpiece in my thesis. The moment any researcher starts working with fluids, they see this intimidating formula shown on Eq. 2.9, that is so popular that I will skip the derivation and leave it for the greatest [120, 121, 122]:

$$\frac{\partial \vec{U}}{\partial t} + (\vec{U} \cdot \nabla)\vec{U} = -\nabla \left(\frac{P}{\rho} \right) + \nu \nabla^2 \vec{U} \ , \tag{2.9}$$

here the fluid velocity is denoted as $\vec{U}$, P is the pressure field, ρ is the mass volume density of the media, and ν is the local kinematic viscosity.

2.2.1 Living on a rotating sphere

Lets take the Navier-Stokes equation and move to a rotating inertial frame with R being the position and ω_c being angular velocity and Ω_p being the precession vector such that $\omega = \omega_c + \Omega_p$. After doing some algebra [7] we can express:

$$\begin{aligned} \vec{U}_i &= \vec{U} + \vec{\omega} \times \vec{R} \ ; \\ \nabla^2 \vec{U}_i &= \nabla^2 \vec{U} \ ; \\ \vec{\omega}' &= \vec{\Omega}_p \times \vec{\omega}_c \ ; \\ \vec{\omega} \times (\vec{\omega} \times \vec{R}) &= -\tfrac{1}{2} \nabla (\vec{\omega} \times \vec{R})^2 \ . \end{aligned} \tag{2.10}$$

By adding the rotational pressure term into the regular equation for P in such a way that $p = P/\rho - \frac{1}{2}\nabla(\vec{\omega} \times \vec{R})^2$, then moving to the precessional frame, we can rewrite the

original equation of motion as:

$$\frac{\partial \vec{U}}{\partial t} + (\vec{U} \cdot \nabla)\vec{U} + 2\vec{\Omega}_p \times \vec{U} + \nabla p = \nu \nabla^2 \vec{U} \ , \tag{2.11}$$

2.2.2 Magnetohydrodynamics (MHD)

Let's take Maxwell equations 2.12 and Ohm's law 2.13

$$\begin{aligned} \nabla \times \vec{E} &= -\tfrac{\partial \vec{B}}{\partial t} \\ \nabla \times \vec{H} &= \vec{J} + \tfrac{\partial \vec{D}}{\partial t} \\ \nabla \cdot \vec{B} &= 0 \\ \nabla \cdot \vec{D} &= \rho_e \ , \end{aligned} \tag{2.12}$$

$$\vec{J} = \sigma \vec{E} + \sigma(\vec{U} \times \vec{B}) \ . \tag{2.13}$$

Here $\vec{E}$ is the electric field, $\vec{D}$ is the displacement field, $\vec{H}$ is the magnetizing field, $\vec{B}$ is the magnetic field, $\vec{J}$ is the current density field, $\vec{U}$ is the fluid velocity field, σ is the electric conductivity, ∇ is the nabla operator, μ_0 is the vacuum magnetic permeability, and ρ_e is the volume charge density.

Combining them and taking curl we obtain:

$$\frac{\partial \vec{H}}{\partial t} = \frac{1}{\sigma \mu_0} \nabla^2 \vec{H} + \nabla \times (\vec{U} \times \vec{H}) \ . \tag{2.14}$$

We assume that we have uniform permeability and $B = \mu H$. This Equation 2.14 is called the magnetic induction equation and it is probably one of the most important equations

in our studies of the dynamo. Without any velocities, it just turns into a magnetic field diffusion equation. In the case of a conductive sphere, the dipole magnetic field would exponentially decay with a characteristic timescale [123]:

$$\tau_D = r_o^2/(\pi^2\eta) \ , \tag{2.15}$$

here $\eta = (\sigma\mu_0)^{-1}\ m^2/s$ is the magnetic diffusivity.

So for us not to let the magnetic fields disappear we need to find a proper configuration of velocities to balance the heartless Laplacian.

2.3 Dynamo Theory

One of the big questions about the creation of magnetic fields is whether a simply-connected, symmetrical body of homogeneous and isotropic fluid is capable of creating a motion that would create a self-amplified dynamo that would continue transforming mechanical energy into a magnetic field without an external magnetic field. These are so-called "homogeneous dynamos", and the theory of determining if a specific motion is capable of creating these dynamos is brilliantly described by Bullard and Gelman [42].

We can start with a simple example of an "engineering dynamo" that is shown on Fig. 2.1. In this model, we have a conductive disc that rotates on an axle, and under it, we have a coil with its ends attached to the edge of the disc and the shaft with conductive brushes. In presence of an external magnetic field H_z that is aligned with the rotation axis, there will be an electromotive force $0.5H_z u_0 a$, where u_0 is the velocity of the edge of the disc and a is its radius. If we take R as the resistance of the circuit, L as its inductance

and do some algebra we get:

$$H = H_0 exp((\pi u - R)/Lt) \ , \tag{2.16}$$

so with a small velocity u any initial magnetic field will exponentially decay, but with a high enough velocity, any initial current or magnetic field will exponentially grow in time. While it is only an idealized process, if we add power dissipation, this would let us have a limit for the magnetic field.

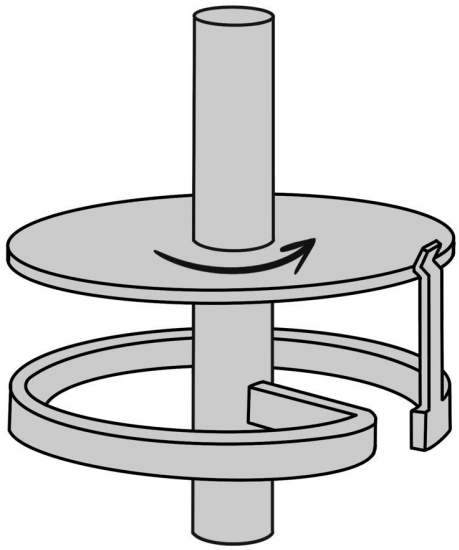

Figure 2.1: A simple homopolar dynamo with a rotating disc and a feedback loop connected to the shaft with a brush.

While this system is capable of transforming mechanical energy into a magnetic field, this disc dynamo is not able to demonstrate a magnetic reversal. To do that, we can take two discs next to each other and put feedback loops into each other's axles. This system can

be solved and shows the magnetic reversals with constant mechanical torque applied to the discs [124]. Even more, this system produces deterministic chaotic reversals. However, one of the most important differences for us between this simple dynamo and a sphere is that here the original system is not symmetrical, there are some core differences between the feedbacks: brushes with wire loops are operating on very different principles from the fluid motions in the core of the planet. Rotating the discs in different directions has a different effect on the outcome [125], while the objects that we are interested in are normally spheres and have more symmetry. So we have two conclusions: we need to be three-dimensional and rotate fast.

Some other dynamo geometries and approaches are studied and analyzed in different sources [50, 126, 127, 128, 129], but in this work, we will stay within the theory of spherical kinematic dynamos.

2.3.1 Spherical Dynamos

Probably the most important mathematical achievement in dynamo theory is called the *Cowling anti-dynamo theorem* [36]. This theorem says: An axisymmetric magnetic field cannot be maintained via dynamo action. In some way, it is the same as a Möbius strip which cannot live on a flat surface. And as we observe the magnetic fields of the planets, we see that only Saturn is acting not the same way the others do. Its magnetic dipole tilt is on a scale of 0.01° [24], while on Earth the magnetic field tilt is $\sim 11.5^\circ$, and other planets also demonstrate a significant tilt. The reasons behind the Saturn being so axisymmetric are still under debate.

To proceed with our three-dimensional systems we will take the magnetic induction equation 2.14 and rewrite it:

$$\frac{\partial \vec{H}}{\partial t} = \frac{1}{\sigma \mu_0} \nabla^2 \vec{H} - (\vec{U} \cdot \nabla)\vec{H} + (\vec{H} \cdot \nabla)\vec{U} \ , \tag{2.17}$$

the first term on the right hand is the familiar magnetic diffusion term and stays the same, the second one represents the gradient of the magnetic field in the direction of the field itself or can be interpreted as the convection of the magnetic field with the moving media, and the last term is the field multiplied by the gradient of the fluid velocity in the direction of velocity and can be interpreted as the fluid stretching the magnetic lines. These two effects are our sources of possible dynamo action, that otherwise would vanish with the heartless Laplacian.

To analyze the energy balance we will multiply Eq. 2.17 by H and integrate over the whole volume of our fluid, and after some algebra [42] we get:

$$4\pi \frac{\mathrm{d}W}{\mathrm{d}t} = -\frac{16\pi^2}{\sigma \mu_0} \int I^2 dV - \int_\sigma H(U \cdot H)\boldsymbol{n} \ d\sigma + \int H(H \cdot \nabla) U dV \ , \tag{2.18}$$

where $d\sigma$ is an element of the surface of the body and $\boldsymbol{n}$ is the normal vector pointing outside of the volume. The first term on the right-hand side is the Joule heat and it is always negative. The second term is the rate at which electromagnetic forces work on the surface of the body, this term converges to zero in case of zero velocities on the surface. The third term is work that is done by stretching the field against the magnetic pressure $H^2/8\pi$.

From this equation, it is not obviously visible if the magnetic field can stay on a non-zero level for a continuous amount of time. It is visible that we can start and generate some field but after some finite time it might decay to zero [121] and not leave us any long-term magnetic field. But here we will be looking for solutions where the magnetic energy does not decay to zero - the kinematic dynamos.

2.3.2 Spherical Harmonics

Solving Maxwell's equations 2.12 and the magnetic induction equation 2.17 directly is quite difficult, so we will switch to the practicable method suggested by Bullard and Gellman (1954) [42], where we expand the solutions in terms of spherical harmonics: $\boldsymbol{T}_n^m$ and $\boldsymbol{S}_n^m$, where $\boldsymbol{T}$ are the toroidal components hence they do not have the radial component, and $\boldsymbol{S}$ are called poloidal. This expansion of vector fields in spherical coordinates is known and used [38, 41, 130].

These solutions satisfy a bunch of criteria like orthogonality on the surface, continuity, zero divergences, any continuous function F with $\nabla \times F$ can be expressed as a sum of these functions, and some normalization rules. These criteria can be found in Chapter 4 of Bullard and Gellman (1954) [42]. These solutions are expressed in some geometrical transformations of Laplace's spherical harmonics and for example, any radial field on the sphere can be expressed as:

$$B_r(r,\theta,\phi) = \sum_{\ell=1}^{\infty}\sum_{m=0}^{\ell} \ell(\ell+1)\left(\frac{a}{r}\right)^{\ell+2} P_\ell^m(\cos\theta)(g_\ell^m \cos(m\phi) + g_\ell^{-m}\sin(m\phi)) \ , \qquad (2.19)$$

here $P_\ell^m(\cos\theta)$ are Schmidt normalized Legendre polynomials, a is the radius of the sphere,

and g_ℓ^m, g_ℓ^{-m} are Gauss coefficients. So for example the axisymmetric dipole magnetic field on the surface of the sphere will be $B_{D0} = 2P_\ell^m(\cos\theta)g_1^0$, and the terms proportional lo $g_1^{\pm 1}$ define the horizontal dipole moment and its direction.

If we take these rules and decompose our magnetic field in the magnetic induction equation 2.14 we get:

$$r^2\frac{\partial S_\gamma}{\partial t} = r^2\frac{\partial^2 S_\gamma}{\partial r^2} - \gamma(\gamma+1) - U\sum_{\alpha\ \beta}\left[(S_\alpha S_\beta S_\gamma) + (T_\alpha S_\beta S_\gamma) + (S_\alpha T_\beta S_\gamma)\right], \tag{2.20}$$

$$r^2\frac{\partial T_\gamma}{\partial t} = r^2\frac{\partial^2 T_\gamma}{\partial r^2} - \gamma(\gamma+1) - U\sum_{\alpha\ \beta}\left[(S_\alpha S_\beta T_\gamma) + (T_\alpha S_\beta T_\gamma) + (S_\alpha T_\beta T_\gamma) + (T_\alpha T_\beta T_\gamma)\right]. \tag{2.21}$$

These equations have a simple physical interpretation: the left-hand side is the rate of growth of the specific (γ) spherical harmonic, the right-hand side is the diffusion hidden in the first two terms, and the rest is the sum of rates of growth of this given spherical harmonic after interaction with α and β harmonics. For a kinetic dynamo, the time derivative should be zero, hence the diffusion should be compensated by the U terms. Having these equations allowed Bullard and Gellman to define the selection rules described in detail in the sixth chapter of their 1954 paper [42]. These include like triangle rules, dependence for odd and even sums, etc. These rules allowed later researchers like Dudley and James [48] and Gubbins [67] to find some solutions for dynamo action in systems with magnetic Reynolds number on the scale of one hundred. Or rephrasing Yoda: *S_α leads to S_β, S_β leads to S_γ,*

S_γ leads to dynamo.

2.4 Inertial Zoo

In this section, we will introduce the reader to the amazing animals (oscillations) that live in the rotating and conductive fluids.

2.4.1 Inertial waves

If we take our favorite Equation (it's always Navier-Stokes) 2.9 and throw away the fluid acceleration we can proceed and get the Taylor-Proudman theorem [131, 132], but if we assume that Ekman and Rossby numbers are infinitesimally small [96, 120, 133], and keep the acceleration we get:

$$\frac{\partial \vec{u}}{\partial t} + 2\hat{z} \times \vec{u} + \nabla p = 0 \ . \tag{2.22}$$

From here we, as always, take a curl to get rid of that gradient term and after some algebra we get:

$$\frac{\partial \nabla \times \vec{u}}{\partial t} - 2(\hat{z} \cdot \nabla)\vec{u} = 0. \tag{2.23}$$

At this point one can look for a solution that would look like

$$\vec{u} = \vec{A} \cdot e^{i(\vec{k}\cdot\vec{r} - \omega t)}, \tag{2.24}$$

and the corresponding dispersion relation:

$$\omega = 2|k|cos(\theta) \ , \tag{2.25}$$

where θ is the spherical polar angle and the frequency is in the units of rotation rates [95, 96, 134, 135, 136].

In media where these waves propagate, the velocity vector of the fluid rotates with the frequency up to the twice the rotation rate, according to Eq. 2.25. In this case, the wave frequency is only a function of the direction of the propagation and the rotation rate of the system, so it does not depend on its wavelength. And the group velocity of the package can be derived [95] as:

$$\mathbf{c}_g = \pm 2 \cdot \hat{\mathbf{k}} \times (\hat{z} \times \hat{\mathbf{k}})/|k| \ , \tag{2.26}$$

and it is perpendicular to the phase velocity of the wave [137].

Planetary (also known as Rossby) waves are a special case of these inertial waves [138]. They are well-known in meteorology and can come from an assumption that the atmosphere is a thin layer. On the other hand, the waves with zero frequency are a different special case of the inertial modes and come directly from the Proudman-Taylor theorem [131, 132].

With a more theoretical/hand-waving approach, one can say that inertial waves are the solutions of the Navier-Stokes equation in a rotating frame with an assumption of infinitesimally small viscosity. In this case, if we are working with a non-viscous linear rotating fluid, any solution can be represented as a superposition of them. While real-life

and physical experiments cannot fully satisfy this assumption, this is still a good place to start. A lot more details about this phenomenon can be found in Greenspan monograph [133], the waves were observed and analyzed by different members of this lab in different experiments [7, 96, 106, 108, 110].

2.4.2 Inertial modes

The inertial waves were derived from the assumption of an infinite rotating media, here we will have all the possible frequencies between zero and two rotation rates. But if we put some constraints on top of this, for example, if we put this in a sphere (the author hopes that the reader has already realized how much we like spheres here), and we add slip-free boundary conditions, we can find that not all waves are created equal. In this spherical configuration, we will call these surviving inertial waves 'inertial modes' [139, 140]. These modes got excited by the rotating fluid and the reflections between the surfaces, while other waves would dissipate never getting into the loop. The important part of the "reflection" of these waves is that it doesn't obey the regular (intuitive) laws. Instead of the reflection angle and incidence angle being equal with respect to the reflection surface, here, due to the dispersion relation shown on Eq. 2.25 the reflected wave should have the same angle with respect to the z-axis. *Akin's Law 12. "There is never a single right solution. There are always multiple wrong ones, though".*

The implicit solutions are known analytically [139, 140, 141], and we would normally identify them by three numbers: the latitudal number ℓ (degree), the azimuthal number m (order), and frequency ω, usually normalized by the rotation rate. The similarity between

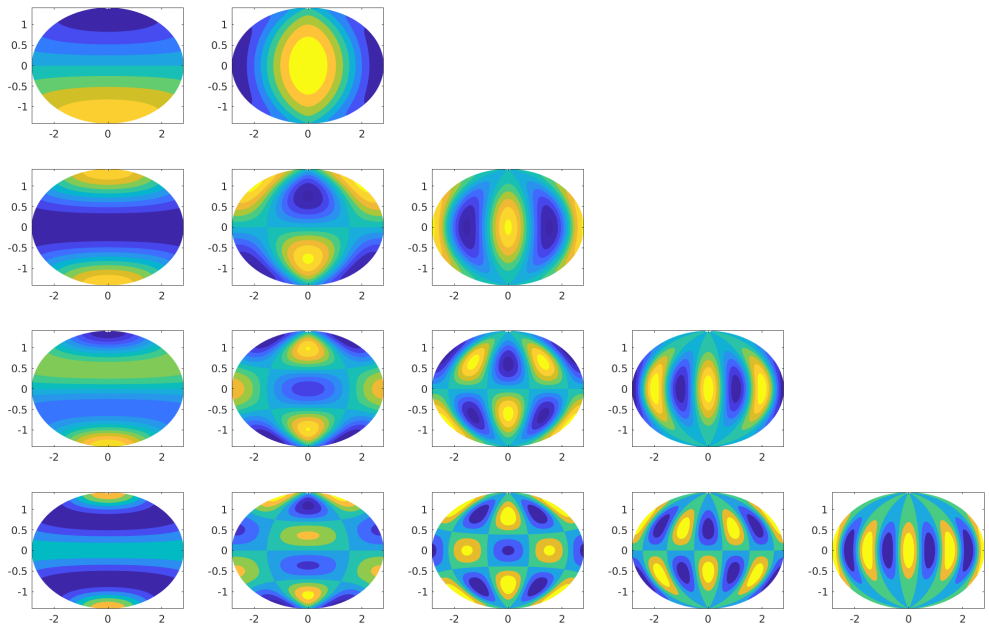

Figure 2.2: Spherical harmonics visual representation: the degree (ℓ) goes from the top (1) to the bottom (4), and order (m) goes from left (0), to the right (4). The negative m numbers are not shown.

spherical harmonics [42] (shown in Fig. 2.2) and inertial modes will help us later. More details on different ways of describing the modes can be found in [133, 142, 143, 144]. Some of the mode selection rules [95, 108] will be important for us when we will discuss the modes observed in the experimental data. In Fig. 2.2 we can see some of the inertial modes for $\ell \leq 4$. We will later mostly talk about the magnetic data observations, for this reason, we not talk about $\ell = 0;\ m = 0$; mode because James Clerk Maxwell would be very sad if we did; and we will skip negative m numbers because in this rotational configuration they can be represented as their phase shifted positive brothers.

2.4.3 Magneto-Coriolis Modes

So here we are sitting on a sphere with an unbearably difficult nonlinear equation 2.9 and we still want to go deeper. So let's add more terms to it. In our case, we want to talk about conductive fluids and the waves that can appear in the spherical configuration. We will linearize the equations that describe the oscillating modes inside the sphere [92], so for these Magneto-Coriolis Modes [92, 111, 119, 132, 136, 139, 141, 145, 146, 147, 148, 149, 150, 151, 152, 153, 154] we get:

$$\begin{aligned}
&\tfrac{\partial \vec{U}_1}{\partial t} = -\nabla p - (\vec{U}_0 \cdot \nabla)\vec{U}_1 - (\vec{U}_1 \cdot \nabla)\vec{U}_0 + Le^2((\nabla \times \vec{B}_0) \times \vec{B}_1 + (\nabla \times \vec{B}_1) \times \vec{B}_0) + \vec{E}\nabla^2\vec{U}_1 \ ; \\
&\tfrac{\partial \vec{B}_1}{\partial t} = \nabla \times (\vec{B}_0 \times \vec{B}_1) + \nabla \times (\vec{U}_1 \times \vec{B}_0) + Em\nabla^2\vec{B}_1 \ ; \\
&\nabla \vec{U}_1 = 0 \ ; \\
&\nabla \vec{B}_1 = 0 \ .
\end{aligned} \tag{2.27}$$

Here, $\vec{U}_1$ and $\vec{B}_1$ are the solutions of the velocity and magnetic fields of these propagating waves in the background states of these fields $\vec{U}_0$ and $\vec{B}_0$. The dimensionless numbers are explained in Section 2.1.

From these equations and some algebra [61] we can get the Magneto Coriolis wave dispersion relation:

$$\omega_{MC} = \pm\frac{\omega_I}{2} \pm \sqrt{\left(\frac{\omega_I}{2}\right)^2 + \omega_A^2} \ , \tag{2.28}$$

where $\omega_I = 2\Omega cos(\theta)$ is the dispersion relation of our regular inertial waves 2.25 and

$\omega_A = B_0 \cdot k/\sqrt{\mu_0 \rho}$ is the Alfvén wave frequency.

If we come back closer to our everyday life, we should say that understanding these traveling hydro-magnetic oscillations is important for us, because they were predicted and observed in the Earth's core [147, 151]. They might be responsible for certain variations of the planet's magnetic field and some of the geomagnetic impulses [47, 146, 153, 155].

Due to the incredible difficulty of numerically modeling these waves [7, 61, 62, 156, 157] especially in a system like the Three Meter Experiment, in this thesis we will stay with the observations and classifications of these Magneto-Coriolis modes. Further in this thesis in Chapter 5, we will demonstrate the observed modes in the experiment, especially the modes whose behavior depends on the value of the applied magnetic field.

2.5 Forecasting the future and neural networks

As far as we can trace human history, we have always been trying to predict what is going to happen next. Predicting floods and droughts, estimating the positions of the planets in the sky, the time when your car needs more air in the tires or more oil, eclipses, stock market prices, etc, all this gave us science as we know it today, and brought us to the world we live in. While some even complex-looking systems can be predicted relatively easily with a certain precision, like the sunset, others might look incredibly similar but appear to behave very unexpectedly. Specifically, we will be talking about nonlinear systems. The difficulties that one can face while trying to predict these nonlinear systems are known for more than fifty years. This problem was described by Edward Lorentz when he tried to run a computer simulation of a simple weather model with just three variables.

His paper "Deterministic Nonperiodic Flow" [158] demonstrated that the behavior of the system might change drastically if run with slightly different initial conditions. After that, many researchers in mathematics, physics, computer science, and earth sciences contributed to research on these nonlinear systems and the ways we could predict their change in time or use them for this purpose. The author would not forgive himself for not mentioning here the pioneers: Stephen Smale, Edward Ott, and James Yorke, who referred to these deterministic but unpredictable systems with the word "chaos", giving it the name that is so known and used these days[159, 160, 161, 162, 163, 164, 165, 166].

While we don't have a tool to exactly predict these nonlinear systems for an infinite amount of time [167, 168, 169], it is still incredibly important to create new models that would allow us to expand the horizon of predictability. We want to predict hurricanes' trajectories and heat waves. Weather for the upcoming weekend might be one of the most difficult and at the same time desirable things to know. The methods and techniques from this new science [170] were successfully used in a number of models. Specifically in this thesis, we would like to talk about neural networks. When it began in the middle of the twentieth century with perceptrons [171], which showed success in pattern recognition. We currently have seen surprising utility in many different areas including art, industry, technology, and science [172, 173, 174, 175, 176, 177, 178, 179, 180, 181, 182, 183, 184]. Particularly, we will be interested in a Recurrent Neural Network technique known as Reservoir Computing [185, 186]. This technique demonstrated a surprising ability to predict the dynamics of Lorentz systems as well as Kuramoto-Sivashinsky turbulence [181, 187, 188].

So in this thesis, we will use a reservoir computer in a combination with an auto-

regressive model to predict the time evolution of the rotating magnetohydrodynamic experiment. Probably the most important part of these techniques is that they are model-free, which means that inside the predictive model there is no information about the system that it is going to forecast. The exact rules of the dynamics of these systems will be described in Chapter 4, but here I would like to say that the reservoir computer predictive model basically gathers the data from observing the system for some time, transforms the observable space into a higher dimensional space while keeping some memory about the past, performs some nonlinear transformation and learns how to transform it back in such a way that it will get the next observed values of the observable space. So in some sense, we will be having a black box where we will throw our data and the box will tell us the future, exactly like astrology (or maybe not exactly) but significantly better.

Chapter 3: A New Hope: Fixes, Upgrades, Data Acquisition

Akin's Law 40. "(McBryan's Law) You can't make it better until you make it work".

In this chapter, we will describe the most time-consuming part of this dissertation project. Here we mostly will talk about the mechanical, electrical, and software engineering that was necessary to redesign, upgrade, and fix the Three Meter Sodium Apparatus. Most of these things were done by Rubén Rojas, Daniel Lathrop, and the author. The author also wants to give thanks to Nolan Ballew, Don Martin, and Bryan Quinn for all the technical help, and another very special and giant thanks to Heidi Myers for all that work that she put into this project, without Heidi it would be significantly more difficult to get there, and would just probably turn into a total mess without her organizational skills.

Back in 2009 The Three Meter first was filled with water and used as a non-magnetic experimental apparatus. In 2012 the crew removed water and filled up the experiment with sodium and so the MHD era of the apparatus began. Sadly, in the Summer of 2016, when the author started the graduate school, the apparatus was not fully functional and there was a long way ahead to make it run again.

3.1 Reasons to upgrade

During an experimental run on April 29'th, 2016, the inner motor was "misbehaving", and the inner sphere seemed to get locked to the outer sphere. After this day the experiment was considered non-functional and needed repair. The main hypothesis was the failure of the inner bearing of the inner sphere shaft, shown on the bottom right of Fig. 3.1.

By mid-2016 the experiment had not yielded a self-sustaining detectable magnetic dynamo. During the experiments with liquid sodium, it demonstrated an ability to amplify the externally applied magnetic field [58] in the radial direction up to 20% and in the azimuthal direction up to eight times. The fact that the experiment showed this amplification lines up with the theoretical studies of the dynamo mechanism [70, 189, 190]. One of the possible ways to increase the chance to achieve the dynamo in this experiment was suggested by the numerical study [114] in 2018. In this study, a rough inner sphere with blades demonstrated an improved coupling between the inner sphere and the fluid, hence creating a stronger equatorial jet, and giving a better chance to reach the dynamo state.

Assuming the Three Meter experiment required major repair to run again and the numerical studies suggested upgrading the inner sphere for reaching the dynamo state, there was a decision to fix and upgrade at the same time. So here we had two questions: how are we going to repair the experiment and what exactly we are going to do with the inner sphere? Here two projects were born: the 40-cm water experiment to study how differently shaped baffles on the surface of the inner sphere would affect the flow [191], and A New Hope project - the one that lead to making the experiment operational again.

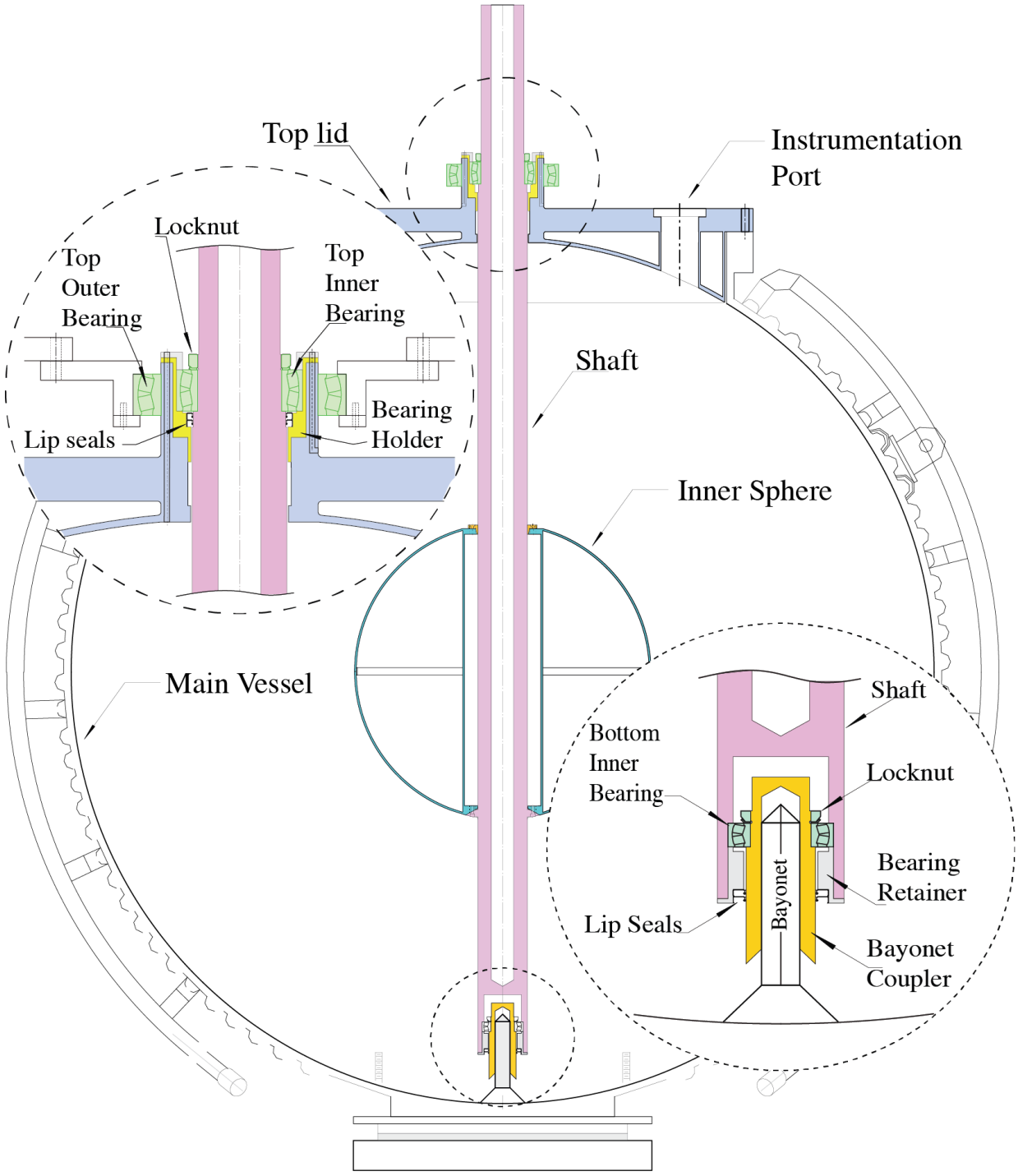

Figure 3.1: The Three Meter experiment schematics in cross-section. Individual drawings taken from [6].

The name "A New Hope" was chosen due to the common observation that the Three Meter experiment is visually similar to The Death Star from the popular movie "Star Wars: Episode IV – A New Hope", and also it was our new hope to achieve the dynamo.

3.2 The 40-cm Water Experiment

To analyze the behavior of the spherical-Couette flow with the different inner sphere designs we decided to make a water model of the Three Meter experiment (which itself is the model of the Earth's core). Here Rubén E. Rojas, Till Zürner, Daniel P. Lathrop, and the author designed and made the 40-cm water experiment: a 40-cm-diameter spherical Couette experiment, with a transparent outer sphere and a 14-cm diameter inner sphere. Both spheres can rotate independently. The maximum rotation rates were 50 Hz and 5 Hz for the inner and outer spheres correspondingly. In the experiment, we used a 6 W continuous laser that with polyethylene fluorescent particles added to the water allowed us to film videos with up to 1000 frames per second and use PIV techniques [192] to analyze the velocity fields in the experiment [191] . A more detailed explanation of the apparatus and the results can be found in Rubén's thesis, and our PRF publication [191]. The schematics of the 40-cm is shown in Fig. 3.2, and the photo of the apparatus is in Fig. 3.3. Significantly more details about the exact techniques, the experimental approaches, and the underlying physics can be found in Rubén's thesis [100] and in his PRF article [191].

We tested four types of the inner sphere, smooth with no baffles, straight baffles, chevron-shaped, and alpha baffles. We 3D-printed the inner spheres with baffles from

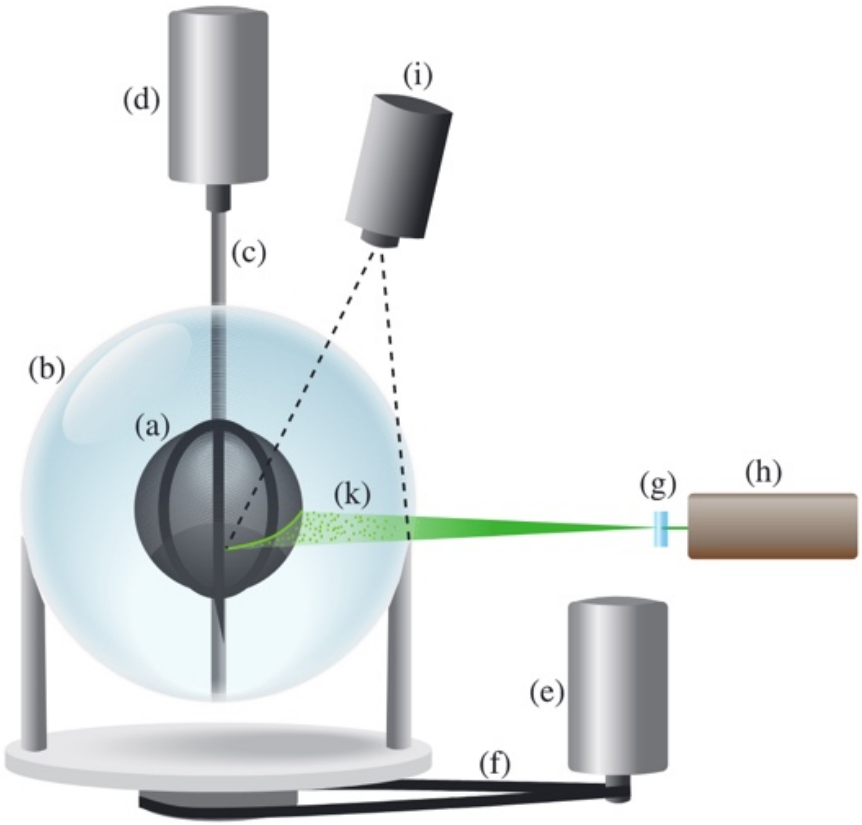

Figure 3.2: The scheme of the 40 cm experiment. (a) inner sphere, (b) transparent outer sphere, (c) inner shaft, (d) inner motor, (e) outer motor, (f) gear belt, (g) cylindrical lens, (h) 6 W laser, (i) 1000 fps camera, (k) polystyrene particles in water

.

Polylactic Acid (PLA). In Fig. 3.4 are shown the listed baffle designs. The study of the 40-cm water experiment let us choose the shape of the baffles we were going to install on the inner sphere of the Three Meter experiment. Some limitations were also set by the machine shops that informed us that they cannot manufacture and weld baffles that would be bent in all three dimensions, like the chevron-shaped baffles. So in the end we decided to go with the alpha baffles.

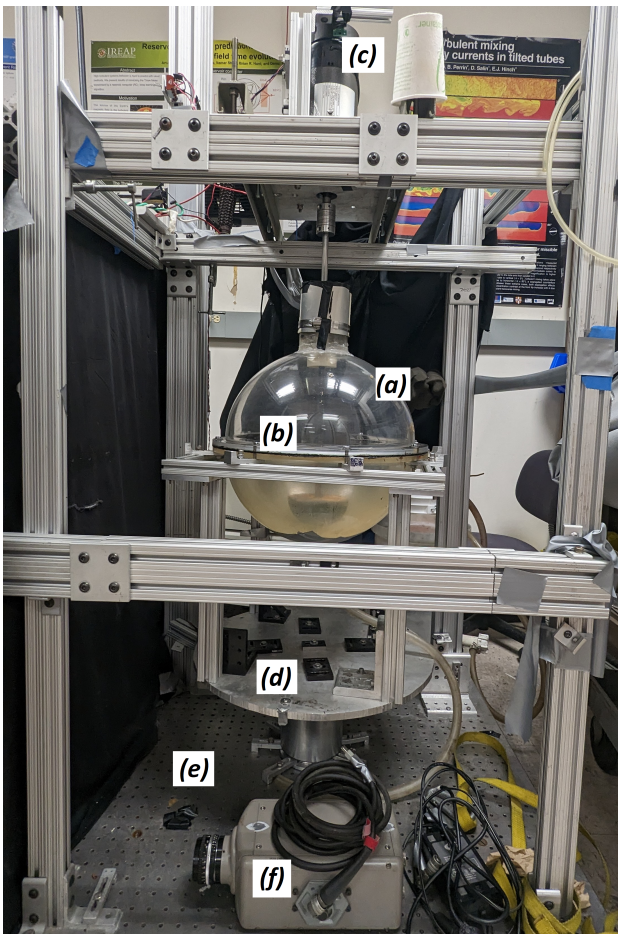

Figure 3.3: The photo of the 40 cm experiment. (a) transparent outer sphere, (b) 3D printed inner sphere, (c) inner motor, (d) rotating platform, (e)optical table, (f) 1000 fps Phantom camera.

(a) Smooth (b) Straight (c) Chevron (d) Alpha

Figure 3.4: Different designs of the inner sphere baffles

.

3.3 Upgrade and Repair

To proceed with the repair of the 3M experiment we needed to disassemble the electronics, move the inner motor frame, transfer the sodium metal, and disassemble the lid with the shaft to reach the inner bearing.

The Three Meter Apparatus finished the experiments with water and switched to experiments with sodium in 2012. One of the most unpleasant and time-consuming procedures was to put the sodium in the sphere from more than sixty 50+ gallon barrels. The filling procedure took over fourth months. In our situation, we decided that we need to do it much faster, and just in one go. For this, we had to have a pressurized container where we could store the sodium and avoid oxidization, and the container would need to have the ability to be heated up to liquefy the sodium.

3.3.1 The Storage Tank

After several months of talking with different companies in the US and from abroad we decided to proceed and order a container from Central Fabricators Inc. The pressurized

container (the tank scheme is on Fig. 3.5) by design would have to withstand pressures up to 30 psi, have 3450 gallons volume, made of a 1/4" thick carbon steel alloy (SA 516 Gr. 70), have a welded heating jacket to receive the hot oil from the existing heater system, have three ports: for diagnostics, sodium filling, and sodium emptying operations. The volume of the container was chosen to be 20% larger than the volume of the transferred sodium. A significant part of the price of the tank was in the dimple jackets. To evaluate the appropriate surface area of the jacket the author developed a code to simulate the heating dynamics, based on the data of the flow of hot oil used for heating the experiment. This simulation predicted that with the 25% of the tank surface being covered with the jacket the necessary time to liquefy the sodium inside was estimated to be on the scale of 10 hours, which was similar to the time we had in the Three Meter experiment. The final design had the dimple jackets covering 30 ft^2 of the bottom section of the sodium storage tank and had two separate sections.

After receiving the tank, and simulating different ways of connecting two dimple jackets to the heating lines to find the most efficient way of doing it, the heater system was connected to the dimple jackets, and heating oil was added. The exact oil piping design is illustrated in Fig. 3.6, it was made mostly by Rubén Rojas (more details are in his thesis) and the assembly was done with Don Martin and the author.

By design, the tank had four nozzles, one on the bottom side of the container, and three on the top. Out of the three on the top, the one on the eastern side (right on Fig. 3.7) had a long duptube integrated, for sodium flow during the refilling operation, one in the middle had a short diptube for sodium flow during the experiment draining operation, and one nozzle with integrated gas ports, pressure relief valve, pressure sensors, temperature

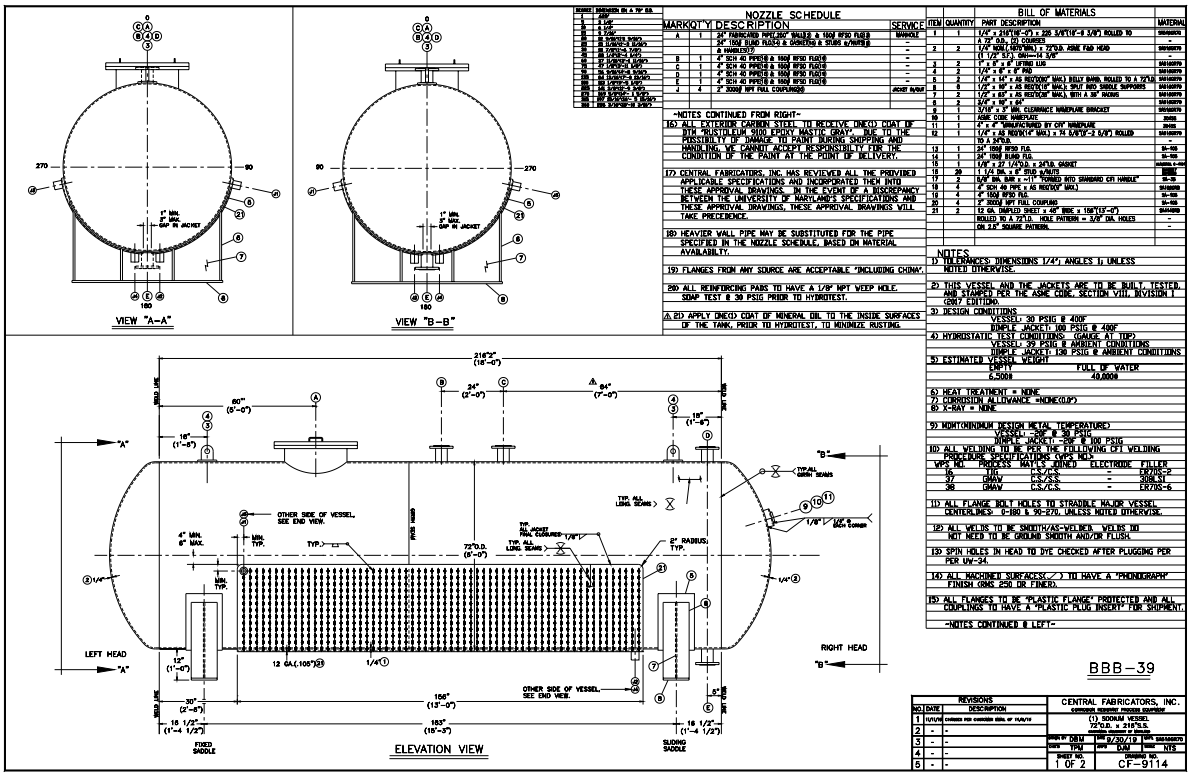

Figure 3.5: The drawing of the purchased sodium storage tank

.

sensor installed on a 3 feet long finger.

The tank was placed close to the experiment and right next to the eastern wall of the High Bay room, where the heating oil piping is going through the wall to reach the pump and the oil heaters located outside of the building. The western side of the tank was placed slightly higher than the eastern to have a slight inclination to allow a smoother refilling operation by letting the sodium flow to the eastern side where the extraction duptibe is located. The tank was fabricated in several months and delivered to Energy Research Facility. The outer surface of the vessel was covered in a DTM Epoxy Mastic that prevents rusting. During the heating tests, this epoxy was producing a limited amount of smell that was considered safe.

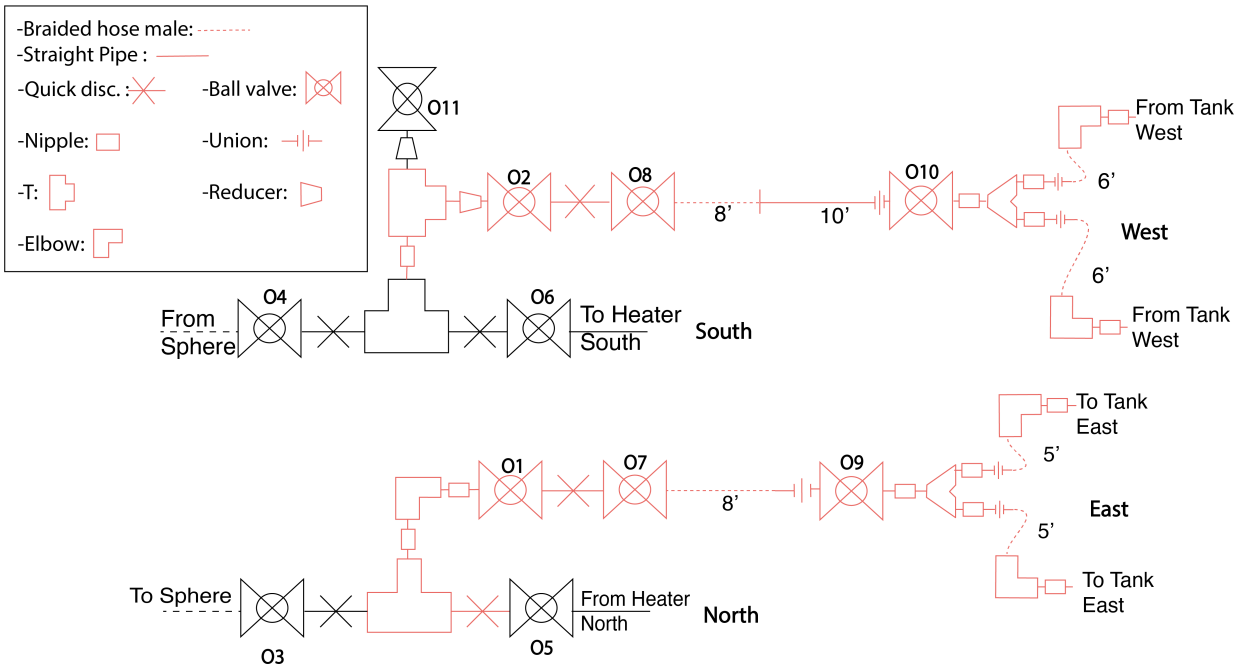

Figure 3.6: Oil lines connection diagram to the storage tank and the sphere. In red are the parts we added and in black are preexisting ones. Credits to Rubén Rojas.

3.3.2 Transfer lines

Akin's Law 1: Engineering is done with numbers. Analysis without numbers is only an opinion.

The next part of the transfer was designing the transfer line. The desirable time for the transfer operation was two hours. With over 12 tons of liquid sodium that corresponds to the average flow of 2 L/s. To estimate the pressure drop and the corresponding flows of nitrogen gas and liquid sodium, the author developed a software simulation in MATLAB [193] that was taking into account the pressure drops in the nitrogen lines, the sodium transfer line, the siphon effect, and the nitrogen leaks. For each part of the system like a straight pipe or a change of section, the pressure drop was estimated using data from

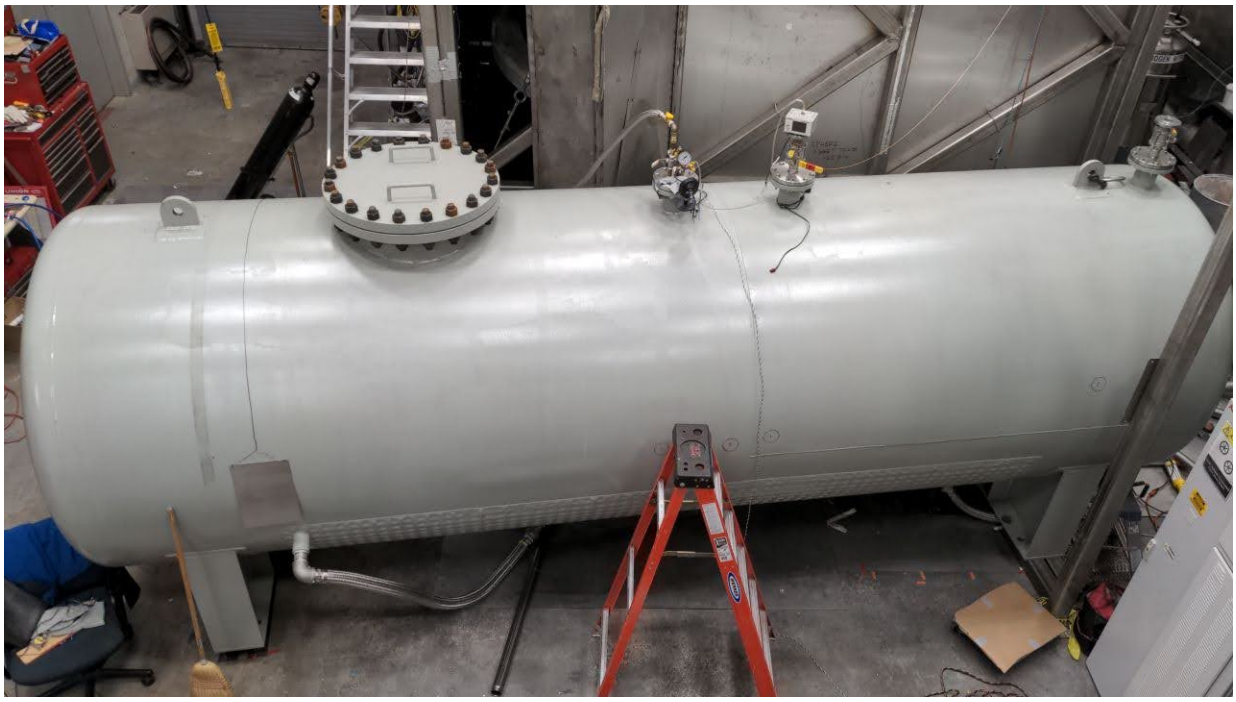

Figure 3.7: The picture of the purchased sodium storage tank.

.

[194] and [195]. During the previous years, we found a relatively small gas leak in the experiment, which probably appeared after our first experimental runs with solid body rotation in the Fall of 2016. With this leak, we had to replace the pressurizing 300 cubic feet nitrogen cylinder once every one or two months. After using a helium leak detector we discovered that the leak is located in the inner bearing, and was probably caused by a failure of the lip seals. Setting up some small experiments let us estimate the flow of the nitrogen through the seals, and later this calculation was used in the transfer simulation to estimate the possible leak. A very unpleasant situation would be possible if the pressurized sphere would start losing too much nitrogen through the leaks and would not let us finish the transfer procedure. The calculation of the flow showed that keeping ≈ 10 *psi* inside the sphere would allow finishing the transfer operation in ≈ 100 minutes.

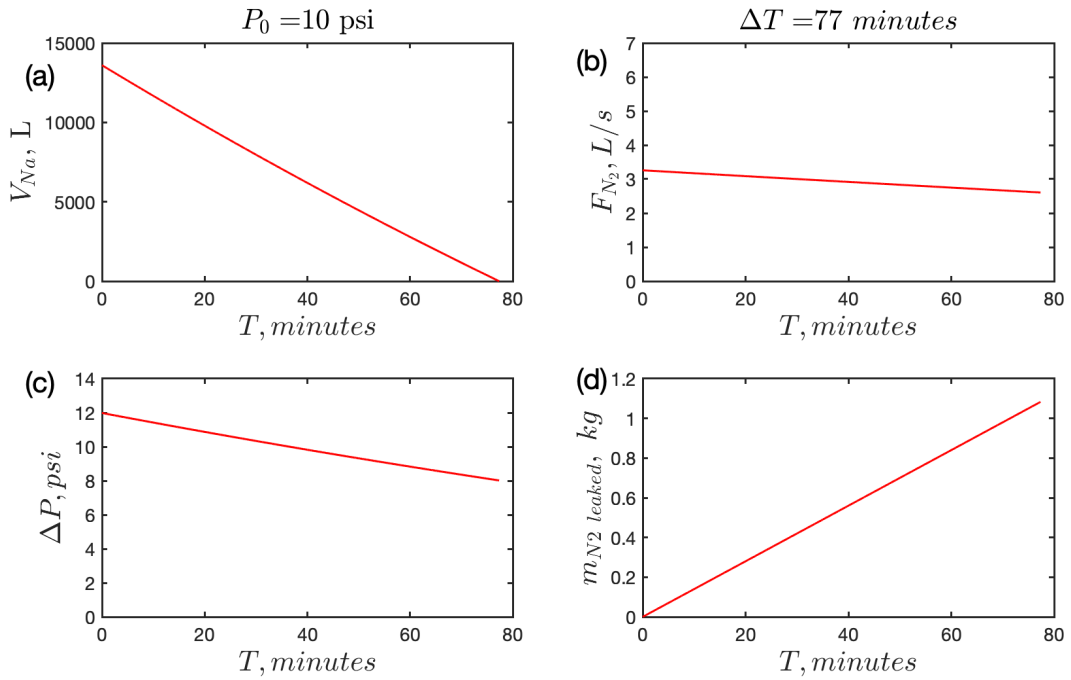

Figure 3.8: Simulation of the sodium transfer operation with constant pressure level 10 psi in the sphere: (a) - the remaining volume of sodium; (b) - sodium volume flow to the storage tank and estimated operation time; (c) - pressure difference between the fluid source and the drain; (d) - total mass of leaked nitrogen gas.

So we had a 1.5" diameter 12' long steel diptube that was bent with $R = 36'$ to put inside the experiment during the hot operation: after the sodium is liquid inside the experiment, it reached the bottom without hitting the inner sphere as shown at Fig. 3.9. We had a 1.8-inch diameter 28-feet long stainless steel flexible transfer line (codename "Anaconda"), shown on Fig. 3.10, it was designed to keep the sodium inside with temperature above 120 C, it had electric heaters powered by a wall plug and controlled by a variable autotransformer. We also had two short diptubes, one for the tank and one for the sphere.

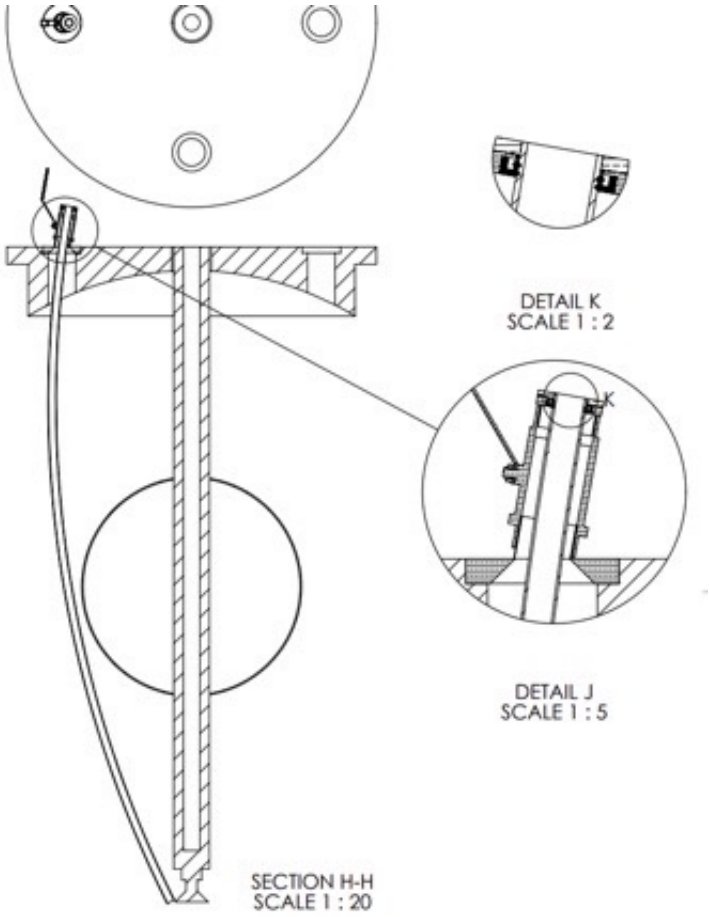

Figure 3.9: The drawing of the purchased diptube and its position inside the sphere during the sodium transfer operation

.

3.3.3 High flow nitrogen lines

To pressurize the tank and the sphere for the transfer operation, the author designed, simulated the pressure drops, assembled, and installed them on the north-western corner of the cube - the gas manifold with four nitrogen 300 cf cylinders, the scheme is shown in Fig. 3.11, and the main hub picture is on Fig. 3.12. The lines were made out of copper tubing and flexible steel hoses which can operate in both cryogenic and hot (over 120 C) temperatures. That was necessary because a large amount of adiabatically expanding

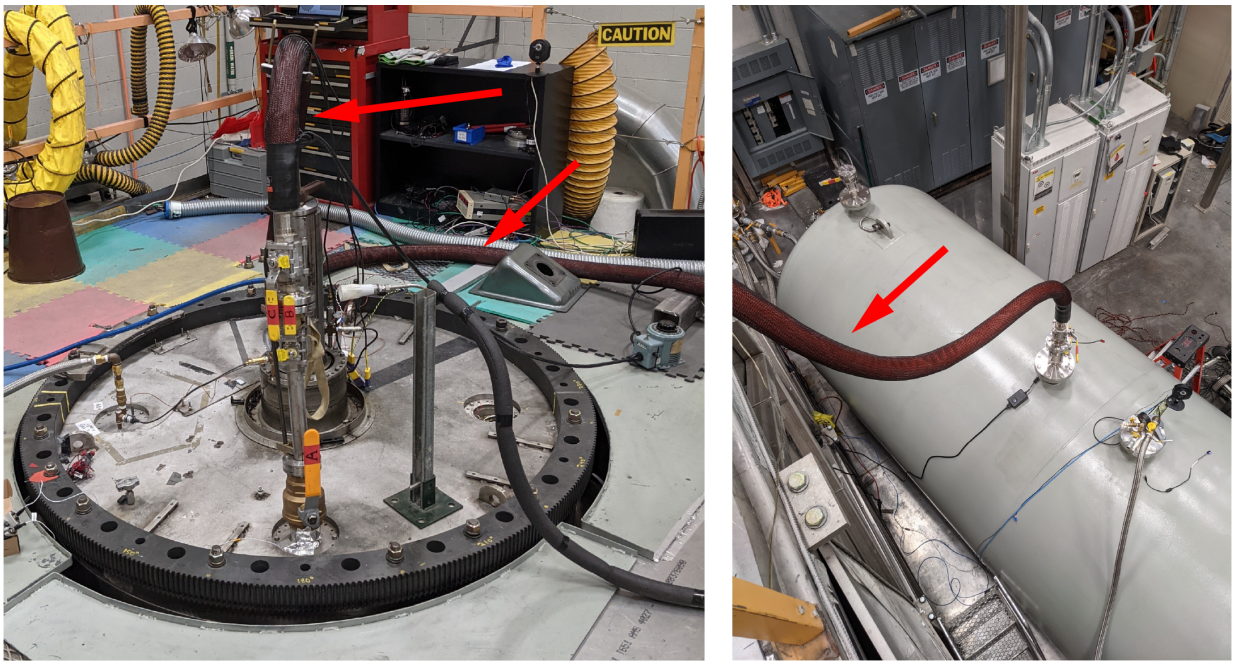

Figure 3.10: The transfer line (Anaconda), indicated by red arrows, attached to the transfer port on the sodium in the left, and the storage tank on the right.

.

nitrogen gas is capable of freezing and damaging plastic tubing. The amount of nitrogen necessary for the operation was calculated by taking into account the leak, the higher pressure in the chambers during the operation, and an additional 50% to be on the safe side. Each accessible part of the nitrogen system had a valve for stopping the flow as well as a valve to relieve the pressure. The nitrogen system design had both high-flow pressure lines for the experiment and the tank for both drain and refill operations, as well as low-flow pressure lines for keeping the vessels inert before and after the operations. Also, we used the high flow line to the tank to vent the atmospheric oxygen from the tank. That was necessary to avoid sodium oxidation during the transfer and storage. It was achieved by consequently pressurizing the tank with nitrogen gas, letting it mix, relieving the pressure, and repeating N times. After using several nitrogen cylinders the estimated amount of

oxygen inside was less than 100 grams, the gas mixture analyzer device was not able to detect any oxygen due to the detection limits, so we considered the tank inert.

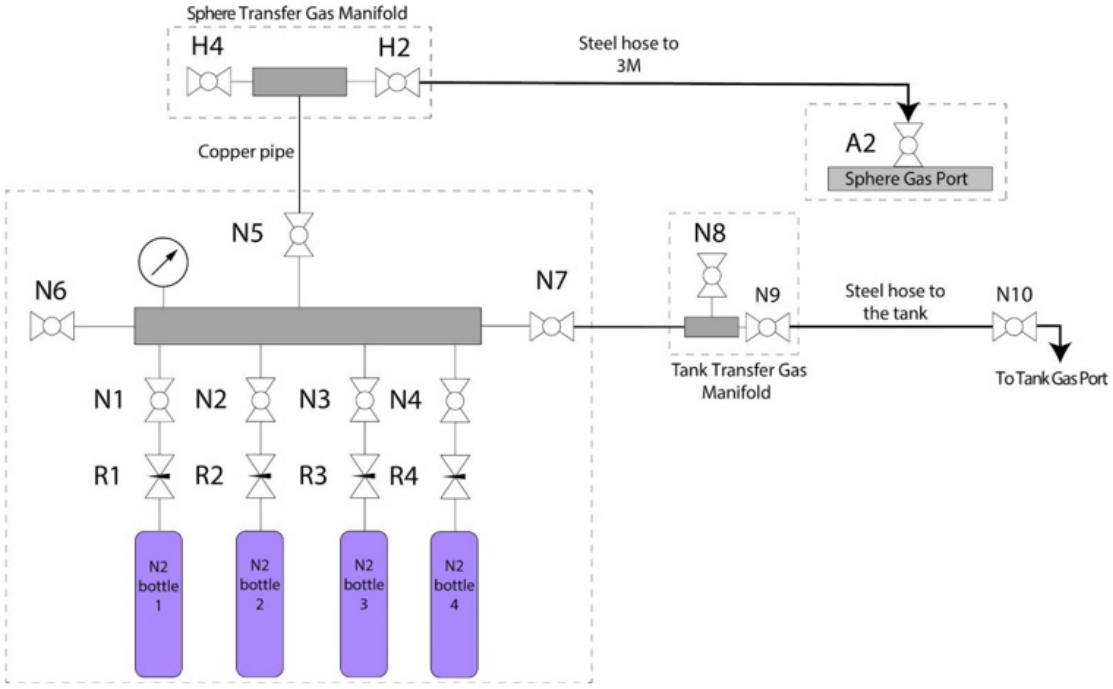

Figure 3.11: The scheme of the nitrogen gas manifold developed for the transfer operations. The four bottles allow to go through the whole operation without replacing a bottle and have a higher flow of nitrogen with a smaller pressure drop.

3.3.4 Lines freezing

One of the concerns that was raised by one of our experienced collaborators: during the transfer operation the nitrogen gas will be adiabatically expanding for a long period of time from the cylinders with 2500 psi to the vessels with 25 psi which will create a flow of cryogenically cold gas in the chambers and this gas might be capable to cool down sodium inside the transfer lines. To estimate this effect the author simulated the heat transfer in the chamber using MATLAB and found that the maximum temperature drop for the

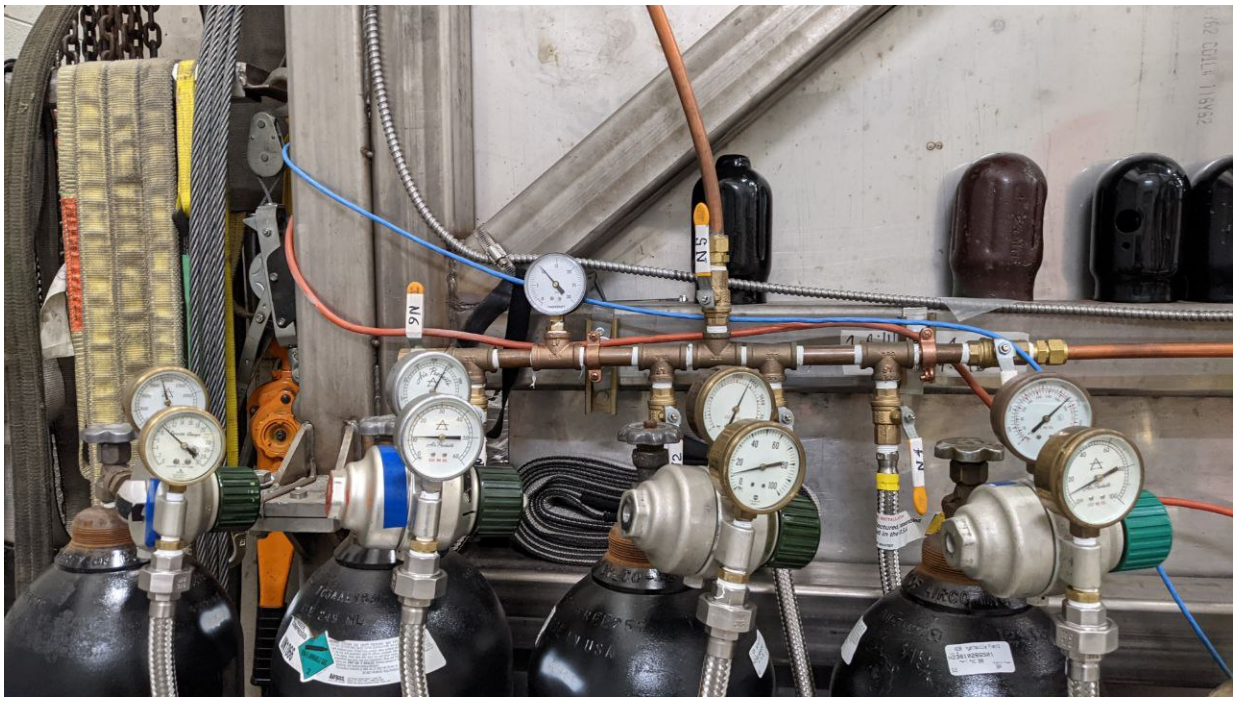

Figure 3.12: The picture of the nitrogen high flow pressure system main hub.

sodium flowing through the diptube surrounded by this cold nitrogen with at least 2 L/s will be much less than 1 K, as plotted on Fig. 3.13. For this simulation, the volume flow was considered constant, as well as the pressure inside the chamber. So here we considered this effect to be negligible for our operation and decided not to use any heating for the nitrogen lines or recuperate the gas with a pump to reuse. Probably our collaborators had most of their experience with significantly lower flows and sizes.

3.3.5 Transfer monitoring

On the lid of the experiment, there are four instrumental ports. We replaced three of them with three other transfer ports for:

- The window port - a port with transparent glass, made to have the ability to monitor the level of the sodium metal during the transfer with a digital distance meter Leica

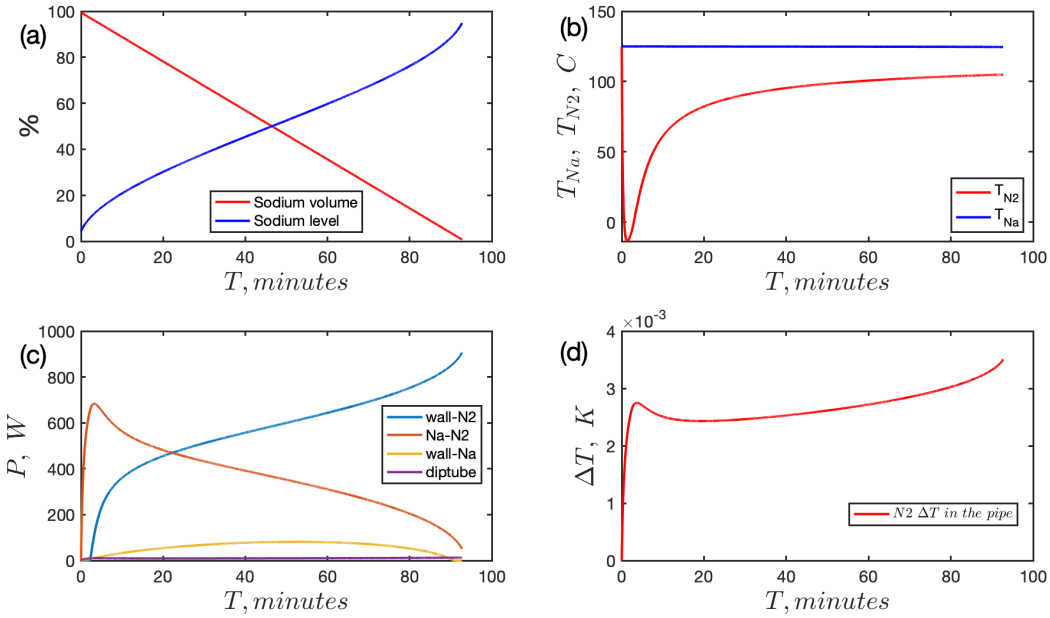

Figure 3.13: Simulation of the power balance in the sphere during the transfer: (a) - remaining volume and the estimated distance between the window and the sodium level; (b) - the average temperature of liquid sodium and gaseous nitrogen in the sphere; (c) - total power exchange between surfaces; (d) - sodium temperature drop in the inserted diptube.

DISTO.

- The gas port - a port with a connector to the nitrogen line to provide a high flow of pressurized nitrogen gas, a long temperature probe, and a pressure relief valve set to 15 psi, to avoid accidental high pressure in the sphere. We had to replace the relief valve because one day before the transfer we managed to pluck it with sodium.

- The transfer port - a port with a 3" ball valve, for putting the diptube in the sphere, as in Fig 3.9.

The port replacement SOP can be found in Appendix D. And a time-lapse video of the process is available at https://youtu.be/Y4Wse0ffhX4 .

To monitor and control the system during the transfer operations author has developed a local web application "TraMon" (Transfer Monitor) as well as hardware necessary for diagnostics. The application can monitor temperatures and pressures in the vessels and transfer lines, store the data, and plot it in real-time, also it is capable of controlling the oil heaters that are necessary for melting sodium. Having the transparent window on the sphere lid allowed us to monitor the level of sodium using a laser distance measure device. After inputting the distance between the window and the sodium into the application it is capable of estimating current and average sodium flow and predicting the remaining time of the operation, as shown in Fig. 3.14. TraMon application allowed any device connected to the campus network to see the current state of the system, so the diagnostics were visible for every member of the crew on their laptops and/or mobile devices.

Transferring such a large amount of liquid metal is considered a highly hazardous operation. While the amount of specific actions that are necessary to execute during the transfer is relatively low, the risks stay very high. In case of a leak from a pressurized container, the height of a geyser with liquid sodium could have reached up to 30 ft and would have probably lead to a liquid sodium fire. To minimize the risks the team had been developing the standard operation procedures (the SOP) for the transfers with a detailed description of every action and necessary checks for proceeding. These SOPs were discussed and changed many times during the years of preparing for the transfer. The Department of Environmental Safety, Sustainability, and Risk (ESSR) at the University of Maryland helped with the development and had plenty of useful comments. The resulting SOP was analyzed and approved by the ESSR and all of the team members. The full sodium transfer

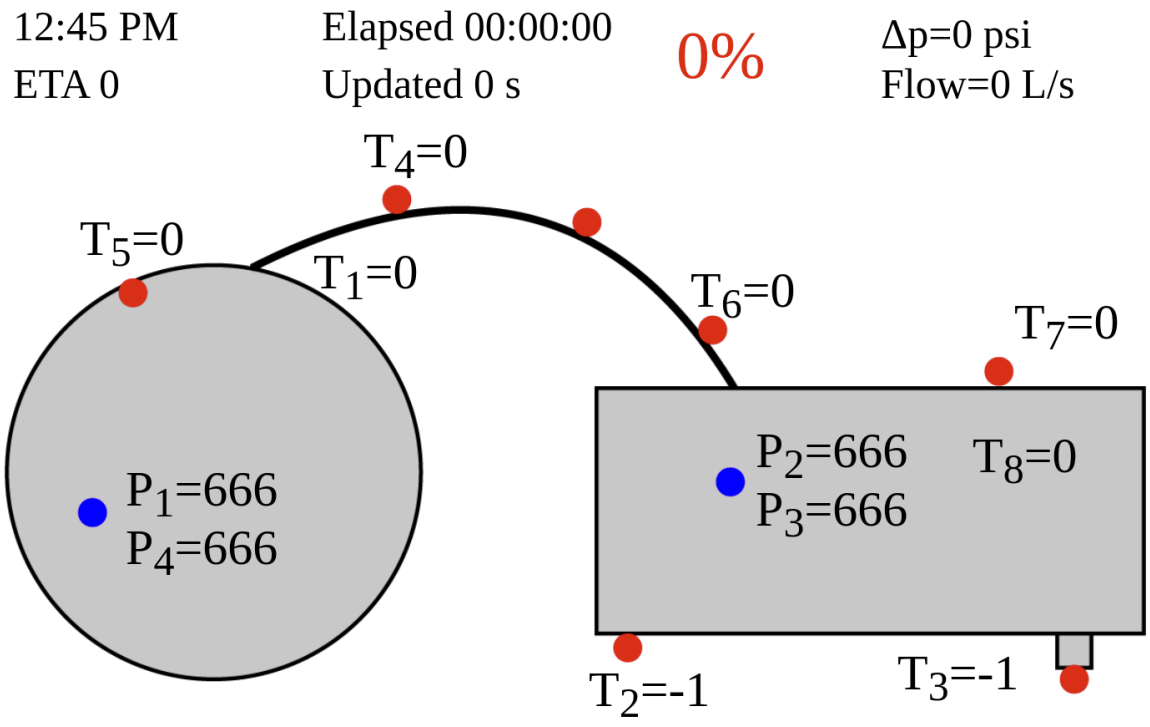

Figure 3.14: The graphics interface of the transfer monitor during the refilling operation, here we are mostly concerned about the tank temperatures so the temperature probes were positioned on the storage tank. The unrealistic numbers represent different errors for a simpler debugging procedure.

SOP is in the Appendix B.

3.3.6 Draining the experiment

On February 11th, 2021, we transferred liquid sodium from the experiment to the storage tank. The hot operation of inserting the diptube inside the sphere went relatively easily and without any anticipated problems. In Fig. 3.15 we can see a picture of the top of the cube during the transfer operation at the moment when the diptube was inserted into the hot sodium. The time-lapse video with a more detailed representation of the insertion, coupling assembly, etc is available at https://youtu.be/B8hQsduh_lA .

After that, we pressurized the sphere to 10 psi and started the transfer. The liquid

Figure 3.15: The insertion procedure: Rubén Rojas (in blue on the left) adjusts the height of the diptube with the overhead crane, Nolan Ballew (in green in the center) pushes the dip tube into the port with the valve and lip seal, and Dan Lathrop (in orange) checks the procedure protocols. The liquid nitrogen dewar is on the right and ready to be used in case of fire.

flow was on the scale of 2-3 liters per second - the same level as designed and predicted with the flow simulation codes described in Section 3.3.2. The flow of sodium was monitored via a mass air flow meter installed on the tanks nitrogen relief port - a transparent conical pipe with a metallic ball inside the pipe, and due to the ability to measure the height of the sodium level in the experiment with a laser distance meter through the window port, the local average flow was calculated by recalculating the height into volume and some simple algebra. The sodium volume flow and the corresponding pressure drop during the draining operation are shown in Fig. 3.16.

During the operation, liquid metal was heating the walls of the sodium tank for a long time and the tank's paint started producing very unpleasant fumes. We set the blowers

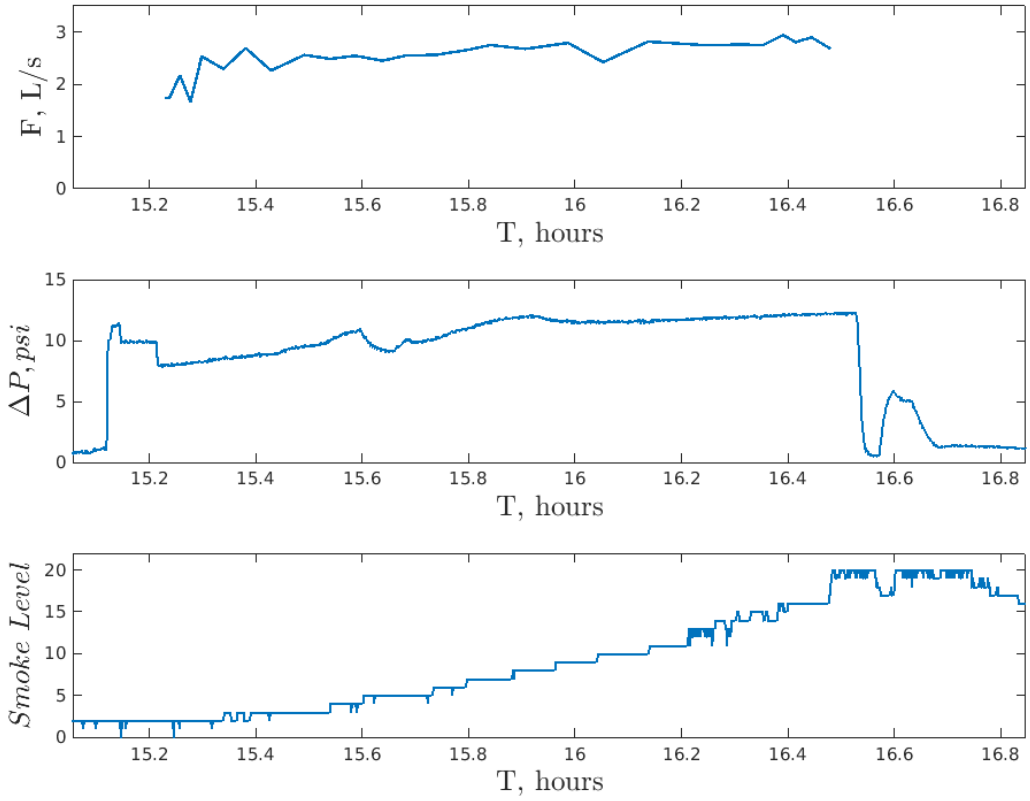

Figure 3.16: Sodium volume flow, the corresponding pressure drop between the experiment and the storage tank during the draining operation, and the smoke level detected by VESDA (max level is 20).

to their maximum level and opened the rolling door, but still, the smoke detectors in the High Bay were detecting a huge increase in the amount of smoke in the room. The fumes were mostly accumulating in the upper part of the room, so people who worked on the top of the cube had to take breaks and we started having shifts. In Fig. 3.17 we can see Bryan Quinn standing on the top of the cube during the last minutes of the transfer when the smoke level was at its maximum.

Figure 3.17: Bryan Quinn on the top of the cube during the draining operation. The haze in the background demonstrates the level of smoke in the room. The smell was bearable on the ground level but not on the cube .

3.3.7 Disassembling the experiment

After draining sodium into the tank we estimated the amount of remaining sodium metal in the sphere by inserting a GoPro camera on a long shaft through one of the instrumental ports. An example of the camera shot at the bottom of the sphere is shown in Fig. 3.18 and the video is available https://youtu.be/gJDpmcPWzVA. The inner sphere had small patches of solid sodium but insignificant compared with the bottom of the sphere. The gas-metal interface was not smooth and plane-like, and we knew the geometrical properties of the bottom of the sphere: sizes of the shaft, couplers, the locations of the

bolts etc; so we estimated the total volume of sodium metal inside between 10 and 100 liters and considered the transfer operation was successful.

Figure 3.18: The picture from a GoPro camera inserted into the sphere after the sodium removal. The inner shaft is in the center of the image, and the bright textured debris at the bottom is sodium metal.

From here the crew proceeded to disassemble the experiment. We removed the lid of the sphere and attached to it the inner shaft and the inner sphere, as shown or Fig. 3.19, and stored it in a prepared position on the east side of the cube. We covered the sphere opening with another lid to avoid excessive oxidization and potential fires and minimize the risk of a person falling inside.

To decouple the lid from the inner sphere shaft we tried attaching the inner sphere to the ground and pulling the lid with the overhead crane, but after reaching more than 6 tons of pulling force, tearing cables, and breaking gear we decided that we need to heat the top inner bearing race and cool down the shaft to allow the temperature gradient lower

Figure 3.19: A picture during the lid and the inner sphere removal.

the friction. We used a Pepsi aluminum can, some duct tape, and an electrical wire to plug the cavity in the shaft at the approximate level of the bearing-shaft junction. From here we installed electric heating tapes on the bearing and filled the shaft cavity with liquid nitrogen, as shown on 3.20. The lid got decoupled from the shaft with approximately 3 tons of force.

From this point, we had easy access to most of the parts of the experiment. The author with Rubén Rojas and Dan Lathrop within several weeks cleaned the inner sphere and the lid from the sodium metal and sodium oxides. For this hazardous operation, we

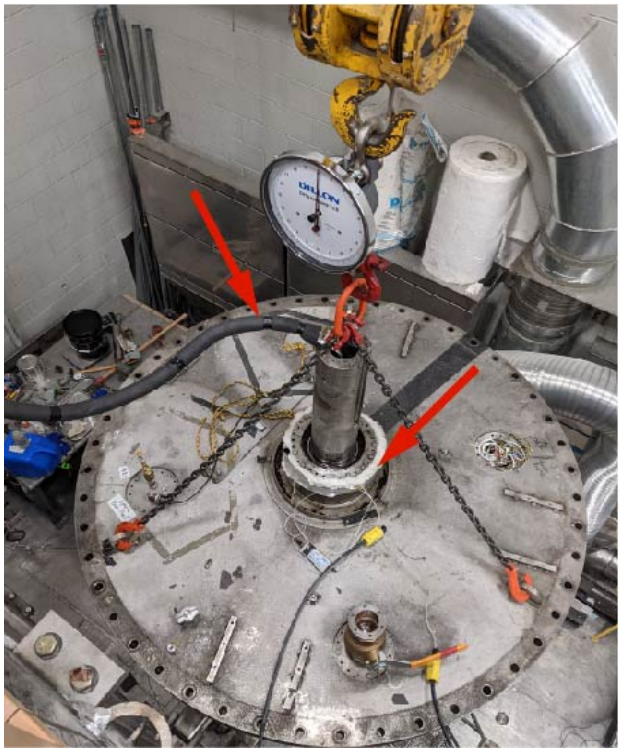

Figure 3.20: The decoupling process required applying liquid nitrogen to the shaft (the left arrow), and heating the bearing with the electrical tape (the right arrow).

always had liquid nitrogen with a dispenser gun and followed a cleaning SOP, added in the Appendix C. But to clean the outer sphere we hired a crew of professionals who were able to remove the sodium from the inside in less than two days. In Fig. 3.21 we can see Rubén showing a piece of solid sodium that was removed from the gap between the shaft and the lid.

Figure 3.21: Rubén demonstrating pieces of sodium metal found in the different parts of the experiment during the cleaning operations.

Figure 3.22: The new inner sphere on the day of delivery back to the lab. The black part of the shaft on the left is the thread covered with duct tape. During the unload we dropped the sphere on the ground from 40 cm height but that was nothing but a scratch.

3.3.8 Upgrading the inner sphere

After we removed the inner sphere from the shaft, carefully cleaned all the cavities from sodium, and assembled it back, we shipped the sphere to Central Fabricators Inc. so they would weld the 1/4" x 1/8" baffles to the sphere. After which the sphere was shipped to a balancing machine shop to make it able to spin smoothly with up to 900 rpm. In Fig. 3.22 we can see the new sphere on the day of the delivery to the lab. The IREAP personnel helped us with the forklift and we were able to deliver the sphere to the lab (not without dropping it to the ground once), where it was lifted, tilted, and put in the vertical position for further assembly, as can be seen on Fig. 3.23.

At this point, we already had a new Inner-Outer sphere coupler, more details about the fabrication can be found in Rubén's thesis. So the only thing that was left - was to assemble everything back and refill the apparatus with sodium. In Fig. 3.23 we can see

the upgraded inner sphere on the shaft and for the scale very happy Rubén Rojas.

Figure 3.23: Rubén standing next to the inner sphere with baffles, realizing we will soon be able to spin it.

Here we put the lid on the shaft, coupled them, attached new bearings and lip seals, added the new coupler on the bottom of the shaft, moved the lid with everything else to the sphere, added PTFE tape between the lid and the sphere to avoid potential liquid and gas leakages. We tested the pressure and eliminated the gas leakages.

3.3.9 Refilling the experiment

"I got a bad feeling about this." — Han Solo

The refill procedure was planned for August 5th 2021 and was designed to be executed almost exactly as the draining procedure, but without the hot insertion operation, because

the draining diptube was already in the tank. Here we had to measure the time it would take to liquefy sodium inside the tank, and meanwhile, we were able to keep the surfaces of the tank at a high temperature to let the paint produce all the unpleasant fumes so we wouldn't have the same experience during the refill operation as the one we had during the draining. The estimated amount of solid sodium inside the storage container was diagnosed by analyzing the reflective acoustic parameters of the surface oscillation and the images of the infrared camera capturing the surface of the tank. In Fig. 3.24 we can see Rubén Rojas making the walls of the tank oscillate with a rubber mallet, by the produced sound we could say if there was gas, liquid, or solid touching the wall at the location of the hit. Additionally, we could see that the temperatures of the regions with different acoustic spectral characteristics had huge temperature gradients. After several weeks of tests, we concluded that we need about twelve hours of heating to be able to proceed with the refilling. So we confirmed the calculations that were done by the author and mentioned in Section 3.3.1.

To control and monitor the process we used the same "Tramon" application (Fig. 3.14) written by the author, with slight adjustments related to relocating temperature probes and increasing the level of sodium in the sphere during the process in contrary with the decreasing one during the draining. In an attempt to speed up the healing process by slowing the convective heat exchange and lowering the fumes production, we covered the tank with oil-absorbing fabric, as can be seen in Fig. 3.25. But as the result, we didn't see any significantly improved heating time. In one of the last parts of the refill preparation, we vented the atmospheric air from the sphere using the same procedure of consecutive filling and relieving nitrogen gas, as described in Section 3.3.3.

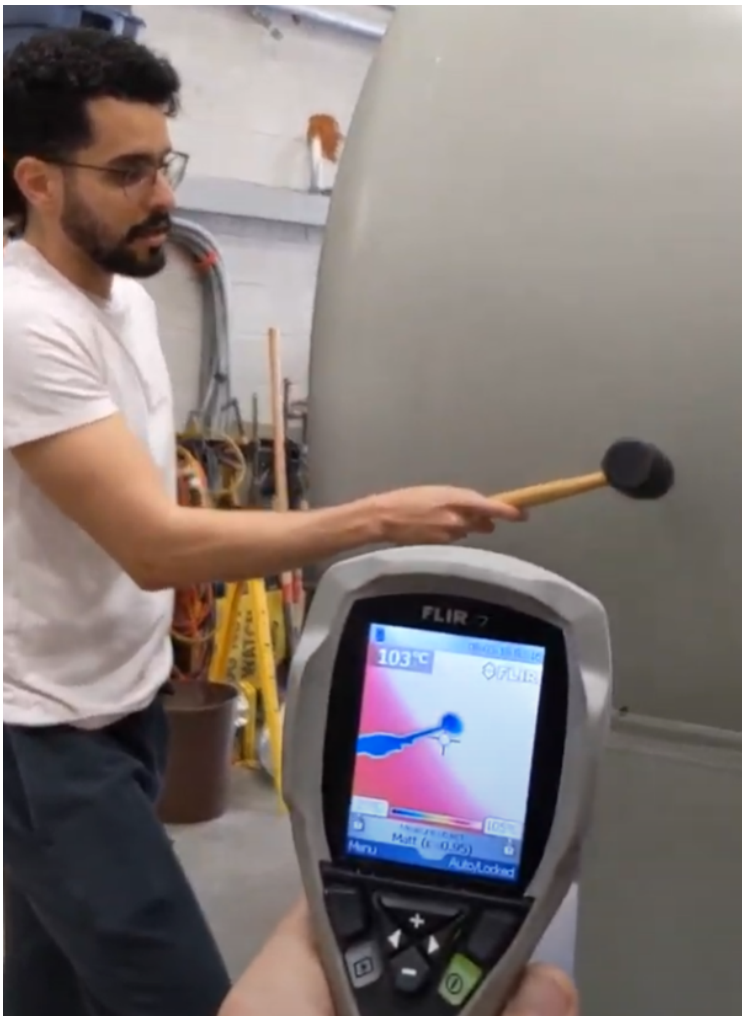

Figure 3.24: Liquid to solid ratio diagnostics in process. Rubén uses a mallet to bounce the surface of the tank, and the produced sound distinguishes the state of the matter inside. Also, the infrared camera shows different surface temperatures for different sounding regions.

On August 5, 2021, after the diagnostics reported that sodium in the tank is fully liquid, we attempted to start the transfer: pressurized the tank and opened the valve on the transfer line. But right after the initial brief start, the sodium flow stopped. After some analysis, the crew found that valve F shown in Fig. 3.26 was not functional anymore and was blocked by something inside. The crew concluded that liquid sodium solidified inside the valve because that was one of the very few places without heating and it was exposed

Figure 3.25: Rubén Rojas adding the heating tape to the valve to heat up and liquefy solid sodium inside the transfer line valve during the refilling operation.

to room temperature. So we attached electric heating tape to the valve and waited. In Fig. 3.25 we can see Rubén Rojas (in blue) adding the tape to the valve, Bryan Quinn (in green) assisting Rubén, and Heidi Meyers (in orange) using the infrared camera to diagnose the surface temperatures. After approximately one hour we heard some "oompf" coming from the sphere, which represented that there is a flow of sodium through the transfer line, and heard splashing sounds from the three meter. In Fig. 3.27 we can see that the operation started later during the day, and even with the higher pressure drop between the vessels, the volume flow was lower during the refill than during the drain (Fig. 3.16), that can be explained by the siphon effect and matches the predictions done by numerical simulations mentioned earlier. The volume flow, like before, was estimated by using a laser distance meter from the top of the sphere through the window port, the view of the liquid

metal occupying the sphere is shown in Fig. 3.28. On the top of the cube during the refill operation was detected a strange smell and seen a flow of slightly visible small particles through the relief opening, where the nitrogen was escaping the experiment. The particles were considered to be either sodium metal particles or oxides, so to avoid any damage to the personnel we started using the chemical masks the author attached an aluminum duct to the escape valve and let it flow to the space between the sphere and the cube.

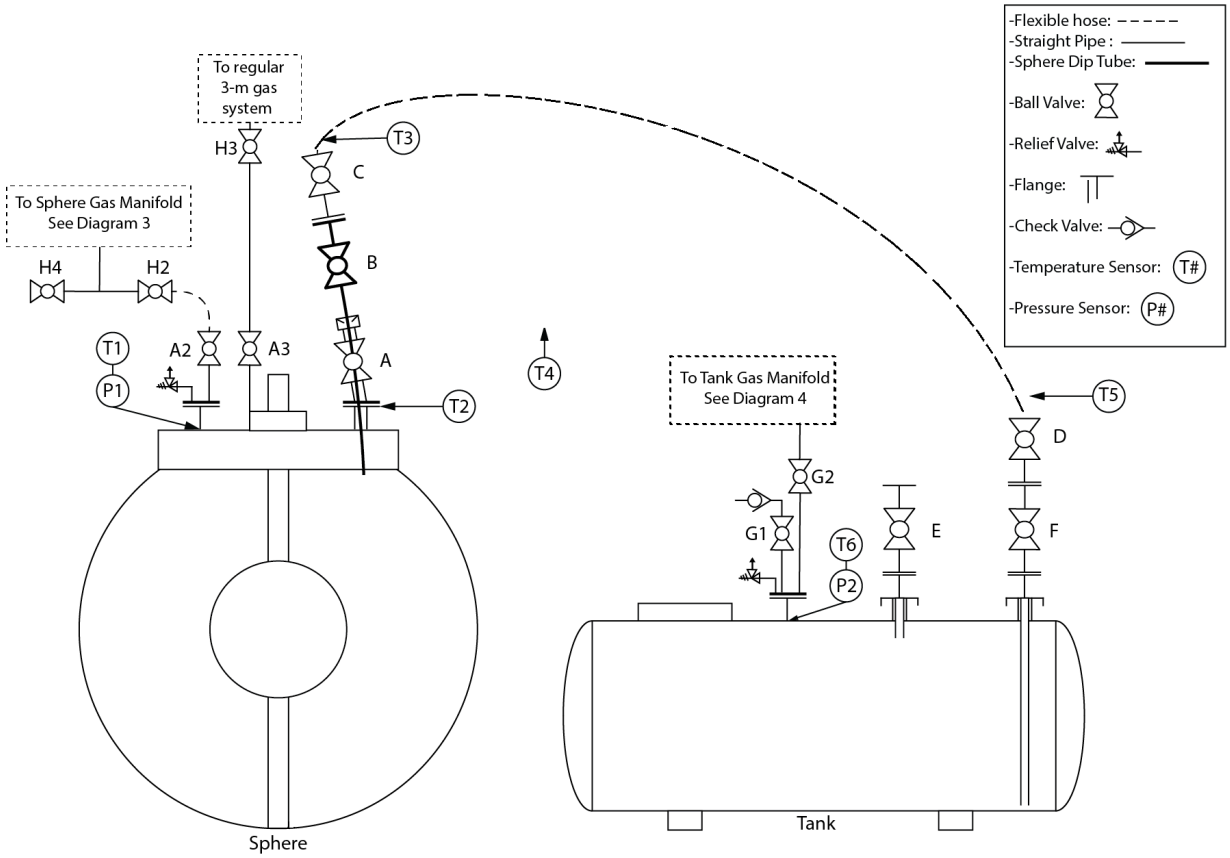

Figure 3.26: Diagram of the refilling operation.

3.3.10 Final assembly

After we successfully refilled the apparatus with sodium we were able to assemble it back. So there was a clear visible way on what to do to make it run again and have

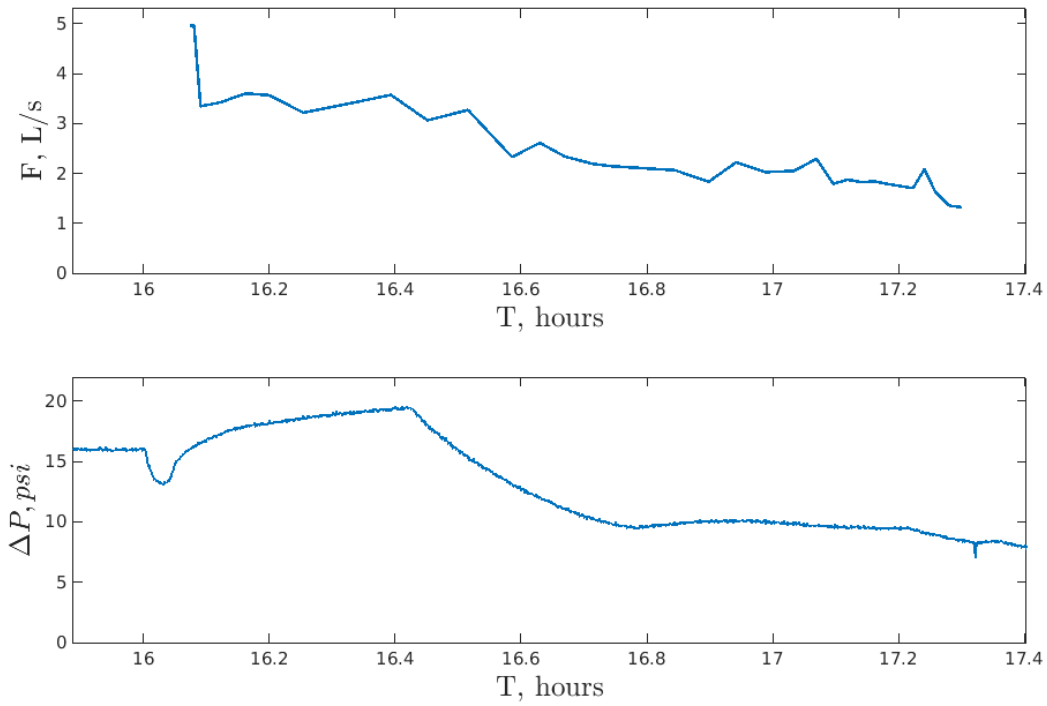

Figure 3.27: The flow of sodium and corresponding pressure drop during the refilling operation. Here we don't show the smoke level in the room because it was staying within the low range during the whole day.

the experiments. We needed to remove all the unnecessary transfer diagnostics, replace the transfer ports with the experimental ones, put back the outer and inner motor frames, attach the sphere to the cube, and detach four steel cables that were holding the sphere in the horizontal position because normally the inner frame keeps it in place. We connected the inner and outer sphere motors to the power cables, coupled the outer sphere gear to the outer motor, and adjusted the gear belt tension to 15 Hz. We coupled the inner motor with the inner sphere shaft as well, this part specifically took a lot of time and extensive hammering.

In Fig. 3.29 we can see the way the crew managed to rig the one-ton outer sphere motor that safely allowed to transfer it from the outer motor frame to a storage location

Figure 3.28: A photo of liquid sodium through the window port, filling up the sphere during the refilling operation.

with an ability to flip the motor ninety degrees so that it would be stored on its mounting surface. And on Fig. 3.30 the process of moving the inner frame motor, here the frame is attached to the overhead crane with two chains and two chain hoists. During the removal procedure we managed to pull one side of the Top Outer Bearing (can be seen in Fig.3.1) so that the outer race tilted enough to let the rolls fall. The bearing had to be replaced afterward.

We added an additional instrumental probe with several magnetic Hall sensors (second "finger") in one of the ports that are located diagonally from the preexisting "finger", we put all the diagnostics and data acquisition hardware with all the necessary power sources

Figure 3.29: Rigging the outer sphere motor with multiple straps secured with cables, and a chain hoist that allows it to slip the motor before landing.

into the lid, more details on the Fig. 3.35 and the corresponding list. We connected 115 wires coming from our 35 Hall probes to the acquisition card, this task, while it might sound like a walk in the park, ended up being one of the most time and labor-consuming procedures: the testing process was achieved by applying low-frequency oscillations of a strong local magnetic field to each probe individually while doing data acquisition, and later observing the time traces of the acquired data (or in other words attaching a strong magnet to a ruler and waving it next to the probes while walking on the magnetic coils). This procedure helped us to find several broken probes and wires, which we replaced and tested again and again.

During these days we realized that the current data acquisition software and hardware are too old, deprecated, and unreliable, so the author designed, purchased, and assembled the new system for the three meter apparatus, but from here and till the end of this thesis

Figure 3.30: The rigging configuration for the inner frame. Two chain hoists allow controlling pitch and roll, while Dan's hands control yaw (bottom right).

we will be talking about the data gathered with the old system. Installation of the new gear will be something that the new generation of scientists in the lab should designate their time to. Specifically, the author finds it important because he had to support the old laboratory computers and local network for years and at some moment the main computers stopped working while having all the important software and data. "Sodium" system drive was 10 years old, its RAID5 was 7 years old, made with consumer-grade hard drives, two of which died in my hands, but with some black magic and dance with a cowbell, the data was saved. The author spent an unrealistic amount of time designing, purchasing, assembling,

setting up the hardware, and writing new applications and would like other people not to have a similar experience. *Akin's Law 3. "Design is an iterative process. The necessary number of iterations is one more than the number you have currently done. This is true at any point in time".*

During testing the fire extinguishing and smoke suppressive systems which have electronically activated valves to provide the regular 40 psi building water to the scrubber that is located outside the building on its east wall, and testing the external magnetic field coils power supply, we have discovered that there is some excessive damage inflicted on these systems. Most probably that happened during the "Copper Thief" events in March 2019. The author was working in the lab, and heard some unusual noises from the building trenches and reported that the next day when some institute authorities were visiting the lab with an unusual revision. As was found later, a person had found an opening and was able to crawl into the High Bay (ERF 0204). The person was able to remove most of the water copper pipes, and high gauge electric cables, and take some waveguides including the property of the other laboratories. In Fig. 3.31 we can see Rubén pointing to the copper that the thief was storing in the trenches. According to the police officer who stopped by to interview the author, the person was arrested that night with a shopping cart full of copper, and police were able to trace back the origin of the copper by the cart's tracks on the ground and informed the institute officials.

With help of the labs' legend Don Martin, Rubén Rojas, and the author proceeded to fix the damage: replacing the water lines, the electrical valve actuator, high voltage lines for the magnetic coils, etc. This part of the project was called "Going to Moria" or "Yippee Ki Yay". Here we were crawling in the trenches, cutting damaged pipes, installing the new

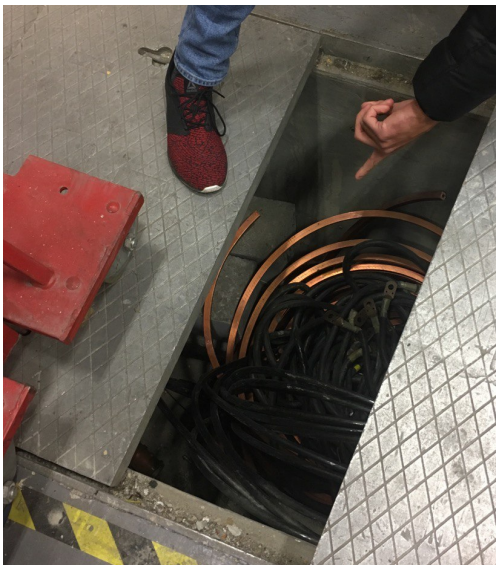

Figure 3.31: Rubén Rojas demonstrates the opened trench where the thief gathered the copper.

ones, soldering copper, replacing valves, and unclogging the water drains. After this was done, we had a fully mechanically operational experiment. And we're ready to spin!

3.4 Experimental setup

3.4.1 Experiment control application

C-3PO: "I suggest a new strategy, Artoo: Let the Wookiee win."

After the problems mentioned above with the old hardware and software, we replaced most of the control systems, the author attempted to recover the old software and run it on the new hardware. With over 90% failure rate the author suggested a new strategy, - Arturito, write everything from scratch. - that also follows *Akin's Law 11: "Sometimes, the fastest way to get to the end is to throw everything out and start over"*.

Starting from this moment, most of the controls and diagnostics were redesigned,

instead of the old control local application "BigSister" and a set of individual applications for live plotting parameters and smoke level analyzer, etc, the author developed a new web-based Python application [196, 197]: "BigMomma" or simpler "BigMo". The app is creating a local web application that allows the operators to control oil heater, control rotation rates of the motors, control the applied magnetic field, monitor the current and time evolution of torque, static pressure, temperatures, as well as observe the apparatus from different angles through the web cameras, see the statuses of the hardware devices, raising the alarms in case the pressure or temperature or smoke level are not in the desirable ranges, it write logs in CSV formats, writing the user controls and comments, all the control parameters. The original code is available on the project's GitHub webpage: https://github.com/Three-Meter-Geodynamo-Experiment and should be updated by the new members of the laboratory.

While the development of the application logic and architecture was taken very seriously, went through a number of hard and soft tests, was discussed with professional software engineers, and debugged and debugged and debugged, the application interface development can be described by *Akin's Law 33. (Patton's Law of Program Planning) "A good plan violently executed now is better than a perfect plan next week"*. In Fig. 3.32 and Fig. 3.33 are shown the operator windows.

The web-based application allows anyone within the campus network to see the current state of the experiment, which helps for debugging hardware and monitor different parameters at the same time from any place. While having a decent level of security, of course, not allowing anyone, except for the operators, to control anything.

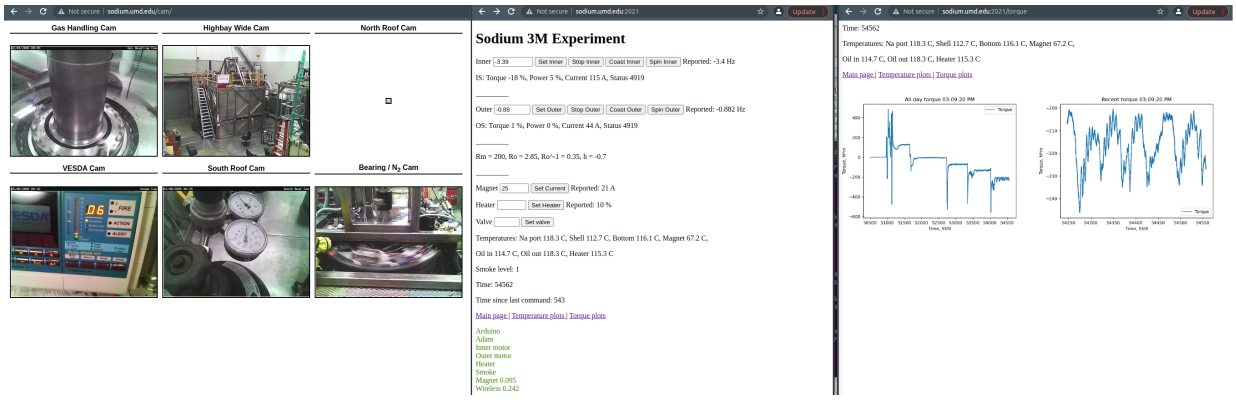

Figure 3.32: BigMo interfaces: on the left - six cameras live broadcasting different parts of the experiment; center - the main control page; right - page with live torque plots.

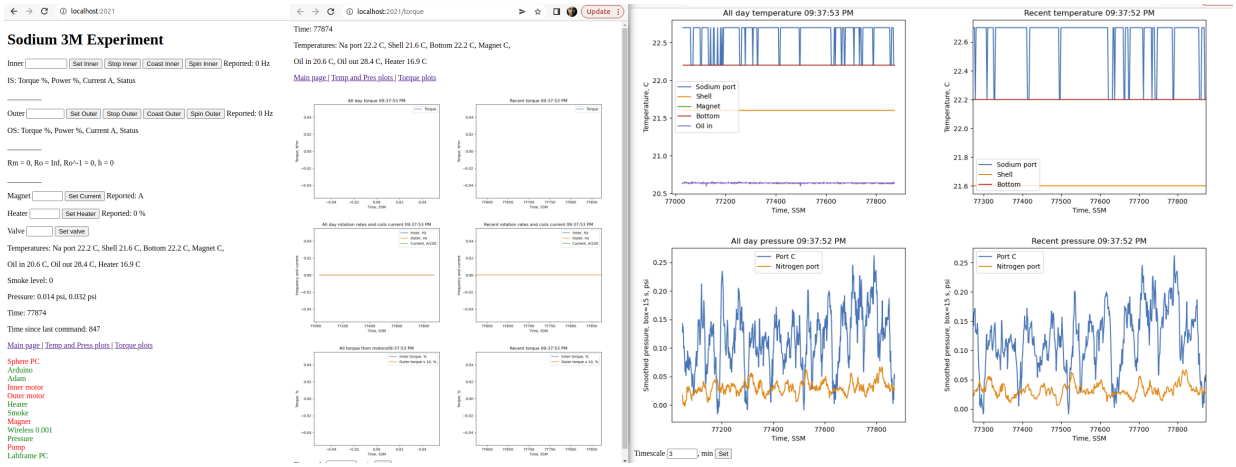

Figure 3.33: BigMo interfaces: on the left - the main control page; center - plots with torque sensor data and the experiment control parameters: rotation rates, applied magnetic field, and torque values from the motors; right - page with live temperature and pressure time evolution.

3.4.2 Local devices, network, the lid devices

Main devices that are vital for the proper experimental control:

1. Sodium PC is the host of the BigMo app, NTP server, data storage, logs, etc. 192.168.1.1 Located in the shed in the rack.

2. ADAM, connected to Sodium via USB, reads temperatures of the heater and the oil lines. Located on the eastern wall of the Highbay right above the oil lines

3. Modbus, connected via RS485, communicates with three devices: the heater, inner, and outer motor, which is the main point of controlling the experiment, it sets up the rotation rates of the spheres and it controls the power of the oil heater that heats the sodium and keeps it at certain temperatures.

4. Arduino, connected via USB, controls the bypass valve, turns on the blower and the scrubber, located in the electronic box in the rack, under Sodium PC

5. Maple, a USB device, located in the electronic box in the rack, under the sodium PC, reads pressures in the pump and the oil lines.

6. Wireless reads the wireless temperature sensors: 3M shell, 3M bottom, 3m Port, Magnetic Coils. Located on the cube, shown in Fig. 3.34, connected via RJ45. 192.168.1.200

7. Magnet, an Arduino with an Ethernet shield, located in the Ling room in the magnet coils power supply, shown in Fig. 3.34. Connected via RJ45. It controls the current in the magnetic coils via a 4-20 mA scheme. The output file is 'magnet.dat', it writes the current data with a sampling rate of 10 Hz, stores time in Seconds Since Midnight (SSM) format, the controlling current in microamps, and the output current in amperes. 192.168.1.177

8. Pressure, an Arduino with an Ethernet shield, located on the 3M lids, shown in Fig. 3.34, reads the static pressure in the 3M from two pressure probes and writes it on its webpage 192.168.1.178

9. Smoke, a web camera located on the west wall of the Highbay, points at Vesda

aspirating smoke detector and reads the level of the smoke indicators. Raises the alarm on high levels of smoke and sends texts to warn the operators and the staff, connected via RJ45.

10. Pump, the heating oil pump located outside the building, on the east wall, the pump controls are located on the front panel of the electronic box in the rack, under Sodium PC, the left buttons control the pump.

11. Scrubber, the air smoke scrubber located outside the building, on the east wall, the water supply to the scrubber is controlled by a mechanical valve and an electric actuator located next to each other in the trench of Ling room, automatically starts with raising alarm in the software or pressing one of the "Stop" buttons.

12. Blowers, the air blowers designed to remove the smoke and fumes from the room, located inside the High Bay on the east wall, the control located between the shed and the experiment, on the right from the motors controllers. Start automatically with a raised alarm.

13. LN2, liquid nitrogen fire suppression system: a 200L liquid nitrogen dewar, should be located on the south-eastern top corner of the cube and attached to the LN2 lines. Should be tested before every run, start only with an operator flipping one of the switches: first in the shed on the rack, second on the southwest corner of the cube on eye level, third on the northwest top of the cube on the rails.

14. N2 line, 300 cu ft nitrogen bottles located on the northeast bottom of the cube, attached to plastic gas lines, and attached to the sphere via a blue hose to the gas

port next to the inner sphere shaft. Necessary to pressurize the sphere all the non-experimental time (up to 3 psi) to avoid sodium oxidization.

Fig. 3.34 is demonstrating the map of the local area network, the IP addresses, the way everything is wired, and their physical locations. This map should be memorized by anyone who is attempting to work with the experiment. The information on this map might save the debugging person sometime between one hour and one month. Also, please, never plug the LAN (SaddleNet) routers or switches into the university network. The author obtained most of his gray hair while looking for the reason the network adapters were misbehaving. The author refuses to put in the text the exact amount of time he spent fixing network issues. And please, no Win XP!

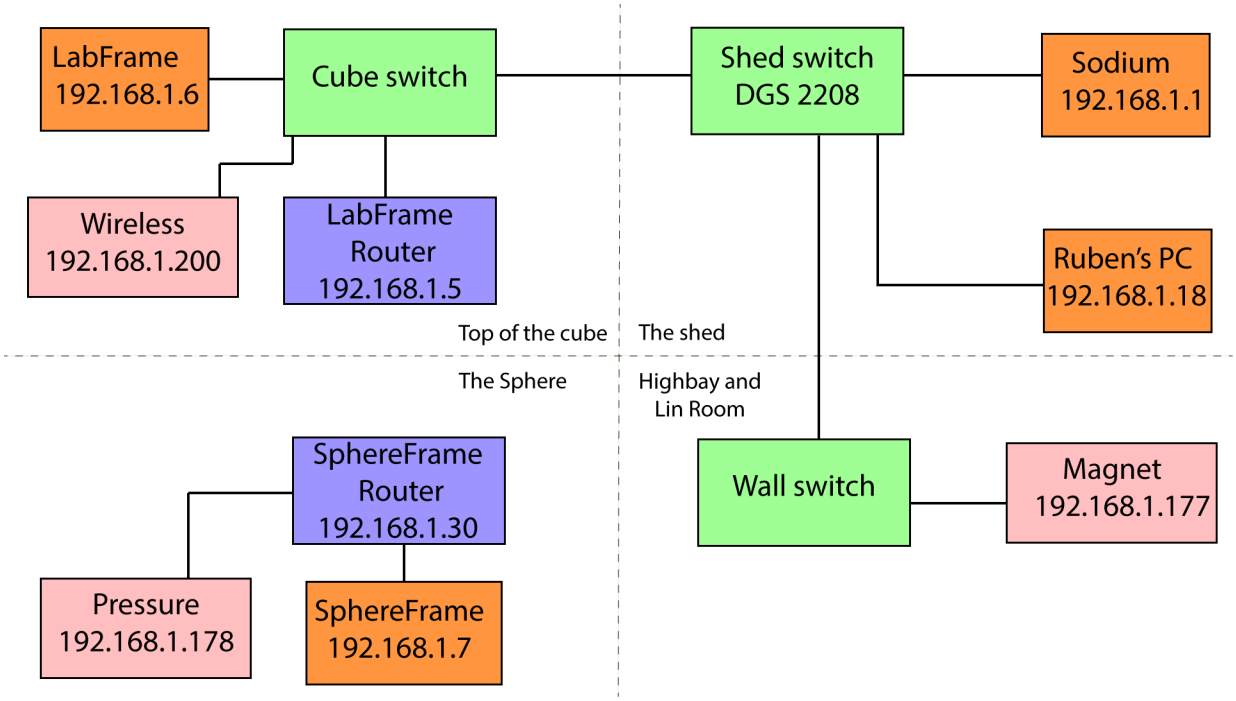

Figure 3.34: The schematics of the SaddleNet Local Area Network, all connections are made with RJ45 cables.

In Fig. 3.35 there is the scheme of the hardware on the lid of the experiment.

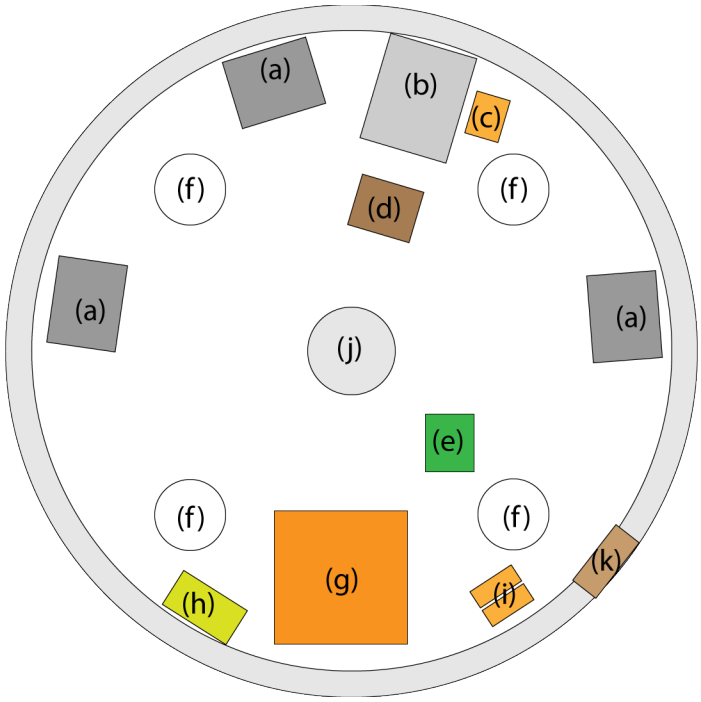

Figure 3.35: The schematics of the lid of the Three-meter experiment.

(a) Three 12 V car batteries.

(b) Power hub with plugs for batteries and chargers.

(c) Pressure Arduino box for monitoring and logging pressure in the sphere.

(d) WiFi router in bridge mode to connect with the local area network.

(e) Main Hall array board with 35 probes connected.

(f) four instrumental ports with AC and DC pressure probes, two "fingers" with Hall probes, and one temperature probe.

(g) Sphere computer box with power supply and data acquisition board.

(h) AC pressure probes amplifier box.

(i) Two remote temperature sensor transmitters.

(j) The inner sphere shaft with the torque sensor on the top of it, an Arduino that reads the torque, the Bluetooth transmitter and receiver, and a socket for the battery, the assembly is shown in Fig. 3.36.

(k) Power board with fuses.

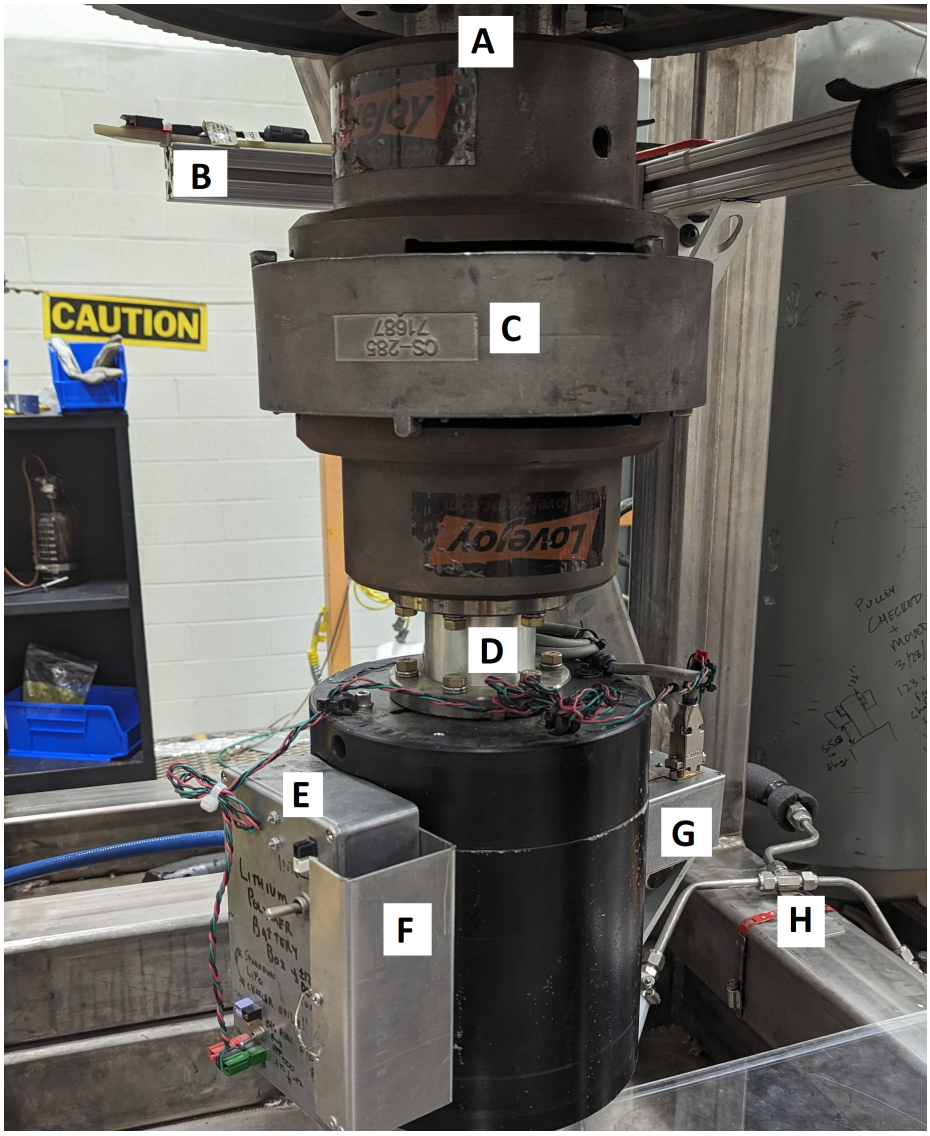

Figure 3.36: The torque sensor assembly: (a) inner motor shaft; (b) Bluetooth receiver connected to Sodium PC through a USB-RJ45-USB extension; (c) flexible shaft coupler; (d) Futek TFF-600 torque sensor; (e) torque sensor power supply; (f) torque sensor battery box; (g) torque sensor signal transmitter; (h) liquid nitrogen line with hoses.

3.5 Data acquisition

The current main scientific measurements are the 35 magnetic Hall probes array and 3 AC pressure probes. The main mindset for the experimental runs and the data acquisition can be described best with *Akin's Law 26. (Montemerlo's Law) "Don't do nuthin' dumb"*. Or with more details as:

Monday - start heating the experiment with the Heating SOP in Appendix E, check if everything is alright, finish heating in the evening, and go home.

Tuesday, repeat the Monday protocol till the sodium is fully molten, and lower the heaters. Follow the Data Acquisition SOP in Appendix F: turn on all the necessary hardware, reach the Sphere and LabFrame computers via the virtual desktop through the Rubéns computer and start the acquisition. Do what you want before you get tired. Finish. Check that everything is alright, and go home.

Apply the Tuesday SOP for the next days if necessary.

And always stay with *Akin's Law 22. "When in doubt, document"*.

3.6 How to do data analysis

Akin's Law 4. Your best design efforts will inevitably wind up being useless in the final design. Learn to live with the disappointment.

When the author started working with the experimental data it was a structured pile of files with no reasonable way to find a specific experiment or a simple way to get debiased data from a known experiment. By the end of 2022, the experimental data is no longer just

the slightly structured pile of files, but it is already a bigger structured pile of files, with a number of useful codes that one can use to relatively easy find a desirable experimental data, plot the parameters during the day, and access the data in a structured way. Most of the currently useful codes are available at the labs GiHub page.

The author would like to specifically talk about the magnetic Hall probes data:

$$V_{probe\ i}(t_N) = V_{Na\ i}(t) + V_{coils\ i}(I) + V_{bias\ i} + V_{misc\ i} + V_{noise}\ , \tag{3.1}$$

Here the stored data has the voltages on each probe as a discreet function of time - $V_{probe\ i}(t_N)$, and this can be decomposed into several voltages:

1. $V_{Na}(t)$ - the voltage induced on the i'th probe by the flow of the sodium inside the sphere;

2. $V_{coils\ i}(I)$ - the voltage on i'th probe induced by the external coils and in our model we assume that the coils' magnetic field doesn't depend on the position of the sphere, but only on the current in the external coils;

3. $V_{bias\ i}$ - the bias level on the i'th probe, usually around 4.8 V, but sometimes changes in time, usually relatively slowly but still sometimes it can look like an induced field on the scale of units of Gauss after 15 minutes;

4. $V_{misc\ i}$ - the miscellaneous voltage induced by other magnetic fields like Earth's magnetic fields, magnetized materials, wires, motors, and lights. Can be seen for example in the uppermost probes that are close to the outer sphere motor;

5. V_{noise} - well, this one is always there, temperature noise, wiring noise, DAC noise, all the zoo.

In the "parsing_data_3m" repository there is a detailed manual on how to use some of the codes, so here I would like to explain the simple logic behind the assumptions taken in Eq. 3.1. We assume that we cannot do anything with the miscellaneous and noise voltage, but we can deal with the rest. To estimate the external coils induced voltage the author used historical data from experiments with no rotation but with a magnetic ramp, recorded our own data with no rotations but with the applied magnetic field, and analyzed the experiments. As the result there is a repository "coils_signal" that has a code that would give you an estimation of the induced magnetic field on each probe as a function of the applied magnetic field and a function of the configuration of the coils, at first there was only one coil, later there were two and with these two there are dipole and quadrupole configurations, also the calibration changes in time on the scales of years, probably due to the probes slight movements or deterioration, so these calibrations should be done at least once a year. Important: don't try to directly decompose these voltages into spherical harmonics with $getcoeff3m.m$. It will not go as well as you hope. For the debiasing procedure, we plan our experiments in such a way that before doing any important measurements we do a 5-10 minute run without applying an external magnetic field and with no shear rotation (solid body rotation). In this case, we assume that during this run the sodium inside is not inducing a DC voltage on the probes, so the averaged values of the voltages during these 5-10 minutes should correspond to the bias level. Also, the DA card needs some time to warm up after you start the computer, so one can expect a

dynamic bias in the first 10 minutes. The author doesn't understand the mentioned "warm up" time, especially because the card is located in the computer on the lid of the sphere with 120 C liquid metal. So knowing these two values, the operator can subtract the bias levels and the coils signal from the measured voltage, and stay with the sodium signal, miscellaneous, and, of course, the noise. And later in this thesis we will be always talking about the magnetic data in the assumption that there are no induced magnetic fields by the external coils, and the subtracted bias is a constant value (that is not specifically true for the long experiments and low measured magnetic fields - on the scale of 1 Gauss)

Finding any specific experiment might be a difficult task in unorganized folders with some data and log files, so some of the codes were developed specifically to make a structured list of all the experimental runs we had in with the Three Meter Experiment.

More details about the useful codes are available at the https://github.com/Three-Meter-Geodynamo-Experiment.

Chapter 4: MHD turbulence prediction

In this chapter we will show the software techniques that we developed to forecast the behaviour of the rotating MHD experiment. These models are model-free - that means that the software doesn't know it this is a sphere, a cube, a cat, or a series of letters. The models are made to learn the dynamic rules just by observing the time evolution. This work was done to create a system that would be capable of learning the way the spherical MHD evolves and possibly reproduce the geodynamo. This chapter mostly follows our publication submitted to Physica D [198].

4.1 Introduction

Turbulence is a ubiquitous phenomenon that appears in natural and engineering processes. The behavior of a turbulent system is usually too complex to be precisely simulated, even with modern computational methods. Experiments offer accurate dynamics but with limited diagnostics. In the present work we examine results from a three-meter diameter spherical Couette flow experiment located at the University of Maryland College Park [58, 110]. It is designed as a model of the Earth's outer core and made to study rotating turbulent magnetohydrodynamic flows, including the dynamo mechanism for magnetic field generation. Recent developments of machine learning and artificial

neural network techniques have shown surprising utility in many different areas including industry, technology, science and entertainment [172, 173, 174, 175, 176, 177, 178, 179, 180, 181, 182, 183, 184]. In particular, we are interested in a technique known as Reservoir Computing (RC) [185, 186]. Some of these techniques are able to predict the time evolution of a particular dynamical system based only on information of its past states. For example this technique has been able to predict time series of a weak turbulent system like Kuramoto–Sivashinsky equation [187].

Due to the high non-linearity of many physical systems, using any numerical technique to solve the governing equations becomes extremely difficult to compute as we increase the complexity of the system. For instance, the complexity increases in turbulent flows as we increase the Reynolds number [199]. One approach to solving this problem is via data assimilation techniques that are widely used in geophysics including weather prediction and analysis of the Earth's magnetic field [200, 201, 202, 203, 204], but this approach is limited by other factors, for instance, by how accurately the model characterizes the physical system.

In this work we will use a model-free prediction technique based on reservoir computer analysis [186], a machine learning method for analyzing sequential data, typically using a recurrent neural network. This method does not depend on any mapping or modeling of the experiment or physical system and can be applied only knowing information from the system's past states. This technique was proposed independently for echo state networks [185] and liquid state machines [205]. Previous works have shown the ability to predict time evolution of chaotic systems including weak turbulence [179, 180, 184] and chimera state behavior in SQUIDS [174].

4.2 Three-meter system

4.2.1 Apparatus

The three-meter experiment apparatus (3m) schematic shown in Fig. 4.1 is a spherical Couette experiment consisting of two concentric spheres with outer radius $r_o = 1.46\ m$ and inner radius $r_i = 0.51\ m$. The ratio between them $\Gamma = r_i/r_o = 0.35$ is the same as the Earth's outer core to inner core ratio [117]. The space between the spheres is filled with metallic sodium. Experimental runs are done at $T \approx 120\ C$ to liquefy the sodium. The inner and outer spheres are able to independently rotate with frequencies up to 4 Hz for the outer sphere and up 15 Hz for the inner sphere.

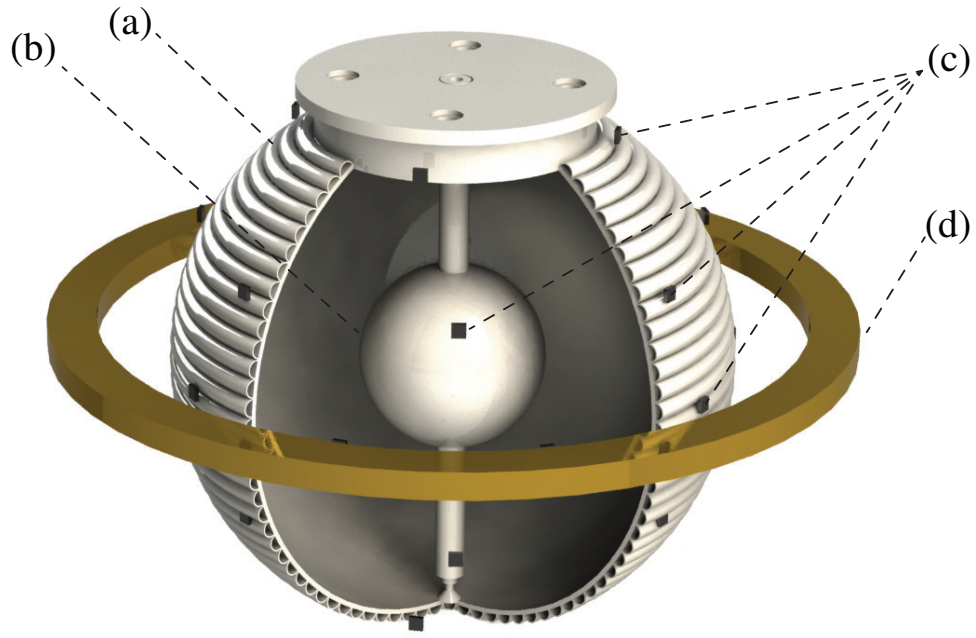

Figure 4.1: Schematic of the three-meter experiment: (a) Three-meter diameter outer sphere, (b) one-meter diameter inner sphere, (c) array of 31 magnetic Hall probes, (d) external electromagnet. The volume between the spheres is filled with metallic sodium.

4.2.2 Data acquisition

During experimental runs, we take data from 31 magnetic Hall probes that are distributed on the surface of the sphere and measure the radial magnetic fields. Additional data is taken from two probes inside the sphere, in contact with the sodium, but we do not use this data in this study. The sampling rate for magnetic Hall probes is $f_s = 256$ Hz. In this study we use data from 32 experimental runs with rotation rates -0.7 to -1 Hz for the outer sphere and -9.7 to 4.7 Hz for the inner sphere. The current in the external magnet in all these experiments was set to 20 A, which creates an external magnetic field in the sphere center of $B_{center} = 10.5 \times 10^{-4}\ T$. To study the fluctuations we subtract the mean values from each of the 31 signals and divide each by their overall standard deviation. This keeps the relative amplitudes of the signals the same as the unnormalized signals, and allows us to reconstruct the original signals by multiplying the normalized signals by the saved standard deviation and adding the saved bias vector.

4.2.3 Parameters

In Table 4.1 we define the dimensionless parameters used to characterise the experiments.

Number	Definition	Range
Reynolds	$Re = \frac{\lvert\Omega_i - \Omega_o\rvert(r_i - r_o)^2}{\nu}$	$(0.2 \ldots 5) \times 10^8$
Rossby	$Ro = \frac{(\Omega_i - \Omega_o)}{\Omega_o}$	$-5.7 \ldots 8.6$
Ekman	$Ek = \frac{\nu}{\Omega_o(r_i - r_o)^2}$	$(1.2 \ldots 1.9) \times 10^{-7}$
Lehnert	$Le = \frac{B}{\Omega_o r_o \sqrt{\mu_0 \rho}}$	$(3.4 \ldots 5.4) \times 10^{-3}$

Table 4.1: Dimensionless parameters. See Section 4.2.3 for notation.

Here Ω_i and Ω_o are the angular velocities of the inner and outer spheres respectively, $r_i = 0.51\ m$ and $r_o = 1.46\ m$ are the radii of the inner and outer spheres. At our temperatures, the mass density of liquid sodium is $\rho = 920\ kg/m^3$, and $\nu = 6.76 \times 10^{-7}\ m^2/s$ [206] is the kinematic viscosity of liquid sodium. Also, $B = 10.5 \times 10^{-4}\ T$ is the external magnetic field in the center of the sphere, and $\mu_0 = 4\pi \times 10^{-7}\ N/A^2$ [207] is the vacuum magnetic permeability.

We measure time in units of the *dipole diffusion timescale* [123] which is the exponential time of an axisymmetric magnetic field decaying through resistivity in a conductive sphere defined by:

$$\tau_D = r_o^2/(\pi^2 \eta)\ , \tag{4.1}$$

where $\eta = (\sigma\mu_0)^{-1}\ m^2/s$ is the magnetic diffusivity of sodium and $\sigma = 10 \times 10^6\ (\Omega\, m)^{-1}$

[208] is the electric conductivity of sodium at our temperatures. For our apparatus $\tau_D \approx 3\ s$, matching experimental observations [58].

4.3 Prediction models

In this section we will introduce the models we used to predict time evolution of the experimental data in the three-meter experiment. The general concept is to create a system that is trained on experimental data for some period of time (training time) and then tested by predicting the behavior of the system in the future (testing phase).

4.3.1 Auto-regressive model

An auto-regressive prediction model (AR) [177] (see also, e.g. [209]) is a relatively simple way to predict the next measurements of a system based on the knowledge of autocorrelations of past measurements of the system. Let U_k denote the normalized vector of measurements taken at time step k. The prediction uses a linear transformation L of the previous N_{AR} measurement vectors to predict the next vector:

$$\hat{U}_{k+1}^{AR} = L \cdot \begin{bmatrix} \\ U_k \\ \\ \\ U_{k\text{-}1} \\ \\ \\ \vdots \\ \\ \\ U_{k\text{-}N_{AR}+1} \\ \\ \end{bmatrix} . \tag{4.2}$$

Here $\hat{U}_{k+1}^{AR}$ is the estimated value of the next time-step in the time series U_{k+1}. To compute L during the training time we create an array with the values of the previous N_{AR} time step values of the data, so we have a matrix Y with size $(N_{AR} \cdot D) \times T_{Tr}$, where T_{Tr} is the number of time steps during training, and D is the dimension of U_k. We also discard the first 250 times steps to train the AR model. To train the model we use linear regression (with QR decomposition and Tikhonov regularization [210]) to find the matrix L that will minimise the cost function evaluated as a Euclidean norm:

$$min(\|L \cdot Y - U\|^2 + \lambda \|L\|^2) \ . \tag{4.3}$$

Here U is a matrix with size $D \times T_{Tr}$ that contains the training experimental data, and λ is a regularization parameter.

After training we can predict many time steps into the future by iterating Eq. 4.2 replacing the unknown values U_j with the predicted values $\hat{U}_j^{AR}$. This model can be controlled by changing the number of time steps in memory N_{AR} and the regularization parameter λ that helps to prevent overfitting. Among powers of 10, we found that $\lambda = 10^{-6}$ yields the smallest prediction errors for the AR model. For our purposes we set $N_{AR} = 250$, which corresponds to the approximate number of time steps in one revolution of the outer sphere for the taken experiments. We analyzed the performance of the AR model with different N_{AR} and we found that for our experimental data sets the error of the prediction almost does not change for $200 < N_{AR} < 500$, while the computational cost significantly increases for larger values.

4.3.2 Reservoir computing

A reservoir [184, 185, 186] performs a type of computation on a time series of vectors U_k and outputs a time series of higher-dimensional vectors X_k such that X_k depends only on past inputs $U_{k-1}, U_{k-2}, \ldots$. Then U_k is estimated by a linear transformation W_{out} of X_k. The analogue of Eq. 4.2 is thus:

$$\hat{U}_{k+1}^{RC} = W_{out} \cdot X_{k+1} = W_{out} \cdot \begin{bmatrix} \\ x_1(U_k, U_{k\text{-}1}, ...) \\ \\ x_2(U_k, U_{k\text{-}2}, ...) \\ \\ \vdots \\ \\ x_{N_{RC}}(U_k, U_{k\text{-}1}, ...) \\ \\ \end{bmatrix} . \tag{4.4}$$

Eq. 4.4 generalizes Eq. 4.2 by allowing nonlinear functions $x_j\,(U_k, U_{k-1}, \ldots)$. For the results we will present the nonlinear functions are states of the reservoir: an array of N_{RC} neuron-like objects that are interconnected with each other according to an adjacency matrix A. That is chosen randomly as follows: each ordered pair of nodes has a probability p to be connected by a nonzero entry in A that is uniformly distributed between -1 and 1. After the random entries are chosen, A is scaled so that its spectral radius (the magnitude of

its largest eigenvalue) is set to ρ_{RC}. The reservoir state X_{k+1} that is used to approximate U_{k+1} is computed according to the iterative mapping:

$$X_{k+1} = (1-\alpha)X_k + \alpha \tanh\left(A \cdot X_k + W_{in} \cdot U_k\right) . \tag{4.5}$$

Here α is called the leakage parameter, A is the adjacency matrix, and W_{in} is the input matrix, which is a matrix of size $N_{RC} \times D$, whose entries are random numbers uniformly distributed between $-w$ and w, where w is an input strength parameter.

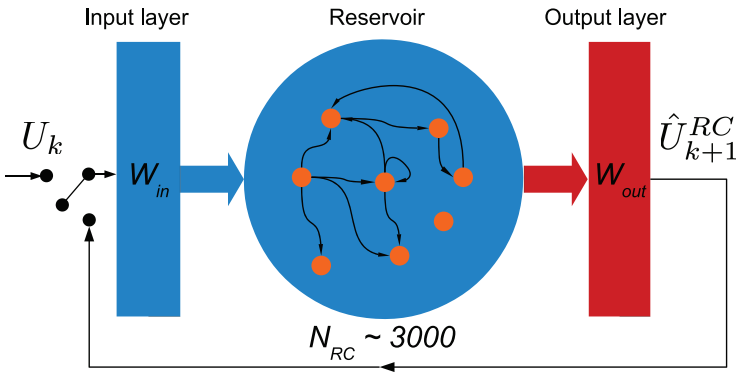

Figure 4.2: Schematic diagram of using a reservoir computer for prediction. Input weights and inner connections are generated with a random number generator. The output matrix is determined during training.

To start initial RC we choose X_1 randomly, and to remove the influence of the randomised start we discard the first 1000 time steps of the data. We take our training data $U_1, U_2, \ldots, U_{T_{Tr}}$ and feed it into the reservoir step by step, storing the outputs $X_1, X_2, \ldots, U_{T_{Tr}+1}$. We then use linear regression with Tikhonov regularization to find W_{out}, as for the auto-regressive model, minimizing the cost function:

$$min(\|W_{out} \cdot X - U\|^2 + \lambda \|W_{out}\|^2) . \tag{4.6}$$

After the training phase is done, we take the estimated value of the next time step $\hat{U}_{k+1}^{RC}$ and use it as the input to the next iteration of Eq. 4.4 as shown in Fig. 4.2, and repeat the iteration for the desired amount of time steps. In some sense, the RC is a nonlinear version of the AR model as can be seen by comparing Eq. 4.2 and Eq. 4.4.

The hyperparameters of this method are N_{RC}, p, ρ_{RC}, λ, α, and w, defined in the previous two paragraphs. An exhaustive search of this 6-dimensional hyperparameter space is unfeasible; thus, we chose values for 4 of the hyperparameters as follows and did a 2-dimensional grid search for appropriate values of α and w, which we describe subsequently. For our experimental data, we found that the prediction error does not change significantly for sizes of the RC for $N_{RC} > 1500$, while the computational time grows substantially. We chose $N_{RC} = 3000$ to be on the safe side while still having a reasonable computational time. We found that varying the connection probability p between 0.01 and 0.5 does not noticeably change the prediction error, while higher probabilities slightly slow down the code; we fixed the value $p = 0.1$. The spectral radius ρ_{RC} is typically chosen to be slightly less than 1, so that the reservoir has significant memory of multiple past inputs, but not infinite memory; we chose $\rho_{RC} = 0.95$. We also chose $\lambda = 10^{-6}$, as for the AR model. With these values fixed, we varied α and w over the grid of values $\alpha = 1/64, 1/32, \ldots, 1/2, 1$ and $w = 3 \times 10^{-5}, 10^{-4}, 3 \times 10^{-4}, \ldots, 10^{-1}, 3 \times 10^{-1}$, and evaluated the prediction errors for the RC trained separately on eight different experimental data sets with $-6 < Ro < 5$, averaging over 20 predictions of 3 dipole timescales each, for each Rossby number. The values $\alpha = 0.25$ and $w = 0.01$ yielded the lowest errors, though the errors were very similar for the neighboring values $\alpha = 0.125, 0.5$ and $w = 0.003, 0.03$. Thus, the hyperparameter values we use in the results we report below are $N_{RC} = 3000$, $p = 0.1$, $\rho_{RC} = 0.95$, $\lambda = 10^{-6}$,

$\alpha = 0.25$, and $w = 0.01$. As a further check on our choices for ρ_{RC} and λ, we varied them individually and found both no improvement and little degradation in the prediction errors for $0.9 \leq \rho_{RC} \leq 1$ and $10^{-7} \leq \lambda \leq 10^{-5}$.

4.3.3 Hybrid model

The hybrid model [187, 211] uses both an auto-regressive model and a reservoir computer in tandem. The input time series fed into the AR and into the input layer of the RC, as shown in Fig. 4.3. During the first 30% of the training data we train auto-regressive model using the same approach as in Section 4.3.1. For the remaining 70%, we use the output of the AR to feed into the RC together with the original experimental data while saving the states of the RC. The dynamics of the reservoir computer in the hybrid model is given by:

$$X_{k+1} = (1-\alpha)X_k + \alpha \tanh\left(A \cdot X_k + W_{in} \cdot \begin{bmatrix} \\ U_k \\ \\ \\ \hat{U}^{AR}_{k+1} \\ \\ \end{bmatrix} \right) . \tag{4.7}$$

The analogue of Eq. 4.4 is:

$$\hat{U}^{HY}_{k+1} = W_{out} \cdot \begin{bmatrix} X_{k+1} \\ \hat{U}^{AR}_{k+1} \end{bmatrix} . \tag{4.8}$$

To train the hybrid model, we use the states of the RC and the outputs of the AR to compute a combined W_{out} that minimizes the prediction error using least squares similar

to Eq. 4.6. In the hybrid model, we use the same set of hyperparameters as in each of the AR and RC previously described, and we also discard the first 250 times steps to train the AR model and the first 1000 time steps for the hybrid training. During the autonomous phase, the output of the hybrid prediction model goes into the input of RC and AR, and output of the AR model also goes to the input of the RC model. In this configuration, after the last data point from training phase is fed into the system and the training is done, the hybrid model predicts the next time step and uses the prediction as its input for the next time step.

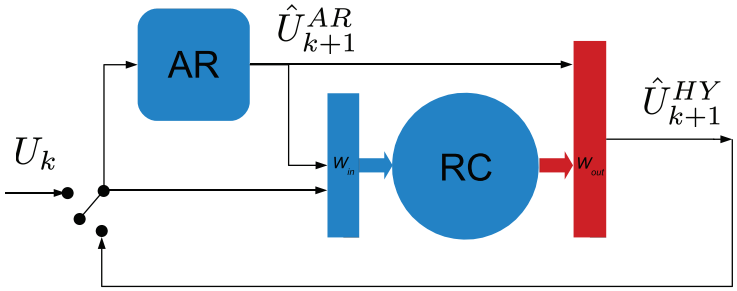

Figure 4.3: Schematic diagram of using hybrid model. Output of AR model goes into the input layer with the original data and in the output layer to be used with RC states together to generate the prediction of the next time step.

4.4 Prediction results

We applied the methods from Section 4.3 to the data described in Section 4.2.2, with one time step of the prediction methods equal to the sampling time (1/256 s) of the data, and using $T_{tr} = 16000$ time samples for the training data. This corresponds to a training time of 62.5 s, which is 20.8 times the dipole timescale τ_D. For each method, we do a separate training for each experimental data set. After the training is done we run the predictive models in a feedback loop, as shown in Fig. 4.3, to generate the predictions. In

Fig. 4.4, we show one of the magnetic Hall probe forecasts with three predictive models for the times $0 \leq t/\tau_D \leq 3$ and $20 \leq t/\tau_D \leq 23$. This particular data was taken at $Ro = 0.75$. Though only one equatorial probe is shown here, all 31 probes are part of the training and prediction. This approach yields substantial improvement over training and predicting only with the data from a single probe.

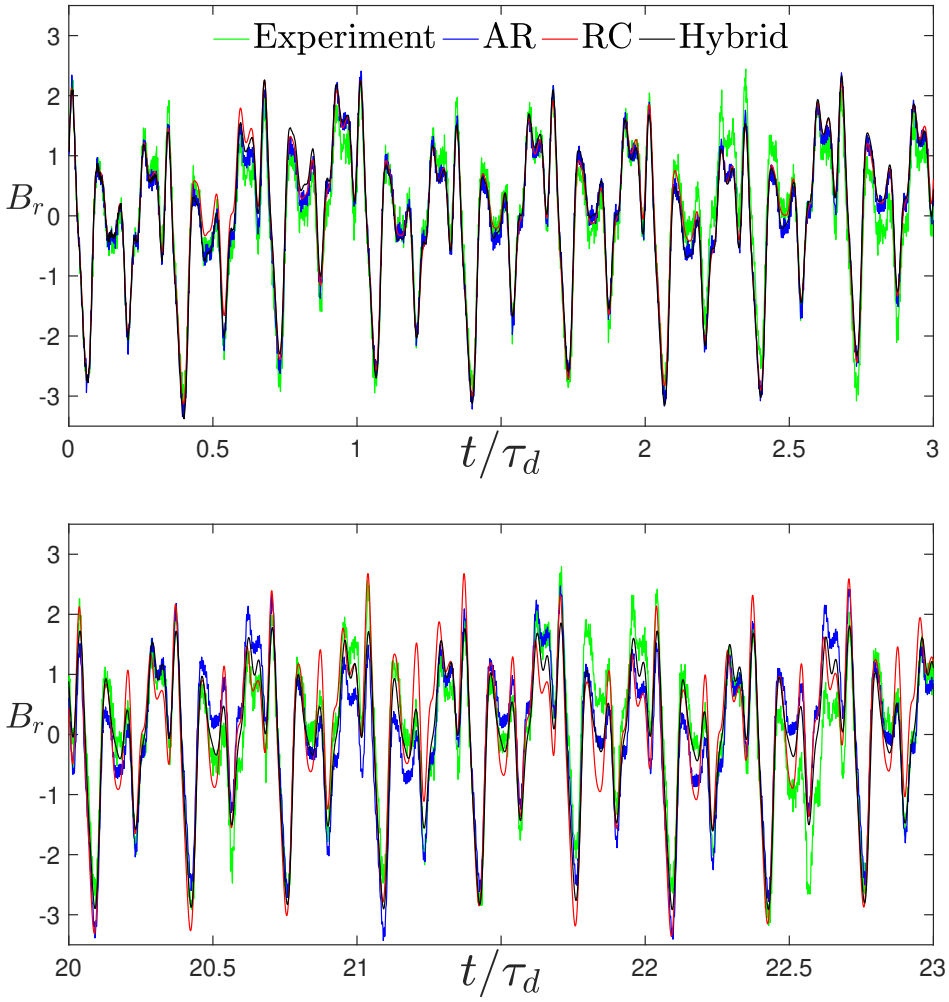

Figure 4.4: Comparison of the measured signal of one of the probes and three prediction models (auto-regressive, reservoir computer, and hybrid), with time in units of dipole timescales. Here B_r is the measurement from the first equatorial probe, normalized as described in Section 4.2.2.

Due to the relatively high dimension of the experimental data, $D = 31$, we cannot

easily compare the quality of the predictions as raw time series, so instead we examine the root mean square error:

$$\mathbb{E}_k = \sqrt{\frac{1}{D}\sum_{j=1}^{D}(\hat{U_k^j} - U_k^j)^2} \tag{4.9}$$

where U_k^j denotes j'th coordinate of the normalized measurement vector U_k, and $\hat{U}_k^j$ is the predicted value from (4.2), (4.4), or (4.8). We also average over $N_{Ro} = 20$ different experimental time series with Rossby number $-4 \leq Ro \leq 9$ and Ekman numbers $Ek = 1.2 \times 10^{-7}$. As a result we are having an RMS error averaged over twenty different experiments as a function of time after the training. We define:

$$\bar{\mathbb{E}}_k = \frac{1}{N_{Ro}}\sum_{Ro}\mathbb{E}_k(Ro)\ . \tag{4.10}$$

In Fig. 4.4 we show the time evolution of the average error $\bar{\mathbb{E}}$ for our three predictive models. Here the errors are evaluated for the data normalized according to Section 4.2.2. To compare them with noise and other baselines, we show three other curves: estimated noise level, persistence error, and one time step error (OTSE), defined as follows: we estimated the noise level as the standard deviation over time of the measurements from the probes when the experiment was at rest, i.e., when the inner and outer spheres were not rotating and we were not applying an external magnetic field. The persistence error is the average error defined by Equations (4.9) and (4.10) in the case that $\hat{U}_k^j = U_0^j$, i.e., when the measurements at the start of the prediction are used to predict all future measurements. The OTSE instead uses $\hat{U}_k^j = U_{k-1}^j$, and is thus the average distance between successive measurements. All of the models show a significantly better performance

than the persistence prediction. The AR and RC demonstrate similar level of error, and compared with them, the hybrid model consistently predicts with a lower error, and is also lower than the OTSE for t/τ_D up to around 10. Notice that the OTSE does not grow with time because it is based on the most recent past measurements, whereas the predictive methods do not use any of the measurements after time 0.

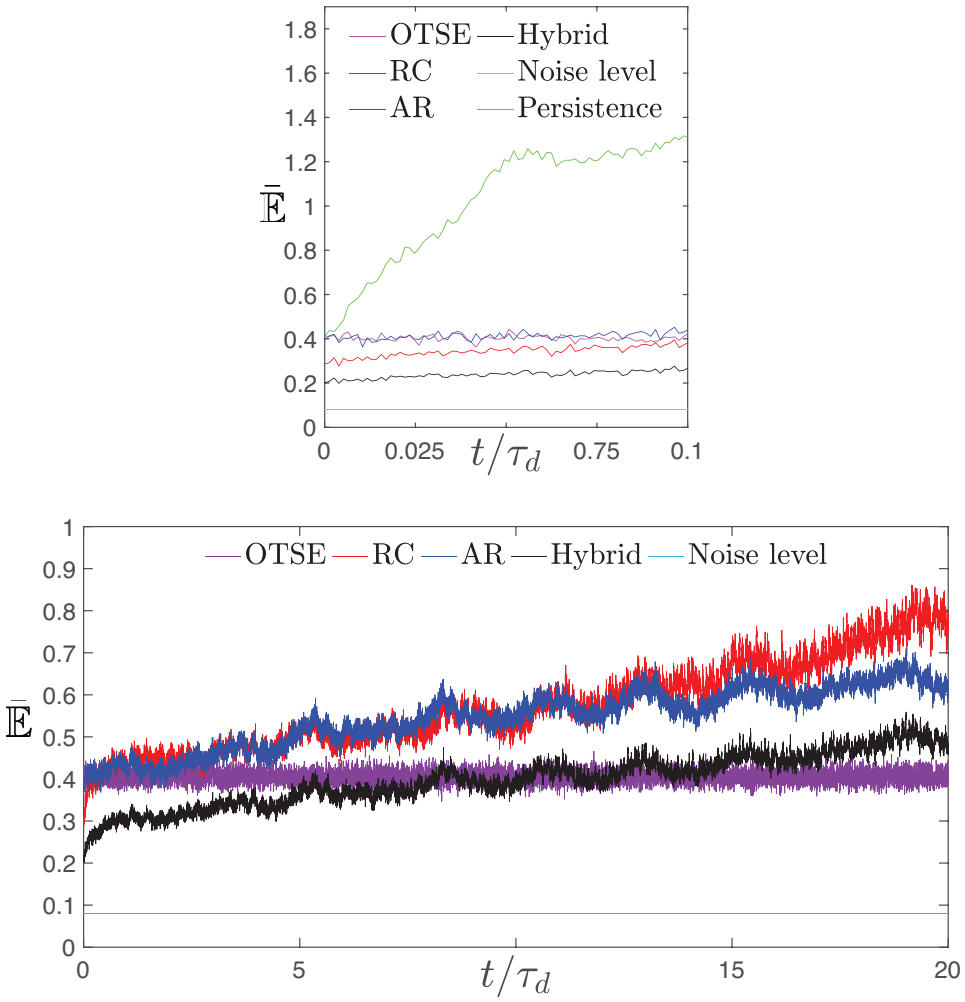

Figure 4.5: Normalized error time evolution for different models for (a) short times $t/\tau_D < 0.1$ and (b) longer times $t/\tau_D < 20$. Averaging is taken over 31 probes and over a series of 20 different experiments with the same outer sphere rotation rate and $-4 \leq Ro \leq 9$. The estimated noise level, persistence error, and OTSE are defined in the text. The persistence error is not shown in the second graph because it remains greater than 1 for $t/\tau_d > 0.1$.

To visualize the time series on larger time scale and compare the ability to predict the climate, we compute at each time step the spherical harmonics g_l^m defined by Eq. 4.11.

$$\hat{r} \cdot \vec{B}(r,\theta,\phi) \approx \sum_{l=1}^{l=4} \sum_{m=0}^{m=l} l(l+1)\left(\frac{r_0}{r}\right)^{l+2} P_l^m(\cos\theta)\left(g_l^m \cos(m\phi) + g_l^{-m} \sin(m\phi)\right) \tag{4.11}$$

Here $\hat{r}$ is a radial unit vector and $\vec{B}(r,\theta,\phi)$ is the magnetic field; we compute g_l^m by performing a least-squares fit of the right side of Eq. 4.11 to the 31 measured or predicted values for the magnetic field. On Fig 4.6 we compare the long timescale behaviour of the predictive models. We plot the dynamics of g_3^1 and g_2^2 in arbitrary units. The experimental data during the training is plotted with green, and the dynamics of the predictive models are plotted for $55 \leq t/\tau_D \leq 70$ with black, blue, and red: hybrid, AR, and RC correspondingly. Here we see that the hybrid model dynamics approaches a periodic orbit that looks like a smoothed version of the experimental data, AR keeps moving in the same shape as the hybrid but with some additional modes, and RC falls on a different shaped orbit with some fluctuations. Thus, the hybrid model seems to best reproduce the large scale climate of the original system.

4.5 Performance dependencies

Further, to compare the performance of the predictive models for different experiments we introduce time average error:

$$\langle \mathbb{E} \rangle = \frac{1}{3 f_s \tau_D} \sum_{k=1}^{3 f_s \tau_D} \mathbb{E}_k \ . \tag{4.12}$$

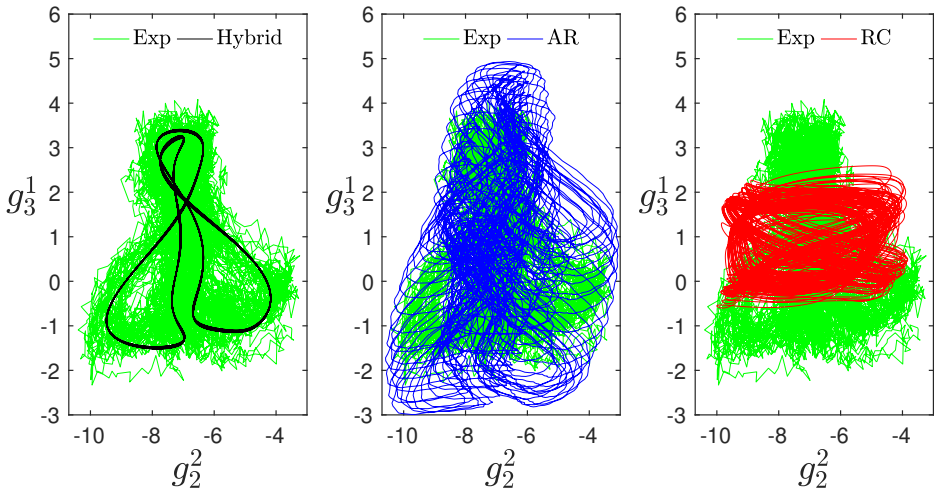

Figure 4.6: A parametric graph of two equatorial spherical harmonics coefficients g_3^1 and g_2^2 during the experiment and prediction. The green corresponds to the experimental data during the training time, and the other colors represent the behavior of the predictive models for times $55 \leq t/\tau_D \leq 70$.

Here time averaging is taken over three dipole timescales so the total number of timesteps is equal to $N_T = 3 f_s \tau_D = 2304$, with each time step having $D = 31$ scalar values, where $f_s = 256\ Hz$. We also average the errors for the set of twenty experiments with $-4 \leq Ro \leq 9$:

$$\overline{\langle \mathbb{E} \rangle} = \frac{1}{N_{Ro}} \sum_{N_{Ro}} \langle \mathbb{E} \rangle \ . \tag{4.13}$$

In Fig. 4.7 we show the average error $\overline{\langle \mathbb{E} \rangle}$ of the hybrid model as a function of the length of training expressed in the units of the dipole timescales. Here the error bars represent the standard deviation of the errors $\langle \mathbb{E} \rangle$ over the 20 different experiments. The standard deviations of the error for $T/\tau_D < 10$ are larger than 3 and are not plotted. Here we observe that the quality of the prediction significantly depends on the amount of data we provide to the system during the training for $T/\tau_D < 20$; after that, increasing the training length does not give us much advantage. Recall that we used $T/\tau_D = 20$ for the

other results in this section.

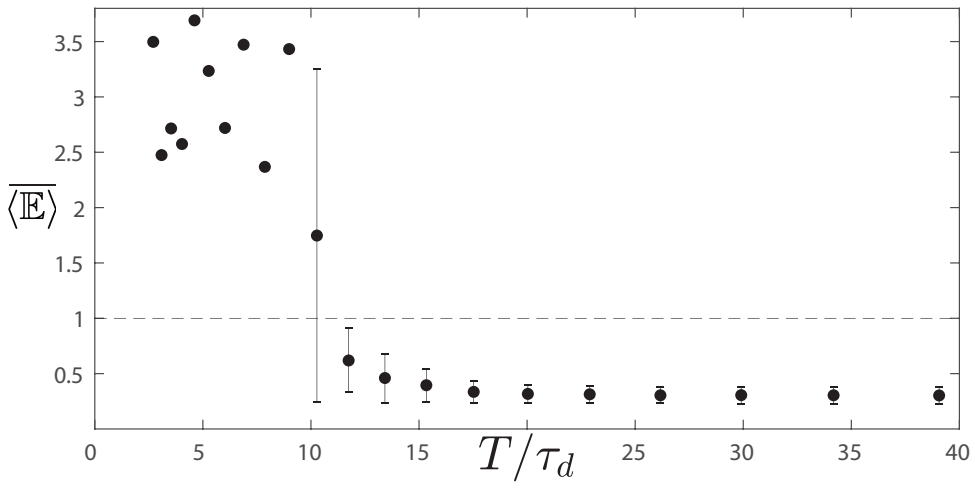

Figure 4.7: Average error of the hybrid model during three dipole timescales for different training times. Averaging is taken over 31 probes, three dipole timescales, and the set of 20 different experiments. Error bars represent the standard deviation of the sets of errors for different experiments. For training times less than 10 dipole timescales, the error bars (not shown) are larger than three.

In Fig. 4.8, we show the dependence of time average error on the inverse Rossby number of the predictions during the first three dipole timescales. Here we show the results for 32 different experimental runs. For each run the error is averaged over all 31 signals and for three dipole timescales; see Eq. (4.12). The area with $Ro^{-1} < -0.2$ corresponds to the inertial modes states (IM) [58, 110]; in these states we observe large nonlinear waves with smaller overall turbulence. The signal here predominantly comes from high power spectral density oscillations. States with $Ro^{-1} > 0.6$ are high torque states (H). This area has more broad-band spectra than IM but stays closer to a more periodic behaviour than other states inside $-0.2 < Ro^{-1} < 0.6$, such as quiet (Q), bursty (B), low (L) and low low (LL) torque states [58]. So we can say that the performance of the predictive models varies on the experimental state. Also the states closer to $Ro^{-1} = 0$ have higher Reynolds

number. These states generally have both higher Rossby number and higher Reynolds number than the IM and H states, and their prediction errors are generally larger. The RC errors can vary considerably from one randomly generated reservoir to another, so we make predictions with ten different RC and choose the one that has the lowest error. The results of auto-regressive model do not change on the same dataset, and the hybrid model, even though it uses an RC, does not change it output significantly with differently generated reservoirs.

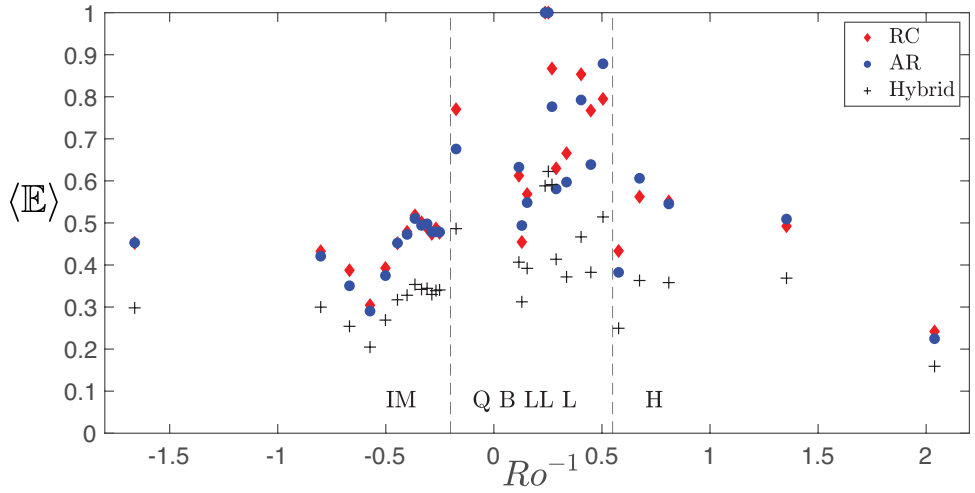

Figure 4.8: Time average error for different experimental runs with different Rossby number. Averaging is over 31 probes and three dipole timescales. Different experimental states have different level of predictability; inertial modes states (IM) and high torque states (H) have on average lower error while compared with quiet (Q), bursty (B), low torque (L, LL) states.

4.6 Implications on prediction for the Earth's magnetic field

Our results indicate that training on time series of more than 10 magnetic dipole timescales were needed by these methods. The magnetic dipole timescale of the Earth is $\tau_{Earth} \approx 70,000$ years. It is estimated using Eq. 4.1 where the outer core conductivity is

$\sigma_{OC} = 1.5 \times 10^6\ (\Omega\, m)^{-1}$ [212] and the radius is $r_{OC} = 3.48 \times 10^6\ m$ [213]. The implications on geomagnetic forecasting by these methods suggest that a minimum of 700,000 years of data at a resolution of $l = 4$ might be need to achieve similar results. Unknowns include that our experiment is in a different dynamical regime, and while some of our dimensionless groups are similar, some are not. An important difference is the experimental rotation period (the day) and the magnetic dipole timescale are relatively similar, unlike the Earth, where the dipole timescale is clearly much longer than a day.

4.7 Conclusion

We tested three different approaches to predict the time evolution of a nonlinear system, our Three-meter experiment, and found that the hybrid of the reservoir computer and the auto-regressive model outperforms each of its components, and is capable of predicting the time evolution for five magnetic dipole timescales with a higher accuracy than the average one time step fluctuation. We applied these techniques to experiments with different fluid dynamical states and demonstrated that some of the states are more predictable than others. We show that the hybrid model is also capable of predicting the long time climate of the system, and even while it might be far from the real data in terms of the RMS error, it keeps converging on a trajectory in phase space that is very similar to what is has learned during the testing phase. We also discovered that for this system it is necessary to have more than ten dipole diffusion timescales of the spatially distributed training data in order to predict the dynamics; a comparable dataset is not currently available for the Earth's magnetic field.

Chapter 5: Inertial and Magneto-Coriolis Animals and Where to Find Them

In this chapter, we will present the observation of strong oscillatory waves traveling in the spherical-Couette experiment. In Chapter 2 we introduced the reader to the concept of inertial waves that appear in rotating fluid, inertial modes (IM) that are the same waves but restricted by the geometry of the sphere, and their analogies in the case when the fluid is also electrically conductive: magneto-Coriolis waves and modes (MC). And here we would like to show the analysis of the experimental data.

In the world of mechanical engineering, applied physics, and mathematics there is a known branch of fluid mechanics that uses numerical methods to simulate the behavior of fluid and turbulent systems - Computational Fluid Dynamics (CFD). In this project, we didn't have much room for this method but we also really wanted to have this acronym, so in our case, we will be talking about Colorful Fluid Dynamics (CFD). Here the reader should expect to see a lot of figures with various colors that will mostly represent magnetic and pressure field spectra in the Three Meter experiment.

Here we will demonstrate experimentally observed modes in various regimes. The hydrodynamic modes were observed previously and we confirm the results of previous works, and we expand the analysis to the magnetohydrodynamical regimes. Most of the data will be presented in spectrograms, and this is where we will have Colorful Fluid

Dynamics.

5.1 Background

In the past Inertial modes and magneto-Coriolis modes were detected and analyzed in the laboratory experiments [7, 106, 111]. It was done by observing the Earth and the Sun [145, 151, 157, 214], as well as running numerical simulations [61, 62, 149].

In observational works normally scientists are limited by only one state of the system, and in most experimental works the researchers can modify the mechanical parameters of the system. Both have non-conductive fluids or are have a very limited range of the external magnetic field. However, in the Three Meter experiment, we can control three different parameters, two mechanical: Reynolds and Rossby numbers, as well as the external magnetic field, hence Lehnert number. On the top of that, we are capable of changing the configuration of the external magnetic field from a dipole to a quadrupole. In addition, after we upgraded the inner sphere with baffles we can compare the results of changing the coupling between the inner sphere and sodium.

A quick reminded of the dimensionless parameters we use here:

Reynolds number is the ratio between inertial and viscous forces:

$$Re = \frac{|\Omega_i - \Omega_o|(r_i - r_o)^2}{\nu}; \tag{5.1}$$

Rossby number is the ratio between rotational shear forces and Coriolis forces:

$$Ro = \frac{\Omega_i - \Omega_o}{\Omega_o}; \tag{5.2}$$

Ekman number is the ratio of viscous forces to Coriolis forces:

$$E = \frac{\nu}{\Omega_o (r_i - r_o)^2}; \tag{5.3}$$

Lehnert number is Alfvén speed over rotational velocity:

$$Le = \lambda = \frac{B}{\Omega_o r_o \sqrt{\mu_0 \rho}}. \tag{5.4}$$

More detailed descriptions can be found in Chapter 2.

And just like before we are going to use spherical harmonics representation of magnetic field on a sphere:

$$B_r(r, \theta, \phi) = \sum_{\ell=1}^{\infty} \sum_{m=0}^{\ell} \ell(\ell+1) \left(\frac{a}{r}\right)^{\ell+2} P_\ell^m(\cos\theta)(g_\ell^m \cos(m\phi) + g_\ell^{-m} \sin(m\phi)) \ . \tag{5.5}$$

The previous work in the Three Meter experiment showed the presence of inertial modes [7, 111]. In Figures 5.1 and 5.2 we can see the experimental power spectral densities (PSD) for different Rossby numbers. The spectrograms are composed of the AC pressure measurements. We are interested in the behavior of the modes in a conductive fluid, especially in cases when we have applied a magnetic field.

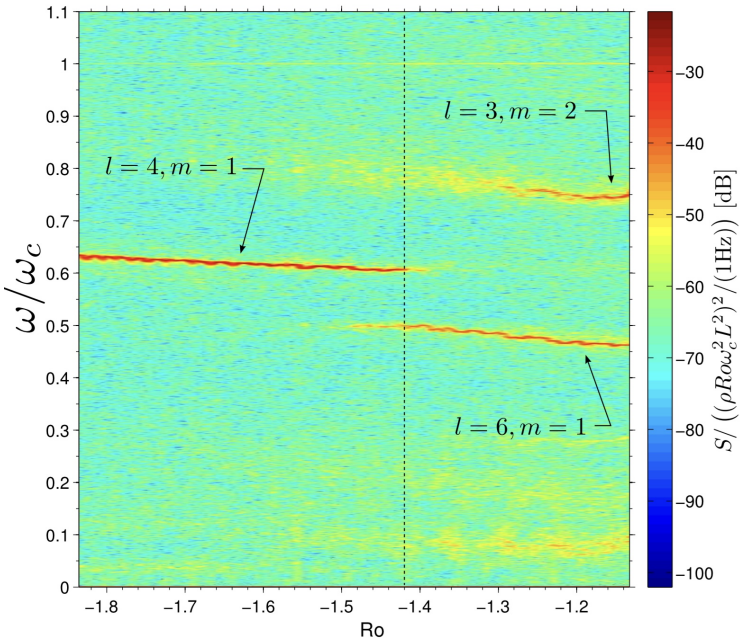

Figure 5.1: Spectrogram of Rossby ramp $-1.9 < Ro < -1.1$ experiment made in water, credits to Triana [7]. Red lines show the frequency and Rossby numbers locations of strong oscillations.

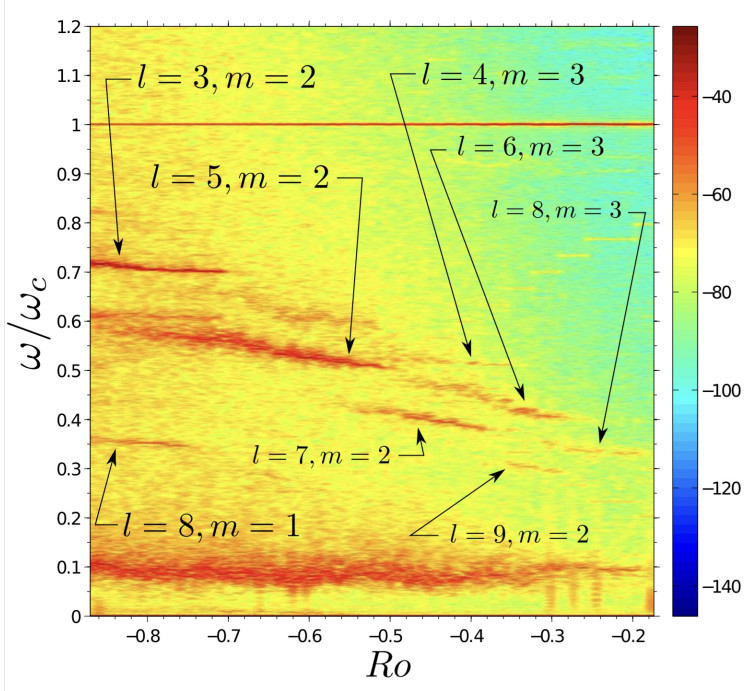

Figure 5.2: Spectrogram of Rossby ramp $-0.9 < Ro < -0.1$ experiment made in water, credits to Triana [7]. Red lines show the frequency and Rossby numbers locations of strong oscillations.

5.2 Diagnostics

In this chapter we will be talking about the data coming from these data acquisition parts:

- Three AC pressure probes located in the instrumental ports (in Fig. 3.1)
- 31 magnetic Hall probes: reasonably uniformly distributed on the sphere's surface to measure radial magnetic fields among five rings, as schematically shown in Fig. 6.1.

The sampling rate is set to $f_s = 256\ Hz$, allowing us to detect frequencies up to 128 Hz, but we will be talking about significantly slower dynamics - on the scale of the outer sphere rotation rates $f_o < 4\ Hz$.

5.2.1 Methodology

Each day data would be separated into parts, and each part would have fixed control parameters: outer and inner rotation rates, and the current in the external magnetic coils. Every part would be several hundred outer sphere revolutions long. For each run, we will calculate the power spectral density of different data sets: pressure, hall probes, and magnetic field spherical harmonics. We used 'pwelch' function from Matlab package: eight windows with 50% overlapping. Because the signals we are interested in have relatively low frequencies, for the signals we subtract mean values and remove linear trends from the raw data to get rid of artificial frequencies that appear after using 'pwelch'. In the result

we are having the estimated PSD that is similar to:

$$PSD(w) = 10 * log_{10}|FFT(F(t))| \ , \tag{5.6}$$

where $F(t)$ is the time series of an the original data. The maximum frequency for us is Nyquist frequency $f_N = f_s/2 = 128\ Hz$ For pressure data we use an averaged signal from AC pressure probes. And for magnetic data we average data from all our radial Hall magnetic probes.

5.2.2 Spectral analysis representation (How to read the plots)

For each given experiment we have records of signals measured with different external magnetic fields. We present the power spectral density of signals on a 2D plane, with Rossby or Lehnert numbers on horizontal axis, the frequency on the vertical axis, and color will represent the corresponding PSD in decibels. For a better visual representation we used *'pcolor'* function in Matlab, it allows plotting on a non-uniform space grid and does not do any interpolation so we can see the spectrograms as they are. Inertial and magneto-Coriolis waves dispersion relations are described in Chapter 2, and here we put a reminder:

$$\omega_I = 2\Omega cos(\theta) \ , \tag{5.7}$$

$$\omega_{MC} = \pm\tfrac{\omega_I}{2} \pm \sqrt{\left(\tfrac{\omega_I}{2}\right)^2 + \omega_A^2} \ ,$$

where ω_A is Alfvén frequency. We are not going to be interested in frequencies above two outer sphere rotation rates, hence we will plot our figures with frequencies from zero to the outer sphere rotation rate. Pressure PSD figures will show the average over DC and the first two DC probes (the third one was dead during most of the runs we are analyzing here). Hall Probes PSD figures will show the average over all 31 radial Hall probes. For a better visual understanding, there is Figure A.1 showing modes on the sphere with corresponding coefficients.

To understand the space configuration: ℓ & m numbers of the observed structures, we decompose the magnetic Hall probes data into Gauss coefficients using the formulation shown in Eq.5.5. To do so we do linear regression from $31D$ vector of probes signals into $24D$ gauss coefficient space g_ℓ^m, that corresponds to harmonics up to $\ell = 4$. And after getting 24 separate time series of gauss coefficients we apply the same $FFT()$ as shown in Eq. 5.6, so we can see the spacial difference. For example in Fig. 5.13 we present the gauss coefficient decomposition of the date presented in Fig. 5.12. This allows us to estimate the shapes of the modes that we are seeing.

We put an asterisk (ℓ^*) on modes in cases when we cannot be sure it is the exact ℓ or m numbers. Our hardware allows us to reconstruct up to 24 gauss coefficients from our 31 probes, meanwhile, all the higher modes should "leak" into our representation. The "Leakage map" is shown in Fig. A.2, on this map we can see the directions where a given higher harmonic would appear in the data.

5.2.3 Experimental runs

5.3 Rossby ramps

Rossby ramp experiments are set in such a way that we keep Ekman number 2.5 fixed (outer sphere rotation rate is constant), the external magnetic field would stay constant during each ramp that allows having constant Lehnert number 2.6, and during each run, we would change the inner sphere rotation rate to modify Rossby number 2.3; meanwhile, it changes Reynolds number 2.1. An example of these ramps is shown in Fig. 5.3, here we can see that three Rossby ramps with different Lehnert numbers took approximately four hours of running time.

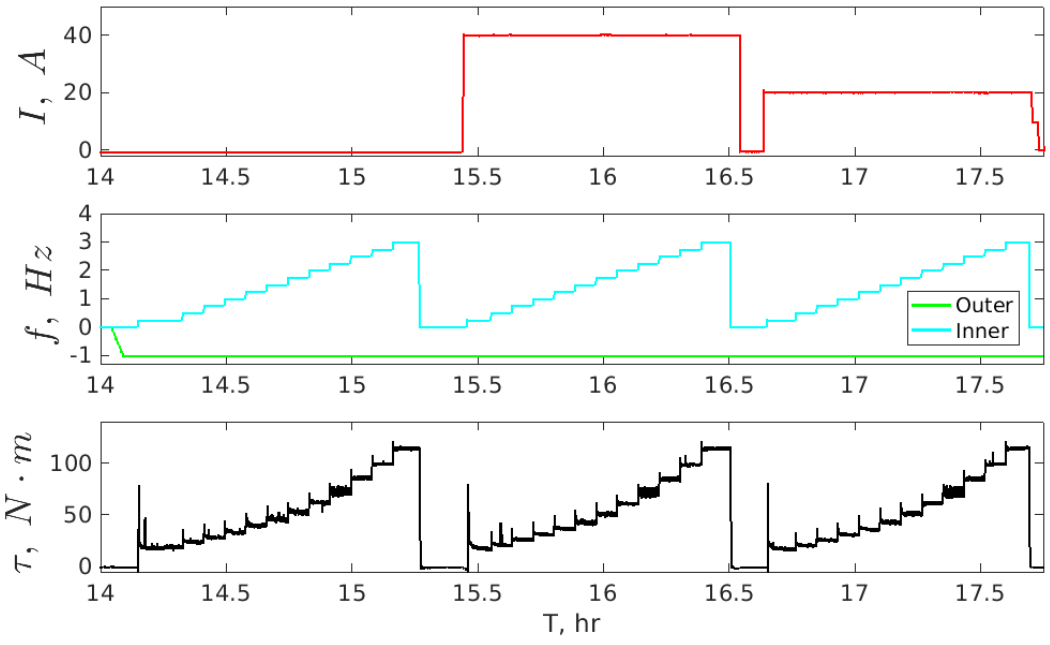

Figure 5.3: An example of experiment design for Rossby ramps. The horizontal axis is time and here we show three runs between 2 pm and 6 pm. At the top we display the current in the external coils; in the middle there are spheres rotation rates: the outer sphere rotation rate is fixed and the inner changes varying the Rossby number; at the bottom we see the torque applied to the inner sphere.

5.3.1 Negative Rossby ramps

Next, we are going to show what the same phase space area looks like in sodium experiments. Here in Fig. 5.4 there is an experiment with the Rossby ramp in the absence of the applied magnetic field.

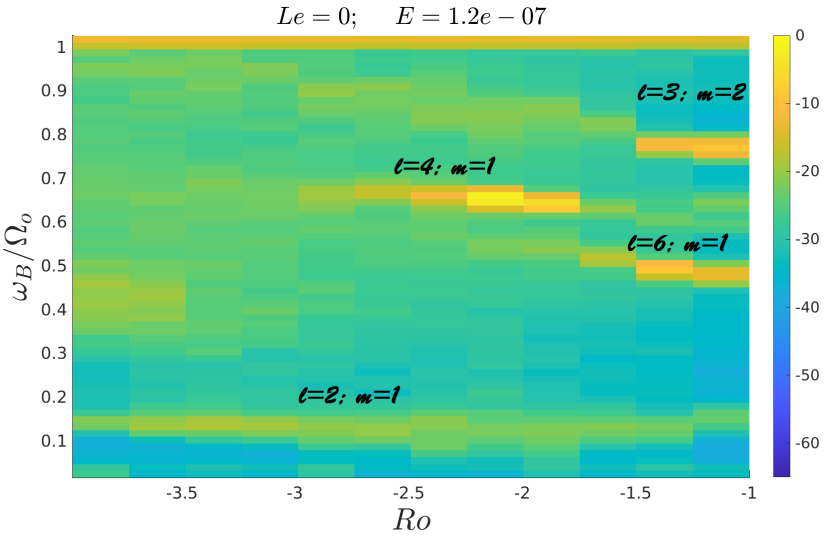

Figure 5.4: A spectrogram of internal magnetic fields without applied external field ($Le = 0$). We can see the same modes as in water experiments in Fig. 5.1. The ℓ & m numbers are estimated to be she same as reported in Triana [7].

A visually appealing gif animations for eight different Lehnert numbers are available on our GitHub account:

1) Average Hall probes spectrograms: spectrograms

github.com/Three-Meter-Geodynamo-Experiment/mc_modes/blob/main/B_spectra.gif

2) Individual Gauss harmonics spectrograms

github.com/Three-Meter-Geodynamo-Experiment/mc_modes/blob/main/B_lm.gif

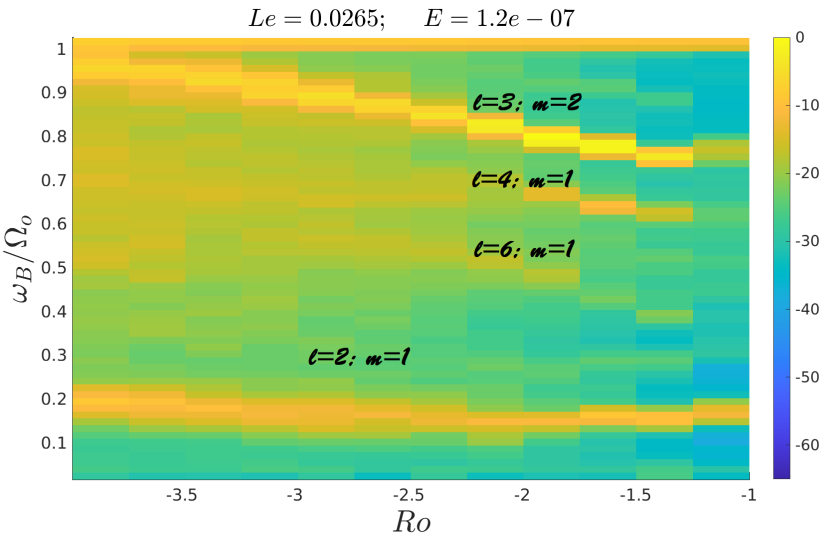

Figure 5.5: A spectrogram with high external magnetic field regime ($B \approx 90$ *gauss*, resulting $Le \approx 0.026$), here we see that most of the modes extend to lower Ro values.

5.3.2 Positive Rossby ramps

Here we are going to look at the modes that appear in the positive Rossby phase space area. Let's take a look at the area with $0 < Ro < 6$. There was some analysis of this region in Three Meter experiments with water. Fig. 5.6 is from Zimmerman (2010) [8], this is a spectrogram of wall pressure We have two high-resolution experiments with low and high external magnetic fields. In Fig. 5.7 and 5.8 we see two pressure spectrograms where we can see quite different oscillations. The Rossby dependence changes in the presence of the external magnetic field. The big yellow island with high amplitudes in the right bottom of Fig. 5.8 is a group of very differently shaped modes. The strongest amplitudes are observed with antisymmetric modes ($\ell - m = odd$).

It is visible that the modes change the frequencies with the magnetic field, they might change their spacial configuration so we might want to focus on the magnetic field dependence.

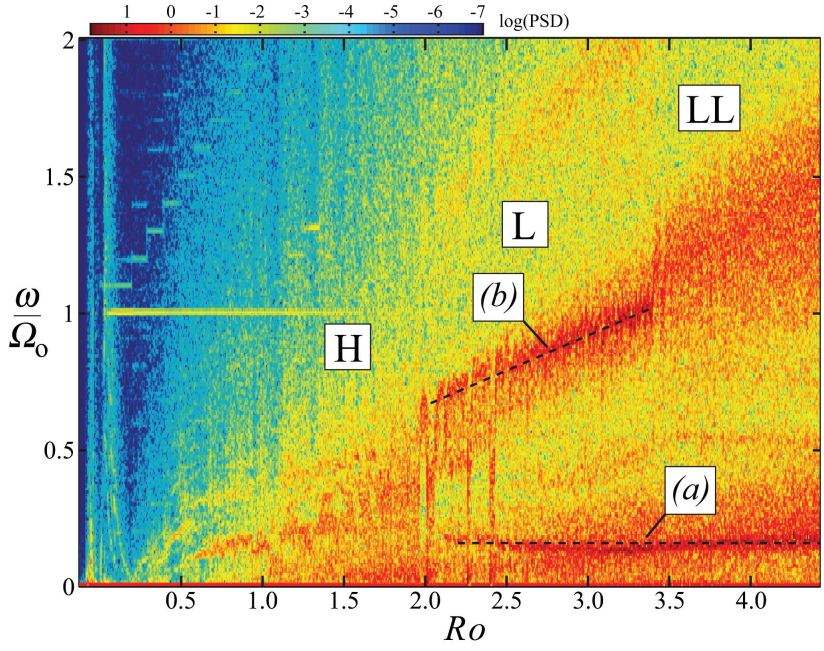

Figure 5.6: In the L state, there are two strong waves, the lower at (a) varies only slightly in frequency with Ro. The higher frequency wave at (b) varies more strongly with Ro, suggesting that advection by the mean flow is important in setting its frequency. Credits to Zimmerman [8]

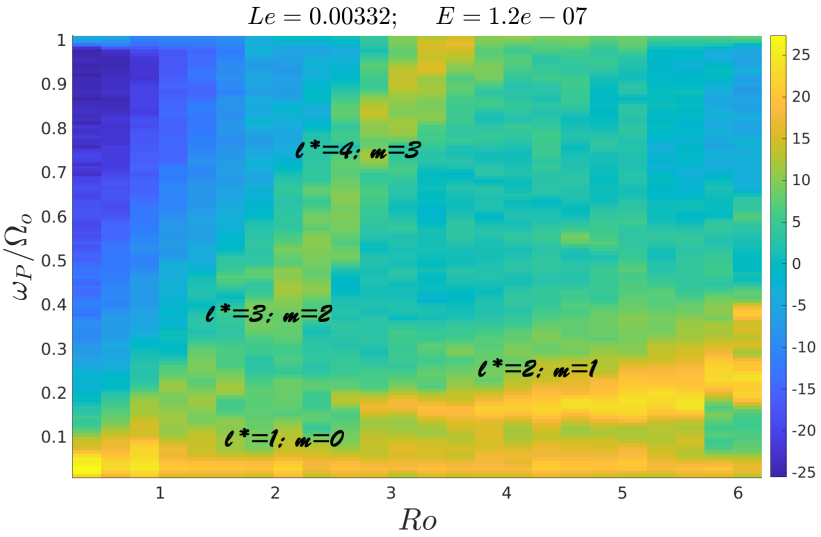

Figure 5.7: A spectrogram of an experiments with a positive Rossby number in the presence of a low magnetic field. This is similar to the date reported by Zimmerman [8], which is shown in Fig. 5.6.

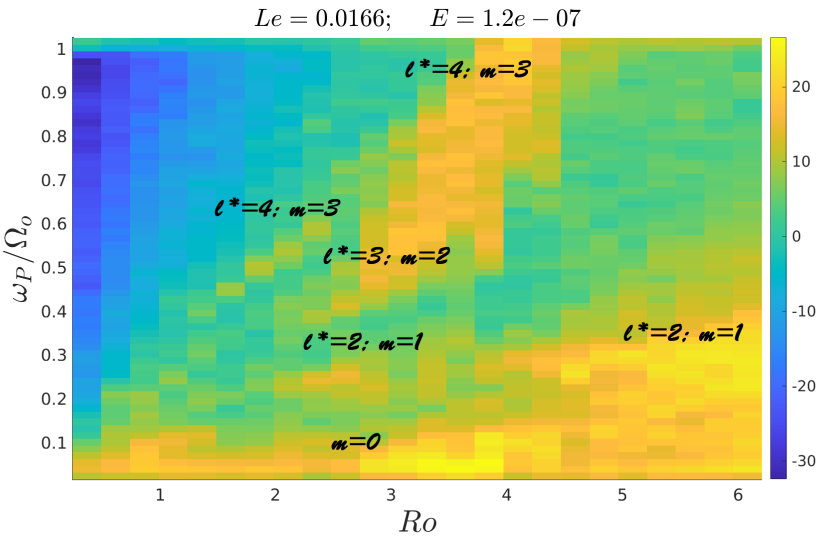

Figure 5.8: A spectrogram of an experiments with a positive Rossby number in the presence of a strong magnetic field. This is different from the same ramp in low field that is shown in Fig. 5.7.

5.4 Magnetic ramps

In this section, we will take a closer look at the modes: their frequencies and shapes, and how the applied external magnetic field changes them. Here we analyze the experimental runs where inner and outer sphere rotation rates were fixed for an extended period of time, and the external magnetic field was gradually increased. An example of the run is shown in Fig. 5.9, on the torque plot (bottom) we can see that coupling between the spheres depends on the external magnetic field: after the current in the external coils is stopped ($T = 18.95\ hr$) the torques drops $\approx 30\%$. This effect will be analyzed in Chapter 6.

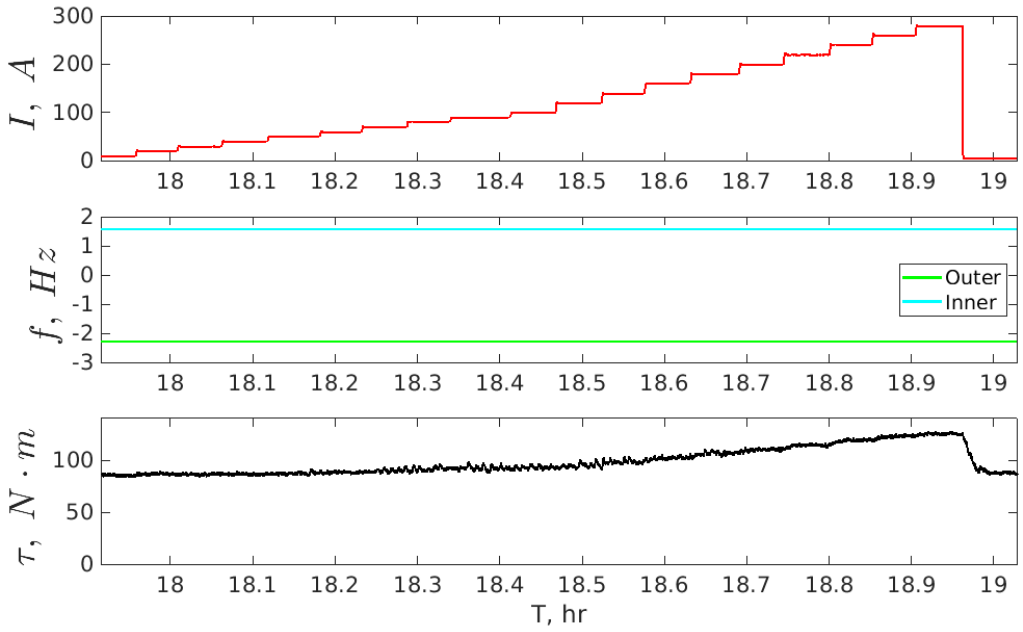

Figure 5.9: An example of experiment design for Lehnert ramps. The horizontal axis is time and here we show three runs between 6 pm and 7 pm. At the top we display the current in the external coils that is gradually increased; in the middle there are spheres rotation rates that stay constant; at the bottom we see the torque applied to the inner sphere.

5.4.1 Negative Rossby

The first one is an experiment with $Ro = -0.6$ and $Le < 0.02$. In Fig. 5.10 we see a strong mode at $\omega/\Omega_0 \approx 0.5$ that appears at hydrodynamic regime ($Le = 0$), most possibly it is $\ell = 5;\ m = 2$ [7, 111]. It slightly decreases its frequency with increasing applied field up until $Le = 0.007$ where it changes its shape (becomes an $m = 3$ mode) and decreases in amplitude. At the same time, another $m = 2$ mode appears with 0.1 shifted frequency; which is very similar to the $\ell = 2;\ m = 1$ mode at the bottom of the plot, known as a spin-over mode or cylinder mode. This transition might be evidence of a magnetic field-induced triadic resonance [42, 62, 215, 216].

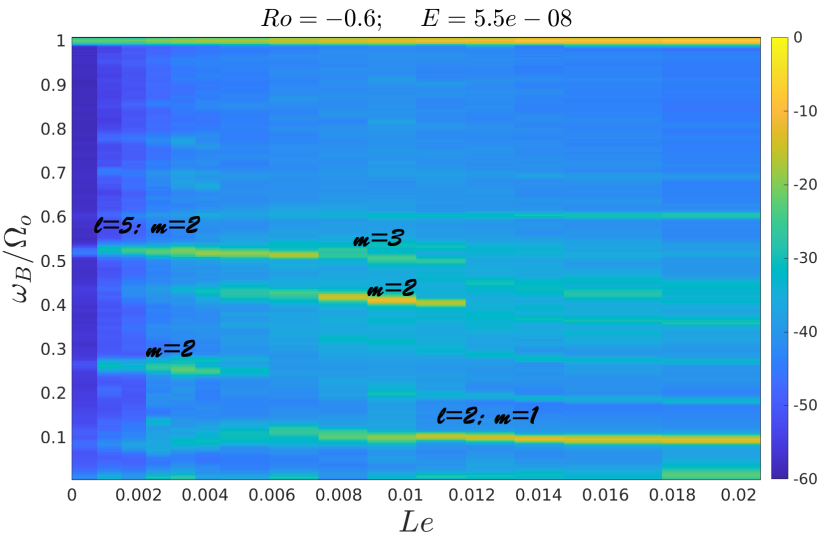

Figure 5.10: A spectrogram of the magnetic Hall probes data. On the vertical axis we have the frequency of the observed oscillations in the data in units of outer sphere rotation rates. The spheres rotation rates stay constant defining $Ro = -0.6$, and we vary the value of the externally applied dipole magnetic field. The corresponding Lehnert numbers are on the horizontal axis. The color represents the power spectral density on the oscillations. On the left the modes match the ones observed in water experiments, but they change their frequencies, amplitudes, and shapes while we increase the external magnetic field.

Here we keep the outer sphere rotation rate the same as in the previous one to fix the Ekman number, but we change the inner one, so we have $Ro = -1.2$. In Fig. 5.11 we can see that just like in the water experiments we start from two modes: $\ell = 6;\ m = 1$ at $\omega/\Omega_0 \approx 0.5$ and $\ell = 3;\ m = 2$ at $\omega/\Omega_0 \approx 0.75$, but in the presence of external fields these modes disappear or maybe only change shapes, and other modes emerge.

We still have the previous Ekman number but we switch to $Ro = -1.7$. In Fig. 5.12 the $Le = 0$ matches with water runs (in Fig 5.1) [7], and we can see $\ell = 4;\ m = 1$ mode, as well as our usual spin-over mode that forms slightly later. But at the same time we have a lot of other things happening:

- $m = 2$ mode appears and changes its frequency $0.75 < \omega/\Omega_0 < 0.85$ with magnetic field strength.

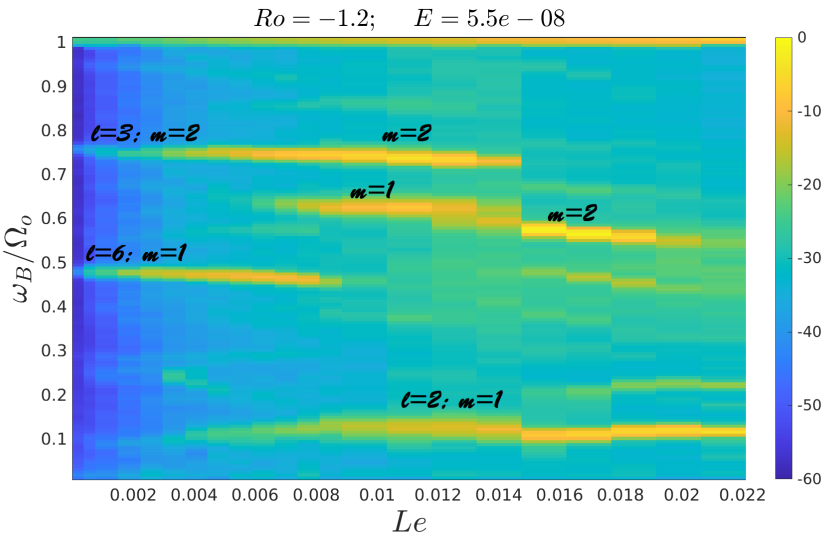

Figure 5.11: A spectrogram of the magnetic Hall probes data. On the vertical axis we have the frequency of the observed oscillations in the data in units of outer sphere rotation rates. The spheres rotation rates stay constant defining $Ro = -1.2$, and we vary the value of the externally applied dipole magnetic field. The corresponding Lehnert numbers are on the horizontal axis. The color represents the power spectral density on the oscillations. On the left the modes match the ones observed in water experiments, but they drastically change their frequencies, amplitudes, and shapes while we increase the external magnetic field.

- the original $\ell = 4;\ m = 1$ almost disappear at $Le = 0.01$ and another $m = 1$ mode briefly forms at $\omega/\Omega_0 \approx 0.5$
- one more $m = 1$ mode reappears at a higher frequency after the previous vanishes.
- two $\ell^* = 3$ modes with different symmetries appear and disappear for $0.004 < Le < 0.01$.

We probably observe multiple triadic resonances here as well as the formation of high-amplitude magneto-Coriolis modes.

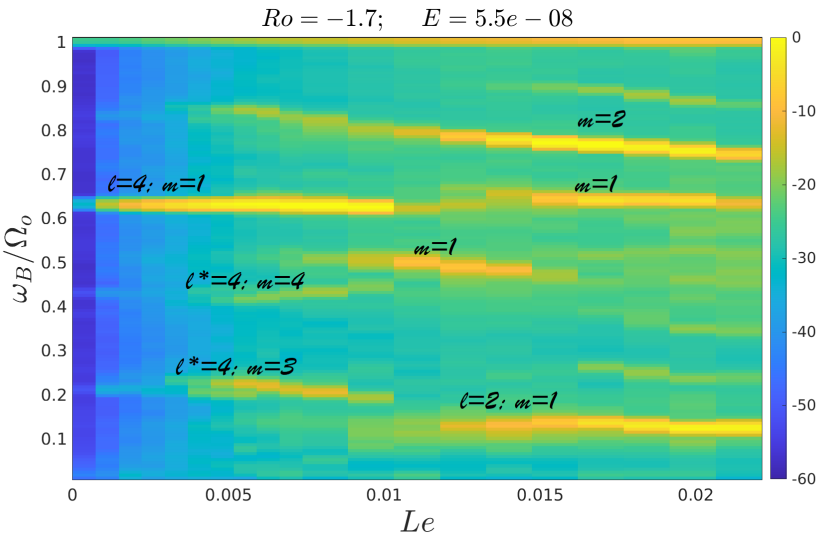

Figure 5.12: A wonderful zoo with inertial and magneto-Coriolis modes: a spectrogram of the magnetic Hall probes data. On the vertical axis we have the frequency of the observed oscillations in the data in units of outer sphere rotation rates. The spheres rotation rates stay constant defining $Ro = -1.7$, and we vary the value of the externally applied dipole magnetic field. The corresponding Lehnert numbers are on the horizontal axis. The color represents the power spectral density on the oscillations. On the left the modes match the ones observed in water experiments, but they drastically change their frequencies, amplitudes, and shapes while we increase the external magnetic field.

We also want to check the area where hydrodynamic experiments were not demonstrating strong waves. This is accomplished by setting $Ro = -4.3$, with a slightly higher Ekman number than before. In Fig. 5.14 the originally poor for structured oscillations area at $Le = 0$ starts showing some strong oscillatory structures:

- a wide gorge of $m = 2$ oscillations that change their frequency nonlinearly with B_{ext}
- an $m = 0$ antisymmetric mode at higher Le
- strong oscillation that branches from $\omega/\Omega_0 = 1$ and decreases frequency with magnetic field strength.
- probably the regular $\ell = 2; m = 1$ spin-over mode that forms after $Le = 0.018$.

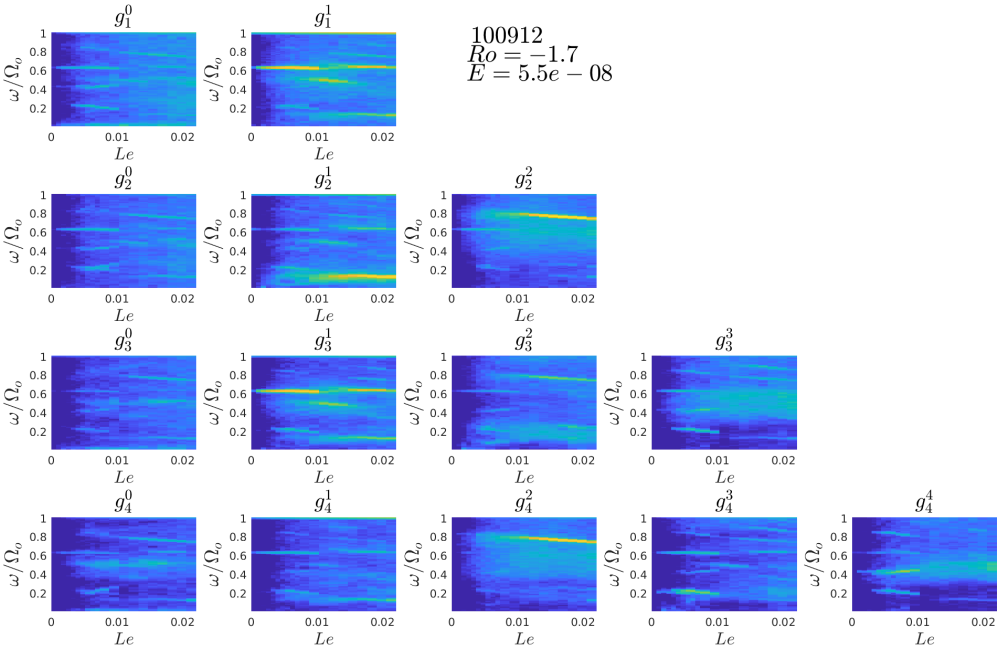

Figure 5.13: A gauss coefficients decomposition of the spectrogram shown in Fig. 5.12. This decomplosition allows us to estimate ℓ and m numbers of specific observed oscillations.

5.4.2 Positive Rossby

Another unexplored area is the positive Rossby number space. Water experiments have shown a lack of high amplitude travailing structures, but sodium experiments in the presence of B_{ext} allow some modes to bloom. In Fig. 5.15 we can see the spectrogram for an experiment with $Ro = 0.49$, here we observe inner sphere mode at $\omega/\Omega_0 = 0.51$ that is the rotation rate of the inner sphere in the outer sphere frame. And we can see several other modes that are quite hard to classify exactly but most of them are antisymmetric modes with all detectable $m = 0, 1, 2, 3$.

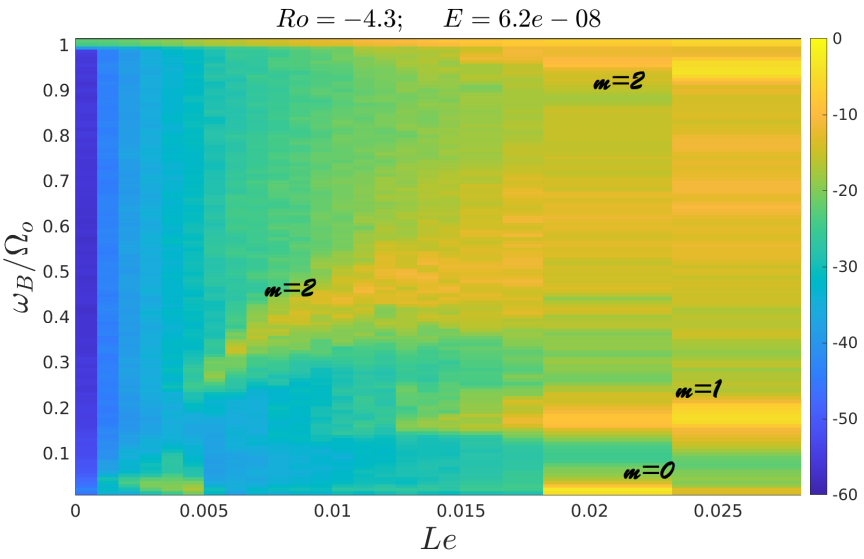

Figure 5.14: A spectrogram of the magnetic Hall probes data. On the vertical axis we have the frequency of the observed oscillations in the data in units of outer sphere rotation rates. The spheres rotation rates stay constant defining $Ro = -4.3$, and we vary the value of the externally applied dipole magnetic field. The corresponding Lehnert numbers are on the horizontal axis. The color represents the power spectral density on the oscillations. Here even more unusual behavior of the modes is observed. $m = 2$ gorge of oscillations change their frequency nonlinearly, possibly related to the square root dependence in the dispersion relation (Eq. 5.7)

In Fig. 5.16 and Fig. 5.17 it can be seen how in experiments with $Ro = 1.5$ and $Ro = 6$ the pale areas without applied magnetic fields turn into a beautiful blossom with a whole variety of structures.

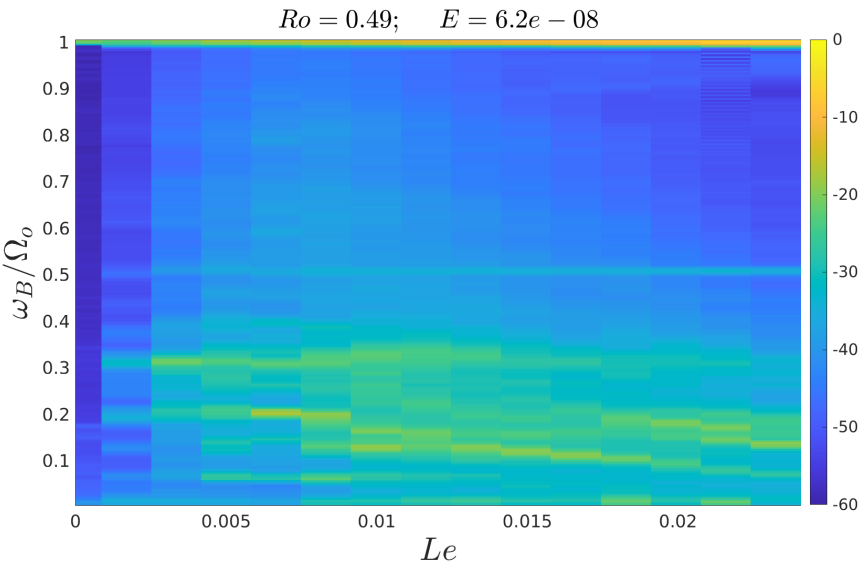

Figure 5.15: A spectrogram of magnetic Hall probes during an experiment with a constant Rossby number ($Ro = -0.49$) and consecutively increasing the external magnetic field, hence increasing the Lehnert number ($Le \leq 0.025$) on the horizontal axis. Here at the bottom of the figure we can see a lot of low-frequency structures that are hard to classify.

5.5 Experiments with baffles

After the inner sphere was upgraded with the baffles, we should expect a significant change in coupling between the sphere and liquid metal, hence we expect a different momentum transfer and different modes appearing in the same Rossby number experiments.

5.5.1 Rossby ramp

Let's take a look at the hydrodynamic regime ($Le = 0$) and compare it with the data from water experiments. In Fig. 5.18 we see a similar $\ell = 3; m = 2$ mode at $Ro \approx -0.8$, and a similar set of $\omega/\Omega_0 \approx 0.1$ modes that we see in water in Fig. 5.2. However, the majority of the water modes does not appear here. Maybe our resolution is too low, or more probably the baffles changed the flows in such a way that they are supressed.

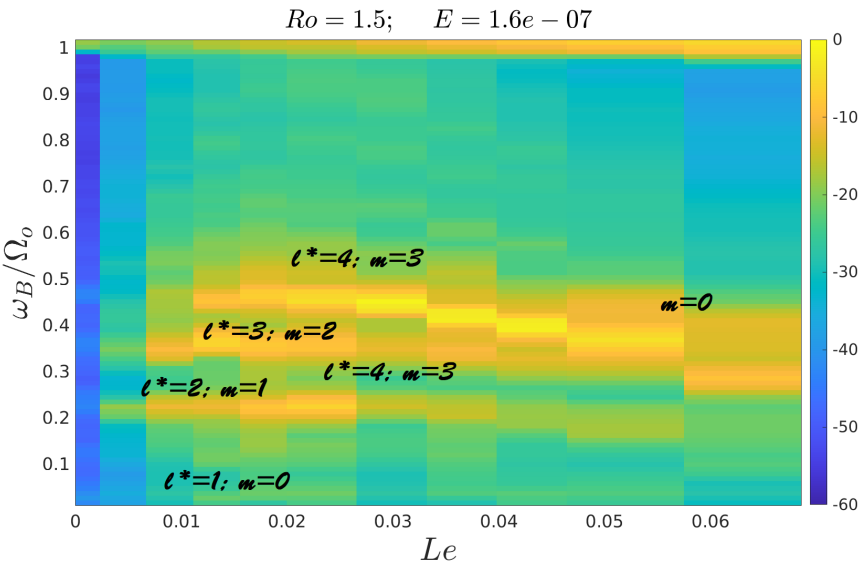

Figure 5.16: A spectrogram of the magnetic Hall probes data. On the vertical axis we have the frequency of the observed oscillations in the data in units of outer sphere rotation rates. The spheres rotation rates stay constant defining $Ro = 1.5$, and we vary the value of the externally applied dipole magnetic field. The corresponding Lehnert numbers are on the horizontal axis. The color represents the power spectral density on the oscillations. A family of strong oscillations appears and evolves with increasing the external magnetic field.

5.5.2 Magnetic ramp

One of the most fruitful regimes with the smooth sphere was at $Ro = -1.7$, so we want to examine this with the upgraded inner sphere. In Fig. 5.19 we can see little apparent structure. That is on one hand disappointing, on the other side it tells us something about how different the sodium flow with baffles is.

In Fig. 5.20 we compare the power spectral density for the smooth and baffled spheres at the same Rossby number ($Ro = -1.7$). During the experiments the spheres rotation rates were constant, but the experiment with the smooth sphere had a higher rate compared with the one with the baffles ($f_{o\ smooth} = -2.25\ Hz$, and $f_{o\ baffled} = -1\ Hz$). So the smooth experiment had a lower Ekman number hence a higher Reynolds number.

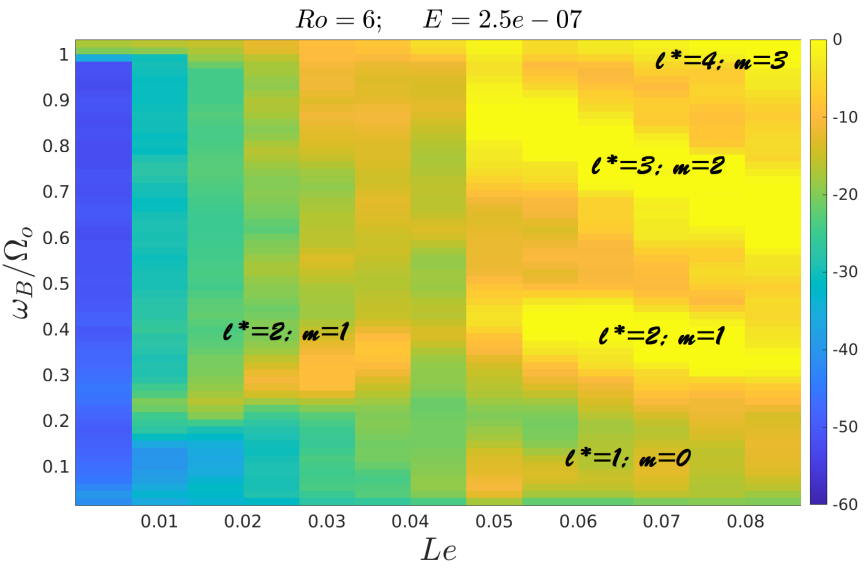

Figure 5.17: A spectrogram of the magnetic Hall probes data. On the vertical axis we have the frequency of the observed oscillations in the data in units of outer sphere rotation rates. The spheres rotation rates stay constant defining $Ro = 6$, and we vary the value of the externally applied dipole magnetic field. The corresponding Lehnert numbers are on the horizontal axis. The color represents the power spectral density on the oscillations. Even more wide spectra and shape-various modes appear and change with increasing Lehnert number.

At the top of Fig. 5.20 we show the PSD of the magnetic Hall probes data during the runs without applying an external magnetic field, and at the bottom with the field that resulted the Lehnert number (Le) on a scale of 0.016. Even the Reynolds number is higher for the smooth experiment, we can see that the base level of oscillations for rough sphere is above the one in the smooth case. But at the same time we cannot see the same distinguishable peaks as in the smooth runs.

We set up a series of experiments with a coarse search in the Rossby and Lehnert numbers phase space while keeping approximately the same Ekman number as in the experiments with the smooth sphere. The goal was to find strong oscillations as we had before. However by February 2022 we couldn't achieve that.

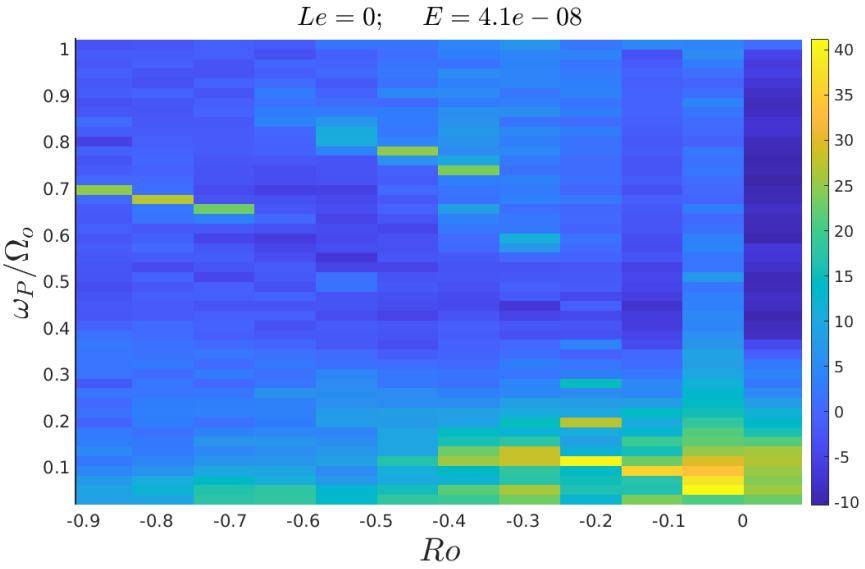

Figure 5.18: Spectrogram for sodium experiment with the baffled inner sphere in absence of B_{ext}. Some of the modes align with those observed in water experiments with the smooth sphere shown in Fig. 5.2.

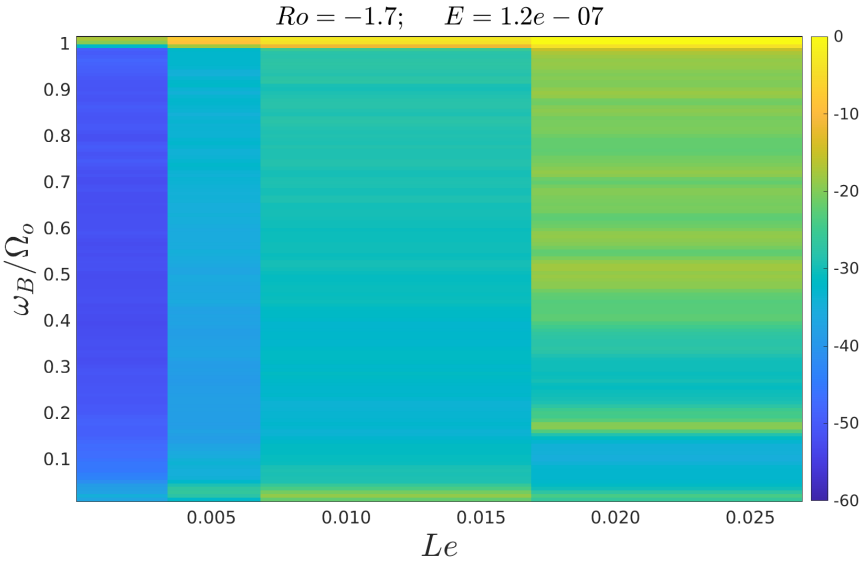

Figure 5.19: A magnetic field ramp with the baffled inner sphere. This regime without baffles has shown rich spectra of oscillations (Fig. 5.12, but with the upgraded sphere we don't see the same picture.

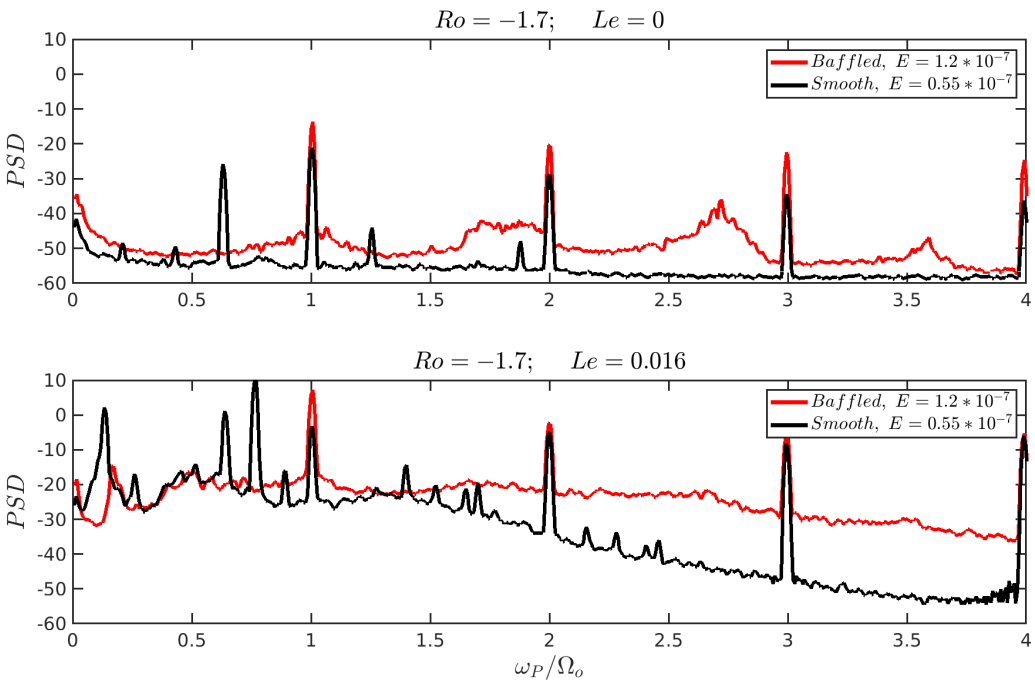

Figure 5.20: Comparison between baffled and smooth spheres at $Ro = -1.7$. At the top we present the zero applied magnetic field regime, and at the bottom we apply an external dipole field resulting $Le = 0.16$. This is the same experimental runs that are presented in Fig. 5.12 and Fig. 5.19.

5.6 Discussion

Akin's Law 9. Not having all the information you need is never a satisfactory excuse for not starting the analysis.

In the Three Meter Experiment, we observed and identified Inertial and Magneto-Coriolis modes. First we confirmed that in sodium experiments in the Three Meter apparatus we can see the similar inertial modes that were observed in water in 3M and in experiments in 60-cm experiment. Second, in the presence of the external magnetic coils and an ability to control the current in these coils within a significant range, we were able to modify the externally applied magnetic field. Here we were able to observe how

the external magnetic field affects the dynamics of modes inside liquid sodium, while the rotation rates of the spheres stay the same. The observed differences prove that we are observing magneto-Coriolis modes. The ability to decompose the observed magnetic field into gauss coefficients allowed us to characterize the modes and estimate the shapes of these traveling structures. With this tool we can see that magnetic field can change the frequency of the oscillations as expected by the magneto-Coriolis waves dispersion relation, but it also is capable of changing the spacial configuration of the specific mode, as well as amplify or suppress them. We also believe that we directly observe triadic resonances.

5.7 Future work

The author suggests taking a deeper look into the data at magnetic ramps experiments. Specifically, it might be useful to extend the decomposition into higher ℓ numbers. This can be done by applying narrow band-pass filters that would keep the phases of each individual mode and using the gauss coefficients decomposition afterward so we could use the leakage map more clearly. If the exact wave numbers and frequencies are defined this would allow us to confirm or refute the hypothesis of triadic resonances. Here we should compare the amount of energy stored in structures with different m numbers as a function of the Lehnert number; this also might be useful to estimate the growth rates.

While these modes travel in the same direction as the outer sphere is rotating, the author encountered several modes that show characteristics of a counter-propagation. This can be an artifact from aliasing or another related effect, but if this is confirmed that will be an interesting mode to look at.

Another analysis should be done within the Le dependence of the oscillation frequencies. This would help to compare the pure hydrodynamic inertial with the MC modes and their hybrids.

And, of course, we have to continue the search for strong modes in the upgraded experiment with baffles, and after limiting the phase space where we can see more of them - analyze the difference between the regimes with dipole and quadrupole-shaped external fields.

Chapter 6: Episode VI: Return of the sphere

6.1 A new era of Big Dynamo Sodium Machine

Although the previous generation of the Three Meter Experiment failed to reach dynamo - the self-sustainable magnetic field. It has achieved amplification of the external field of up to $\approx 20\%$ [58]. To reach the desired field generation we upgraded the inner sphere with baffles (Project "A New Hope" is described in detail in Chapter 3). By early November 2021, we had a fully functional machine, so we started running experiments. The upgraded apparatus scheme is illustrated in Fig. 6.1. The main difference between this and the previous generation is the presence of so-called "alpha" baffles on the surface of the inner sphere.

The first experiments with the upgraded device were designated to investigate the scaling of torque in the system as a function of the Reynolds number, specifically for the infinite Rossby number. Or in other words: we wanted to learn how much torque we need to apply to the inner sphere in the case when we don't let the outer sphere rotate. These experiments are important for understanding the coupling between the rough sphere and liquid sodium. We discuss this research in detail in Chapter 7, where we show results that have been submitted for publication in to Physica D [217].

For a comparison between Three-Meter and the 40-cm spherical-Couette experiments,

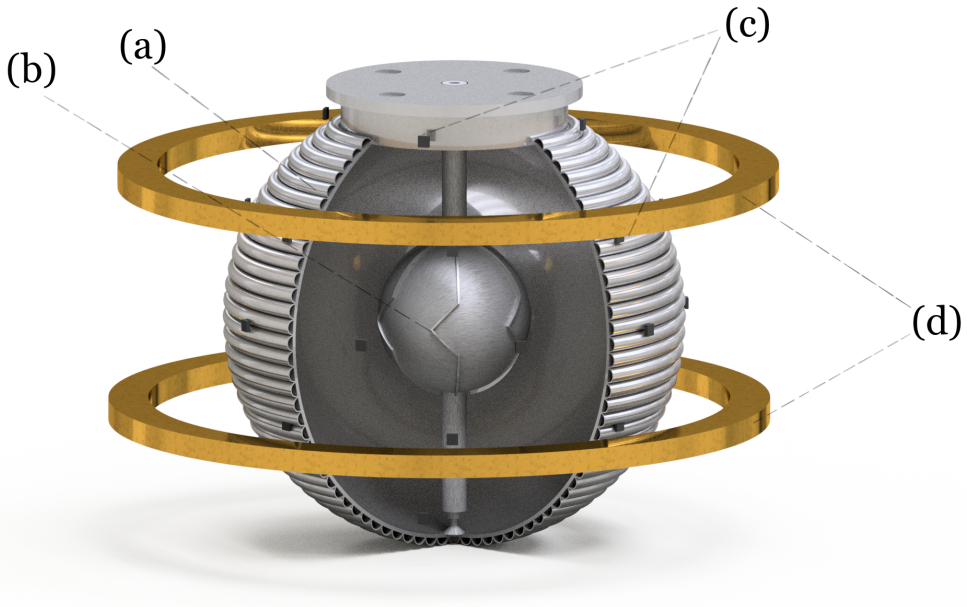

Figure 6.1: Schematic of the three-meter experiment with rough inner sphere and two magnetic coils: (a) Three-meter diameter outer sphere, (b) one-meter diameter alpha-baffled inner sphere, (c) array of 31 magnetic radial Hall probes, (d) external electromagnet. The volume between the spheres is filled with metallic sodium. The torque sensor measures the applied torque to the inner sphere, it is shown in Fig. 3.36.

the reader should check the sibling thesis by Rubén Rojas 2022[191].

6.2 Mechanical difficulties

6.2.1 Bearing jam

So here we are, six years after we started fixing and upgrading the broken apparatus, and after just several days of running:

"I felt a great disturbance in the Force. As if millions of voices suddenly cried out in terror and were suddenly silenced." — Obi-Wan Kenobi. The inner motor was acting weirdly. The logs of the run are shown in Fig. 6.2. On November 9, 2021, during a corotational run with the inner going faster than the outer and $Ro \approx -1$ the torque suddenly increased from 400 $N \cdot m$ to 1500 $N \cdot m$, and the inner sphere slowed down from -6.1 Hz to -5.2 Hz within two seconds. After several seconds the rotation rate restored, and a minute later the torque normalized. We had heard unusual noises during the operation but only found the slowdown later in the logs. At the end of the day we discovered that the ≈ 500 L cavity inside the sphere that allows sodium to expand was no longer able to hold even slightly pressurized (≈ 0.5 psi) gaseous nitrogen. It was likely that the lip seals had failed and that liquid sodium had probably reached the top inner bearing (shown on the top of Fig. 3.1) and jammed it.

To continue taking data we designed a plastic transparent cover that goes on top of the top inner bearing and maintain gaseous nitrogen inside the cavity so we would avoid liquid sodium fire in case liquid sodium escapes the vessel. With this temporary solution, we were able to run the experiment for another full week until it failed to start on December

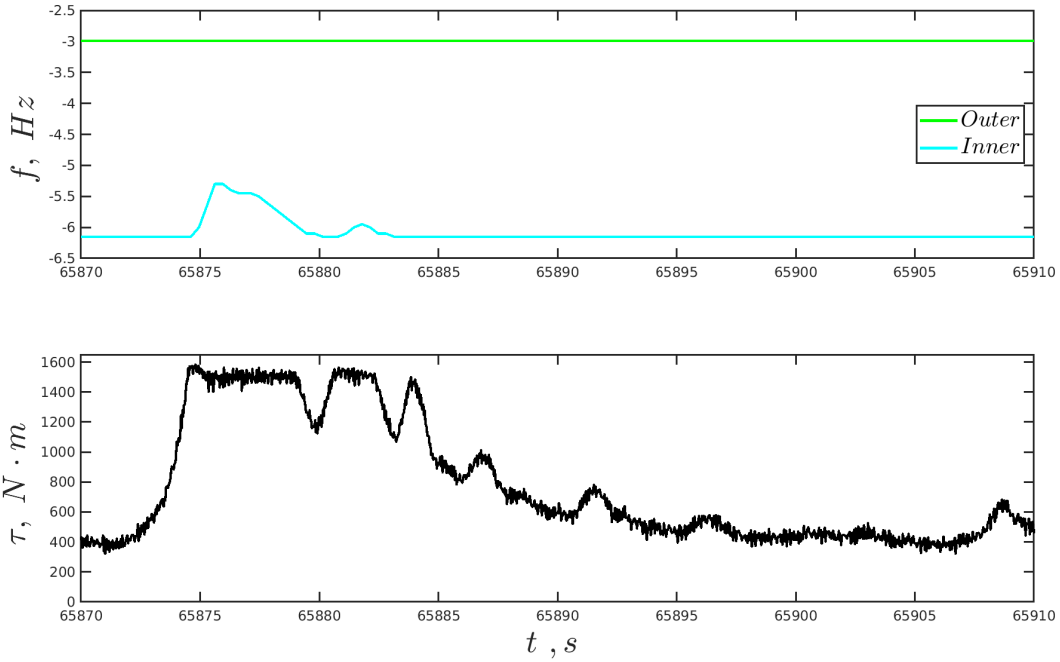

Figure 6.2: A sudden increase of the torque and a rapid slowdown of the inner sphere. This event is the main suspect for inflicting damage to the lip seals and top inner bearing.

9, 2021. The inner sphere was locked with the outer. Our attempts to use the inner motor to unlock the spheres failed too; the torque was not sufficient to make the sphere move freely.

6.2.2 Unjamming operation

"Use the Force, Luke." - Obi-Wan Kenobi

After several days of excessive heating and using the inner sphere motor to wiggle the inner shaft in different directions, we ended up completely locking the spheres together in one position. So we took a break to go to conferences and rest during winter break. Later in January 2022 we continued the same technique but failed again. The last resort before starting disassembling the experiment again was to use the outer sphere rotation

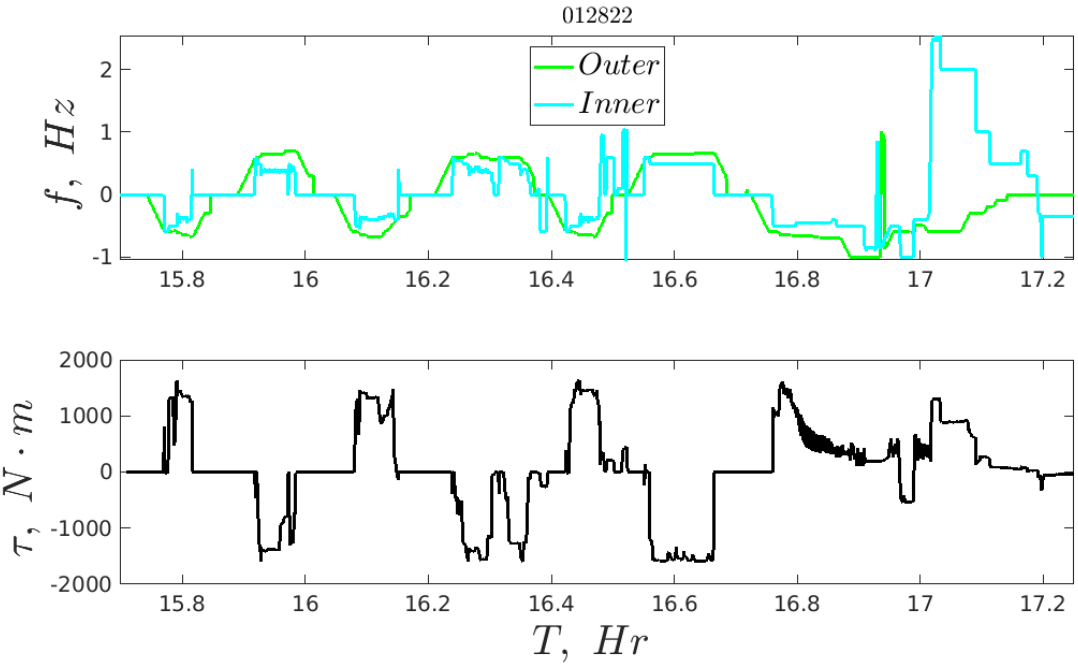

Figure 6.3: The unjamming procedure involved consecutively spinning up the spheres together and applying torque by the inner sphere allowed us to decouple the spheres and continue the experiments.

in pair with the inner to increase the applied torque, and we succeeded. The logs of "Unjamming Day" are shown in Fig. 6.3. During this day, we were accelerating the outer sphere periodically in alternating directions and applied torque using the inner motor to accelerate and decelerate. After multiple attempts, we saw that the inner sphere was moving relative to the outer so we rotated them for some time and considered the spheres unjammed.

Running the apparatus after the unjamming was as smooth as before and the new torque measurements we consistent with the previous runs. Hence we considered it a successful operation and proceeded with the experiments.

6.3 The new experiments

6.3.1 Torque analysis

In Chapter 3 we discussed the reasoning behind fabricating and installing asymmetrical baffles. In this case, we can investigate differences between antisymmetrical experiments (when each sphere's rotation rate is multiplied by -1). The first thing to do would be to find the difference between the torque required to spin the inner sphere with the same frequency but in different directions.

To parameterize the flow we will be using our regular Reynolds number: $Re = |\Omega_i - \Omega_o|(r_i - r_o)^2/\nu$, and G - dimensionless torque defined as:

$$G = \frac{T}{\rho\nu^2 r_i} \ . \tag{6.1}$$

Here T is torque in $N \cdot m$, $r_i = 0.51\ m$ is the inner sphere radius, $\rho_{Na} = 920\ kg/m^3$ is liquid sodium mass volume density, and $\nu_{Na} = 6.76 \times 10^{-7}\ m^2/s$ the kinematic viscosity of liquid sodium.

6.3.1.1 Stationary outer sphere

In Fig. 6.5 we show a plot of the of dimensionless torque for infinite Rossby number: $G_\infty = G(Ro = \infty)$. In other words, this represents the torque as a function of the inner sphere rotation rate with the stationary outer sphere. In Fig. 6.4 we show the directions of the Scoop and Wedge modes. Apparently the naming should be obvious for a native

English speaker, so the author has struggled to understand it and still failed. We can see that Scoop mode requires a lower torque for the same rotation rate when compared with Wedge mode. It agrees with our observations in the 40-cm water experiment [100, 191]. In this chapter we will not focus on the exact scaling of torque, this will be discussed in detail in Chapter 7. Meanwhile, we will just interpolate G_∞ as a third-degree polynomial and use it in this chapter.

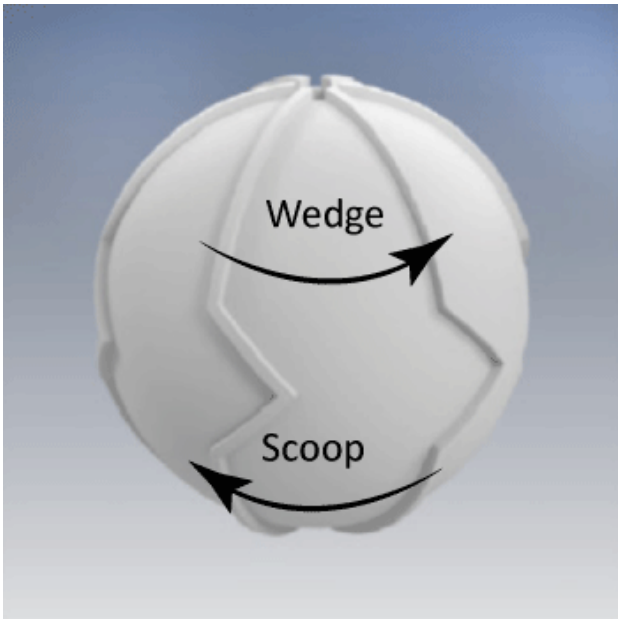

Figure 6.4: The Wedge and Scoop modes correspond to the opposite directions of rotation of the inner sphere relative to the outer. Here arrows represent the direction of rotation of the baffled inner sphere.

6.3.1.2 Rossby number dependence

Here we will add the outer sphere rotation rate. We will vary both inner and outer spheres rotation rates. The outer sphere rotation rate is within range $-4 < f_o < 4\ Hz$, and for the baffled inner sphere we were capable of spinning with up to $|f_i - f_o| < 5\ Hz$ difference.

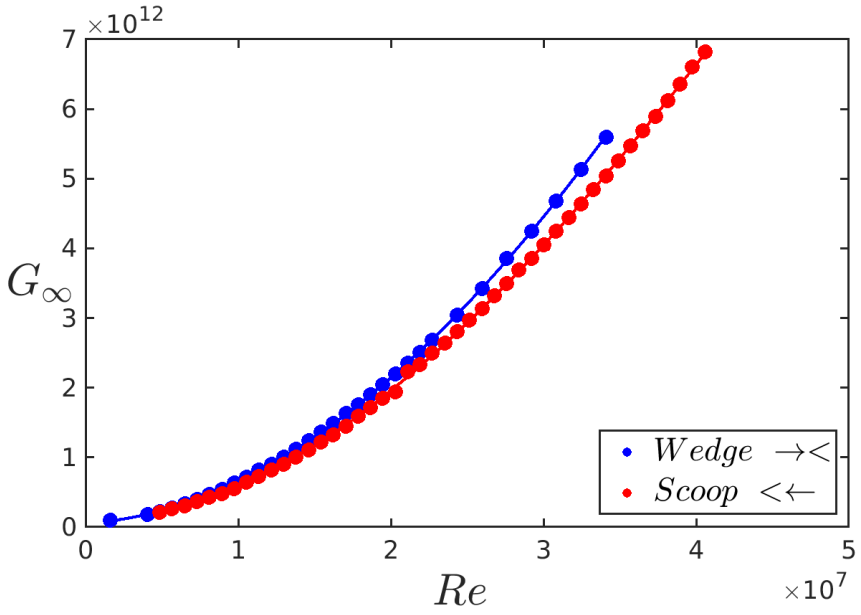

Figure 6.5: Dependence of the dimensionless infinite Rossby number torque on the Reynolds number. The Wedge mode requires more torque than the Scoop mode. The modes naming is explained in Fig. 6.4.

To take into account the outer sphere rotation rate the regular approach is to separate the torque into two parts:

$$G(Re, Ro) = G_\infty(Re) \cdot H(Ro) \ , \tag{6.2}$$

here we assume that torque depends on two separable functions: $G_\infty(Re)$ that depends only on the difference between rotation rates, and $H(Ro)$ that only depends on the ratio between rotation rates. In Fig. 6.6 we present the experimental data for this $H(Ro) = G/G_\infty$ values for three different experimental setups: with baffles: red - Scoop mode, and blue - Wedge mode; and black - pre-upgrade smooth sphere. We use data for experimental runs without any externally applied magnetic field and with applied field $B_{ext} < 10$ *gauss*. Our experiments showed that the presence of this level of external field does not affect the torque

in the system within the detectable range. The visible peaks in Fig. 6.6 are well known for Taylor-Couette (cylindrical) experiments and are usually called optimal transport regime [112, 218]. Similar peaks have also been observed and documented for spherical-Couette flows [58, 191], and we will be referring to them as the maximum torque regimes.

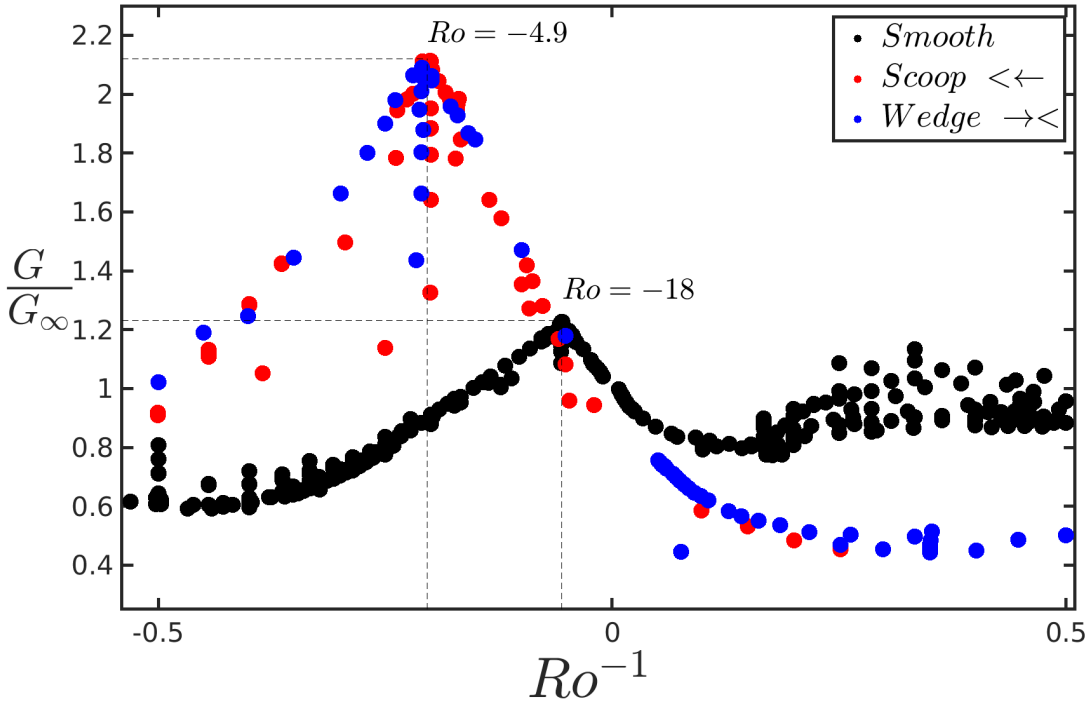

Figure 6.6: Rossby dependence of the torque in the experiment. It is normalized by the infinite dimensionless torque in the assumption shown in Eq. 6.2. The peak locations are shown by dashed lines. The difference between the smooth and baffled experiment is visible here.

The location of maximum torque is different for the smooth ($Ro = -18$) and baffled spheres ($Ro = -4.9$); additionally, while the smooth maximum torque is approximately 22% higher than with stationary outer sphere, the baffled regime is showing 110% increase. The current amount of data does not allow us to say if Wedge is different from Scoop mode in terms of the peak location or height. The difference between smooth and baffled spheres can be explained by the change in the underlying nature of the boundary layer

hence additional angular momentum transfer [1, 2, 112, 113, 114, 191].

6.3.1.3 Maximum torque regimes

In Fig. 6.6 we can also see that close to the maximum torque regime some of the points are located below the peak value. This dependence is visible for all the inner sphere configurations and can be explained by an additional Reynolds-dependent factor. This effect should be investigated in the future. The normalized torque at $Ro = -5$ is plotted as a function of Reynolds number in Fig. 6.7. Here we see that at lower Reynolds numbers the H function from Eq. 6.2 is not a constant value as we assumed earlier. We do not observe the same dependence in other regimes, so we conclude that torque dynamics at maximum torque regimes has a more complicated dependence than we originally assumed. Ekman number here is not constant and drops linearly with Reynolds number, the lowest value is $E = 2 \cdot 10^{-7}$.

6.3.1.4 Magnetic fields affecting torque

During the experimental runs, we see that sometimes the presence of the external magnetic field can significantly affect the torque in the system. We will look at multiple cases:

In case when we are talking about maximum torque regimes (in Fig. 6.8) the normalized dimensionless torque drops in presence of a dipole magnetic field in experiments with $Ro = -5$ drops on a scale of $5 - 10\%$ with $Le \approx 0.08$ and $Rm = 200 - 250$. For these two experiments, we can fit the results with $G = G|_{Le=0} \cdot (1 - \sqrt{Rm} \cdot Le^2)$. Where $G|_{Le=0}$

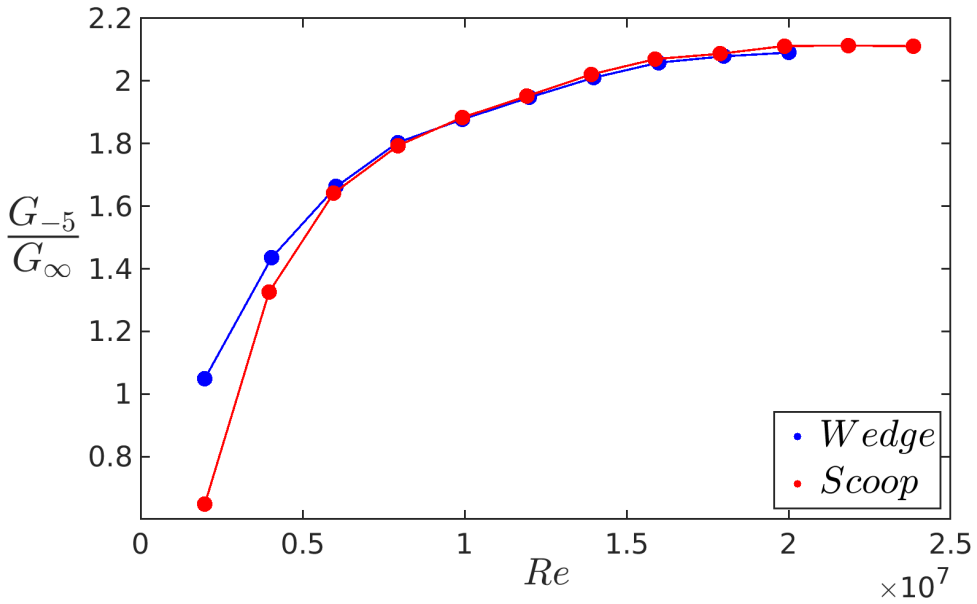

Figure 6.7: Reynolds number scaling of normalized dimensionless torque at the maximum torque regime. This shows that torque dependence cannot be fully separated in this regime.

is torque in absence of the applied magnetic field. More data is needed for investigating this scaling.

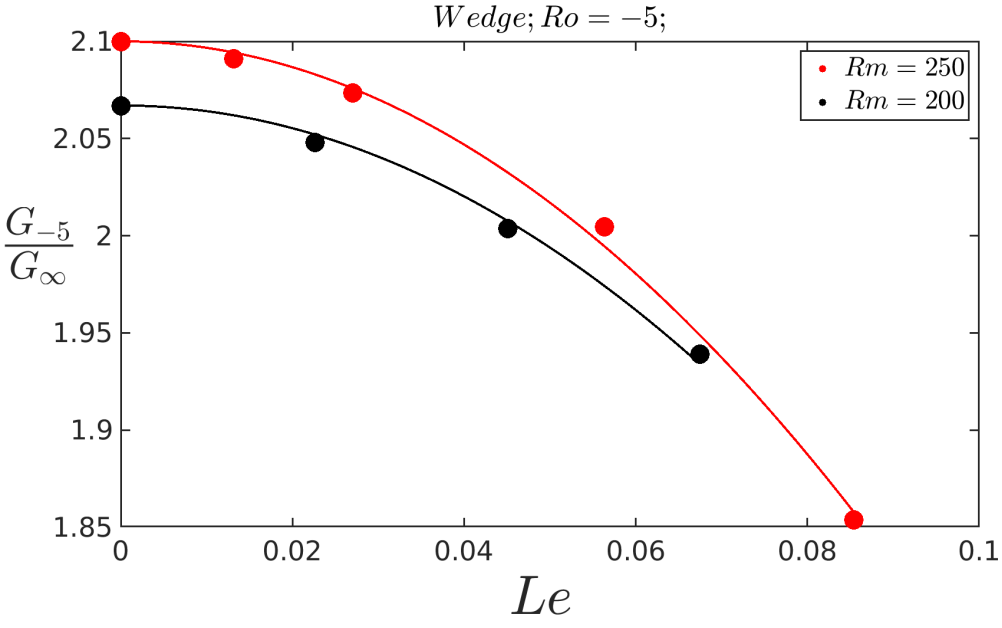

Figure 6.8: The externally applied magnetic field can lower torque with $\approx 10\%$ in case of the higher Rm. The fit is made with: $G = G|_{Le=0} \cdot (1 - \sqrt{Rm} \cdot Le^2)$

On the other hand, we see that torque can increase with increasing Le, for example in Wedge experiments with $Ro = 2.85$. In. Fig. 6.9 we show that torque value increases quadratically with Le: $G = G|_{Le=0} \cdot (1 + 400 \cdot Le^2)$. These are corotational experiments with the inner sphere going 3.85 times faster than the outer. In a situation when the torque reaches some critical value, the inner sphere starts applying too much torque to the outer. The experimental setup does not allow us to apply a lot of braking to the outer sphere so in this case, the outer sphere started accelerating, so could not investigate higher Le values.

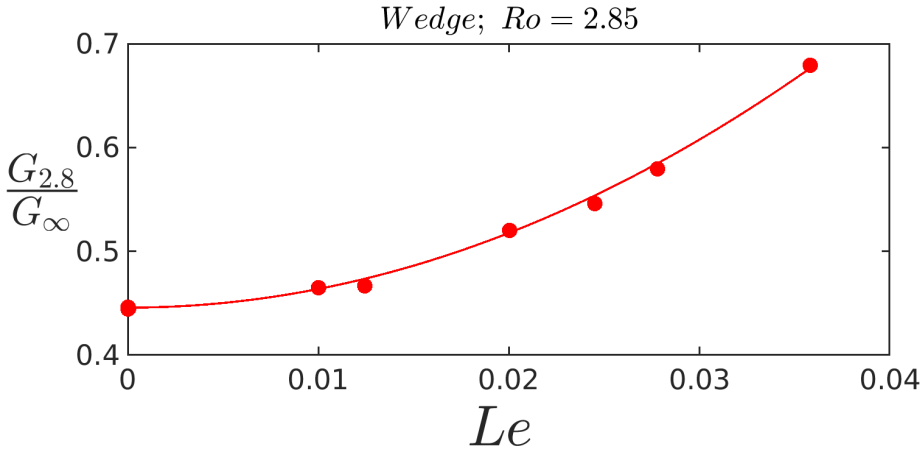

Figure 6.9: Torque scaling with the applied external magnetic field in Wedge corotational experiments: $Rm = 250$ & 300, $E \approx 10^{-7}$. The fitted line: $G = G|_{Le=0} \cdot (1 + 400 \cdot Le^2)$.

In some other cases, we cannot see the same pattern. In Fig. 6.10 the torque stays on the same level while the Lehnert number is increased up to similar values as in previous cases. Ekman and Reynolds's numbers also match the experiments above. This stability in these experiments is observed in Rossby range $2 \leq Ro \leq 2.27$ with $E = 1.2 \cdot 10^{-7}$

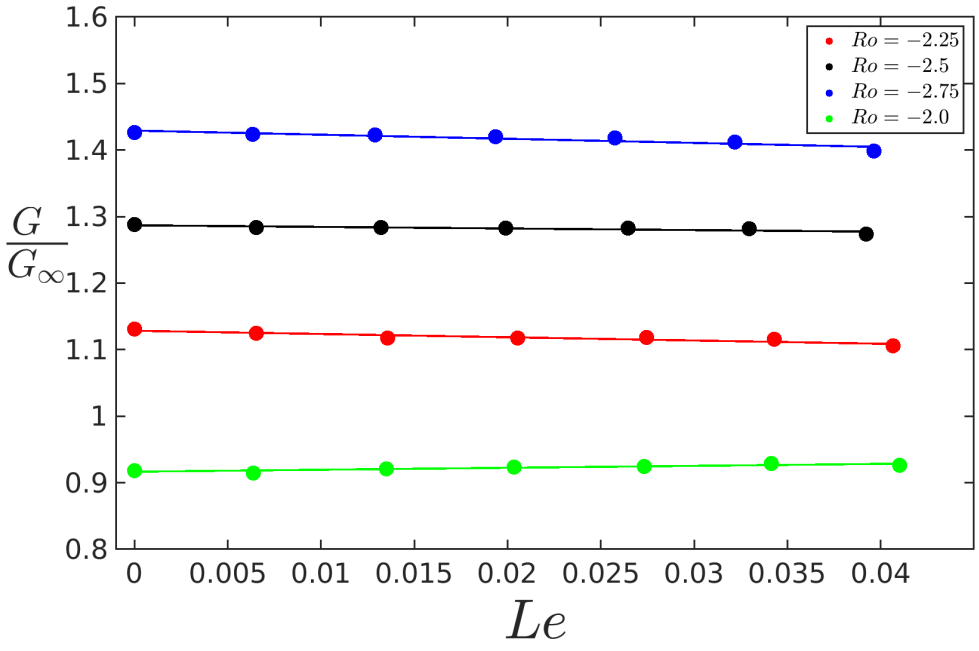

Figure 6.10: Torque does not show the dependence patterns we saw before, the magnetic field does significantly affect the mechanical drag in this case.

6.3.1.5 Bistability

In the previous generation of the Three Meter experiment were observed multiple regimes where torque was not stabilizing at one value but rather transitioned between two different states, jumping one between another. We investigated the area where this bistability was reported in Zimmerman 2011 [8]. In Fig. 6.11 we show the probability distribution function of torque value for five different experiments with the same Ekman number ($E = 1.2 \cdot 10^{-7}$).

The distance between torque probability peaks changes with Rossby number, and if the linear trend would be assumed as shown in Fig. 6.12 they would overlap approximately at $Ro = 2.5$. This matches with results obtained in experiments with the smooth inner sphere. On the one hand, it confirms the previous results, on the other hand, it is a little

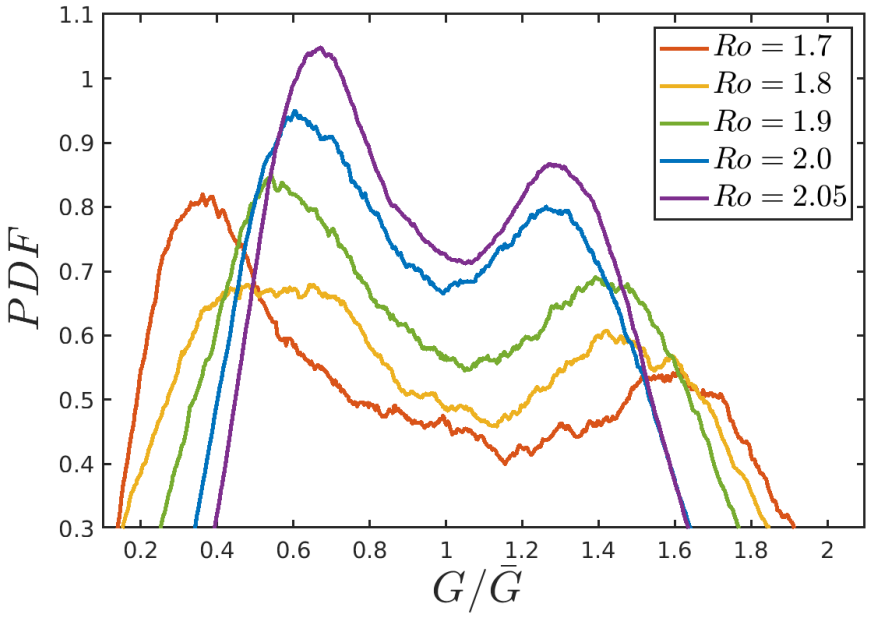

Figure 6.11: Normalized torque Probability Density Function for multiple Rossby numbers in the proximity of previously observed bistability regimes.

bit surprising because, as we saw before, the baffled inner sphere changed the locations of the regimes. Further investigation is necessary. Specifically, we need more steps in Rossby space in the range of $Ro = 1 - 3$ with experiments covering multiple hundreds of outer sphere revolutions, and, of course, the difference between Wedge and Scoop modes is interesting in this research.

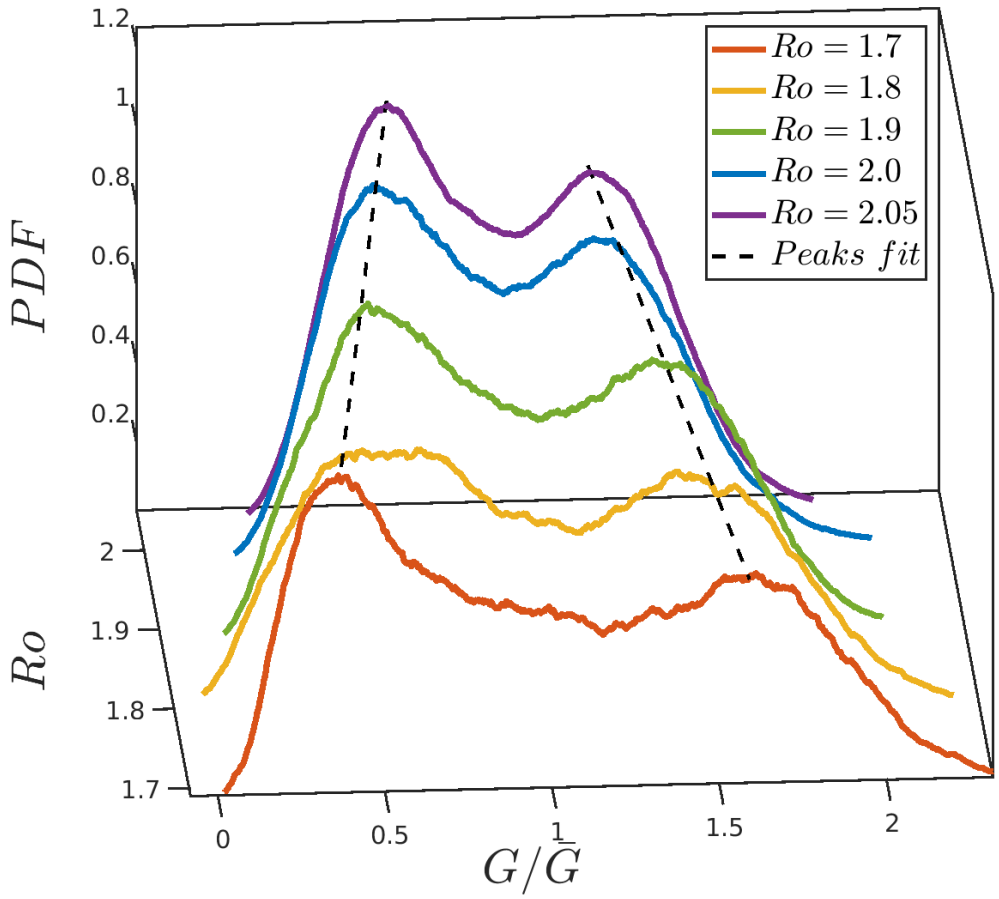

Figure 6.12: A Joy Division plot representing the normalized torque PDF in 3D as a function of Rossby number. The linear fit of the peaks intersects at $Ro \approx 2.5$ what matches previous results [8] .

6.3.2 Dynamo search

"These aren't the droids you're looking for." — Obi-Wan Kenobi, A New Hope

Finally, we want to take a deep dive into the search for a dynamo state! In this section, we will be using values of magnetic energy as integrated over volume density of magnetic field:

$$\mathbb{E} = \int W dV = \int \frac{1}{2} \frac{B^2}{\mu_0} dV \ . \tag{6.3}$$

In our experiment we are capable of observing radial magnetic field in 31 places - an almost uniformly distributed array of magnetic Hall probes with sensitivity $S = 31.5\ mV/gauss$. This allows us to deconstruct the observable voltages on the probes into a series of 24 gauss coefficients (g_l^m). To estimate the energy stored in the proximity of the surface of the outer sphere we convert the calculated gauss coefficients into values of magnetic fields that would be observed in approximately 1000 uniformly distributed points on the surface of the sodium sphere. These magnetic field values are squared and multiplied with a predefined constant that depends on the thickness of the integrated layer. But in our studies due to the normalization this constant disappears from the presented data. In the presence of an externally applied magnetic field, we will normalize the observed energy over the estimated energy of this applied magnetic field. To do so we subtract the estimated values of the fields induced by the external coils, convert the results to gauss coefficients and proceed from there.

6.3.2.1 Coarse swipe

First, we will look at a wide range of Rossby ($-20 \leq Ro \leq 20$) numbers and we will not apply any external magnetic field. In this experiment Ekman number was fixed at the same value: $E = 5 \cdot 10^{-7}$, no externally applied magnetic field, hence Lehnert number is zero, while Reynolds was increased up to $Rm_{max} = 400$.

In our data acquisition setup, we see a decent level of diagnostic noise that, by the authors' estimations, would not let us confirm the presence of 1 gauss dynamo. So we should hope to see something above that level. In the absence of the external magnetic

field, we normalize the observable by a dipolic five-gauss (fully hypothetical) field. In. Fig. 6.13 we plot the average magnetic energy as a function of inverse Rossby number; just as when we talk about torque scaling in Fig. 6.6.

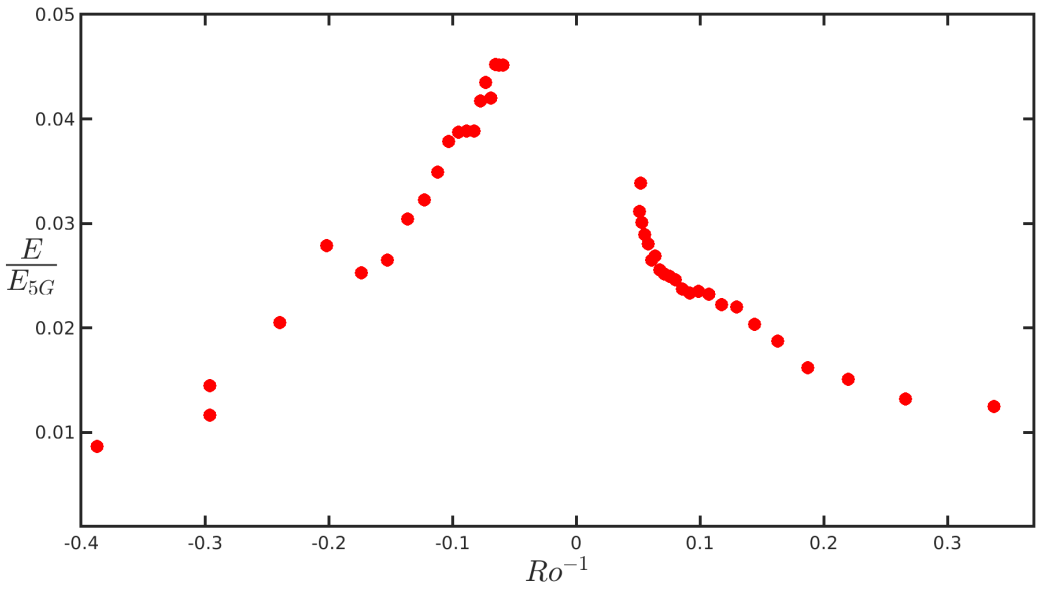

Figure 6.13: Magnetic energy in the sphere surface area relative to the hypothetical 5 *gauss* dipolar magnetic field, as a function of inverse Rossby number.

Here we see that in the absence of the external magnetic field the energy confined close to the surface of liquid metal is under 5% of a hypothetical 5 *gauss* dipole field. At the same time, we can see a kink close to the maximum torque regime ($Ro = -5$), so we should take a closer look into that area.

6.3.2.2 Fine search

Previously we saw that there is possibly something interesting near $Ro = -5$. So we designed an experiment with a fine Rossby search close to the maximum torque regime, keeping Magnetic Reynolds number constant ($Rm = 200$). In this experiment we were

applying an external dipolic field on the scale of 20 *gauss*, so we are normalizing by the estimated energy of this field. We present the results in Fig. 6.14. The additional magnetic energy seems to have a maximum close to $Ro \approx 4.8$. In the original "back-of-the-envelope calculation" we estimated the maximum at $Ro = -5$ and went there to do a more detailed analysis.

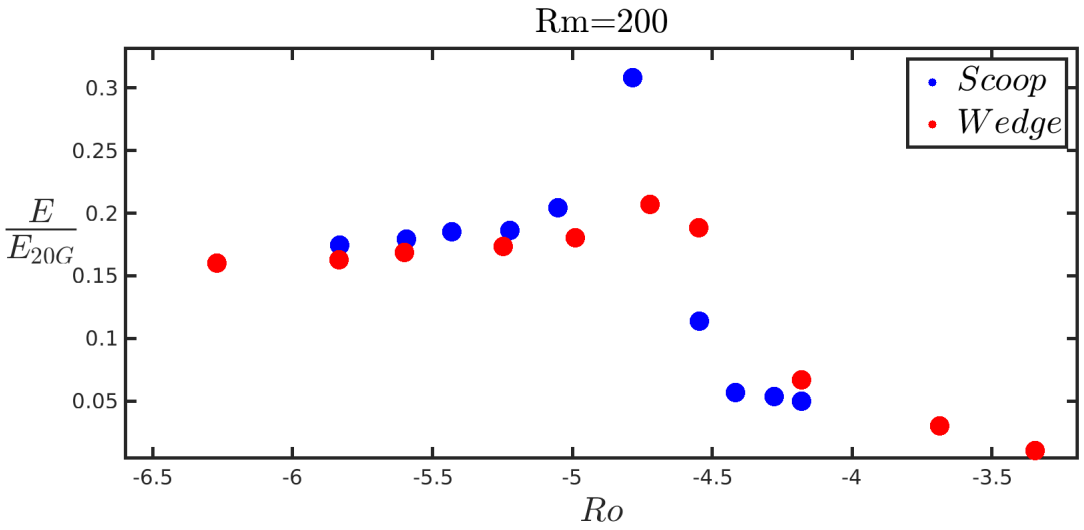

Figure 6.14: Additional magnetic energy as a function of Rossby number in the proximity of the maximum torque regime. The energy is normalized by the externally applied fields' energy.

6.3.2.3 Reynolds ramp at max torque regime

Here we aim to $Ro = -5$, apply an external $B = 20$ *gauss* dipole field and ramp up Magnetic Reynolds Number up to the limit of our inner sphere motor (in this case $Rm \approx 240$). To save the inner motor from overheating we add an induced convection cooling system (a huge metal fan on the top of the motor). And here we hope for the best!

In Fig. 6.15 we can see that the additional magnetic energy grows nonlinearly but monotonously with increasing Reynolds number. At the maximum Rm we observe that

the energy of the generated field is on a scale of 30% of the induced one. But where is it stored? If we decompose this energy by the spherical components we will see that 90% of this energy is stored in $\ell = 3; m = 0$ component and the rest is in $\ell = 1, 2, 4; m = 0$. The original externally applied magnetic field has the main component $\approx$ 75% in the axisymmetric dipole field: $\ell = 1; m = 0$, and the second biggest $\approx 20\%$ in this $\ell = 3; m = 0$ configuration.

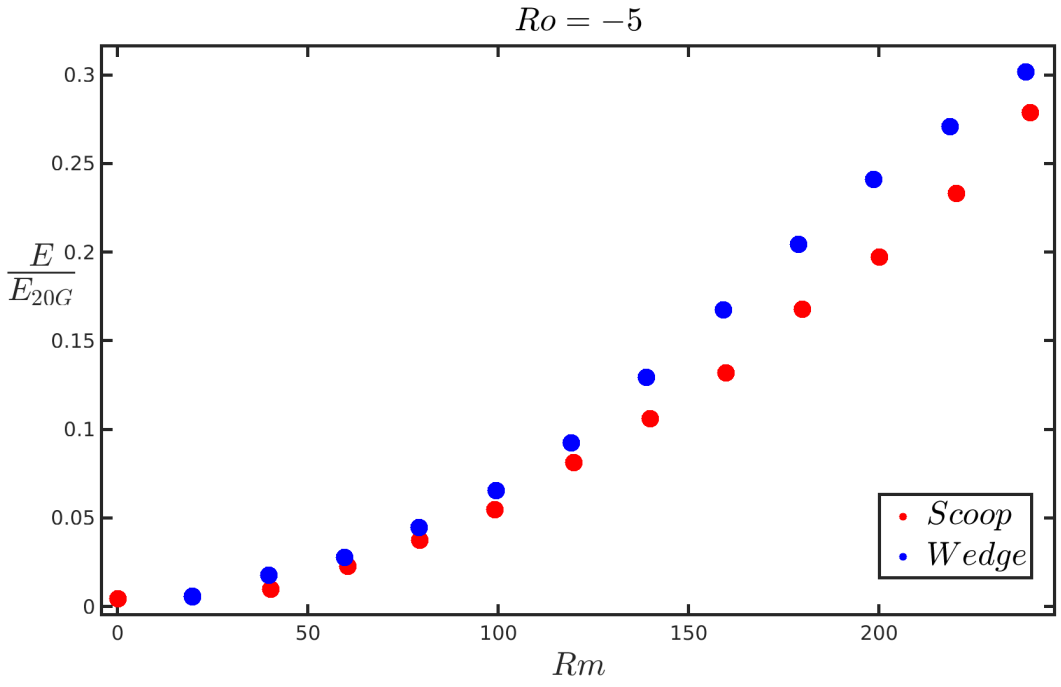

Figure 6.15: Additional magnetic field energy scaling with magnetic Reynolds number at the maximum torque regime. The energy is normalized by the energy of the externally applied magnetic field. At the maximum Rm we estimate a 10 *gauss* additional $\ell = 3;\ m = 0$ field.

6.4 Here comes the pump

During an experimental week in August 2022, we were notified that our oil heater system located on the east wall outside Energy Research Facility was spraying hot oil. After some investigation, we discovered that the oil was not hermetically sealed inside the

system and the pump needed maintenance. So once again, the experiment was considered non-operational and is waiting to be repaired.

6.5 Conclusions

We performed multiple series of experimental runs with the renewed inner sphere. The observed torque scaling confirmed the results of the 40-cm experiment: that to reach the same Reynolds numbers now we need ≈ 5 times more torque in most regimes. Analyzing Rossby dependence demonstrated that the maximum torque regime location (Fig. 6.6) is very different from the smooth sphere experiments. The author suggests augmenting the definition of Reynolds in the case of spherical-Couette experiments to implement the difference between various surface conditions. Hopefully in such a way that the maximum torque regime would be happening at the same "Effective Rossby Number". Plus having a new "Effective Reynolds number" which could contribute to the explanation of differences in torque scaling.

The assumption (Eq. 6.2) that torque dependence in this experiment can be separated into two different functions: one Reynolds number function and one Rossby number function - does not work in at least maximum torque regimes. This difference should be investigated.

In the presence of the externally applied magnetic field, the torque changes with no obvious pattern. We need more experiments with a variety of Rossby and Lehnert numbers, with different direction applied fields, and with quadrupole fields.

In bistability regimes we see similar patterns observed and reported for the smooth sphere. This is more surprising than expected, so there should be more collected data. The

author thinks that investigating the bistability in the presence of the external is promising.

While talking about our New Hope for dynamo the author would like to say that we achieved the mechanical goals and ran some promising experiments but still haven't obtained the desirable dynamo effect. In other words, probably we are seeing how the Reconnection Strikes Back. We are still not seeing a full-scale self-generated field. There is a chance that we observe a seeded generation of $\ell = 3; m = 0$ field on the scale of $B_{g_3^0} \approx 10$, that we would like to call *Dynamito*. *"Your eyes can deceive you; don't trust them." —Obi-Wan Kenobi.* Due to the way we do our energy confinement analysis we cannot confirm that this *Dynamito* is an additional generated $\ell = 3; m = 0$ field or this is exactly an opposite effect because we would see similar plots in a situation with Three Meter Experiment would be converting this g_3^0 externally applied field into something else. *"Many of the truths that we cling to depend on our viewpoint." — Obi-Wan Kenobi*

Chapter 7: Turbulent dissipation in rotating shear flows: an experimental perspective

Akin's Law 6 (Mar's Law) Everything is linear if plotted log-log with a fat magic marker.

In this chapter, we will show a published at Physica D paper [217], where we talk about the torque scaling as a function of Reynolds number in spherical-Couette and Taylor-Couette experiments. That publication is dedicated to the memory of Charles (Charlie) Doering

7.1 Introduction

The dissipation of kinetic energy to heat in viscous flows has significant implications in nature and technology. Here we experimentally examine the scaling of dissipation in rotating turbulent shear flows as measured in laboratory experiments via torque measurements. The motivation is to better understand natural rotating turbulence in atmospheres, oceans and liquid planetary cores, as well as to also understand the approach to the asymptotic Kolmogorov-Constantin-Doering limit where the small, but non-zero, viscosity becomes irrelevant. In both cylindrical and spherical Couette flows, differential rotation can either enhance or reduce the observed dissipation. As well, we document new

results in the increase in scaling exponents expected, and here observed, for rough spherical Couette flows.

Hydrodynamic turbulence occurs in nature and technology but remains difficult to understand due to its strongly nonlinear spatiotemporal complexity. Understanding turbulent drag is equivalent to asking about how turbulence converts kinetic energy to thermal energy via viscous dissipation. These are central to understanding the power necessary to maintain a turbulent flow or motion involving turbulence, e.g. vehicle motion, water flow in pipes, and fluid flows in planetary atmospheres, oceans, and liquid cores. Considerable theoretical and experimental research has focused on understanding how energy dissipation depends on the imposed parameters in a turbulent fluid flow, i.e. the velocity, the system size, and the viscosity. The classical Kolmogorov scaling, that the energy dissipation per unit mass ϵ would scale as the velocity scale U^3 was made rigorous (mathematically proven) by the theoretical work of Constentin and Doering [219]. We refer to this scaling as Kolmogorov-Constantin-Doering Scaling. We examine this experimentally by measuring the total power dissipation and its dependence on the velocity scale made dimensionless using the Reynolds number, which for rotating cylindrical or spherical flows we define as $Re = |\Omega_i - \Omega_o|(r_i - r_o)^2/\nu$, where Ω_i and Ω_o are the inner and outer container rotation rates, r_i and r_o the inner and outer radii, and ν the kinematic viscosity.

We quantify the experimentally observed power dissipation using the measured torque. In general $P = T\Omega$ for systems rotating at an angular velocity Ω experiencing a torque T. As our systems have two differentially rotating boundaries this generalizes to $P = T_i\Omega_i + T_o\Omega_o$ where the subscripts specify outer or inner torques and rotation rates. In a statistically steady state $T_i = -T_o$ for the average torques, as the angular momentum is

assumed to fluctuation about its mean value. The power then simplifies to $P = T_i(\Omega_i - \Omega_o)$ so that only observations of the average inner boundary torque are necessary.

Many turbulent systems show approximate power law $T \sim Re^{\alpha}$ scaling of the torque (and thereby the power). Here our analysis of Couette flow observational data shows that this α changes, perhaps continuously, with Re. We compare power-law models of the torque scaling to a Prandtl-von Karman skin friction law (Eq. 7.5) which shows a better agreement at high Reynolds numbers.

7.2 Experiments

7.2.1 Parameters

Here we describe aspects of our spherical Couette flow experiment where we have taken measurements with either water or liquid sodium as the working fluids (but of course not both). The hydrodynamic state of our spherical Couette system depends on two primary dimensionless parameters: the Reynolds number (Re) - ratio of inertial forces to viscous forces, and the Rossby number (Ro) - characterising the differential rotation: $Ro = (\Omega_i - \Omega_o)/\Omega_o$

We use the dimensionless torque defined as:

$$G = \frac{T}{\rho \nu^2 L} \ . \tag{7.1}$$

Our spherical Couette experiment has $r_i = 0.51\ m$ and $r_o = 1.46\ m$. At the experimental temperatures, the mass density of the liquid sodium is $\rho_{Na} = 920\ kg/m^3$ at $T = 120^{\circ}$ C,

of water $\rho_{H2O} = 1000\ kg/m^3$ at $T = 20°$ C, and the kinematic viscosity of liquid sodium $\nu_{Na} = 6.76 \times 10^{-7}\ m^2/s$, and water $\nu_{H2O} = 1.0 \times 10^{-6}\ m^2/s$ [206]. We use $L = r_i$ - for the length scale in the definition of G for the spherical Couette flows.

7.2.2 Three meter device

The three-meter experiment apparatus (here after 3m) schematic shown in Fig. 7.1 is a spherical Couette experiment consisting of two concentric spheres. The ratio between them $\eta = r_i/r_o = 0.35$ is similar to the Earth's outer core to inner core radius ratio [117]. The space between the spheres is filled with water for some experiments described here, and later with metallic sodium. Experimental runs with sodium are done at $T \approx 120\ C$ to ensure the metal is liquid. The inner and outer spheres are able to independently rotate with frequencies up to 4 Hz for the outer sphere and up 15 Hz for a smooth inner sphere and 4.5 Hz for the case of the inner sphere with baffles. Two 260 kW motors drive the inner and outer spheres. The inner motor is connected and directly aligned with the shaft. The torque measurements in the 3m sysetem are done using a torque sensor (Futek TFF-600) mounted between the shaft and the inner motor. The measurements are taken with sampling rate $f_s = 10\ Hz$ and boxcar averaged over a time between 150 and 400 seconds. An offset torque due to the lip seals at the top of the experiment is subtracted for the each of the experiments.

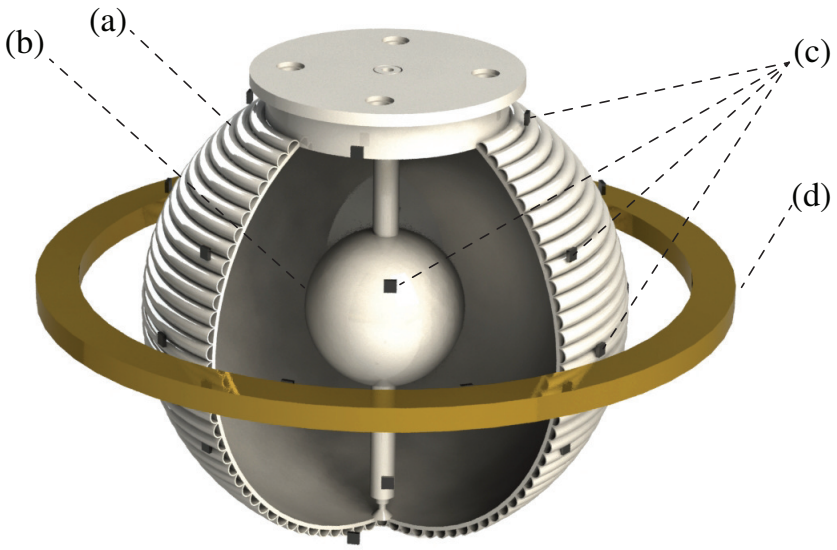

Figure 7.1: Schematic of the three-meter experiment with smooth inner sphere and one magnetic coil: (a) Three-meter diameter outer sphere, (b) one-meter diameter smooth inner sphere, (c) array of 31 magnetic Hall probes, (d) external electromagnet. The volume between the spheres is filled with metallic sodium. A torque sensor measures the applied torque to the inner sphere.

7.2.3 Experimental measurements

The 3m experiment has a torque sensor located between the motor and the inner sphere shaft. The measurements are taken with sampling rate $f_s = 10Hz$ and boxcar averaged over a time between 150 and 400 seconds. An offset torque due to the lip seals at the top of the experiment is subtracted for the each of the experiments. Initial measurements are done with a stationary outer sphere and the inner sphere rotating $Ro = \infty$ or equivalently $Ro^{-1} = 0$. We present data from experiments using water as the working fluid and measurements with liquid sodium with the same smooth inner sphere configuration. In addition, we also present sodium measurements with an inner sphere after baffles have been installed (the so-called rough case). To differentiate the regimes of positive and negative rotational rates we call them "scoop" and "wedge" modes, Fig 7.2.

The maximum rotation rate that can be achieved for the inner sphere with baffles is lower due to the fact that the torque that was necessary to rotate the inner sphere can be as much as eight times larger for the same rotation rates compared with the smooth inner sphere, so at the highest Re numbers we reached the torque limit of our current motor.

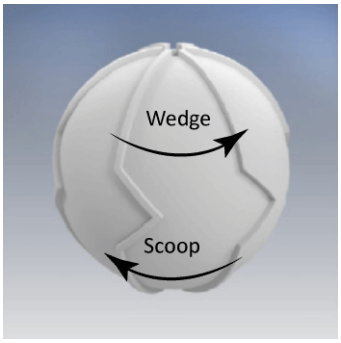

Figure 7.2: Schematic diagram of the roughened inner sphere. Six baffles, equally spaced azimuthally, extend into the fluid 5% of the radius of the originally smooth inner sphere.

7.2.4 Methodology of the data analysis

We present torque measurements are made in units of dimensionless torque G that is evaluated according to Equation 7.1. The Reynolds number Re in Equation 2.1 is a function of the difference of the rotation rates of the spheres and parameters of the liquid and does not depend on the roughness of the surfaces. To evaluate the local exponents we take multiple experimental runs for each configuration, so as to reduce errors due to the slight difference in experimental conditions. For every experimental configuration (water, smooth sodium, scoop sodium, wedge sodium) we estimate using a forward different the local power law slope α:

$$\alpha = \frac{dlog(G_{i+k}/G_i)}{dlog(Re_{i+k}/Re_i)}, \tag{7.2}$$

for $k = 2 \ldots 6$, where i is the measurements index for each experimental data point ascending in Re. Those estimates are then box averaging over $\sim$ 20 logarithmically uniformly distributed boxes, the results are plotted on Figure 7.4.

7.3 Comparison of Taylor-Couette and spherical Couette flows

7.3.1 Local exponents

The dissipation scaling in Taylor-Couette flows has been examined by a number of authors. In Figure 7.3 we show the primary result from Lathrop et al. [1] where the torque G was measured for Reynolds numbers in the range $10^3 < Re < 1.2 \times 10^6$. For Taylor-Couette flow definition of G, we use the length of the inner cylinder for the length scale L_i. Figure 7.3b shows the local power law exponent α for those measurements. Clearly over this range or Reynolds numbers no single power law explains the observed dependence.

Instead, the observed torque is four to five magnitudes above the lower bound laminar scaling. As well the observed torque is more than one magnitude below the rigorous upper bound, defined in Eq. 7.3, as derived by in Constantin and Doering 1992 [219].

$$G \leq 0.00141 \left(\frac{L}{h}\right)^2 Re^2 \; ; \; G \geq (2\pi)^{-1} \left(\frac{L}{h}\right)^2 Re \; . \tag{7.3}$$

The lack of power law dependence is evident from the lack of constant α regions in the Figure 7.3b. There is a clear transition taking place at $Re_T = 1.3 \times 10^4$. Here the local exponent growth is different for $Re \leq Re_T$ and $Re \geq Re_T$. This change in the local

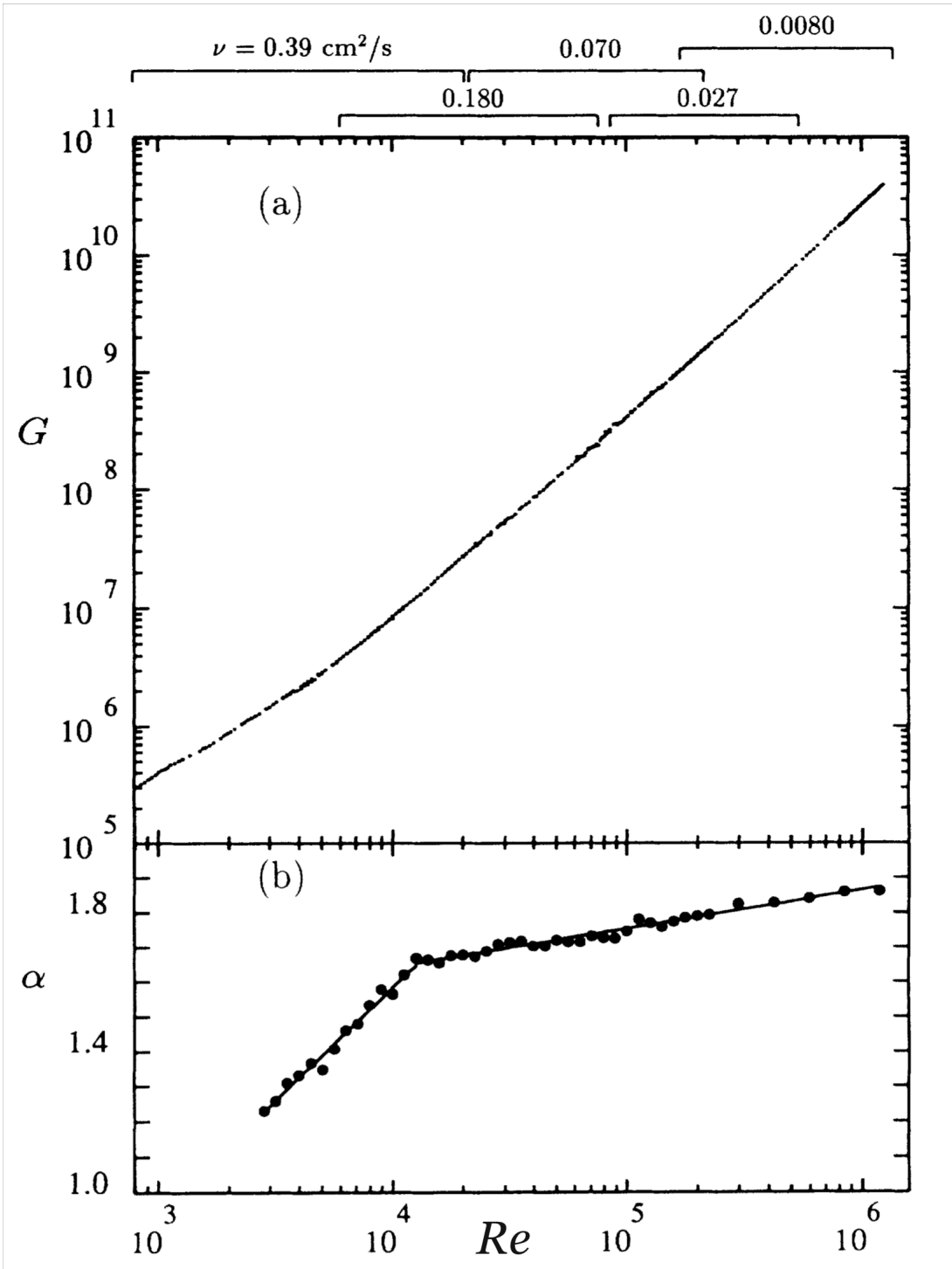

Figure 7.3: (a) The dimensionless torque as a function of the Reynolds Number for the Taylor-Couette experiment in [1]. (b) Corresponding local exponents α for the Taylor Couette data shown above as a function of the Reynolds number. Dashed lines indicate the upper and lower bounds for Taylor Coette flows defined in Equation 7.3.

scaling exponent is described in [83] as transition toward states dominated by shear driven (boundary layer dominated) turbulence.

We compare these results with spherical Couette Flows including the case of a of rough inner boundary in a similar way that was done in van den Berg et. al. [2] for rough boundary Taylor-Couette flows. In Figure 7.4 we can see analogous torque plots to Figure 7.3 but for spherical Couette flows in the 3M experiment for the 4 different combinations. The behaviour of the exponents have similarities with those observed in Lathrop et. al. [1], where there is a visible transition between lower and higher Re. Smooth sphere experiments in water and sodium are similar and have a transition near to $Re \sim 2 \times 10^7$ while the rough inner sphere setup has a transition with a lower $Re \sim 7 \times 10^6$, which is about three times lower than for the smooth case. These results is consistent with the work of Zhu et.al. [112] where they showed that wall roughness seem to converge asymptotically to a Kolmogorov-Constantin-Doering turbulence regime, though only reaching $\alpha = 1.8$ for the Reynolds numbers in van den Berg, et. al. [2]. For a rough inner sphere, then, the required Reynolds number to reach the shear dominated turbulence regime is smaller by a factor of six with respect to the smooth case. Surprisingly, the local exponent for the rough inner sphere Spherical Couette is not significantly higher than the smooth wall case, as was expected following the results in Taylor-Couette flows [2, 112]. We speculate that this may be due to the much wider gap (smaller radius ratio) and thereby less relative coupling of the inner sphere. This could be due to the factor of nine times smaller inner sphere area relative to the outer sphere, while for Taylor-Couette flows discussed here (for [83]) that ratio is 1.4. Hence, the presence of baffles might affect the transition to the shear-driven turbulence regime (after the change in the local exponent) but not the transition to the $\alpha = 1.8 \pm 0.02$

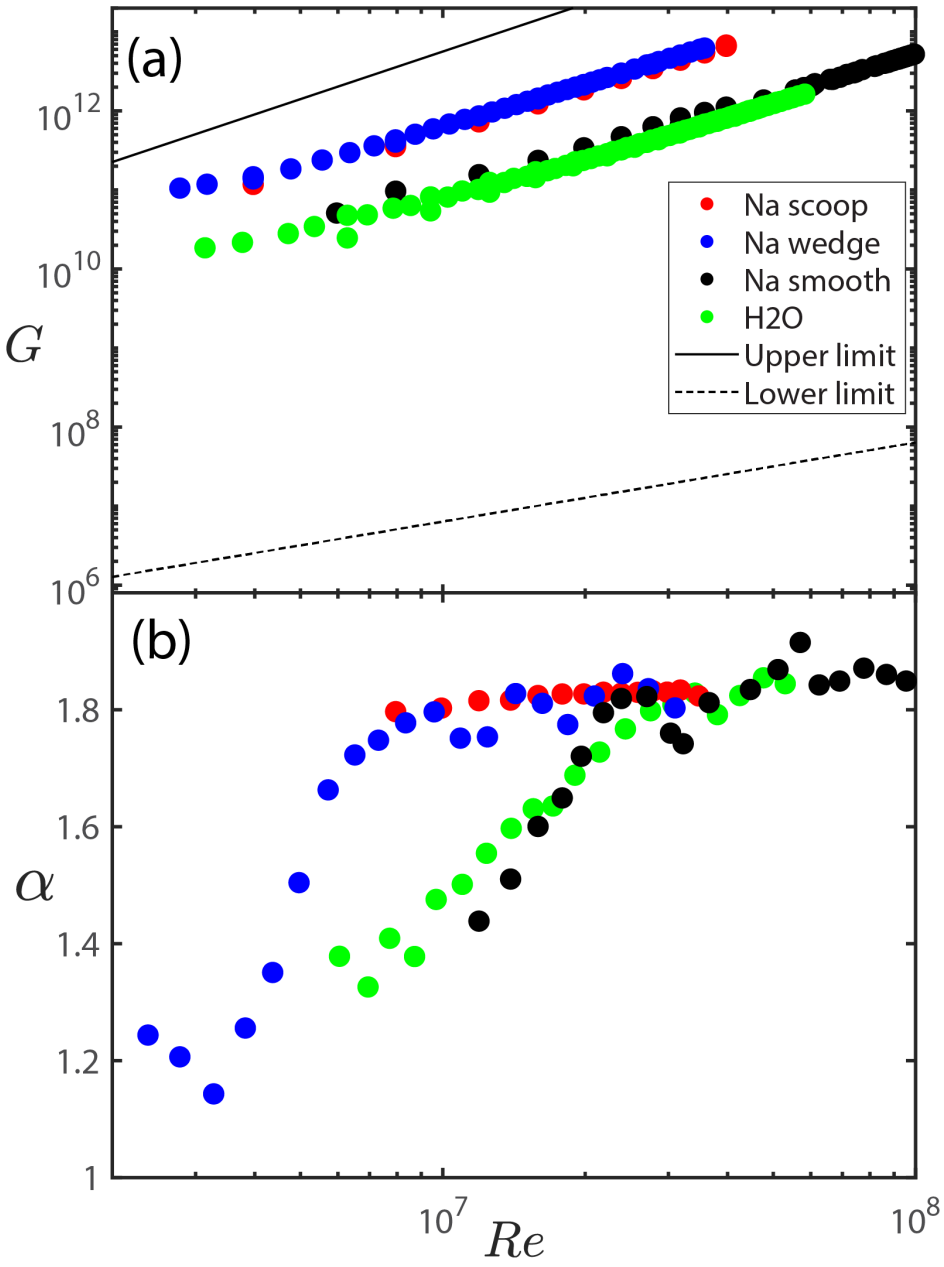

Figure 7.4: Spherical Couette dimensionless torque G in the 3m system as a function of the Reynolds Number Re with a stationary outer sphere for four different experimental configurations: smooth sphere: green - water, black - sodium; and with rough sphere: red - scoop, blue - wedge. To guide the eye, the solid and dashed lines correspond to the upper and lower bounds for Taylor-Couette flow defined in Eq. 7.3. While we do not expect the prefactors to be the same between Taylor-Couette and spherical Couette, the exponents $\alpha = 1$ and $\alpha - 2$ are expected to be the same. The lower part of this figure shows our estimates for the local exponents α for the four experimental setups shown above as a function of the Reynolds number, calculated according to the Section 7.2.4.

scaling regime that is experimentally observed for all cases.

7.3.2 Examining the Prandtl-von Karman description

The Prandtl-von Karman skin friction law relates the friction coefficient $f = G/Re^2$ with the Reynolds number Re and it has been extensively utilized in pipe flows, plane Couette flows, flows over a flat plate and Taylor-Couette flows. In particular in van den Berg, Doering, Lohse, and Lathrop 2003 [2] it was used to analyze Taylor-Couette torque data with different types of rough boundaries as shown in Figure 7.5. The Prandtl-von Karman law is [82, 83, 85]:

$$\frac{1}{\sqrt{f}} = c_1 log_{10}(Re\sqrt{f}) + c_2 \tag{7.4}$$

or equivalently in terms of the dimensionless torque G:

$$\frac{Re}{\sqrt{G}} = c_1 log_{10}(\sqrt{G}) + c_2 \tag{7.5}$$

which was fit to the data shown in Figure 7.5 by Lathrop et. al. [1] and van den Berg et. al. [2]. Both papers concluded that the Prandtl-von Karman skin friction law worked for all four cases of various rough and smooth walls. For the case of two smooth cylinders (ss) the data are well described by the skin friction law shown in solid line. In the case of both cylinders roughened by baffles (rr), $1/\sqrt{f}$ becomes nearly independent of Re for large enough Re. This is equivalent to an approach to the Kolmogorov-Constantin-Doering scaling of $\alpha = 2$. The cases rs and sr with one rough wall only are in between these extreme cases. Due to the persistent effects of one smooth wall and the corresponding boundary

layer, f still depends on Re for large Re, consistent to our observations above on spherical Couette flow with only one rough sphere.

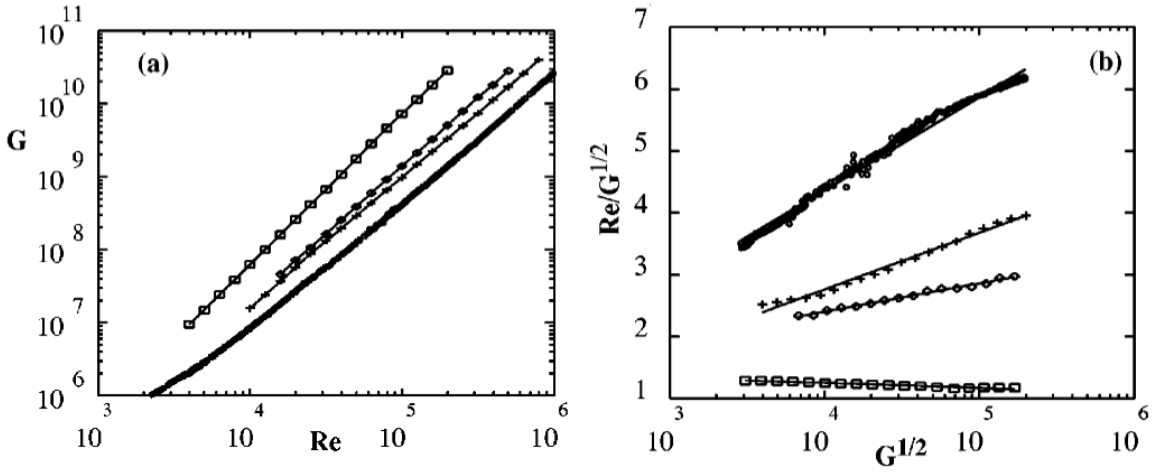

Figure 7.5: (a) The Taylor-Couette dimensionless torque as a function of the Reynolds Number for the Taylor-Couette experiment in [1]. (b) An examination of Prandtl-von Karman law for for the Taylor-Couette data. Note the vertical axis is equivalent to $1/\sqrt{(f)}$. Four cases are shown (o) ss, (+) sr, ($\diamond$) rs, and ($\square$) rr, bottom to top. Here ss refers to both cylinders smooth, sr just the outer cylinder rough, rs, just the inner cylinder rough, and rr both cylinders are roughened by baffles. From van den Berg, Doering, Lohse, and Lathrop 2003 [1, 2].

We perform a similar Prandtl-von Karman analysis for our 3m spherical Couette data as shown in Figure 7.6. The results are comparable to those obtained in Taylor Couette flows. The plot for sodium shows a higher skin friction coefficient (lower $Re/\sqrt{G}$) compared with water. The cause for this is uncertain, but may be due to some weak magneto-hydrodynamic effect in the sodium. The results for rough inner sphere show the highest skin friction coefficient of the 4 setups, with a small difference between wedge and scoop mode. The wedge modes shows a slightly higher skin friction coefficient than the scoop mode. However, there is a clear reduction on the skin friction coefficient for the rough inner boundary case in a similar way that it happens for Taylor Couette flows. The skin

friction coefficient in the 3m experiment rough inner boundary (wedge and scoop) is higher than its corresponding Taylor Couette slope for the case RS ('$\diamond$') in Figure 7.5, which is the equivalent for our 3m experiment setup (rough inner sphere and smooth outer sphere). The reduction in the skin friction in the 3m experiment by adding baffles is approximately 4 times relative to the smooth sphere case, whereas, for the Taylor Couette flows, the reduction of the skin friction by adding roughness to the inner cylinder is about 2 times with respect to the smooth inner cylinder case. Thus, at these radius ratios, roughness in spherical Couette flows is more effective at increasing the skin friction coefficient than for Taylor Couette flows. Additional future work could examine the radius ratio effects in these two systems. We summarize the results of the Prandtl-von Karman analysis experimentally measured coefficients in Table 1.

7.3.3 Rossby Number dependence of the Torque

The torque depends strongly on the presence of differential rotation, as shown by the Rossby number dependence shown in Figure 7.7. There, we normalize the torque G as G/G_∞ to remove most of the Re dependence. The presence of a sharp peak located at $Ro^{-1} = -0.25$ indicates that there is a particular differential rotation that maximizes the torque. This peak is well know for Taylor Couette flows and has been called the optimal transport regime [112, 218]. For spherical Couette flows it has also been documented [58, 191] but we refer at it as the maximum torque regime.

For the 3M spherical Couette experiment with rough walls, we show the Rossby number dependence of the torque in Figure 7.8. There we also show the 3M smooth case

Experiment	c_1	c_2
3M-Na Alpha Scoop 5% ($\Gamma = 0.35$)	3.5	-6.6
3M-Na Alpha Wedge 5%	4.0	-11.4
3M-Na Smooth	13.3	-40
3M-Water Smooth	11	-21
TC ($\Gamma = 0.73$) [1]	1.52	-1.63
TC ss ($\Gamma = 0.73$) [2]	1.51	-1.66
TC sr [2]	0.92	-0.917
TC rs [2]	0.457	0.575
TC rr [2]	-0.792	1.52

Table 7.1: Results from the analysis of the Prandtl-von Karman skin friction law as applied to Spherical Couette (the 3M experiment) and Taylor Couette flows. The data shown here for the Taylor Couette experiments is from Lathrop et. al. [1] and van den Berg at. al. [2]. "Na" stands for sodium experiments. All the Taylor Coeutte experiments use water or water-glycerin mixtures.

for comparison as was done for the water experiments in Rojas et al. [191]. Additionally, we document the location and amplitude of the maximum torque peak in Table 7.2. Note the large increase in the torque G/G_∞ values for the rough inner sphere cases, but only for negative Rossby numbers. The location of the torque peak for the rough inner sphere have moved to more negative inverse Rossby numbers as expected from the 40-cm spherical Couette water experiments discussed Rojas, et al. 2021 [191]. With rough inner sphere, the location of the peak has moved now to Rossby number values closer to the ones observe in

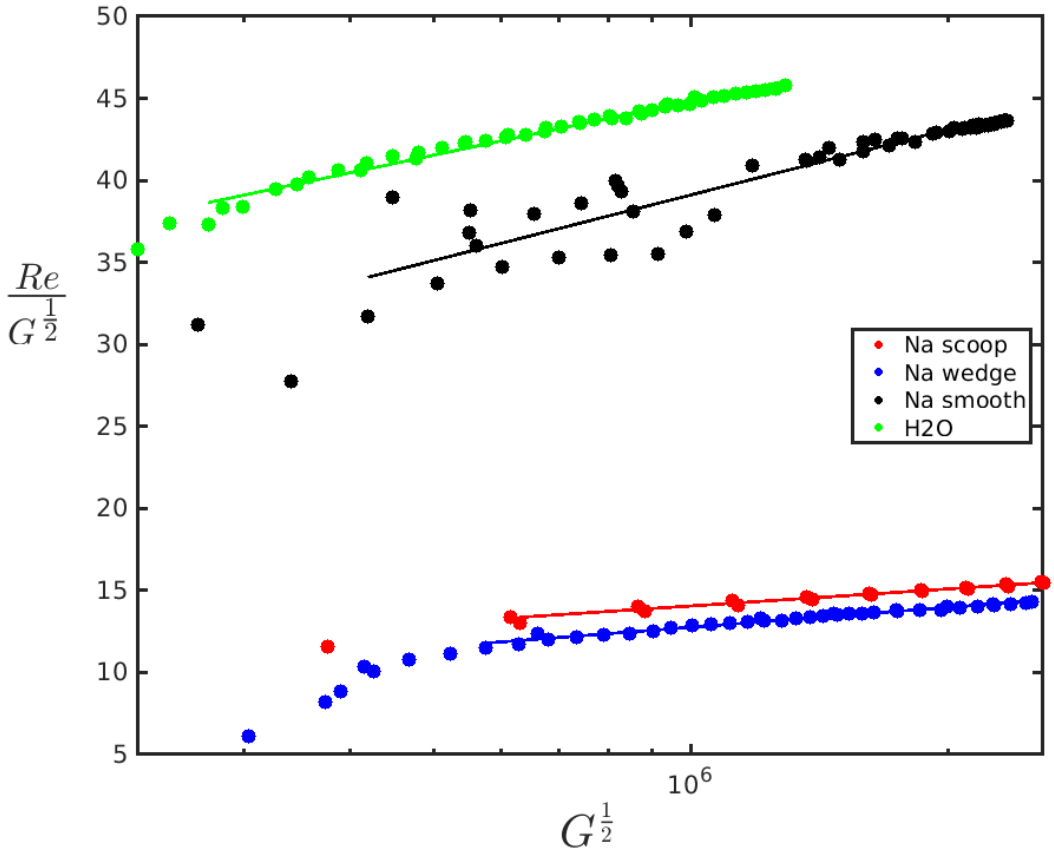

Figure 7.6: Prandtl-von Karman law analysis for 3M spherical Couette data for the four different experimental setups, with smooth sphere: green - water, black - sodium; and with rough sphere: red - scoop, blue - wedge. The points are the experimental data and the lines are linear regressions to each data set. The resulting linear regression coefficients are presented in Table 7.1

the Taylor Couette flows peak. [9, 218]. This is consistent with increasing the influence of the inner sphere on the dynamics of the system. That suggests that turbulent states that required a certain rotation rate of a smooth inner sphere, now require a lower rotation rate of the rough inner sphere, shifting everything to higher Ro^{-1}.

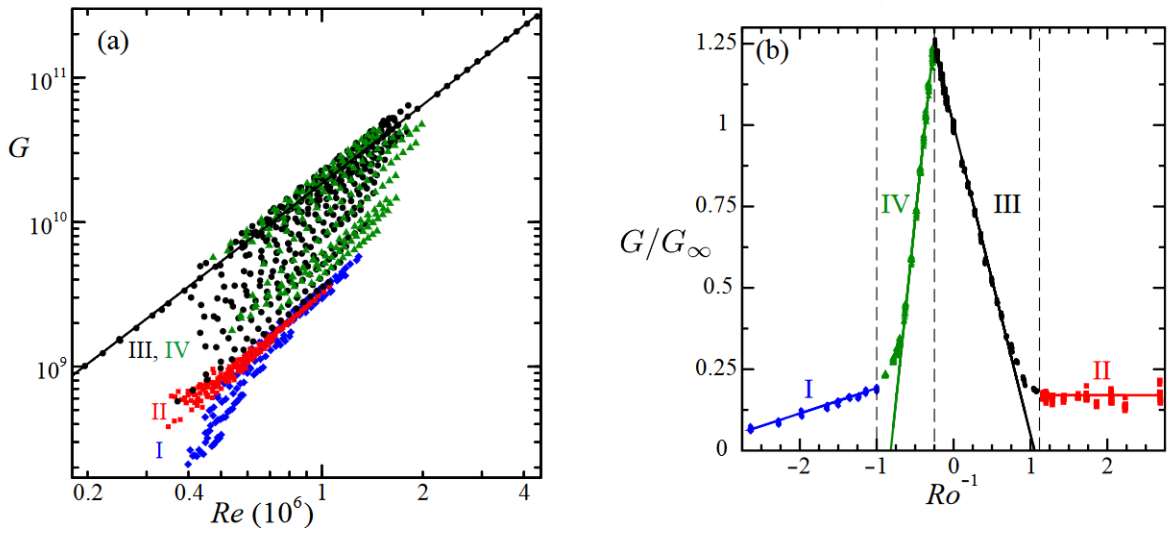

Figure 7.7: Experimental measurements of the dimensionless torque G as a function of (a) Re and (b) Ro^{-1} for the Taylor Couette experiment from Paoletti et al. [9] Region I (blue diamonds) is defined as $-1 \leq Ro^{-1} < 0$. Region II (red squares) has $0 < Ro^{-1} < \eta^{-2} - 1$, where $Ro^{-1} = \eta^{-2} - 1$ defines the Rayleigh stability criterion. Region III (black circles) is for $Ro^{-1} < -4$ and $\eta^{-2} - 1 < Ro^{-1}$. Finally, region IV (green triangles) has $-4 < Ro^{-1} < -1$. The solid line in (a) represents the fit G_∞ for $Ro^{-1} = \infty$.

7.4 Conclusions

The scaling of turbulent dissipation as measured by the torque to drive the inner boundary in Taylor-Couette and spherical Couette flows shows many similarities. For smooth walled flows both systems show a gradual increase of the local scaling exponent α toward the $\alpha = 2$ Kolmogorov-Constantin-Doering scaling. That (logarithmically) slow approach to that scaling is well captured by the empirical Prandtl-von Karman skin friction law for these flows. It is possible the the fluid dynamics community has shown an over-reliance on power law scalings. One might speculate that this stems from the importance placed on the results from Kolmogorov 1941, both for dissipation scaling as well as power law scaling. While we would never underestimate the importance and impact of K41,

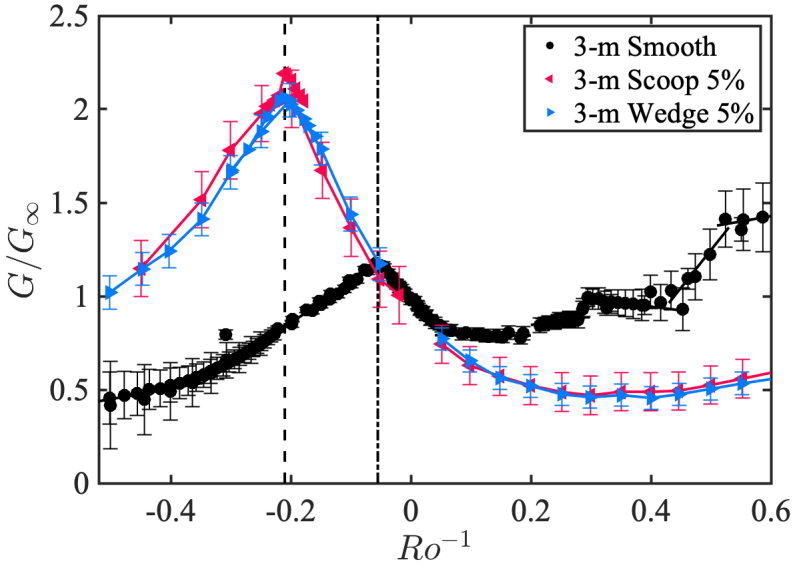

Figure 7.8: Rossby number dependence of the measured inner sphere torque for the 3m spherical Couette flow. The magnitude of the torque G is normalized by $G_\infty(Re)$ at a given Ro^{-1} and Re to remove most of the Re dependence. The vertical lines indicate the location of the peak for the local maximum relative dimensionless torque for smooth (dot dashed line) and rough (dashed line) inner sphere cases.

experimentalists should be sceptical of each new proposed power law.

We demonstrate the peak torque that occurs in Taylor-Couette flow at a negative Rossby number also occurs both in smooth walled turbulent Spherical Couette as well as the case with a rough (baffled) inner sphere. The Rossby number for these peak torques are an open theoretical puzzle. We speculate that that value either achieves a minimum fluid total angular momentum, or alternatively, a fluid averaged angular velocity.

Experiment	G/G_∞	Ro^{-1}
3M-Water Smooth ($\Gamma = 0.35$) [58]	1.20	-0.05
3M-Na Alpha Scoop 5%	2.19	-0.21
3M-Na Alpha Wedge 5%	2.06	-0.21
TC ($\Gamma = 0.72$) [9]	1.25	-0.25

Table 7.2: Location and amplitude of the local maxima in Torque -vs- Ro^{-1} in Figure 7.7 and Figure 7.8. "Na" stands for sodium experiments. All the TC experiments use water and water-glycerin mixtures.

Chapter 8: Conclusions and Recommendations

8.1 Conclusions

To understand the dynamics of magnetic fields of astronomical objects we should continue investigate these systems in numerical simulation and experimental approaches. At the University of Maryland, at the Geodynamo lab, we have this amazing experimental device that is designed as a model of Earth's core. This experiment has the same geometrical properties and symmetries as the core, and it doesn't have any internal sources of magnetic fields or ferromagnetic materials. In 2016-2022 we fixed and upgraded the experiment. That was done to increase the roughness of the inner sphere and increase the helicity of the fluid. The helicity is believed to be connected to "alpha" effect that would be necessary for creating a self sustainable magnetic field in this configuration.

We developed a protocol and designed and made/bought the hardware for the sodium removal procedure. This allows us to drain the Three Meter Experiment, allows to fix or redesign it if necessary.

We fabricated the water 40-cm model of the Three Meter system and investigated the velocity of the fluid in this spherical-Couette experiment. We analyzed differences in flows with different baffles designs. In this 40-cm project we investigated the torque and power dependence as a function of the Reynolds and Rossby numbers. The location of

the maximum torque regimes appeared to be different for spheres with different boundary conditions . This experiment helped us to choose the design of the baffles that were later installed on the inner sphere of the Three Meter experiment.

By the end of 2022, we finally have a reasonably organized database with the experimental data, and more importantly, we have a scalable system for storing, finding, and processing the desirable data. To control the experiment we have a code written with modern technological standards solutions. The software should be operational for an extensive period of time. At the same time, these codes and protocols are stored in the labs' GitHub repositories, which have manuals and comments. *Akin's Law 37. (Henshaw's Law) One key to success in a mission is establishing clear lines of blame.* So when something is not acting the way it supposes to, you can always track back the reasoning behind the actions and, hopefully, find someone who can help you.

We drained and took apart the Three Meter experiment. We cleaned the hardware and replaced the non-functional gear. We upgraded the inner sphere with the alpha baffles, assembled the apparatus, and filled it up with sodium. We reinstalled the systems that are necessary for the experimental runs, safety, and data acquisition.

We tested multiple techniques to predict the time evolution of the rotating MHD experiment and found that the hybrid of the reservoir computer and the auto-regressive model outperforms each of its components, and is capable of predicting the time evolution for five magnetic dipole timescales with higher accuracy than the average one-time step fluctuation. We applied these techniques to experiments with different fluid dynamical states and demonstrated that some of the states are more predictable than others.

We show that the hybrid model is also capable of predicting the long time climate of

the system, and even while it might be far from the real data in terms of the RMS error, it keeps converging on a trajectory in phase space that is very similar to what it has learned during the testing phase. We also discovered that for this system it is necessary to have more than ten dipole diffusion timescales of the spatially distributed training data to predict the dynamics; a comparable dataset is not currently available for the Earth's magnetic field. But at the same time we show that this relatively simple software architecture can be used for forecasting time evolution of a high dimensional nonlinear system.

We found, analyzed, and classified inertial and magneto-Coriolis modes. We confirmed the previous results in water and expanded the observations into the magnetized regimes for the Lenhert number up to $Le \leq 0.025$. Here we explored a variety of complex traveling structures. We saw evidence of triadic resonances and possibly other interactions between the modes. We set up new experiments with the upgraded sphere and discovered that previously strong modes are not present in the same phase space locations. The observed structures and their interactions are important for understanding the processes that happen in conductive rotating spheres like stars or planets, and potentially can give us more insight of the internal structures of these objects.

After upgrading the Three Meter we designed and set new experiments. Here we investigated the torque scaling of the system. We analyzed the exact scaling of the torque in the sphere and compared it with Taylor-Couette. The scaling of turbulent dissipation as measured by the torque to drive the inner boundary in Taylor-Couette and spherical Couette flows shows many similarities. For smooth walled flows both systems show a gradual increase of the local scaling exponent α toward the $\alpha = 2$ Kolmogorov-Constantin-Doering scaling. That (logarithmically) slow approach to that scaling is well captured by

the empirical Prandtl-von Karman skin friction law for these flows.

We analyzed the Rossby dependence of the torque in the system and found that the upgraded experiment has a different mapping of the states compared with the smooth era, for example, the maximum torque regime now requires 110% more torque than the same Reynolds runs with stable outer sphere, while with the smooth inner sphere we needed only 22% more. We demonstrate the peak torque that occurs in Taylor-Couette flow at a negative Rossby number also occurs both in smooth walled turbulent Spherical Couette as well as the case with a rough (baffled) inner sphere. The Rossby number for these peak torques are an open theoretical puzzle. We speculate that that value either achieves a minimum fluid total angular momentum, or alternatively, a fluid averaged angular velocity.

We found that in these maxima regimes our original assumption of the ability to separate Rossby and Reynolds dependence does not stand anymore.

We observed that the external magnetic field is capable of significantly affecting the torque in the system, but we still didn't gather enough data to find a pattern and be able to predict the torque.

We confirmed that bistability is still in the same Rossby range as in smooth experiments and it shows similar behavior in this Rossby range.

We observed the "dynamito" - a ten gauss g_3^0 field that appears in the high torque regime. But we observed it only in the energy balance. And we still couldn't see a self-generated magnetic field. We speculate that it can be related to the fact that we cannot reach the necessary magnetic Reynolds numbers because we hit the torque limit of our motors now with significantly lower Rm. In this regime, we are capable to use only ~ 60 hp instead of the motors maxima at 350 hp due to the lower rotation rates. This is the first

evidence of creating a self sustainable magnetic field in a spherical-Couette experiment without using ferromagnetic materials.

8.2 Recommendations

"Difficult to see; always in motion is the future." —Yoda, The Empire Strikes Back

The experiments should continue! To do so we need to fix the oil pump and, if necessary, replace the inner shaft lip seals.

The air inside the "skirt" of the lid should be removed for a better thermal isolation.

For getting higher quality data we should upgrade to the new data acquisition system.

The "BigMo" applications interface should be improved. Also alerts for the accelerating outer sphere. The next generations of scientists should maintain the current software and hardware and update them when necessary.

In terms of the dynamics predicting software, it would be interesting to apply the same system to predict the climate based on a big training set: create a software model that would be able to predict the shape of some data trajectories in different regimes. And the current dynamics predictive system can be used to quantitatively classify different experimental states.

Another solution for torque scaling as a function of Rossby, Reynolds, and Lehnert numbers would be to use another neural network approach to fit the observed values on a parameter space.

The author considers this experiment and the data as an amazing source of information about the dynamics of magneto-Coriolis modes. These modes need to be

analyzed with a more careful approach. Specifically, we need to find them in the new experiment, try quadrupole external fields, and investigate Wedge vs Scoop modes.

The bistability states need to be investigated in more detail. We speculate that the Scoop and Wedge modes should demonstrate very different behaviors.

For further investigation in search of the self-generated magnetic field, we should increase the torque, hoping that the dynamo awakens. Maybe a gearbox or a bigger motor, or a belt system. This upgrade would be quite time-consuming and one should carefully plan it before diving into it.

For a better understanding of the hydrodynamics of the spherical-Couette experiments, we should implement the boundary roughness into the definitions of Rossby and maybe Reynolds numbers. It should be done in such a way that the same regimes like the maximum torque regimes would appear at the same value of the Rossby number.

Additionally, we should investigate torque scaling in the case of rotating the outer sphere and fixing the inner. As the exact opposite of what we do with G_∞ when we scale the dimensionless torque. This might be helpful for the mentioned earlier redefining Reynolds and Rossby numbers.

FIN

Appendix A: Spherical harmonics visualization tools

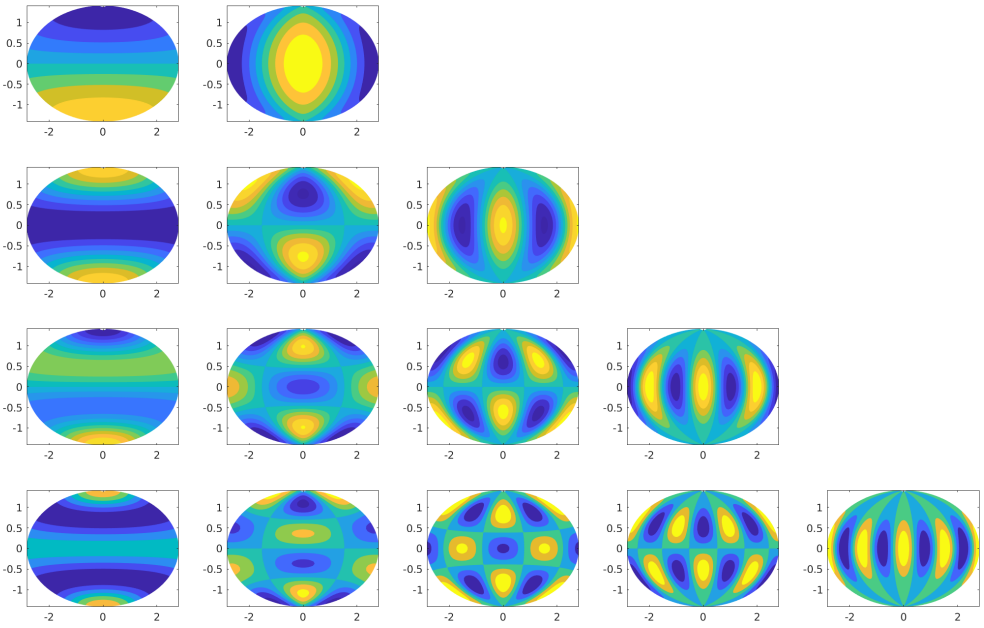

Figure A.1: Spherical harmonics visual representation up to $l = 4$.

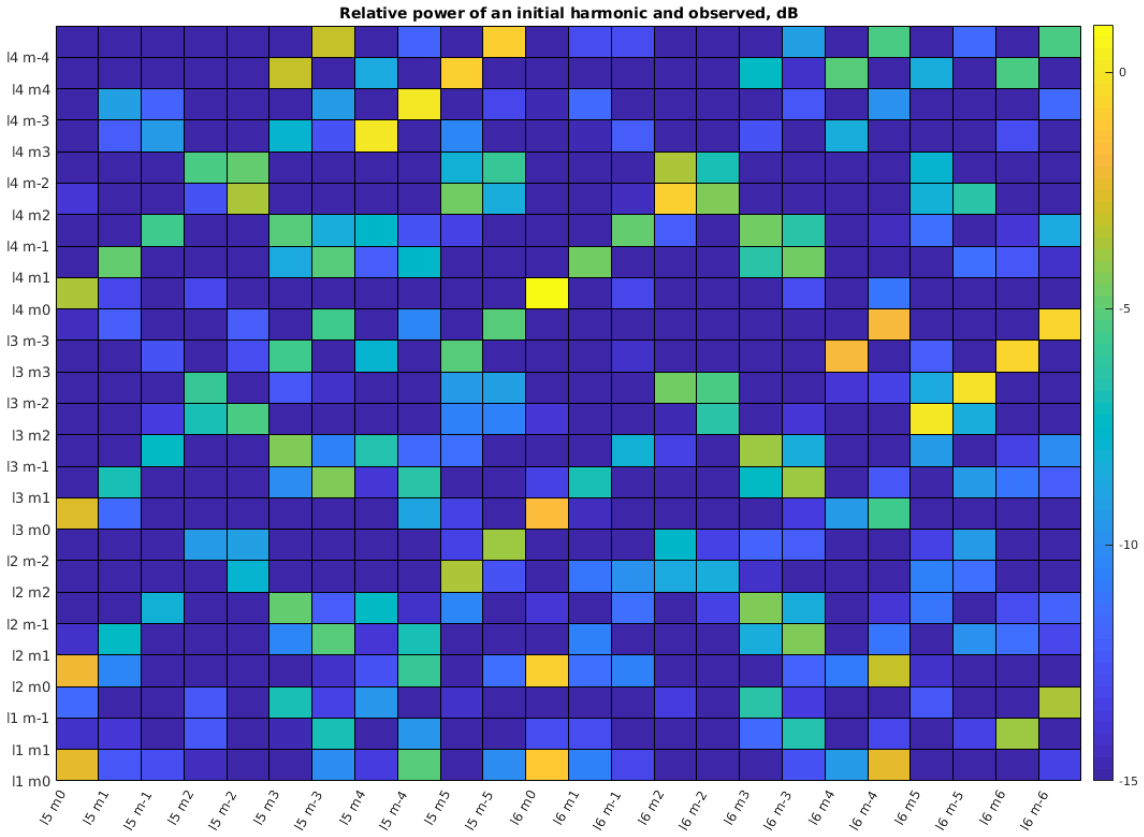

Figure A.2: Spherical harmonics leakage map. Shows where $l > 4$ modes will be visible on $l \leq 4$ set. Modes from the x-axis would be represented as a series of modes on the y-axis with the coefficients set by colors.

Appendix B: Sodium Removal SOP

3-m Sodium Transfer from Sphere to Tank SOP

Emergency Response Procedure

Incident: FIRE (NON-SODIUM)
- Follow FMDT (Failure Mode Decision Tree) section VI.

Incident: SODIUM FIRE
- Follow FMDT section I.1.b if small
- Follow FMDT section I.2.b if large

Incident: SODIUM LEAK (NO FIRE)
- Follow FMDT section I.1.a if small
- Follow FMDT section I.2.a if large

Incident: PRESSURE-RELATED INJURY
- Follow FMDT section V.5 for minor injury
- Follow FMDT section V.1-4 for major injury

Incident: BURN INJURY
- Follow FMDT section V.

Incident: BLEEDING INJURY
- Follow FMDT section V.

Incident: SECURITY BREACH
- Follow FMDT section VIII.

Incident: SEVERE WEATHER OR DISASTER
- Follow FMDT section IX.

University Police Department: 301-405-3333

TRANSFER PREPARATIONS: Describes the preparations to be done in the lab and in the experiment before day one of sodium transfer operation.

Potential Hazards

Fire: NO

Pressure: YES

- **Limit pressure settings to within the acceptable ranges for each item (all pressure rating information is displayed on the exterior of the devices)**

Oil Spray: NO

Temperature: NO

Nitrogen gas: YES

- **Wear oxygen sensors at all times whenever nitrogen (N2) is used, ensure monitors have been calibrated within the past year, perform fresh air check before use**

Tripping: YES

- **Wear closed-toe shoes, walk carefully**

Fall from height: YES

- **Do not lean over railings, keep both hands on railings when going up or down stairs**

Do not proceed if any of the following items are deficient (GO condition requirement)

If equipment is non-functioning, resolve with PI before proceeding

- ❑ **Full dry-run of SOP with ALL operators present**
- ❑ **Full review of FMDT (Failure Mode Decision Tree) with ALL operators present**
- ❑ **Full review of JHA (Job Hazards Analysis) with ALL operators present**

- ❑ **Clear out top of the cube.**
  - ❑ **Remove all electronics from the top of the cube and sphere.**
  - ❑ **Maintain only temperature measurement devices and battery chargers.**
- ❑ **Change three ports.**
  - ❑ **install the Sphere Transfer Port with the lip seal secured by the lip seal holder.**
  - ❑ **install visualization port.**

- ❑ **Install Sphere Gas Port**

❑ **Inert sphere/pressure testing.**
❑ **Remove inner motor.**
❑ **Remove the inner motor frame.**
❑ **Remove the outer motor.**
❑ **Remove the outer motor frame.**
❑ **Install flooring on top of the cube at the former inner motor frame/outer motor location.**
❑ **Visually inspect oil plumbing lines, ensure there are no leaks.**
❑ **Check the drain in the trench.**
- ❑ **Ensure water flows, no clogs.**
- ❑ **Check scrubber/blower connections.**
- ❑ **Turn on the blower from inside Shed.**
- ❑ **Check both power sources for the blower.**
  - ❑ **Change the power source outside while the blower is ON.**

❑ **Check vent connections**
- ❑ **Overhead vent configuration**

<u>Prepare the Tank Connections:</u>

❑ **Make sure the storage tank is still inert at 0.5 psi.**
❑ **Connect transfer line to storage tank.**
❑ **Close Valve E on Storage Tank.**
❑ ***Perform a leak check of the transfer line configuration*: Install Valve B2 flange set up (add photo) to end of transfer line (Valve C). Add 10 psi using Primary 3-m Gas System, opening valve H5 and B2. When done, close H5 and B2 and disconnect the blue hose (flex line between valve H5 and B2. See diagram 1-a). Check on day two of operations.**
❑ **Set the transfer line in position on top of the cube.**
❑ **Set transfer line monitoring system hardware:**
- ❑ **Locate Omega Thermocouple reader and bring to the top of the cube**
- ❑ **Locate Transfer Arduinos 1 and 2 and connect to tank pressure probes and transfer line temperature sensors.**
- ❑ **Power the Arduinos using the USB cables located on top of the cube that connect with the Sodium computer.**
- ❑ **At the Omega Thermocouple reader press the up and down arrow buttons together to start reading the probes.**

❑ **Locate and bring the Autotransformer to power and regulate the Transfer Line. Connect directly to the wall plug, not to the UPS.**
❑ **Locate Dip Tube and situate on top of the cube.**
❑ **Check that O2 monitors have been calibrated in the past year**
- ❑ **Perform fresh air check**
  - ❑ **All sensors must read between 20.7-21% outdoors**
- ❑ **Provide record of calibration to ESSR**

DAY ONE BEFORE RUN CHECKLIST: Describes the steps to be done during the day one, and before the beginning of the operations.

Potential Hazards

Fire: YES

- **Wear fire-resistant clothing (jumpsuit or pants/jacket, gloves), ensure fire extinguishers are easily available**

Pressure: YES

- **Limit pressure settings to within the acceptable ranges for each item (all pressure rating information is displayed on the exterior of the devices)**

Oil Spray: NO

Temperature: NO

Nitrogen gas: YES

- **Wear oxygen sensors at all times whenever nitrogen (N2) is used, ensure monitors have been calibrated within the past year, perform fresh air check before use**

Tripping: YES

- **Wear closed-toe shoes, walk carefully**

Fall from height: YES

- **Do not lean over railings, keep both hands on railings when going up or down stairs**

Do not proceed if ANY of the following items are deficient (GO condition requirement)

If equipment is non-functioning, resolve with PI before proceeding

- ❑ **Clear all steps in "Transfer preparations" section above**
- ❑ **Ensure Sodium Computer in Control room is connected to electrical outlet and has hardwired internet connection**
- ❑ **Locate PPE and fire resistant clothing**
  - ❑ **6 pairs fire resistant jumpsuits or pants with jacket**
  - ❑ **6 pairs fire resistant gloves**
  - ❑ **6 pairs safety glasses**
  - ❑ **4 helmets w/shield**

- ❑ **6 pairs closed-toe shoes**
- ❑ **2 oxygen monitors**

❑ **Locate and test walkie-talkies**

❑ **Locate and test laser height sensor**

- ❑ **Store at top of cube**

❑ **Prerequisite weather conditions: no ice/snow, or other severe weather conditions**

❑ **Perform pre-heater check**

- ❑ **Visually inspect for leaks**

❑ **Check water supply for scrubber in Ling room (0204D)**

- ❑ **Energize solenoid in Shed**
- ❑ **Ensure water flows**
- ❑ **Check vents are set for the overhead blower system.**
  - ❑ **If cold: drain outside lines with valve outside trapdoor**

❑ **Check liquid nitrogen supply and fire suppression system**

- ❑ **2 dewars required: One on the top of the cube and other near the tank in front of the motor drivers.**
  - ❑ **Minimum weight: 231 kg (100kg of liquid nitrogen plus 131 kg of the dewar)**
- ❑ **Connect power and hose to dewar liquid port and open dewar liquid valve**
- ❑ **Test fire suppression system by pressing red LN_2 button briefly (until liquid is visibly ejecting)**
  NOTE: this controls the ventilation/scrubber system

❑ **Check the LN2 gun (sodium fire extinguisher) next to storage tank is operational**

- ❑ **Press trigger until liquid is visibly ejecting**

❑ **Check UPS battery backup for solenoid valves**

❑ **Check oil system**

- ❑ **Ensure system is connected**
- ❑ **Ensure all valves are operable**

❑ **Check nitrogen gas supply**

- ❑ **6 bottles required**
- ❑ **Minimum pressure: 2200 psi for each bottle**
- ❑ **At the Transfer Gas Manifold (See Diagram 3):**
  - ❑ **Set the output pressure to 10 psi at pressure regulators (R1-R4) and open valves according to Diagram 3: Valves N1-N5 Open, Valves N6, N7 Closed.**
- ❑ **Check that the flexible metal hose is attached to the 3-m gas port (valve A2 closed, H2 open)**
- ❑ **Install check valve above G1 valve on the tank gas port**

<u>START PUMP/HEATER CHECKLIST</u>

Located in Control Room, on Sodium computer

Program Initialization Startup

❑ Start terminal (ctrl+alt+t)

❑ Navigate: `cd /data/bin/transfer_monitor`

- ❏ Start transfer monitor application: `python3 tramon.py`
- ❏ Open on the internet browser: http://sodium.umd.edu:2020/
- ❏ Confirm the bypass valve is open by checking the yellow LED is lit on the control box
- ❏ Ensure valves at pipe penetrations through wall are **open**
- ❏ Ensure that outside cooling units are valved **off**
- ❏ Start pump
- ❏ Press white “ON” button on control box
- ❏ Listen to ensure pump is on
- ❏ Visually inspect pumping system for leaks
- ❏ Turn off the pump

DAY ONE: Heating Operations

Potential Hazards

Fire: YES

- ❖ **Wear fire-resistant clothing (jumpsuit or pants/jacket, gloves), ensure fire extinguishers are easily available**

Pressure: YES

- ❖ **Limit pressure settings to within the acceptable ranges for each item (all pressure rating information is displayed on the exterior of the devices)**

Oil Spray: YES

- ❖ **When opening Valve A3: wear safety glasses, helmet with shield, fire resistant gloves, and fire resistant clothing**

Temperature: YES

- ❖ **Use caution near the storage tank and walls of the 3-meter cube**
- ❖ **Do not touch the surface of the storage tank of walls of the 3-meter cube**

Nitrogen gas: YES

- ❖ **Wear oxygen sensors at all times whenever nitrogen (N2) is used, ensure monitors have been calibrated within the past year, perform fresh air check before use**

Tripping: YES

- ❖ **Wear closed-toe shoes, walk carefully**

Fall from height: YES

- ❖ **Do not lean over railings, keep both hands on railings when going up or down stairs**

Number of Operators Required	Training Requirements
2	❑ **Sodium Safety Training** ❑ **UMD Campus Safety Training**

Before Beginning Run

- ❑ **Call campus police 301-405-3333: "beginning hot sodium operations in ERF Bldg #223"**
- ❑ Check the high bay for clear egress around the cube and high-bay.

Do not proceed until all three of the following items are cleared (GO condition Requirements):

- ❑ **Ensure two exit doors are operable with a clear path to each.**
- ❑ **Inspect for clutter, combustible materials and remove as needed.**
- ❑ **Check class D materials and portable fire extinguishers are present.**
- ❑ **Check LN2 sodium fire suppression system is present with full LN2 tank.**

Program Initialization Startup (Sodium Computer)

- ❑ Open to edit **notes.txt** file for daily operations notes
- ❑ On sodium desktop, open four command line terminals
- ❑ Terminal 1:
  - ❑ **cd /data/bin/transfer_monitor**
  - ❑ `python3 tramon.py &`
- ❑ Terminal 2:
  - ❑ **cd /data/bin/3mcontrol**
  - ❑ `python3 smoke5.py`
- ❑ Open web browser and go to the status page, and LOCAL camera page:
  - http://sodium.umd.edu:2020
  - http://sodium.umd.edu:2020/plot_recent
  - http://localhost/cam/
- ❑ Gather infrared cameras and chargers in Shed
  - ❑ Test cameras/chargers
  - ❑ Plug cameras in to charge
- ❑ Put on PPE and fire resistant clothing (ALL operators):
  - ❑ fire resistant jumpsuit OR fire resistant pants with jacket
  - ❑ fire resistant gloves
  - ❑ safety glasses
  - ❑ helmet w/shield

- ❏ closed toe shoes
- ❏ oxygen sensors

❏ Ensure that oil system is plumbed for appropriate operation - Heating ONLY Sphere:
- ❏ Valve O1 open
- ❏ Valve O2 open
- ❏ Valve O3 closed.
- ❏ Valve O4 closed.

❏ Start pump (press white “ON” button on control box)
- ❏ Listen to ensure pump is on
- ❏ Visually inspect pumping system (check inside the cube as well) for leaks
  - ❏ If leak is found:
    - ❏ Turn system off, fix leak, proceed ONLY after system is confirmed with no leaks

❏ Check thermometry
- ❏ Ensure all temperature readouts are within 1-2 degrees of one another

Heating

❏ At Sodium computer:
- ❏ In sodium.umd.edu:2020/heater press button “Connect the heater”
- ❏ In the input form type 100 and hit Enter (or press Submit)

❏ Monitor gas pressure with camera as sphere starts to heat
http://localhost/cam/
- ❏ Ensure gas pressure in sphere: <= 1psig
- ❏ When pressure starts to approach 1 psig (on order of 15 min. to one hour):
  - ❏ Close 3-m N_2 line at A3
  - ❏ Close valve H3.
  - ❏ Vent sphere pressure down to <0.5 psig using lever at manifold connected to A3.
  - ❏ Close valve A3.
  - ❏ Remove gas manifold from A3.
  - ❏ Attach oil bubbler to A3.
  - ❏ SLOWLY open valve A3.
    Caution: *oil can spray if opened too quickly*
  - ❏ Make sure nitrogen “gas handling” camera can see the bubbler

❏ Monitor bubbler to make sure it’s bubbling
- ❏ If bubbler camera has failed:
  - ❏ STOP heating
  - ❏ Repair/replace camera as necessary
  - ❏ Proceed ONLY when issue is cleared by PI
- ❏ If bubbler has stopped:
  - ❏ STOP heating
  - ❏ Check connections between bubbler and sphere
  - ❏ Check hot oil system functioning

        - ❏ Proceed ONLY when issue is cleared by PI
- ❏ Monitor **http://sodium.umd.edu:2020/**

End of Day

- ❏ Set heater power to 0.
    - ❏ Wait 2 minutes
- ❏ Turn heaters **off** at circuit breaker
- ❏ Turn pump **off.**
    - ❏ Make sure you can hear the pump turning off.
        - ❏ If you cannot hear the pump, go and visually inspect the pump outside.
- ❏ Close Valve A3.
- ❏ Remove bubbler.
- ❏ Flow gas through the gas line for 30 seconds
    - ❏ Open Valve H3.
    - ❏ Set nitrogen gas regulator to 0.5 psig
    - ❏ Attach to sphere port Valve A3.
    - ❏ Open Valve A3.
- ❏ Adjust nitrogen “Gas Handling Cam” to view gas gauge
- ❏ Verify outside that pump is **off** and that the heaters are off with IR camera
- ❏ Monitor **all** temperatures in system graph to ensure they are decreasing over time
- ❏ At http://sodium.umd.edu:2020/heater click “Disconnect”
- ❏ Keep smoke5.py open and running

- ❏ **Call campus police 301-405-3333: “ending hot sodium operations for the day in ERF bldg #223”.**

DAY TWO: Continuing Heating and Sodium Transfer

Potential Hazards

Fire: YES

- ❖ **Wear fire-resistant clothing (jumpsuit or pants/jacket, gloves), ensure fire extinguishers are easily available**

Pressure: YES

- ❖ **Limit pressure settings to within the acceptable ranges for each item (all pressure rating information is displayed on the exterior of the devices)**

Oil Spray: YES

- ❖ **When opening Valve A3: wear safety glasses, helmet with shield, fire resistant gloves, and fire resistant clothing**

Temperature: YES

- **Use caution near the storage tank and walls of the 3-meter cube**
- **Do not touch the surface of the storage tank of walls of the 3-meter cube**

Nitrogen gas: YES

- **Wear oxygen sensors at all times whenever nitrogen (N2) is used, ensure monitors have been calibrated within the past year, perform fresh air check before use**

Tripping: YES

- **Wear closed-toe shoes, walk carefully**

Fall from height: YES

- **Do not lean over railings, keep both hands on railings when going up or down stairs**

Number of Operators Required	Training Requirements
6 (including PI)	❑ Sodium Safety Training ❑ UMD Campus Safety Training

Do not proceed if any of the following items are deficient (GO condition requirement)

If equipment is non-functioning, resolve with PI before proceeding

Before Beginning Run

- ❑ **Call campus police 405-5333: "beginning day of hot sodium operations in ERF Bldg #223"**
- ❑ Check high bay for clutter and clear egress

Check the Tank Connections

- ❑ Make sure the storage tank is still inert at 0.5 psi.
- ❑ Check that the transfer line is still at 10 psi with valve E closed.
  - ❑ If transfer line is **NOT** at 10 psi:
    - ❑ Redo all transfer line connections
    - ❑ Perform another leak check
    - ❑ Make sure gaskets are in good condition.
    - ❑ Turn the bolts in on alternate order until ALL are firmly tight.
  - ❑ If transfer line is still at 10 psi.:
    - ❑ Slowly open Valve B2 to release pressure.

- ❑ Disconnect Valve B2 flange set up from the transfer line and install it on the dip tube. (Use new gasket)

BEFORE RUN CHECKLIST

- ❑ **Clear all steps in "Transfer preparations" section**
- ❑ **Locate PPE and fire resistant clothing:**
  - ❑ **6 pairs fire resistant jumpsuits or pants with jacket**
  - ❑ **6 pairs fire resistant gloves**
  - ❑ **6 pairs safety glasses**
  - ❑ **4 helmets w/shield**
  - ❑ **6 pairs closed-toe shoes**
  - ❑ **2 oxygen monitors**
- ❑ **Locate and test walkie-talkies**
- ❑ **Locate and test laser height sensor**
  - ❑ **Store at top of cube**
- ❑ **Prerequisite weather conditions: no ice/snow conditions outside**
- ❑ **Perform pre-heater check**
  - ❑ **Visually inspect for leaks**
- ❑ **Check water supply for scrubber in Ling room (0204D)**
  - ❑ **Energize solenoid in Shed**
  - ❑ **Ensure water flows**
  - ❑ **Check vents are set for the overhead blower system.**
    - ❑ **If cold: drain outside lines with valve outside trapdoor**
- ❑ **Check liquid nitrogen supply and fire suppression system**
  - ❑ **2 dewars required: One on the top of the cube and other near the tank in front of the motor drivers.**
  - ❑ **Minimum weight: 231 kg (100kg of liquid nitrogen plus 131 kg of the dewar)**
  - ❑ **Connect power and hose to dewar liquid port and open dewar valve**
  - ❑ **Test fire suppression system by pressing red LN_2 button briefly (10 seconds)**
    NOTE: this controls the ventilation/scrubber system
- ❑ **Check that LN2 gun (sodium fire extinguisher) is operational**
  - ❑ **Press trigger until liquid is visibly ejected**
- ❑ **Check battery backup for solenoid valves**
- ❑ **Check oil system**
  - ❑ **Ensure system is connected**
  - ❑ **Make sure all valves are operable**
- ❑ **Check nitrogen gas supply**
  - ❑ **6 bottles required**
  - ❑ **Minimum pressure: 2200 psi for each bottle**
  - ❑ **Install bottles and open valves according to Diagram 3: Valves N1-N5 Open. Valve N6 Closed.**
- ❑ **Check ventilation system**

- ❏ **Turn on blower from inside Shed**
- ❏ **Check both power sources for blower**
    - ❏ **Change power source outside while blower is ON**

<u>In Control Room, at Sodium computer:</u>

Program Initialization Startup

- ❏ Open to edit **notes.txt** file for daily operations notes
- ❏ On sodium desktop, open four command line terminals
- ❏ Terminal 1:
    - ❏ **cd /data/bin/transfer_monitor**
    - ❏ **`python3 tramon.py &`**
- ❏ Terminal 2:
    - ❏ **cd /data/bin/3mcontrol**
    - ❏ **`python3 smoke5.py`**
- ❏ Open web browser and go to the status page, and LOCAL camera page:

    http://sodium.umd.edu:2020
    http://sodium.umd.edu:2020/plot_recent
    http://localhost/cam/

Pump/heater starting

- ❏ Put on PPE and fire resistant clothing:
    - ❏ fire resistant jumpsuit OR fire resistant pants/jacket
    - ❏ fire resistant gloves
    - ❏ safety glasses
    - ❏ helmet w/shield
    - ❏ closed toe shoes
    - ❏ oxygen monitor
- ❏ Check thermometry
    - ❏ Ensure all temperature readouts are within 1-2 degrees of one another
- ❏ Gather infrared cameras and chargers in Shed
    - ❏ Test cameras/chargers
    - ❏ Plug cameras in to charge
- ❏ Ensure that oil system is plumbed for appropriate operation - Heating ONLY Sphere:
        - ❏ Valve O1 open
        - ❏ Valve O2 open
        - ❏ Valve O3 closed.
        - ❏ Valve O4 closed.
- ❏ Start pump (press white “ON” button on control box)
    - ❏ Listen to ensure pump is on
    - ❏ Visually inspect pumping system (check inside the cube as well) for leaks
        - ❏ If leak is found:
            - ❏ Turn system off, fix leak, proceed ONLY after system is confirmed with no leaks
- ❏ At Sodium computer:

- ❏ In sodium.umd.edu:2020/heater press button “Connect the heater”
- ❏ In the input form type 100 and hit Enter (or press Submit)

Heating

- ❏ Monitor **http://sodium.umd.edu:2020/**
  - ❏ Ensure gas pressure in sphere: <= 1psig
  - ❏ When pressure starts to approach 1 psig (on order of 15 min. to one hour):
    - ❏ Close 3-m N_2 line at A3: Close valve H3.
    - ❏ Vent sphere pressure down to <0.5 psig using lever at manifold connected to A3.
    - ❏ Close valve A3.
    - ❏ Remove gas manifold from A3.
    - ❏ Attach oil bubbler to A3.
    - ❏ SLOWLY open valve A3.

      Caution: *oil can spray if opened too quickly*
    - ❏ Make sure “gas handling” camera can see the bubbler
- ❏ Monitor bubbler to make sure it’s bubbling
  - ❏ If bubbler camera has failed:
    - ❏ STOP heating
    - ❏ Repair/replace camera as necessary
    - ❏ Proceed ONLY when issue is cleared by PI
  - ❏ If bubbler has stopped:
    - ❏ STOP heating
    - ❏ Check connections between bubbler and sphere
    - ❏ Check hot oil system functioning
    - ❏ Proceed ONLY when issue is cleared by PI
- ❏ Monitor **http://sodium.umd.edu:2020/**
- ❏ Monitor temperature and look for plateau at approximately 95°C when sodium is melting

  When shell bottom temperature measurement >115°C:
- ❏ *Close* bubbler valve A3
- ❏ *Remove bubbler*
  - ❏ *Store in downstairs cabinets*
- ❏ Monitor pressure to make sure it remains between 0-5 PSI
  - ❏ reduce pressure using valve A3 if > 5 PSI
- ❏ Heat approximately 10° more to 115°C

Tank Heating Procedure

- ❏ When temperature reaches 115°C start heating the tank by setting Oil Valves in the proper position.
  - ❏ Open Valves O4.(See diagram 5)
  - ❏ Slowly open Valve O3.
- ❏ Check Valves Status
  - ❏ Valve O1 open
  - ❏ Valve O2 open

- ❏ Valve O3 open
- ❏ Valve O4 open.

❏ Turn down heating to 50% at a few degrees below operating temperature (120°C)

❏ Continue to monitor the temperature on the sphere.

- ❏ Goal: maintain 120 +/- 5 C
  - ❏ If temperature shows a negative slope, make slight adjustments to heating settings in response.

Sodium Transfer Phase

Potential Hazards

Fire: YES

- ❖ **Wear fire-resistant clothing (jumpsuit or pants/jacket, gloves), ensure fire extinguishers are easily available**

Pressure: YES

- ❖ **Limit pressure settings to within the acceptable ranges for each item (all pressure rating information is displayed on the exterior of the devices)**

Oil Spray: YES

- ❖ **When opening Valve A3: wear safety glasses, helmet with shield, fire resistant gloves, and fire resistant clothing**

Temperature: YES

- ❖ **Use caution near the storage tank and walls of the 3-meter cube**
- ❖ **Do not touch the surface of the storage tank of walls of the 3-meter cube**

Nitrogen gas: YES

- ❖ **Wear oxygen sensors at all times whenever nitrogen (N2) is used, ensure monitors have been calibrated within the past year, perform fresh air check before use**

Tripping: YES

- ❖ **Wear closed-toe shoes, walk carefully**

Fall from height: YES

- ❖ **Do not lean over railings, keep both hands on railings when going up or down stairs**

Number of Operators Required	Training Requirements
7 (including PI)	❑ Sodium Safety Training ❑ UMD Campus Safety Training

Role(s)	Number of Operators	Physical Location
❖ 3-m dip-tube insertion ❖ Assist with dip-tube insertion (PI only) ❖ Monitoring sodium height on 3-m ➢ Thermal Camera ➢ Laser height sensor	2 (+ PI for dip-tube insertion)	On top of 3-m cube
❖ Continuous monitoring of Control Room computers	1	Remote (VPN to Control Room)
❖ Storage Tank transfer line monitoring, checking for leaks ❖ LN2 gun operation	2	Next to Storage Tank
❖ Monitoring gas handling manifold ❖ Making pressure adjustments as needed ❖ Assisting with ground-level operations as needed	1	❖ Between Storage Tank and Gas Handling Manifold ❖ At Storage Tank, as needed
❖ Tracking SOP steps ❖ Logging status of transfer ❖ Coordinating safety efforts as needed	1	Between Control Room and Storage Tank

Operation Requirements (ALL must be cleared for GO condition)

- ❏ Two operators on top of the cube with liquid nitrogen extinguisher
  - ❏ verbal confirmation from operators that they are responsible for reading temperature and pressure sensors on top of the cube
  - ❏ verbal confirmation from operators that they are responsible for dip tube insertion
- ❏ Two operators next to the storage tank with liquid nitrogen extinguisher
  - ❏ verbal confirmation from operators that they are responsible for checking the transfer line for leaks
  - ❏ verbal confirmation that LN2 gun is operational and ready
- ❏ One operator in the control room (remote)
  - ❏ verbal confirmation that they are responsible for monitoring temperature and cameras.
- ❏ One operator between the Storage Tank and control room
  - ❏ verbal confirmation that they are responsible for monitoring the SOP and coordinating the whole procedure.
- ❏ Ensure SOP and FMDT (Failure Mode Decision Tree) are in accessible locations for every member of the team.
- ❏ Make sure the storage tank is still pressurized at 0.5 psi.
- ❏ Locate laser height sensor and FLIR thermal camera and bring to the top of the cube.
- ❏ Locate the second thermal camera (phone attachment) to be used downstairs.

Transfer monitor on the cube

- ❏ Make sure the transfer monitor is running http://sodium.umd.edu:2020/
- ❏ Set a laptop connected to wifi on the top of the cube and open sodium.umd.edu:2020
- ❏ In case of errors reboot the app by pressing `Ctrl+C` twice in the terminal 1 and run `python3 tramon.py` again.

Dip tube preparation

- ❏ Cap dip tube with Gas Flange (Valve B2) removed from transfer line at the beginning of day two.
- ❏ Place the O-ring and O-ring holder in position after ValveB by sliding it upward from the bottom of the dip tube.

- ❏ Connect dip tube to N_2 gas line (Valve B2 to Primarily 3-m Gas System - Valve H5)
- ❏ Open Valve B2 and close Valve H5.
- ❏ Suspend the dip tube with the crane and pulley system above the port A connected to the Primary 3-m Gas System. (See diagram 1-a)

Dip tube insertion

- ❏ When temperature has reached approximately 120°C:
    - ❏ Set the pressure on the Primarily 3-m Gas System to **0.5 psi**.
    - ❏ Valve N2 out of the Sphere using A3 until it reaches **0.5 psi**.
    - ❏ Flow N_2 through the dip tube by opening valve H5 for 2 minutes.
    - ❏ Ensure valve status: (Diagram 1-A)
        - ❏ Valve B open
        - ❏ Valve B2 open
        - ❏ Valve H3 open
        - ❏ Valve H5 open
        - ❏ Valve H2 closed
        - ❏ Valve H4 closed
        - ❏ Valve A closed
        - ❏ Valve A3 open.
- ❏ Place the dip tube in position, right above Valve A.
- ❏ Reduce pressure on the Sphere to 0.5 psi by valving air out using A3
- ❏ Place the tip of the dip tube through the lip seal of the extraction flange until it hits the Valve A inner ball.
- ❏ Slowly open the Valve A on the extraction flange while holding the dip tube:
    - ❏ 1 operator manually stabilizing dip tube
    - ❏ 1 operator using overhead hoist to lower dip tube
- ❏ Insert the dip tube into the sodium (It should slide around the inner sphere thanks to its curvature and the inclination of the valve A)
    - ❏ Stop when the dip tube touches the bottom of the outer sphere
- ❏ Make sure the dip tube is inserted at the correct height and angle:
    - ❏ Check for reference angles and **markups on the dip tube and dip tube flange**
    - ❏ Adjust position of dip tube if necessary.
- ❏ Tighten o-ring on the flange above Valve A.
- ❏ Secure the dip tube in place using Dip Tube Spacers.

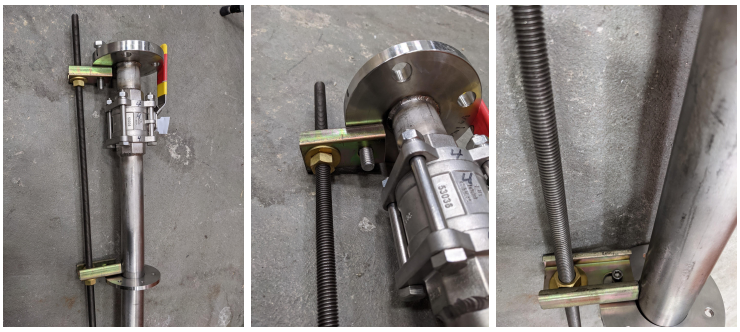

- ❏ Close Valve B

- ❏ Close Valve H5.
- ❏ Close Valve B2.
- ❏ Ensure valve status: (Diagram 1-a)
    - ❏ Valve A open.
    - ❏ Valve H2 closed.
    - ❏ Valve H4 closed.
    - ❏ Valve B closed.
    - ❏ Valve B2 closed.
    - ❏ Valve H3 open.
    - ❏ Valve A3 open.
- ❏ Lock out valve B closed.
- ❏ Remove Gas Flange from dip tube (Valve B2).
- ❏ Open Valve C 45 degrees.
- ❏ Connect the transfer line flange to the dip tube flange. Use a new graphite gasket. (see Diagram 1-b).
- ❏ Ensure pressure in the storage tank should be **0.5 ± 0.1 psi**.
    - ❏ Adjust using valve G1 on the Storage tank if necessary.
- ❏ Fully Open Valve C.
- ❏ Start heating the transfer line until temperature reaches **120C**.
    - ❏ Use the Autotransformer to lower voltage until temperature stabilizes.
- ❏ Ensure valve status:
    - ❏ Valve A open.
    - ❏ Valve C open.
    - ❏ Valve D open.
    - ❏ Valve E open.
    - ❏ Valve B closed.
    - ❏ Valve H2 closed.
    - ❏ Valve H4 closed.
    - ❏ Valve H3 open.
- ❏ Ensure temperature on sphere is **120C ± 5C**
- ❏ **On Transfer Gas Manifold:**
    - ❏ Open valve A2 on Transfer Gas Port (TGP) in the Sphere.
    - ❏ Open valve H2 on the Transfer Gas Manifold (TGM).
    - ❏ Close valve A3 on the Sphere.
    - ❏ Close valve H3 on Primary 3-m Gas System.
    - ❏ Monitor increase in pressure in sphere to **10 ± 0.1 psi.**
- ❏ Ensure Storage Tank pressure is **0.5 ± 0.1 psi.**
- ❏ Stop incoming gas to the Storage Tank:
    - ❏ Close Valve G2 on Tank Gas Port (TGP) (See Diagram 1-b).
- ❏ Open **Valve G1** on Tank Gas Port (TGP) to release the pressure to 0 psi.
- ❏ Locate and aim LN2 nozzle on top of the cube in the direction of the Valve B - Valve C connection.
- ❏ Ensure valve status:
    - ❏ Valve A open.

- ❑ Valve C open.
- ❑ Valve D open.
- ❑ Valve E open.
- ❑ Valve H2 open.
- ❑ Valve A2 open.
- ❑ Valve B closed.
- ❑ Valve H4 closed.
- ❑ Valve H3 closed.
- ❑ Valve A3 closed.
- ❑ Valve G1 open.
- ❑ Valve G2 closed.

BEGINNING SODIUM EXTRACTION

- ❑ **Open valve B**

NOTE: Sodium should start flowing into the tank. Use infrared thermometry and temperature sensors to see temperature raising on transfer line and Storage Tank.

- ❑ Monitor the pressure at P1
  - ❑ Acceptable range: 10 ± 1 psi
- ❑ Increase transfer gas pressure to avoid sphere pressure decreases.
  - ❑ In case of partial vacuum:
    - ❑ Prepare to partially close Valve B.

NOTE: During a nominal transfer, static pressure in the sphere should be 10 ± 1 psi throughout the transfer. The incoming gas flow rate should be about 2-3 L/s. The sodium level should decrease 0.5-2 inches per minute as measured by the laser height sensor depending on the level. Temperature should be less than 130 C.

- ❑ Keep monitoring pressure sensors during the extraction.
- ❑ Check the sodium level of the 3-m system using thermal camera and visualization port.
- ❑ Check the sodium level on the storage tank using the IR camera.
- ❑ Use the laser height sensor to measure and log the level of sodium in the sphere approximately every 10 minutes.
- ❑ Input the height into the transfer monitor input page http://sodium.umd.edu:2020/input

NOTE: Time for emptying is approximately 2 hours

Finishing procedure

- ❑ Check that sodium flow stops by different means:
  - ❑ hearing

- ❏ pressure decreasing on 3-m and flow rate increase
- ❏ temperature decreasing on transfer line

❏ When sodium flux stops:

- ❏ Lift the dip tube 10 cm.
  - ❏ Secure dip tube with the Dip Tube Spacer.
- ❏ Stop gas flow from the Transfer Gas Manifold:
  - ❏ Close A2.
  - ❏ Close H2.
- ❏ Set the pressure on the sphere to 1 psi on the Primary 3-m Gas System.
- ❏ Release pressure on the tank and sphere to 1 psi using release valves.
- ❏ Open valve H3 on Primary 3-m Gas System.
- ❏ Open valve A3.

❏ Close Valve C on the transfer line.
❏ Close Valve B on the dip tube.
❏ Turn off transfer line heaters
❏ Close Valve G1 on Tank Gas Port.
❏ Open Valve G2 on Tank Gas Port.
❏ Set pressure regulators to maintain 1 psi pressure in both the 3-m and storage tank during the cool down.
❏ Ensure valves status:

- ❏ Valve A open.
- ❏ Valve D open.
- ❏ Valve E open.
- ❏ Valve A3 open.
- ❏ Valve B closed.
- ❏ Valve C closed.
- ❏ Valve H2 closed.
- ❏ Valve H4 closed.
- ❏ Valve H3 open.
- ❏ Valve A2 closed.
- ❏ Valve G1 closed.
- ❏ Valve G2 open.

End of Run SOP

❏ In Control Room, on Sodium computer:

- ❏ Set 3-m heater power to 0 in http://sodium.umd.edu:2020/heater and press “Disconnect”

❏ Turn pump off

- ❏ Check pump is off.

❏ Remove main power from the heater control system.
❏ DO NOT LEAVE until all temperatures are decreasing everywhere.
❏ **Call campus police 301-405-3333: “end of hot sodium transfer operations.”**
❏ Prepare for cleaning the dip tube the next day after cooling down.

END OF SODIUM REMOVAL SOP

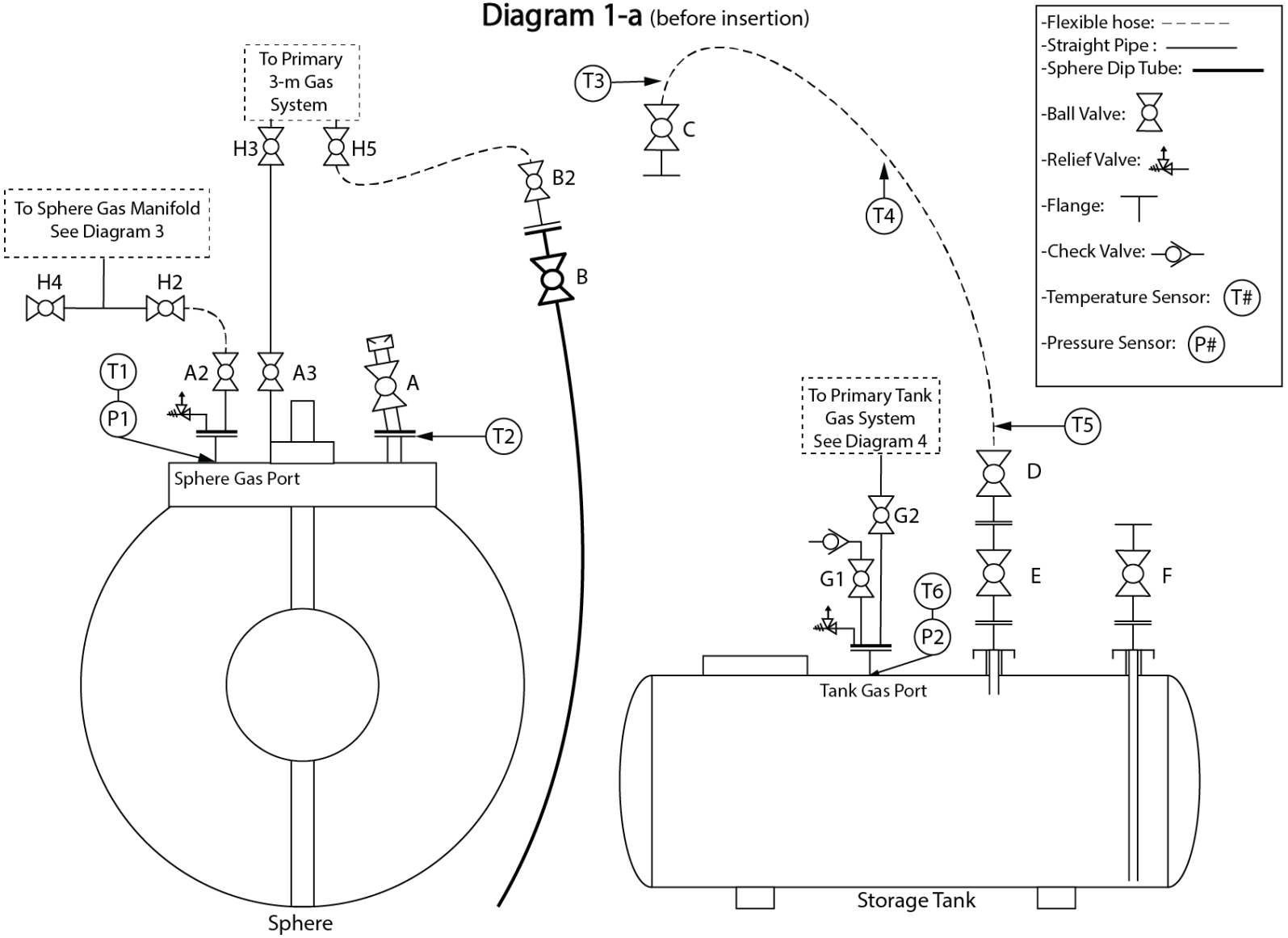
Diagram 1-a (before insertion)
-Flexible hose:
-Straight Pipe :
-Sphere Dip Tube:
-Ball Valve:
-Relief Valve:
-Flange:
-Check Valve:
-Temperature Sensor: T#
-Pressure Sensor: P#
To Primary 3-m Gas System
To Sphere Gas Manifold See Diagram 3
To Primary Tank Gas System See Diagram 4
H3
H5
H4
H2
B2
B
C
T3
T4
T5
T1
P1
A2
A3
A
T2
Sphere Gas Port
D
G2
G1
E
F
T6
P2
Tank Gas Port
Sphere
Storage Tank

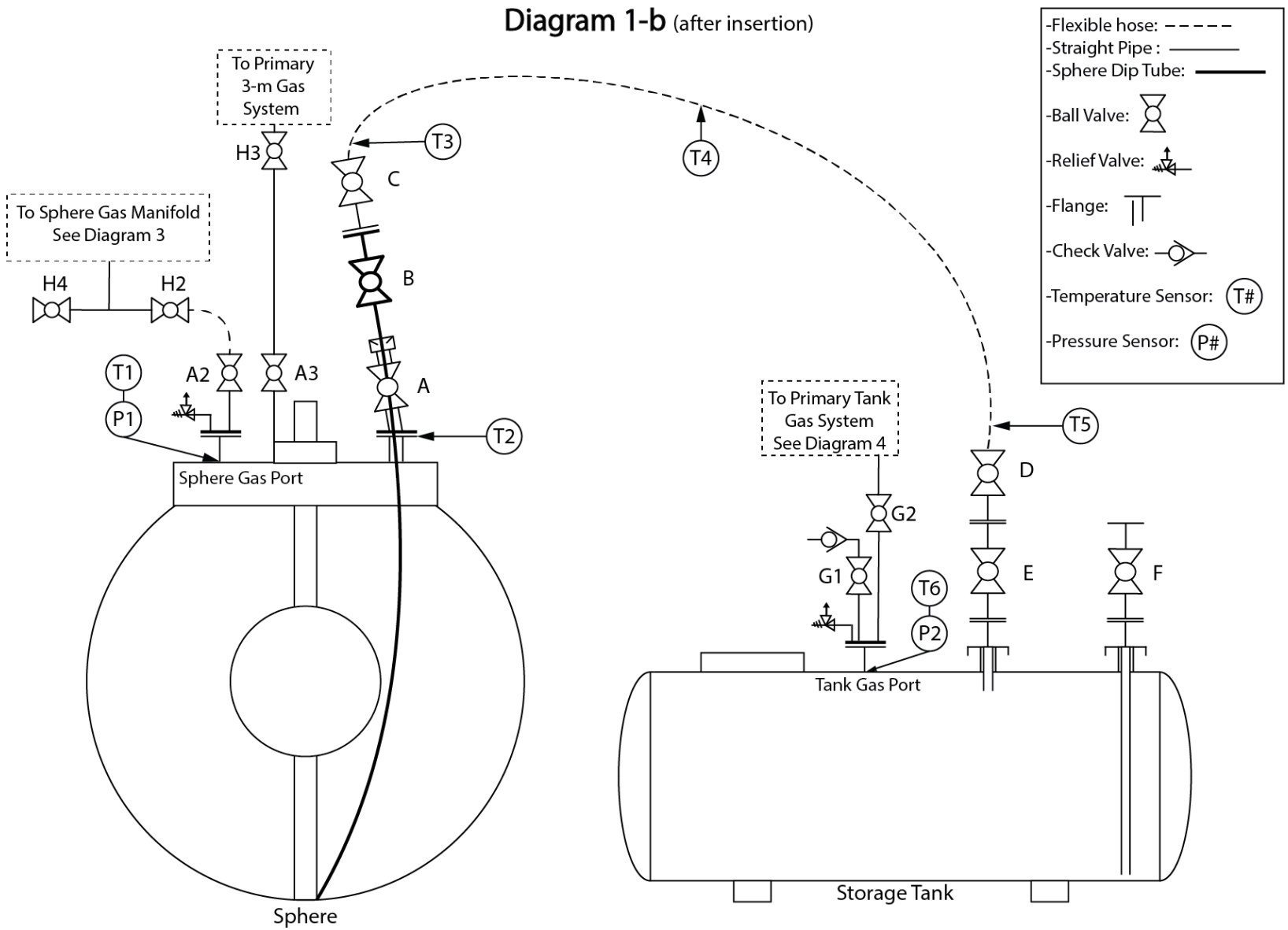
Diagram 1-b (after insertion)
-Flexible hose:
-Straight Pipe :
-Sphere Dip Tube:
-Ball Valve:
-Relief Valve:
-Flange:
-Check Valve:
-Temperature Sensor: T#
-Pressure Sensor: P#
To Primary 3-m Gas System
To Sphere Gas Manifold See Diagram 3
To Primary Tank Gas System See Diagram 4
H3
H4
H2
T1
P1
A2
A3
C
B
A
T2
T3
T4
T5
D
G2
G1
T6
P2
E
F
Sphere Gas Port
Tank Gas Port
Sphere
Storage Tank

Diagram 2 - Tank Arrangement

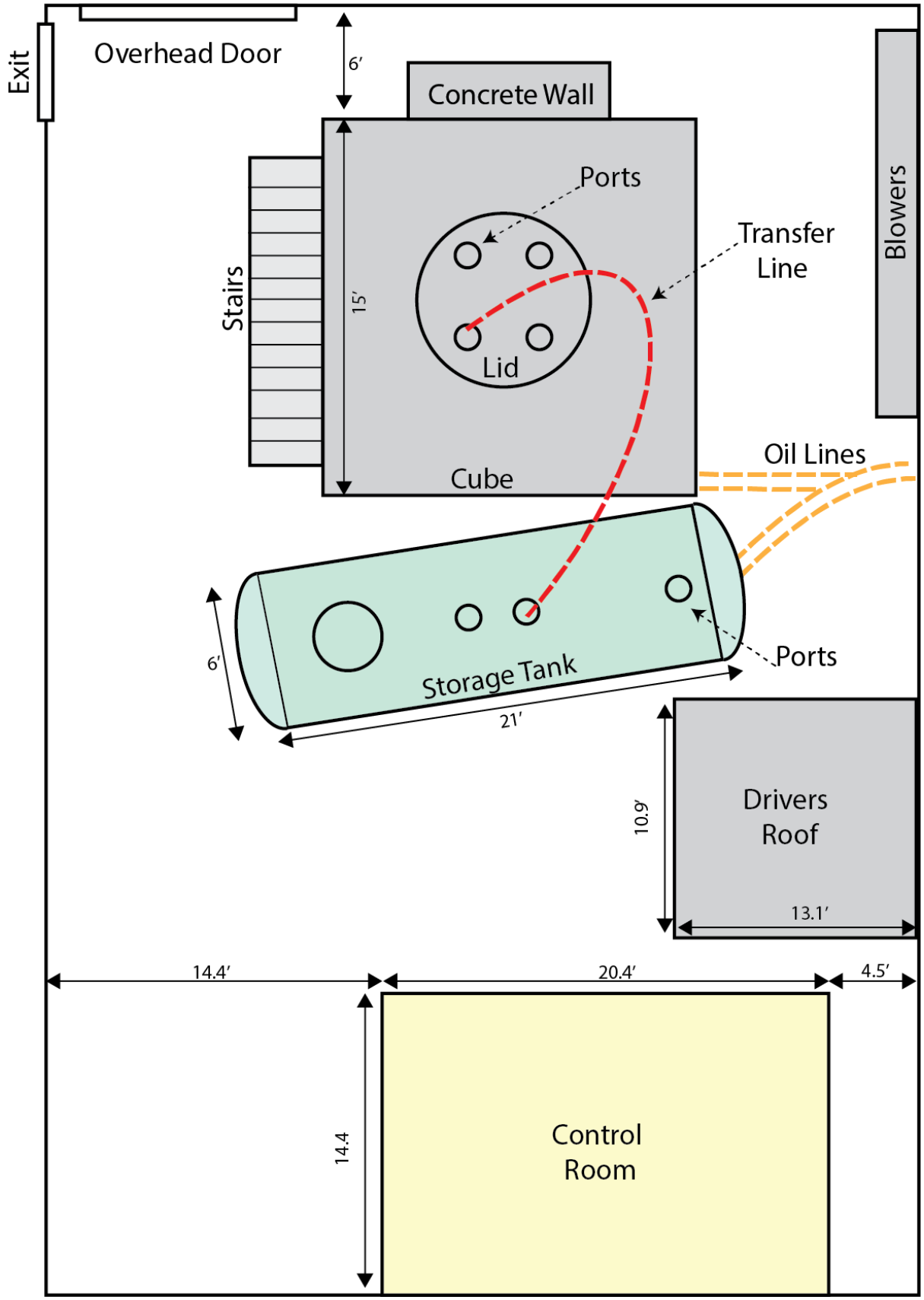

Diagram 3 - Transfer Gas Manifolds

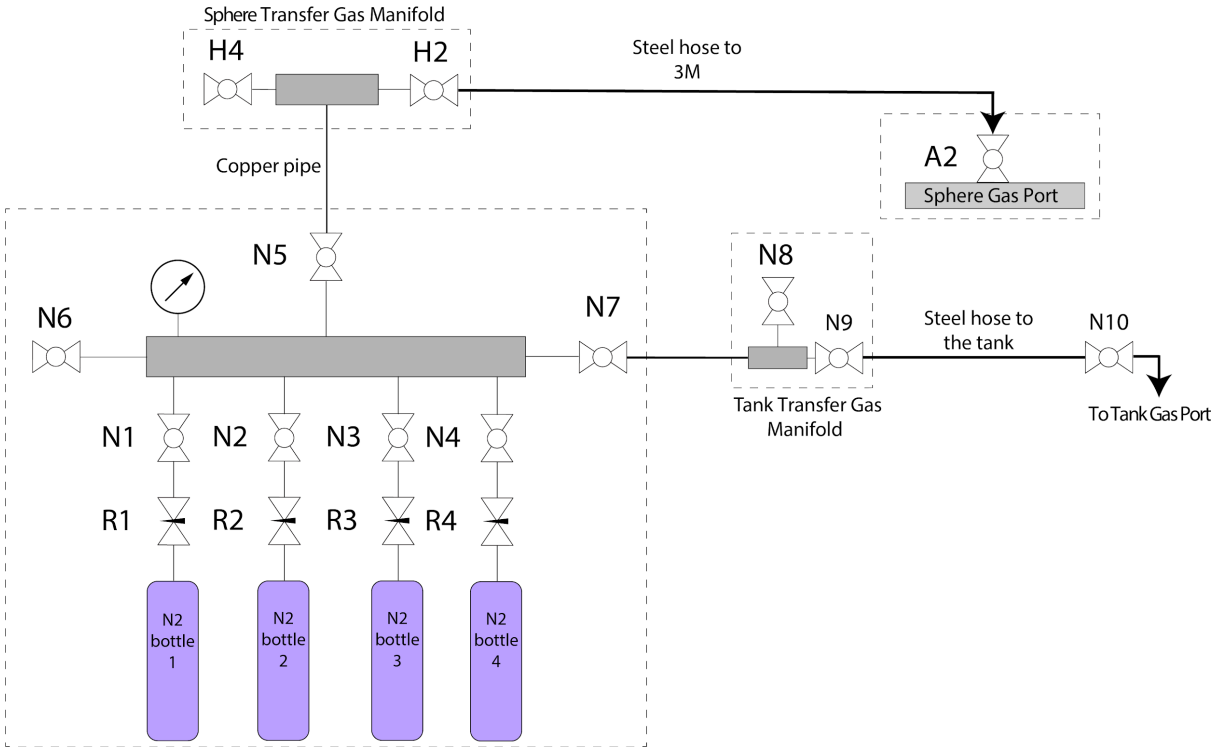

Diagram 4 - Primary Tank Gas System

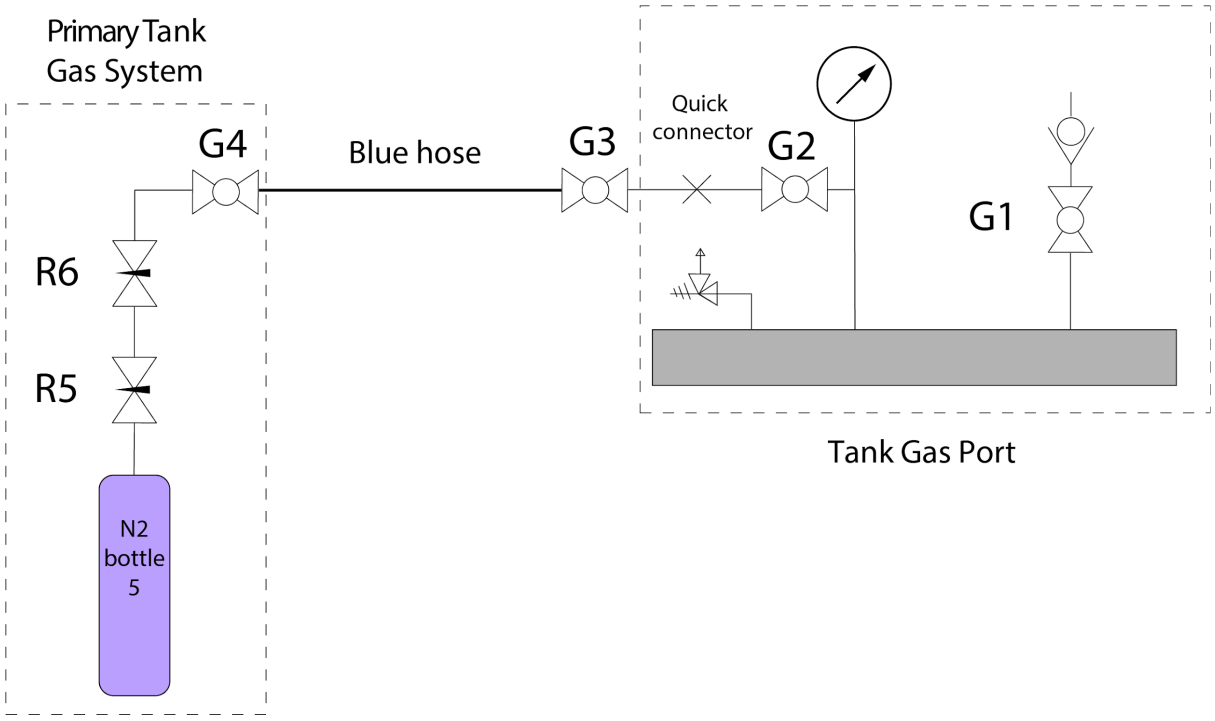

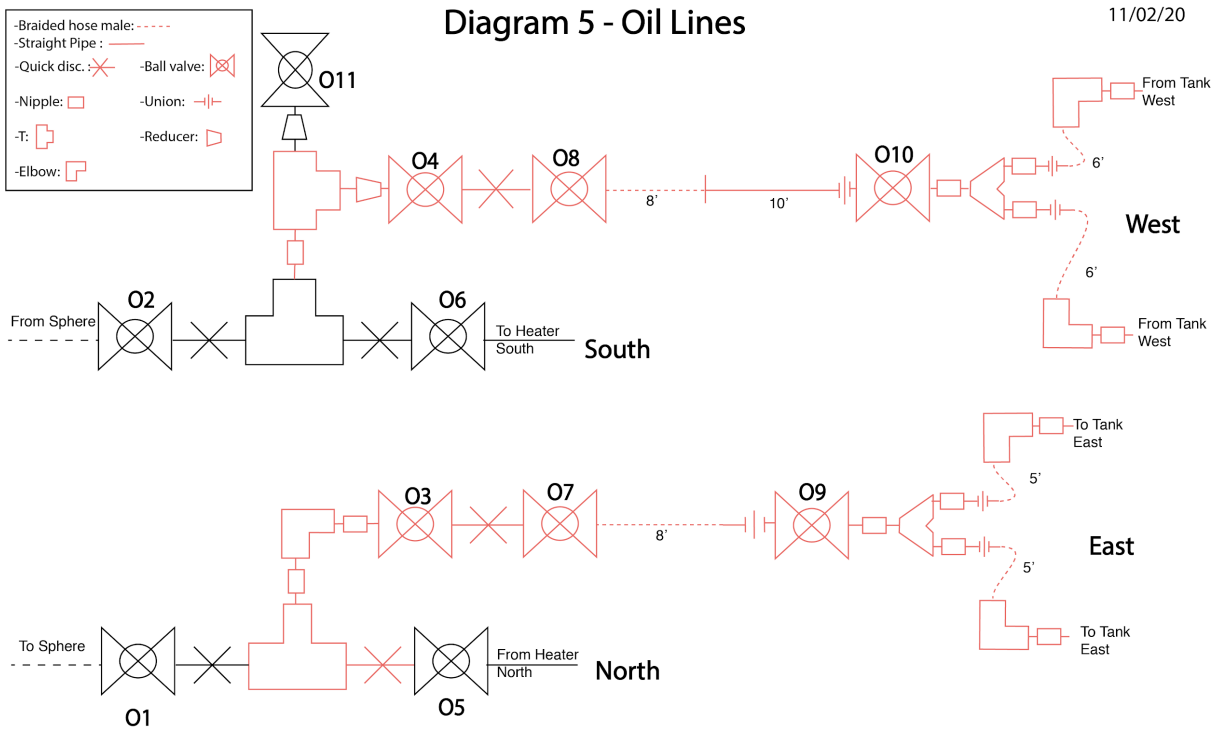
Diagram 5 - Oil Lines
11/02/20
-Braided hose male:
-Straight Pipe :
-Quick disc. :
-Ball valve:
-Nipple:
-Union:
-T:
-Reducer:
-Elbow:
O11
O4
O8
O10
8'
10'
6'
6'
From Tank West
From Tank West
West
O2
O6
From Sphere
To Heater South
South
O3
O7
O9
8'
5'
5'
To Tank East
To Tank East
East
To Sphere
From Heater North
North
O1
O5

Appendix C: Cleaning SOP

Cleaning Inner Sphere Combo SOP
(08/26/2019)

This is after **Lid Extraction SOP.** Assembly (Lid, shaft, sphere, joe) will be resting on the east side of the cube. Condom should be removed before setting to rest. See **Lid Extraction SOP.**

- ***Two person required with full protective equipment.***
- ***Make sure liquid nitrogen tank with gun is ready to use nearby. Test.***
- ***Sodium waste bucket prepared. Set nearby.***

Procedure:

- Remove lid and place between control room and tank on a stainless sheet (procedure detail required)
- Move shaft inner sphere and joe to horizontal on roller base. (procedure detail required)
- With steel tools extract the sodium oxide and metal where possible.
- If sodium metal is found, remove carefully with tools and deposit in waste bucket.
- Disassemble and remove Joe.
- Disassemble inner sphere from shaft.
- Check again for sodium oxide and metal in cavities in Joe.
- Check again for sodium oxide and metal in cavities in the inner sphere.
- Check again for sodium oxide and metal in cavities in the shaft.
- Once all big chunks of sodium and sodium oxide are removed clean the shaft and joe with wipes (towells?)
- Set inner sphere in rollers to be moved outside for water cleaning.
- Finish

Appendix D: Port Removal SOP

3M - Sphere Port Removal Protocol

Preparation:
- Sodium safety gear: garment clothes, gloves, face shield/goggles.
-Covid19 safety gear: face masks.
- Pusher bolts.
- 10'' threaded rod.
- Glove bag 34'' opening diameter.
- Sealing tape or gorilla tape.
- Razor (if modification to bag are necessary and/or to cut open ports)
- Tools needed for port installation: allen keys size (¼'' -20, 5/16'' - 18), 1/16'' wrench , wonder bar, claw hammer (other prying tools).
- Cleaned replacement Port with graphite gasket.
- Liquid nitrogen fire (LN_2) extinguisher
- Stainless steel tray for bolts.
- N2 gas line.
- Bolt box or tray to storage tools.

Procedure

1. Make sure working area is clear and that all sphere electronics are powered off (if present).
2. Loosen bolts connecting port to sphere, but do not remove.
3. Place tools, tray and port replacement sufficiently close to working area.
4. Place opening of the glove bag around/over working area and seal edges with tape (or special sealing provided by manufacturer), leave space for inserting the N2 gas line and for the LN2 gun.
5. Insert gas line and seal with tape against the lid.
6. Plce tip of LN2 gun aiming at the port and seal with tape against the lid.
7. Inflate bag with nitrogen gas and deflate (manual pressure) glove bag 3-4 times.
8. Leave bag inflated. Let rest until pressure stabilizes.
9. Check adhesion of bag to lid. Make sure it is firm after inflated. Introduce your arms and check.
10. Check N_2 gas cylinder pressure, must have greater than 750 psi to proceed.
11. Close gas line to the sphere and vent sphere out, until valve stops hissing.
12. Remove bolts.
13. On the port, locate vacant threaded holes labeled “PUSH OFF” and insert pusher bolts. Do not tight yet.
14. Check if port is loose by pulling upward in the pusher bolts by hand.
15. If the port is not loose, tighten pusher bolt by alternate tightening ½ turn on opposite bolts, until port appears dislodged and ready to be removed.
16. Remove port slowly and place into bin or tray.

17. Secure port over sphere opening, and secure in place with bolts finger tight. When tightening the bolts, do it on an alternating pattern. Finally, fully tighten the first bolt and then fully tighten the second bolt. Do not over tighten.
18. Resume gas flow to the sphere at ½ psi.
19. Stop the flow of gas into bag.
20. Remove glove bag.
21. Clean any residual sodium which may have contaminated the surface of the sphere (at and around working area)
22. Leave port in steel tray overnight in order to be cleaned the following day.

Appendix E: Heating SOP

Three Meter Heating SOP (Monday)

081222

Before Beginning Run

1) Two people required for hot sodium operation.
2) Make PI aware of the beginning of the hot operations.
3) Confirm N2 level and spares sufficient for cooling after run (>500 psi)
4) Check inside of cube for obstructions for spinning outer sphere and close cube door

Program Initialization Startup

On sodium desktop, open four terminals and **cd /data/bin/3mcontrol** *in all four terminals*
Terminal 1:

mkdir /data/3m/<todaysdate in mmddyy format> *(example: mkdir /data/3m/060413)*
chmod 777 /data/3m/<todaysdate>

Terminal 2:

python bigmo.py

open web browser and go to the status page, oil status page, and LOCAL camera page:
http://sodium.umd.edu:2021
localhost/cam
*important note: chrome and other browsers cannot open enough simultaneous connections to view the camera feeds and status pages from ***the same host*** so always use sodium.umd.edu for status pages and localhost or 192.168.1.1 for the cameras*

Pump/heater starting SOP

1) Cycle bypass valve on bigmo: 99/closed (confirm blue “Closed” light for bypass valve lit on control box) and back to 1/open. (confirm orange “Open” light for bypass valve lit on control box)
1) Ensure that valves at pipe penetrations through wall are open and outside cooling units are valved off.
2) Start pump (press white “ON” button on control box)
3) Listen to ensure pump is on and visually inspect pumping system for leaks.
4) Make sure Oil Heaters breakers are on.
5) Set heaters to 100% in main control program (set the number and click. Hitting ENTER key doesn’t work).
6) Install liquid nitrogen Dewar and test liquid nitrogen fire suppression system:
    1. Confirm >120 liters of LN2 using scale ((weight – Dewar Tare weight) / 0.8 kg/L)
    2. Connect power and hose to Dewar liquid port and open Dewar valve
    3. Test fire suppression system by pressing red LN2 button briefly (2-10 seconds)
7) Disconnect battery charger on top of the cube (You can also keep them connected).
8) Set up cooling for sphere frame computer and batteries.
9) Locate PPE (jacket, gloves, safety glasses, helmets w/shield).

Heating SOP

1) Monitor gas pressure with camera as sphere starts to heat. When pressure starts to rise measurably from heating (~30 minutes after heating begins):
    1. Close N2 line at gas tree.
    2. Vent sphere pressure down to <0.5 psi using manifold.
    3. Attach oil bubbler to second gas port.
    4. SLOWLY open bubbler (don't want oil to spray).
    5. Make sure “gas handling” camera can see the bubbler.
2) Monitor the bubbler to make sure it’s bubbling: **http://sodium.umd.edu:2021**

End of Run SOP

1) Set heater power to 0.
2) Turn pump off.
3) Check to make sure ports are clear with tee tool.
4) Set income pressure to 1 psi on the gas manifold.
5) Flow gas through gas line for 30s, attach to sphere port, and open valve.
6) Adjust gas camera to view gas gauge.
7) Make sure pressure is rising on the sphere.
8) Connect battery charger and ensure it's charging.
9) DO NOT LEAVE until you are sure **temperature is decreasing** everywhere and **pressure rising** on the sphere.
10) Make PI aware of the end of the hot operations.
11) Don’t close BigMo.
12) Monitor temperature from home if needed. Use campus VPN **http://sodium.umd.edu:2021**

Appendix F: Data Acquisition SOP

Three Meter Data Acquisition SOP

081222

Begin ~20 minutes before acquisition to allow sphere computer NTP to synchronize with sodium

Acquiring Torque Sensor Data (On Shed)

1) Open terminal on Sodium (directly or through ssh)
2) **cd /data/3m/<todaysdate>**
3) **/data/bin/3mcontrol/tqUSB >> torque.dat** to save torque data to torque.dat

Note: torque sensor program will not start acquiring data until torque sensor turned on

Turning On Sphere Frame Computer and Sensors (On Cube)

1) Turn on sphere frame router if not on (to check communication with sphere frame router, ping or connect to 192.168.1.30)
2) Boot sphere frame data acquisition computer.
3) Cool sphere computer with blower (unless not heating sodium)
4) Turn on all sensors:
    1. pressure sensor box.
    2. main Hall array switch.
    3. Confirm that red LED on Hall array board is on.
5) Install and connect torque sensor battery in box on inner shaft.
6) Turn switch next to battery to “Ext”. Red and green lights under red/black/green powerpole connector should turn on.
7) Turn on arduino box on other side of inner shaft. Red and green power lights should be on. Other two lights should be blinking.

Sphere Frame Computer (On Shed)

1) Connect to sphere frame computer (192.168.1.7) via RDP on Axl's computer
2) Start “SpeedFan” on sphere frame computer to view motherboard temperatures (in task bar notification area)
3) Make sure NTP time server is running and synchronized (in task bar)
4) Start acquisition for the first time (start MATLAB R2006b, load the saved data acquisition environment, set a sample rate, set a log file name, and run the “changefile” script to start logging). In MATLAB, type:
    load inout2020.mat
    fs = 256
    namestr = ‘<your daq filename here>’ like namestr = ‘magtest2.daq’
    changefile

At this point, all scientific measurements are logged to .daq file and binlog

Lab Frame Computer (On Shed)

1) Connect to lab frame computer (192.168.1.6) via RDP on Axl's computer
2) Open Matlab
3) type a sample rate **fs = 256**
4) type **startacc** (First time it gives an error, run it a second time)
5) Open **http://sodium.umd.edu/acc3m.php** to look at data.

At this point, we're acquiring encoders and accelerometers and have vibration shutdown

---

Changing or Pausing Sphere Computer Data Acquisition

To start a new acquisition file, choose a sample rate (if you want to keep it the same, don't type a new one, fs already stored), change namestr, and run "changefile" script

fs = 256
namestr = '<new daq filename here>'
changefile

To stop acquisition for a long pause, stop the daq object and the status timer object by typing:
stop(sta_timer); stop(daq);

End of Day – Sphere Computer

1) To stop sphere computer data acquisition at the end of the day, stop the daq object and the status timer object by typing:
   stop(sta_timer); stop(daq);
2) Close MATLAB
3) Shut down sphere computer using desktop shutdown link. Alternately, you can type **<Ctrl><Alt><End>** and press the "Shut Down…" button (also works for restart). **<Ctrl><Alt><End>** is a key combination that does the same thing as **<Ctrl><Alt><Del>** but will be SENT to the RDP computer. **<Ctrl><Alt><Del>** will always be interpreted by the LOCAL computer, not sent over the RDP connection.

End of Day – Lab Frame Computer

1) Type **stop(ai)** in MATLAB on lab frame
2) Close MATLAB
3) In TwoEnc_v1.1.exe DOS window on lab frame, hit **<Ctrl-C>** and close window
4) Close lab frame computer window

End of Day – Sensors

1) Stop torque sensor data acquisition by hitting **<Ctrl-C>** in terminal running it
2) Turn off arduino box on inner shaft.
3) Turn switch next to torque sensor battery to internal
4) Remove torque sensor battery

5) Turn off all sensors:
    1. pressure sensor box
    2. main Hall array by disconnecting power plug on wire breakout board
6) Turn off sphere frame router.
7) Connect battery charger and ensure it's charging.

End of Day – Back Up Data

PENDING

Bibliography

[1] Daniel P. Lathrop, Jay Fineberg, and Harry L. Swinney. Turbulent flow between concentric rotating cylinders at large Reynolds number. *Physical review letters*, 68(10):1515, 1992. Publisher: APS.

[2] Thomas H. van den Berg, Charles R. Doering, Detlef Lohse, and Daniel P. Lathrop. Smooth and rough boundaries in turbulent Taylor-Couette flow. *Physical Review E*, 68(3):036307, September 2003.

[3] Philip W. Livermore, Christopher C. Finlay, and Matthew Bayliff. Recent north magnetic pole acceleration towards Siberia caused by flux lobe elongation. *Nature Geoscience*, 13(5):387–391, May 2020.

[4] Daniel R. Sisan, Nicolás Mujica, W. Andrew Tillotson, Yi-Min Huang, William Dorland, Adil B. Hassam, Thomas M. Antonsen, and Daniel P. Lathrop. Experimental Observation and Characterization of the Magnetorotational Instability. *Physical Review Letters*, 93(11):114502, September 2004.

[5] Douglas H. Kelley, Santiago Andrés Triana, Daniel S. Zimmerman, Barbara Brawn, Daniel P. Lathrop, and Donald H. Martin. Driven inertial waves in spherical Couette flow. *Chaos: An Interdisciplinary Journal of Nonlinear Science*, 16(4):041105, December 2006. Publisher: American Institute of Physics.

[6] Santiago Andres Triana. INERTIAL WAVES IN A LABORATORY MODEL OF THE EARTH'S CORE. page 173.

[7] Santiago Andres Triana. *Inertial waves in a laboratory model of the Earth's core*. PhD Thesis, 2011.

[8] Daniel S. Zimmerman, Santiago Andrés Triana, and D. P. Lathrop. Bi-stability in turbulent, rotating spherical Couette flow. *Physics of Fluids*, 23(6):065104, June 2011. Publisher: American Institute of Physics.

[9] M. S. Paoletti and D. P. Lathrop. Angular Momentum Transport in Turbulent Flow between Independently Rotating Cylinders. *Physical Review Letters*, 106(2):024501, January 2011.

[10] Alexandra Witze. Greenland rocks suggest Earth's magnetic field is older than we thought. *Nature*, 576(7787):347–347, December 2019.

[11] Colin Barras. New signs of a shielding magnetic field found in Earth's oldest rock crystals. *Science*, January 2020.

[12] William Gilbert. *Guilielmi Gilberti Colcestrensis, medici londinensis, De magnete.* Excudebat Petrus Short, 1600.

[13] C. F. Gauss. Resultate aus den Beobachtungen magnetischen Vereins im Jahre 1838. *Reprinted in "Werke", 5 121-193, Gottingen, 1877; Translated by Sabine, E., in Taylor, R., "Scientific Memoirs Vol. 2", R. & J. E. Taylor, London, 1841*, pages 1–57, 1839.

[14] Vincent Courtillot and Jean Louis Le Mouel. Time Variations of the Earth's Magnetic Field: From Daily to Secular. *Annual Review of Earth and Planetary Sciences*, 16:389, January 1988. ADS Bibcode: 1988AREPS..16..389C.

[15] Andrew Jackson, Art R. T. Jonkers, and Matthew R. Walker. Four centuries of geomagnetic secular variation from historical records. *Philosophical Transactions of the Royal Society of London. Series A: Mathematical, Physical and Engineering Sciences*, 358(1768):957–990, March 2000.

[16] G. Hulot, C. Eymin, B. Langlais, M. Mandea, and N. Olsen. Small-scale structure of the geodynamo inferred from Oersted and Magsat satellite data. *Nature*, 416:620–623, April 2002.

[17] G. Hulot, C. C. Finlay, C. G. Constable, N. Olsen, and M. Mandea. The Magnetic Field of Planet Earth. *Space Science Reviews*, 152(1-4):159–222, May 2010.

[18] Alan Buis. Flip Flop: Why Variations in Earth's Magnetic Field Aren't Causing Today's Climate Change.

[19] Alan Cooper, Chris S. M. Turney, Jonathan Palmer, Alan Hogg, Matt McGlone, Janet Wilmshurst, Andrew M. Lorrey, Timothy J. Heaton, James M. Russell, Ken McCracken, Julien G. Anet, Eugene Rozanov, Marina Friedel, Ivo Suter, Thomas Peter, Raimund Muscheler, Florian Adolphi, Anthony Dosseto, J. Tyler Faith, Pavla Fenwick, Christopher J. Fogwill, Konrad Hughen, Mathew Lipson, Jiabo Liu, Norbert Nowaczyk, Eleanor Rainsley, Christopher Bronk Ramsey, Paolo Sebastianelli, Yassine Souilmi, Janelle Stevenson, Zoë Thomas, Raymond Tobler, and Roland Zech. A global environmental crisis 42,000 years ago. *Science*, 371(6531):811–818, February 2021.

[20] Brian J. Anderson, Mario H. Acuña, Haje Korth, Michael E. Purucker, Catherine L. Johnson, James A. Slavin, Sean C. Solomon, and Ralph L. McNutt. The Structure of Mercury's Magnetic Field from MESSENGER's First Flyby. *Science*, 321(5885):82–85, July 2008.

[21] Ulrich R. Christensen. A deep dynamo generating Mercury's magnetic field. *Nature*, 444(7122):1056–1058, December 2006.

[22] Ajay Manglik, Johannes Wicht, and Ulrich R. Christensen. A dynamo model with double diffusive convection for Mercury's core. *Earth and Planetary Science Letters*, 289(3-4):619–628, January 2010.

[23] Hao Cao, Christopher T. Russell, Johannes Wicht, Ulrich R. Christensen, and Michele K. Dougherty. Saturn's high degree magnetic moments: Evidence for a unique planetary dynamo. *Icarus*, 221(1):388–394, September 2012.

[24] Michele K. Dougherty, Hao Cao, Krishan K. Khurana, Gregory J. Hunt, Gabrielle Provan, Stephen Kellock, Marcia E. Burton, Thomas A. Burk, Emma J. Bunce, Stanley W. H. Cowley, Margaret G. Kivelson, Christopher T. Russell, and David J. Southwood. Saturn's magnetic field revealed by the Cassini Grand Finale. *Science*, 362(6410):eaat5434, October 2018.

[25] C. Milbury, G. Schubert, C. A. Raymond, S. E. Smrekar, and B. Langlais. The history of Mars' dynamo as revealed by modeling magnetic anomalies near Tyrrhenus Mons and Syrtis Major: MARS' DYNAMO HISTORY. *Journal of Geophysical Research: Planets*, 117(E10), October 2012.

[26] W. Dietrich and J. Wicht. A hemispherical dynamo model: Implications for the Martian crustal magnetization. *Physics of the Earth and Planetary Interiors*, 217:10–21, April 2013.

[27] David J. Stevenson. Metallic helium in massive planets. *Proceedings of the National Academy of Sciences*, 105(32):11035–11036, August 2008.

[28] T. Gastine, J. Wicht, L. D. V. Duarte, M. Heimpel, and A. Becker. Explaining Jupiter's magnetic field and equatorial jet dynamics. *Geophysical Research Letters*, 41(15):5410–5419, August 2014.

[29] Ulrich R. Christensen. Iron snow dynamo models for Ganymede. *Icarus*, 247:248–259, February 2015.

[30] P. A. Davidson. *An Introduction to Magnetohydrodynamics*. Cambridge University Press, 2001.

[31] E. Wiechert. Nachrichten von der Gesellschaft der Wissenschaften zu Göttingen, Mathematisch-Physikalische Klasse. 1897.

[32] R. D. Oldham. Earthquake Origins. *Nature*, 73(1904):620–621, April 1906.

[33] B.. Gutenberg. "Ueber Erdbebenwellen. VII A. Beobachtungen an Registrierungen von Fernbeben in Göttingen und Folgerung über die Konstitution des Erdkörpers (mit Tafel)." Nachrichten von der Gesellschaft der Wissenschaften zu Göttingen, Mathematisch-Physikalische Klasse 1914. 1914.

[34] Harold Jeffreys. Some cases of instability in fluid motion. *Proceedings of the Royal Society of London. Series A, Containing Papers of a Mathematical and Physical Character*, 118(779):195–208, March 1928.

[35] Lehmann, I. Publications du Bureau central séismologique international. Serie A: Travaux scientifiques. (no.):no., 1924. Place: Toulouse [etc.].

[36] T. G. Cowling. The Magnetic Field of Sunspots. *Monthly Notices of the Royal Astronomical Society*, 94(1):39–48, November 1933.

[37] Walter M. Elsasser. On the Origin of the Earth's Magnetic Field. *Physical Review*, 55(5):489–498, March 1939.

[38] Walter M. Elsasser. Induction Effects in Terrestrial Magnetism Part I. Theory. *Physical Review*, 69(3-4):106–116, February 1946.

[39] Walter M. Elsasser. The Earth's Interior and Geomagnetism. *Reviews of Modern Physics*, 22(1):1–35, January 1950.

[40] Edward Crisp Bullard. The magnetic field within the earth. *Proceedings of the Royal Society of London. Series A. Mathematical and Physical Sciences*, 197(1051):433–453, July 1949.

[41] E. C. Bullard. Electromagnetic Induction in a Rotating Sphere. *Proceedings of the Royal Society of London. Series A, Mathematical and Physical Sciences*, 199(1059):413–443, 1949.

[42] Edward Crisp Bullard and H. Gellman. Homogeneous dynamos and terrestrial magnetism. *Philosophical Transactions of the Royal Society of London. Series A, Mathematical and Physical Sciences*, 247(928):213–278, November 1954. Publisher: Royal Society.

[43] George Backus. A class of self-sustaining dissipative spherical dynamos. *Annals of Physics*, 4(4):372–447, August 1958.

[44] Herzenberg. Geomagnetic dynamos. *Philosophical Transactions of the Royal Society of London. Series A, Mathematical and Physical Sciences*, 250(986):543–583, August 1958.

[45] Eugene N. Parker. Hydromagnetic Dynamo Models. *The Astrophysical Journal*, 122:293, September 1955.

[46] M. Steenbeck, F. Krause, and K.-H. Rädler. Berechnung der mittleren Lorentz-Feldstärke für ein elektrisch leitendes Medium in turbulenter, durch Coriolis-Kräfte beeinflußter Bewegung. *Zeitschrift für Naturforschung A*, 21(4):369–376, April 1966.

[47] P. H. Roberts. Kinematic Dynamo Models. *Philosophical Transactions of the Royal Society of London. Series A, Mathematical and Physical Sciences*, 272(1230):663–698, 1972.

[48] M. L. Dudley, Reginald William James, and Paul Harry Roberts. Time-dependent kinematic dynamos with stationary flows. *Proceedings of the Royal Society of London. A. Mathematical and Physical Sciences*, 425(1869):407–429, October 1989. Publisher: Royal Society.

[49] H. K. Moffatt. *Magnetic field generation in electrically conducting fluids*. Cambridge monographs on mechanics and applied mathematics. Cambridge University Press, Cambridge [Eng.] ; New York, 1978.

[50] Stephen Childress and Andrew D. Gilbert. *Stretch, twist, fold: the fast dynamo*. Number m37 in Lecture notes in physics. Springer, Berlin ; [New York], 1995.

[51] Takahiro Nakajima and Masaru Kono. Kinematic dynamos associated with large scale fluid motions. *Geophysical & Astrophysical Fluid Dynamics*, 60(1-4):177–209, November 1991.

[52] R. Holme. Optimised axially-symmetric kinematic dynamos. *Physics of the Earth and Planetary Interiors*, 140(1):3–11, November 2003.

[53] D. N. Tomin and D. D. Sokoloff. Magnetic field in a fluctuating ABC flow. *Astronomy Letters*, 35(5):321–325, May 2009.

[54] Mingtian Xu. Impact of small scale turbulent flows on dynamo actions. *Physics Letters A*, 379(6):577–580, March 2015.

[55] Ashley P. Willis. Optimization of the Magnetic Dynamo. *Physical Review Letters*, 109(25):251101, December 2012.

[56] D. Holdenried-Chernoff, L. Chen, and A. Jackson. A trio of simple optimized axisymmetric kinematic dynamos in a sphere. *Proceedings of the Royal Society A: Mathematical, Physical and Engineering Sciences*, 475(2229):20190308, September 2019.

[57] F. Stefani, G. Gerbeth, and A. Gailitis. Velocity Profile Optimization for the Riga Dynamo Experiment. In A. Alemany, Ph. Marty, and J. P. Thibault, editors, *Transfer Phenomena in Magnetohydrodynamic and Electroconducting Flows: Selected papers of the PAMIR Conference held in Aussois, France 22–26 September 1997*, Fluid Mechanics and Its Applications, pages 31–44. Springer Netherlands, Dordrecht, 1999.

[58] Daniel S. Zimmerman, Santiago Andrés Triana, Henri-Claude Nataf, and Daniel P. Lathrop. A turbulent, high magnetic Reynolds number experimental model of Earth's core. *Journal of Geophysical Research: Solid Earth*, 119(6):4538–4557, 2014.

[59] N. Schaeffer, D. Jault, H.-C. Nataf, and A. Fournier. Turbulent geodynamo simulations: a leap towards Earth's core. *Geophysical Journal International*, 211(1):1–29, October 2017.

[60] J. Aubert, N. Gillet, and P. Cardin. Quasigeostrophic models of convection in rotating spherical shells. *Geochemistry, Geophysics, Geosystems*, page 1, July 2003.

[61] Ankit Barik. *Inertial modes, turbulence and magnetic effects in a differentially rotating spherical shell: Instabilities of spherical Couette flow*. PhD thesis, Georg-August-University Göttingen, 2017.

[62] A. Barik, S. A. Triana, M. Hoff, and J. Wicht. Triadic resonances in the wide-gap spherical Couette system. *Journal of Fluid Mechanics*, 843:211–243, May 2018.

[63] G. A. Glatzmaier and P. H. Roberts. A three-dimensional self-consistent computer simulation of a geomagnetic field reversal. *Nature*, 377:203–207, 1995.

[64] Akira Kageyama and Tetsuya Sato. Computer simulation of a magnetohydrodynamic dynamo. II. *Physics of Plasmas*, 2(5):1421–1431, May 1995.

[65] Ataru Sakuraba and Paul H. Roberts. Generation of a strong magnetic field using uniform heat flux at the surface of the core. *Nature Geoscience*, 2(11):802–805, November 2009.

[66] Johannes Wicht and Sabrina Sanchez. Advances in geodynamo modelling. *Geophysical & Astrophysical Fluid Dynamics*, 113(1-2):2–50, March 2019.

[67] David Gubbins, C. N. Barber, S. Gibbons, and J. J. Love. Kinematic Dynamo Action in a Sphere II. Symmetry Selection. *Proceedings: Mathematical, Physical and Engineering Sciences*, 456(1999):1669–1683, 2000.

[68] Johannes Wicht. Flow instabilities in the wide-gap spherical Couette system. *Journal of Fluid Mechanics*, 738:184–221, January 2014.

[69] Edward R. Benton. Kinematic dynamo action with helical symmetry in an unbounded fluid conductor: Part 2. Further development of an explicit solution for the prototype case of lortz. *Geophysical & Astrophysical Fluid Dynamics*, 12(1):345–358, January 1979.

[70] Agris Gailitis, Olgerts Lielausis, Ernests Platacis, Sergej Dement'ev, Arnis Cifersons, Gunter Gerbeth, Thomas Gundrum, Frank Stefani, Michael Christen, and Gotthard Will. Magnetic Field Saturation in the Riga Dynamo Experiment. *Physical Review Letters*, 86(14):3024–3027, April 2001.

[71] Agris Gailitis, Olgerts Lielausis, Sergej Dement'ev, Ernests Platacis, Arnis Cifersons, Gunter Gerbeth, Thomas Gundrum, Frank Stefani, Michael Christen, Heiko Hänel, and Gotthard Will. Detection of a Flow Induced Magnetic Field Eigenmode in the Riga Dynamo Facility. *Physical Review Letters*, 84(19):4365–4368, May 2000.

[72] Agris Gailitis, Olgerts Lielausis, Ernests Platacis, Gunter Gerbeth, and Frank Stefani. Riga dynamo experiment and its theoretical background. *Physics of Plasmas*, 11(5):2838–2843, May 2004.

[73] A. Gailitis, G. Gerbeth, Th Gundrum, O. Lielausis, G. Lipsbergs, E. Platacis, and F. Stefani. Self-excitation in a helical liquid metal flow: The Riga dynamo experiments. *Journal of Plasma Physics*, 84(3):735840301, June 2018.

[74] Henri-Claude Nataf. Magnetic induction maps in a magnetized spherical Couette flow experiment. *Comptes Rendus Physique*, 14(2):248–267, February 2013.

[75] F. Ravelet, A. Chiffaudel, F. Daviaud, and J. Léorat. Toward an experimental von Kármán dynamo: Numerical studies for an optimized design. *Physics of Fluids*, 17(11):117104, November 2005.

[76] J Boisson and B Dubrulle. Three-dimensional magnetic field reconstruction in the VKS experiment through Galerkin transforms. *New Journal of Physics*, 13(2):023037, February 2011.

[77] R Stieglitz and U Muller. Experimental demonstration of a homogeneous two-scale dynamo. *PHYSICS OF FLUIDS*, 13(3):561–564, March 2001.

[78] André Giesecke, Tobias Vogt, Thomas Gundrum, and Frank Stefani. Nonlinear Large Scale Flow in a Precessing Cylinder and Its Ability To Drive Dynamo Action. *Physical Review Letters*, 120(2):024502, January 2018.

[79] Siegfried Grossmann, Detlef Lohse, and Chao Sun. High–Reynolds Number Taylor-Couette Turbulence. *Annual Review of Fluid Mechanics*, 48(1):53–80, 2016.

[80] Sander G. Huisman, Dennis P. M. van Gils, Siegfried Grossmann, Chao Sun, and Detlef Lohse. Ultimate Turbulent Taylor-Couette Flow. *Physical Review Letters*, 108(2):024501, January 2012.

[81] X. Chavanne, F. Chill\textbackslash‘{a}, B. Castaing, B. Hébral, B. Chabaud, and J. Chaussy. Observation of the Ultimate Regime in Rayleigh-Bénard Convection. *Physical Review Letters*, 79(19):3648–3651, November 1997.

[82] Gregory S. Lewis and Harry L. Swinney. Velocity structure functions, scaling, and transitions in high-Reynolds-number Couette-Taylor flow. *Physical Review E*, 59(5):5457–5467, May 1999.

[83] Daniel P. Lathrop, Jay Fineberg, and Harry L. Swinney. Transition to shear-driven turbulence in Couette-Taylor flow. *Physical Review A*, 46(10):6390–6405, November 1992. Publisher: American Physical Society.

[84] B. Dubrulle and F. Hersant. Momentum transport and torque scaling in Taylor-Couette flow from an analogy with turbulent convection. *The European Physical Journal B - Condensed Matter and Complex Systems*, 26(3):379–386, April 2002.

[85] Bruno Eckhardt, Siegfried Grossmann, and Detlef Lohse. Torque scaling in turbulent Taylor–Couette flow between independently rotating cylinders. *Journal of Fluid Mechanics*, 581:221–250, June 2007.

[86] S. Chandrasekhar. *Hydrodynamic and Hydromagnetic Stability*. Dover, New York, 1961.

[87] E. L. Koschmieder. *Bénard cells and Taylor vortices*. Cambridge monographs on mechanics and applied mathematics. Cambridge University Press, Cambridge [England] ; New York, 1993.

[88] F. H. Busse. Bounds for turbulent shear flow. *Journal of Fluid Mechanics*, 41(1):219–240, March 1970.

[89] Robert H. Kraichnan. Turbulent Thermal Convection at Arbitrary Prandtl Number. *The Physics of Fluids*, 5(11):1374–1389, November 1962.

[90] Ronald T. Merrill, M. W. McElhinny, and Phillip L. McFadden. *The magnetic field of the earth: paleomagnetism, the core, and the deep mantle*. Number v. 63 in International geophysics series. Academic Press, San Diego, Calif, 1996.

[91] Arnaud Prigent, Bérengère Dubrulle, Olivier Dauchot, and Innocent Mutabazi. The Taylor-Couette Flow: The Hydrodynamic Twin of Rayleigh-Bénard Convection. In Innocent Mutabazi, José Eduardo Wesfreid, and Etienne Guyon, editors, *Dynamics of Spatio-Temporal Cellular Structures: Henri Bénard Centenary Review*, Springer Tracts in Modern Physics, pages 225–242. Springer, New York, NY, 2006.

[92] D. Schmitt, T. Alboussière, D. Brito, P. Cardin, N. Gagnière, D. Jault, and H. C. Nataf. Rotating spherical Couette flow in a dipolar magnetic field: Experimental study of magneto-inertial waves. *J. Fluid Mech.*, 604:175–197, 2008.

[93] H. C. Nataf, T. Alboussiere, D. Brito, P. Cardin, N. Gagniere, D. Jault, and D. Schmitt. Rapidly rotating spherical Couette flow in a dipolar magnetic field: An experimental study of the mean axisymmetric flow. *PHYSICS OF THE EARTH AND PLANETARY INTERIORS*, 170(1-2):60–72, September 2008.

[94] E. J. Spence, K. Reuter, and C. B. Forest. A Spherical Plasma Dynamo Experiment. *The Astrophysical Journal*, 700(1):470–478, July 2009.

[95] Douglas H. Kelley. *Rotating, hydromagnetic laboratory experiment modelling planetary cores*. PhD Thesis, 2009.

[96] Daniel Zimmerman. *Turbulent Shear Flow in a Rapidly Rotating Spherical Annulus*. PhD Thesis, 2010.

[97] Matthew M. Adams. *Magnetic and Acoustic Investigations of Turbulent Spherical Couette Flow*. PhD Thesis, 2016.

[98] Anthony Robert Mautino. *Inverse Spectral Methods in Acoustic Normal Mode Velocimetry of High Reynolds Number Spherical Couette Flows*. PhD Thesis, 2016.

[99] Sarah Burnett. *Predicting the magnetic field of the three-meter spherical Couette experiment*. PhD thesis, 2021. Accepted: 2022-02-04T06:43:44Z.

[100] Rubén E. Rojas. *INCREASING HELICITY TOWARDS A DYNAMO ACTION WITH ROUGH BOUNDARY SPHERICAL COUETTE FLOWS*. PhD thesis, 2022.

[101] Nicholas L. Peffley, Alexei G. Goumilevski, A. B. Cawthrone, and Daniel P. Lathrop. Characterization of experimental dynamos. *Geophysical Journal International*, 142(1):52–58, July 2000.

[102] Barbara E. Brawn, Kaveri Joshi, Daniel P. Lathrop, Nicolas Mujica, and Daniel R. Sisan. Visualizing the invisible: Ultrasound velocimetry in liquid sodium. *Chaos: An Interdisciplinary Journal of Nonlinear Science*, 15(4):041104, December 2005.

[103] W. L. Shew. *Liquid sodium model of earth's outer core*. PhD Thesis, University of Maryland, 2004.

[104] Daniel P. Lathrop, Woodrow L. Shew, and Daniel R. Sisan. Laboratory experiments on the transition to MHD dynamos. *Plasma Physics and Controlled Fusion*, 43(12A):A151–A160, November 2001.

[105] Woodrow L. Shew and Daniel P. Lathrop. Liquid sodium model of geophysical core convection. *Physics of the Earth and Planetary Interiors*, 153(1):136–149, November 2005.

[106] Douglas H. Kelley, Santiago Andrés Triana, Daniel S. Zimmerman, Andreas Tilgner, and Daniel P. Lathrop. Inertial waves driven by differential rotation in a planetary geometry. *Geophysical & Astrophysical Fluid Dynamics*, 101(5-6):469–487, October 2007.

[107] S.A. Triana, D.H. Kelley, D. Zimmerman, D. Sisan, and D.P. Lathrop. Hopf bifurcations with fluctuating gain. *Astronomische Nachrichten*, 329(7):701–705, September 2008.

[108] Douglas H. Kelley, Santiago Andrés Triana, Daniel S. Zimmerman, and Daniel P. Lathrop. Selection of inertial modes in spherical Couette flow. *Physical Review E*, 81(2):026311, February 2010.

[109] H. Matsui, M. Adams, D. Kelley, S.A. Triana, D. Zimmerman, B.A. Buffett, and D.P. Lathrop. Numerical and experimental investigation of shear-driven inertial oscillations in an Earth-like geometry. *Physics of the Earth and Planetary Interiors*, 188(3-4):194–202, October 2011.

[110] S. A. Triana, D. S. Zimmerman, and D. P. Lathrop. Precessional states in a laboratory model of the Earth's core. *Journal of Geophysical Research: Solid Earth*, 117(B4), 2012.

[111] Michel Rieutord, Santiago Andrés Triana, Daniel S. Zimmerman, and Daniel P. Lathrop. Excitation of inertial modes in an experimental spherical Couette flow. *Physical Review E*, 86(2):026304, August 2012. Publisher: American Physical Society.

[112] Xiaojue Zhu, Ruben A. Verschoof, Dennis Bakhuis, Sander G. Huisman, Roberto Verzicco, Chao Sun, and Detlef Lohse. Wall roughness induces asymptotic ultimate turbulence. *Nature Physics*, 14(4):417–423, April 2018. Number: 4 Publisher: Nature Publishing Group.

[113] Ruben A. Verschoof, Xiaojue Zhu, Dennis Bakhuis, Sander G. Huisman, Roberto Verzicco, Chao Sun, and Detlef Lohse. Rough-wall turbulent Taylor-Couette flow:

The effect of the rib height. *The European Physical Journal E*, 41(10):125, October 2018.

[114] K. Finke and A. Tilgner. Simulations of the kinematic dynamo onset of spherical Couette flows with smooth and rough boundaries. *Physical Review E*, 86(1):016310, July 2012.

[115] Akin. https://spacecraft.ssl.umd.edu/akins_laws.html.

[116] Christopher Davies, Monica Pozzo, David Gubbins, and Dario Alfè. Constraints from material properties on the dynamics and evolution of Earth's core. *Nature Geoscience*, 8(9):678–685, September 2015.

[117] Daniel P. Lathrop and Cary B. Forest. Magnetic dynamos in the lab. *Physics Today*, 64(7):40–45, July 2011. Publisher: American Institute of Physics.

[118] H. Alfvén. Existence of Electromagnetic-Hydrodynamic Waves. *Nature*, 150(3805):405–406, October 1942.

[119] E. R. Priest and Terry Forbes. *Magnetic reconnection: MHD theory and applications*. Cambridge University Press, Cambridge ; New York, 2000.

[120] L. D. Landau and E. M. Lifshitz. *Fluid Mechanics*. Theoretical Physics. Elsevier, Oxford, England, second edition, 2004.

[121] G. K. Batchelor. *An introduction to fluid dynamics*. Cambridge University Press, 1967.

[122] D. J. Tritton. *Physical fluid dynamics*. Oxford science publications. Clarendon Press ; Oxford University Press, Oxford [England] : New York, 2nd ed edition, 1988.

[123] Chris A. Jones. Course 2 Dynamo theory. In Ph. Cardin and L. F. Cugliandolo, editors, *Les Houches*, volume 88 of *Dynamos*, pages 45–135. Elsevier, January 2008.

[124] T. Rikitake and W. Bullerwell. Book Reviews. *Geophysical Journal International*, 12(3):319–320, March 1967.

[125] Franck Plunian and Thierry Alboussière. Axisymmetric dynamo action is possible with anisotropic conductivity. *Physical Review Research*, 2(1):013321, March 2020.

[126] Ph Cardin, L. F. Cugliandolo, and Centre national de la recherche scientifique (France), editors. *Dynamos: École d'été de physique des Houches, session LXXXVIII, 30 July-24 August 2007: École thématique du CNRS*. Elsevier, Amsterdam ; Boston, 1st ed edition, 2008.

[127] A. Gailitis, O. Lielausis, B. G. Karasev, I. R. Kirillov, and A. P. Ogorodnikov. The Helical MHD Dynamo. In J. Lielpeteris and R. Moreau, editors, *Liquid Metal Magnetohydrodynamics*, Mechanics of Fluids and Transport Processes, pages 413–419. Springer Netherlands, Dordrecht, 1989.

[128] Andrew D. Gilbert. Chapter 9 - Dynamo Theory. In S. Friedlander and D. Serre, editors, *Handbook of Mathematical Fluid Dynamics*, volume 2, pages 355–441. North-Holland, January 2003.

[129] Andrew D. Gilbert. Fast dynamo action in the Ponomarenko dynamo. *Geophysical & Astrophysical Fluid Dynamics*, 44(1-4):241–258, December 1988.

[130] Julius Adams Stratton. *Electromagnetic theory*. International series in pure and applied physics. McGraw-Hill, New York, 1941.

[131] On the motion of solids in a liquid possessing vorticity. *Proceedings of the Royal Society of London. Series A, Containing Papers of a Mathematical and Physical Character*, 92(642):408–424, July 1916.

[132] Motion of solids in fluids when the flow is not irrotational. *Proceedings of the Royal Society of London. Series A, Containing Papers of a Mathematical and Physical Character*, 93(648):99–113, March 1917.

[133] H. P. Greenspan. *The Theory Of Rotating Fluids*. Cambridge monographs on mechanics and applied mathematics. Cambridge University Press, London, 1968.

[134] K. D. Aldridge and A. Toomre. Axisymmetric inertial oscillations of a fluid in a rotating spherical container. *J. Fluid Mech.*, 37:307–323, 1969.

[135] K. D. Aldridge. Axisymmetric inertial oscillations of a fluid in a rotating spherical shell. *Mathematika*, 19:163–168, 1972.

[136] K. D. Aldridge and I. Lumb. Inertial waves identified in the Earth's fluid outer core. *Nature*, 325:421–423, January 1987.

[137] A. Tilgner. Kinematic dynamos with precession driven flow in a sphere. *Geophysical and Astrophysical Fluid Dynamics*, 101:1–9, February 2007.

[138] C.-G. Rossby. Relation between variations in the intensity of the zonal circulation of the atmosphere and the displacements of the semi-permanent centers of action. *J. Marine Res.*, pages 38–55, 1939.

[139] G. H. Bryan. The waves on a rotating liquid spheroid of finite ellipticity. *Phil. Trans. R. Soc. London A*, 180:187–219, 1889.

[140] M. D. Kudlick. *On transient motions in a contained, rotating fluid*. PhD Thesis, Massachusetts Institute of Technology, February 1966.

[141] Keke Zhang, Paul Earnshaw, Xinhao Liao, and F. H. Busse. On inertial waves in a rotating fluid sphere. *Journal of Fluid Mechanics*, 437:103–119, June 2001.

[142] H. Poincaré. Sur la précession des corps déformables. *Bull. Astron. I*, 27:321–356, 1910.

[143] H. Poincaré. Sur l'équilibre d'une masse fluide animée d'un mouvement de rotation. *Acta Mathematica*, 7(0):259–380, 1885.

[144] K. Zhang and X. Liao. A new asymptotic method for the analysis of convection in a rapidly rotating sphere. *J. Fluid Mech.*, 518:319–346, November 2004.

[145] F. Gerick, D. Jault, and J. Noir. Fast Quasi-Geostrophic Magneto-Coriolis Modes in the Earth's Core. *Geophysical Research Letters*, 48(4), February 2021.

[146] R. Hide. Free Hydromagnetic Oscillations of the Earth's Core and the Theory of the Geomagnetic Secular Variation. *Royal Society of London Philosophical Transactions Series A*, 259:615–647, June 1966.

[147] S. I. Braginsky. Magnetic waves in the core of the earth. II. *Geophysical & Astrophysical Fluid Dynamics*, 14(1):189–208, January 1979.

[148] P H Roberts and A M Soward. Magnetohydrodynamics of the Earth's Core. *Annual Review of Fluid Mechanics*, 4(1):117–154, January 1972.

[149] D. Schmitt, P. Cardin, P. La Rizza, and H. C. Nataf. Magneto–Coriolis waves in a spherical Couette flow experiment. *European Journal of Mechanics - B/Fluids*, 37:10–22, January 2013.

[150] Keke Zhang, Xinhao Liao, and Gerald Schubert. Nonaxisymmetric Instabilities of a Toroidal Magnetic Field in a Rotating Sphere. *The Astrophysical Journal*, 585(2):1124–1137, March 2003.

[151] Nicolas Gillet, Felix Gerick, Dominique Jault, Tobias Schwaiger, Julien Aubert, and Mathieu Istas. Satellite magnetic data reveal interannual waves in Earth's core. *Proceedings of the National Academy of Sciences*, 119(13):e2115258119, March 2022.

[152] Keke Zhang, Xinhao Liao, and Paul Earnshaw. The Poincaré equation: A new polynomial and its unusual properties. *Journal of Mathematical Physics*, 45(12):4777–4790, December 2004.

[153] D. Jault, C. Gire, and J. L. Le Mouel. Westward drift, core motions and exchanges of angular momentum between core and mantle. *Nature*, 333(6171):353–356, May 1988.

[154] Dominique Jault. Axial invariance of rapidly varying diffusionless motions in the Earth's core interior. *PHYSICS OF THE EARTH AND PLANETARY INTERIORS*, 166(1-2):67–76, January 2008.

[155] Christopher C. Finlay and Andrew Jackson. Equatorially Dominated Magnetic Field Change at the Surface of Earth's Core. *Science*, 300(5628):2084–2086, June 2003.

[156] Jiawen Luo, Long Chen, Kuan Li, and Andrew Jackson. Optimal kinematic dynamos in a sphere. *Proceedings of the Royal Society A: Mathematical, Physical and Engineering Sciences*, 476(2233):20190675, January 2020.

[157] Jiawen Luo and Andrew Jackson. Waves in the Earths core. I. Mildly diffusive torsional oscillations. *Proceedings of the Royal Society A*, March 2022.

[158] Edward N. Lorenz. Deterministic Nonperiodic Flow. *Journal of Atmospheric Sciences*, 20:130–148, March 1963. ADS Bibcode: 1963JAtS...20..130L.

[159] S. Smale. Differentiable dynamical systems. *Bulletin of the American Mathematical Society*, 73(6):747–817, 1967.

[160] Edward Ott and Mark Spano. Controlling Chaos. *Physics Today*, 48(5):34–40, May 1995.

[161] Tien-Yien Li and James A. Yorke. Period Three Implies Chaos. *The American Mathematical Monthly*, 82(10):985, December 1975.

[162] Edward Ott, Tim Sauer, and James A. Yorke, editors. *Coping with chaos: analysis of chaotic data and the exploitation of chaotic systems*. Wiley series in nonlinear science. J. Wiley, New York, 1994.

[163] Edward Ott. *Chaos in dynamical systems*. Cambridge University Press, Cambridge, U.K. ; New York, 2nd ed edition, 2002.

[164] Steven H. Strogatz. *Nonlinear dynamics and chaos: with applications to physics, biology, chemistry, and engineering*. Studies in nonlinearity. Westview Press, Cambridge (Mass.), 1994.

[165] Henry D. I. Abarbanel. *Analysis of observed chaotic data*. Springer, Berlin Heidelberg, study ed edition, 1997.

[166] Henry D. I. Abarbanel, Reggie Brown, John J. Sidorowich, and Lev Sh. Tsimring. The analysis of observed chaotic data in physical systems. *Reviews of Modern Physics*, 65(4):1331–1392, October 1993. Publisher: American Physical Society.

[167] Yaneer Bar-Yam. *Dynamics of complex systems*. Studies in nonlinearity. Westview Press, Boulder, CO, 2003.

[168] W.-H. Steeb. *The nonlinear workbook: chaos, fractals, cellular automata, genetic algorithms, gene expression programming, support vector machine, wavelets, hidden Markov models, fuzzy logic with C++, Java and symbolic C++ programs*. World Scientific, Hackensack, New Jersey, 6th edition edition, 2015.

[169] Holger Kantz and Thomas Schreiber. *Nonlinear time series analysis*. Cambridge University Press, Cambridge, UK ; New York, 2nd ed edition, 2004.

[170] James Gleick. *Chaos: making a new science*. Penguin Books, New York, 1988.

[171] F. Rosenblatt. The perceptron: A probabilistic model for information storage and organization in the brain. *Psychological Review*, 65(6):386–408, 1958.

[172] Mohamed Abdel-Nasser and Karar Mahmoud. Accurate photovoltaic power forecasting models using deep LSTM-RNN. *Neural Computing and Applications*, 31(7):2727–2740, July 2019.

[173] Sepp Hochreiter and Jürgen Schmidhuber. Long Short-Term Memory. *Neural Computation*, 9(8):1735–1780, November 1997. Publisher: MIT Press.

[174] George Neofotistos, Marios Mattheakis, Georgios D. Barmparis, Johanne Hizanidis, Giorgos P. Tsironis, and Efthimios Kaxiras. Machine Learning With Observers Predicts Complex Spatiotemporal Behavior. *Frontiers in Physics*, 7, 2019. Publisher: Frontiers.

[175] Pantelis R. Vlachas, Wonmin Byeon, Zhong Y. Wan, Themistoklis P. Sapsis, and Petros Koumoutsakos. Data-driven forecasting of high-dimensional chaotic systems with long short-term memory networks. *Proceedings of the Royal Society A: Mathematical, Physical and Engineering Sciences*, 474(2213):20170844, May 2018. Publisher: Royal Society.

[176] Maciej Wielgosz, Andrzej Skoczeń, and Matej Mertik. Using LSTM recurrent neural networks for monitoring the LHC superconducting magnets. *Nuclear Instruments and Methods in Physics Research Section A: Accelerators, Spectrometers, Detectors and Associated Equipment*, 867:40–50, September 2017.

[177] Robert H. Shumway and David S. Stoffer. *Time Series Analysis and Its Applications: With R Examples*. Springer Texts in Statistics. Springer International Publishing : Imprint: Springer, Cham, 4th ed. 2017 edition, 2017.

[178] Ramazan Gençay and Tung Liu. Nonlinear modelling and prediction with feedforward and recurrent networks. *Physica D: Nonlinear Phenomena*, 108(1):119–134, September 1997.

[179] Zhixin Lu, Jaideep Pathak, Brian Hunt, Michelle Girvan, Roger Brockett, and Edward Ott. Reservoir observers: Model-free inference of unmeasured variables in chaotic systems. *Chaos: An Interdisciplinary Journal of Nonlinear Science*, 27(4):041102, April 2017. Publisher: American Institute of Physics.

[180] Jaideep Pathak, Zhixin Lu, Brian R. Hunt, Michelle Girvan, and Edward Ott. Using machine learning to replicate chaotic attractors and calculate Lyapunov exponents from data. *Chaos: An Interdisciplinary Journal of Nonlinear Science*, 27(12):121102, December 2017.

[181] Jaideep Pathak, Brian Hunt, Michelle Girvan, Zhixin Lu, and Edward Ott. Model-Free Prediction of Large Spatiotemporally Chaotic Systems from Data: A Reservoir Computing Approach. *Physical Review Letters*, 120(2):024102, January 2018. Publisher: American Physical Society.

[182] David Silver, Julian Schrittwieser, Karen Simonyan, Ioannis Antonoglou, Aja Huang, Arthur Guez, Thomas Hubert, Lucas Baker, Matthew Lai, Adrian Bolton, Yutian

Chen, Timothy Lillicrap, Fan Hui, Laurent Sifre, George van den Driessche, Thore Graepel, and Demis Hassabis. Mastering the game of Go without human knowledge. *Nature*, 550(7676):354–359, October 2017. Number: 7676 Publisher: Nature Publishing Group.

[183] Oriol Vinyals, Igor Babuschkin, Wojciech M. Czarnecki, Michaël Mathieu, Andrew Dudzik, Junyoung Chung, David H. Choi, Richard Powell, Timo Ewalds, Petko Georgiev, Junhyuk Oh, Dan Horgan, Manuel Kroiss, Ivo Danihelka, Aja Huang, Laurent Sifre, Trevor Cai, John P. Agapiou, Max Jaderberg, Alexander S. Vezhnevets, Rémi Leblond, Tobias Pohlen, Valentin Dalibard, David Budden, Yury Sulsky, James Molloy, Tom L. Paine, Caglar Gulcehre, Ziyu Wang, Tobias Pfaff, Yuhuai Wu, Roman Ring, Dani Yogatama, Dario Wünsch, Katrina McKinney, Oliver Smith, Tom Schaul, Timothy Lillicrap, Koray Kavukcuoglu, Demis Hassabis, Chris Apps, and David Silver. Grandmaster level in StarCraft II using multi-agent reinforcement learning. *Nature*, 575(7782):350–354, November 2019. Number: 7782 Publisher: Nature Publishing Group.

[184] Herbert Jaeger and Harald Haas. Harnessing Nonlinearity: Predicting Chaotic Systems and Saving Energy in Wireless Communication. *Science*, 304(5667):78–80, April 2004. Publisher: American Association for the Advancement of Science Section: Report.

[185] Herbert Jaeger. The" echo state" approach to analysing and training recurrent neural networks-with an erratum note'. *Bonn, Germany: German National Research Center for Information Technology GMD Technical Report*, 148, January 2001.

[186] Mantas Lukoševičius and Herbert Jaeger. Reservoir computing approaches to recurrent neural network training. *Computer Science Review*, 3(3):127–149, August 2009.

[187] Jaideep Pathak, Alexander Wikner, Rebeckah Fussell, Sarthak Chandra, Brian R. Hunt, Michelle Girvan, and Edward Ott. Hybrid forecasting of chaotic processes: Using machine learning in conjunction with a knowledge-based model. *Chaos: An Interdisciplinary Journal of Nonlinear Science*, 28(4):041101, April 2018. Publisher: American Institute of Physics.

[188] Heidi Komkov, Levon Dovlatyan, Artur Perevalov, and Daniel P. Lathrop. Reservoir Computing for Prediction of Beam Evolution in Particle Accelerators. *NeurIPS ML4PS Workshop*, 2019.

[189] Romain Monchaux, Michael Berhanu, Sébastien Aumaître, Arnaud Chiffaudel, François Daviaud, Bérengère Dubrulle, Florent Ravelet, Stephan Fauve, Nicolas Mordant, François Pétrélis, Mickael Bourgoin, Philippe Odier, Jean-François Pinton, Nicolas Plihon, and Romain Volk. The von Kármán Sodium experiment: Turbulent dynamical dynamos. *Physics of Fluids*, 21(3):035108, March 2009.

[190] R. Monchaux, M. Berhanu, M. Bourgoin, M. Moulin, Ph. Odier, J. F. Pinton, R. Volk, S. Fauve, N. Mordant, F. Petrelis, A. Chiffaudel, F. Daviaud, B. Dubrulle,

C. Gasquet, L. Marie, and F. Ravelet. Generation of a magnetic field by dynamo action in a turbulent flow of liquid sodium. *PHYSICAL REVIEW LETTERS*, 98(4), January 2007.

[191] Rubén E. Rojas, Artur Perevalov, Till Zürner, and Daniel P. Lathrop. Experimental study of rough spherical Couette flows: Increasing helicity toward a dynamo state. *Physical Review Fluids*, 6(3):033801, March 2021.

[192] William Thielicke and Eize J. Stamhuis. PIVlab – Towards User-friendly, Affordable and Accurate Digital Particle Image Velocimetry in MATLAB. *Journal of Open Research Software*, 2, October 2014.

[193] MATLAB. *MATLAB (R2019b)*. The MathWorks Inc., Natick, Massachusetts, 2018.

[194] http://www.pressure-drop.com/Online-Calculator/.

[195] A.W. Loomis, C.R. Westaway. *Cameron Hydraulic Data, 16th ed. (Woodcliff Lake, NJ: Ingersoll-Rand, 1981) pp. 4–53.* 1981.

[196] Guido Van Rossum and Fred L. Drake. *Python 3 Reference Manual*. CreateSpace, Scotts Valley, CA, 2009.

[197] Miguel Grinberg. *Flask web development: developing web applications with python*. " O'Reilly Media, Inc.", 2018.

[198] Artur Perevalov, Rubén E. Rojas, Brian R. Hunt, and Daniel P. Lathrop. Machine learning predictions of high Reynolds number rotating MHD turbulence. *(Under review) Physica D: Nonlinear Phenomena*, 2021.

[199] Peter S Bernard and James M Wallace. *Turbulent Flow Analysis, Measurement, and Prediction*. 2002.

[200] Eugenia Kalnay. *Atmospheric Modeling, Data Assimilation and Predictability*. Cambridge University Press, 2003.

[201] Michael Ghil and Paola Malanotte-Rizzoli. Data Assimilation in Meteorology and Oceanography. In Renata Dmowska and Barry Saltzman, editors, *Advances in Geophysics*, volume 33, pages 141–266. Elsevier, January 1991.

[202] Atieh Alizadeh Moghaddam and Amir Sadaghiyani. A deep learning framework for turbulence modeling using data assimilation and feature extraction. *arXiv:1802.06106 [physics]*, February 2018. arXiv: 1802.06106.

[203] Sabrina Sanchez, Johannes Wicht, and Julien Bärenzung. Predictions of the geomagnetic secular variation based on the ensemble sequential assimilation of geomagnetic field models by dynamo simulations. *Earth, Planets and Space*, 72(1):157, October 2020.

[204] Alexandre Fournier, Gauthier Hulot, Dominique Jault, Weijia Kuang, Andrew Tangborn, Nicolas Gillet, Elisabeth Canet, Julien Aubert, and Florian Lhuillier. An Introduction to Data Assimilation and Predictability in Geomagnetism. *Space Science Reviews*, 155(1-4):247–291, August 2010.

[205] Wolfgang Maass, Thomas Natschläger, and Henry Markram. Real-Time Computing Without Stable States: A New Framework for Neural Computation Based on Perturbations. *Neural Computation*, 14(11):2531–2560, November 2002. Publisher: MIT Press.

[206] J. K. Fink and L. Leibowitz. Thermodynamic and transport properties of sodium liquid and vapor. Technical Report ANL/RE-95/2, Argonne National Lab., IL (United States), January 1995.

[207] Peter Linstrom. NIST Chemistry WebBook, NIST Standard Reference Database 69, 1997.

[208] J. F. Freedman and W. D. Robertson. Electrical Resistivity of Liquid Sodium, Liquid Lithium, and Dilute Liquid Sodium Solutions. *The Journal of Chemical Physics*, 34(3):769–780, March 1961.

[209] VII. On a method of investigating periodicities disturbed series, with special reference to Wolfer's sunspot numbers. *Philosophical Transactions of the Royal Society of London. Series A, Containing Papers of a Mathematical or Physical Character*, 226(636-646):267–298, January 1927.

[210] Howard A. Levine. Book Review: Solutions of ill posed problems. *Bulletin of the American Mathematical Society*, 1(3):521–525, May 1979.

[211] Alexander Wikner, Jaideep Pathak, Brian Hunt, Michelle Girvan, Troy Arcomano, Istvan Szunyogh, Andrew Pomerance, and Edward Ott. Combining machine learning with knowledge-based modeling for scalable forecasting and subgrid-scale closure of large, complex, spatiotemporal systems. *Chaos: An Interdisciplinary Journal of Nonlinear Science*, 30(5):053111, May 2020. Publisher: American Institute of Physics.

[212] Monica Pozzo, Chris Davies, David Gubbins, and Dario Alfè. Thermal and electrical conductivity of iron at Earth's core conditions. *Nature*, 485(7398):355–358, May 2012. Number: 7398 Publisher: Nature Publishing Group.

[213] T. J. Ahrens, editor. *Global earth physics: a handbook of physical constants*. Number 1 in AGU reference shelf. American Geophysical Union, Washington, D.C, 1995.

[214] Santiago Andrés Triana, Daniel S Zimmerman, Henri-Claude Nataf, Aurélien Thorette, Vedran Lekic, and Daniel P Lathrop. Helioseismology in a bottle: modal acoustic velocimetry. *New Journal of Physics*, 16(11):113005, 2014.

[215] F. Garcia, A. Giesecke, and F. Stefani. Modulated rotating waves and triadic resonances in spherical fluid systems: The case of magnetized spherical Couette flow. *Physics of Fluids*, 33(4):044105, April 2021.

[216] Michael Hoff, Uwe Harlander, and Santiago Andrés Triana. Study of turbulence and interacting inertial modes in a differentially rotating spherical shell experiment. *Physical Review Fluids*, 1(4):043701, August 2016.

[217] Artur Perevalov, Rubén E. Rojas, and Daniel P. Lathrop. Turbulent dissipation in rotating shear flows: An experimental perspective. *Physica D: Nonlinear Phenomena*, page 133616, December 2022.

[218] Dennis P. M. van Gils, Sander G. Huisman, Gert-Wim Bruggert, Chao Sun, and Detlef Lohse. Torque Scaling in Turbulent Taylor-Couette Flow with Co- and Counterrotating Cylinders. *Physical Review Letters*, 106(2):024502, January 2011.

[219] Charles R. Doering and Peter Constantin. Energy dissipation in shear driven turbulence. *Physical Review Letters*, 69(11):1648–1651, September 1992.